Minerals Research Institute
of Western Australia

REPORT No. 554

Evolution of Proterozoic Multistage Rift Basins – Key Controls on Mineral Systems

Results of research carried out as MRIWA Project M0554

at

Centre for Exploration Targeting, University of Western Australia (1), Monash University (2) and University of Sydney (3)

by

Weronika Gorczyk[1], Patrice F Rey[3], Sandy Cruden[2], Peter Betts[2], Lu Li[1], Joe Ibrahim[3], Sinan Ozaydin[3], Alan Aitken[1], Uchitha Nissanka[2], Joel Kumwenda[2], Fatemeh Amirpoorsaeed[2], Anindita Samsu[2], and Mark Jessell[1]

January 2026

Distributed by: MRIWA
1 Adelaide Terrace
Perth WA 6000
to which all enquiries should be addressed

Acknowledgements

MINISTER FOR MINES AND PETROLEUM
Hon David Michael MLA

CHIEF EXECUTIVE OFFICER, MINERALS RESEARCH INSTITUTE OF WESTERN AUSTRALIA
Nicole Roocke

LEAD INVESTIGATOR, UNIVERSITY OF WESTERN AUSTRALIA
Professor Mark Jessell

AUTHORS:
Weronika Gorczyk, Patrice Rey, Sandy Cruden, Peter Betts, Lu Li, Joe Ibrahim, Sinan Ozaydin, Alan Aitken, Uchitha Nissanka, Joel Kumwenda, Fatemeh Amirpoorsaeed, Anindita Samsu, and Mark Jessell

REFERENCE
The recommended reference for this publication is:
Gorczyk, W., Rey, P., Cruden, S., Betts, P., Li, L., Ibrahim, J., Ozaydin, S., Aitken, A., Nissanka, U., Kumwenda, J., Amirpoorsaeed, F., Samsu, A., and Jessell, M. (2026). *Evolution of Proterozoic Multistage Rift Basins – Key Controls on Mineral Systems*. Minerals Research Institute of Western Australia Report 554. DOI 10.71342/573576910654

This report is available from the
National Library of Australia

PARTICIPATING ORGANISATIONS
Anglo American Exploration (Australia) Pty Ltd, Anglo American PLC, Australian Research Council, BHP Group Operations Pty Ltd, IGO Ltd, Monash University, Teck Australia Pty Ltd

Report DOI 10.71342/573576910654

FUNDING ACKNOWLEDGEMENT
This research was funded by MRIWA as Project M0554.

KEYWORDS AND TAGS
Basins, geodynamics, mineral systems

Published 2026 by the Minerals Research Institute of Western Australia
This report is published in digital format (PDF) and is available online at
https://www.mriwa.wa.gov.au/research-projects/project-portfolio/

CONTACT
Minerals Research Institute of Western Australia
1 Adelaide Terrace
Perth WA 6000
+61 8 6180 4340
mail@mriwa.wa.gov.au
https://www.mriwa.wa.gov.au/

Executive Summary

This study, undertaken as MRIWA Project M0554, investigates the evolution of Proterozoic multistage rift basins and their role in controlling mineral systems across northern Australia. By integrating numerical modelling, analogue modelling, geophysical interpretation, and isotopic datasets, the project develops a predictive framework for understanding basin evolution and metallogenic fertility in the North Australian Craton (NAC).

The research demonstrates that the NAC is a polyphase, composite craton formed through successive accretion of Archean and Paleoproterozoic terranes stitched along lithospheric-scale sutures. These inherited structures exerted long-lived control on basin geometry, sedimentation, inversion, and the localisation of mineralising fluids. Forward geophysical modelling shows that steep, WNW-trending faults extend to mid-crustal depths and coincide with isotopic boundaries, confirming their role as fossil terrane sutures and long-lived zones of weakness.

Analogue modelling provided a lithospheric-scale framework for testing how inherited structures, margin geometry, and kinematic boundary conditions influenced Proterozoic basin development and inversion. Experiments reproduced the coupled brittle–ductile behaviour of the lithosphere, showing that inward-dipping craton margins localised extension into asymmetric half-grabens that were later efficiently inverted along the same detachments. Outward-dipping margins, by contrast, generated broad, distributed faulting with limited reactivation during shortening, demonstrating how lithospheric inheritance dictates inversion efficiency. Oblique extension experiments (particularly at 30°) produced complex, multi-directional fault networks, *en echelon* geometries, and linkage structures that closely resemble those of the Isa and Calvert superbasins. These results show that single oblique tectonic phases can mimic structural overprinting often attributed to multiple sequential events. Selective inversion experiments further revealed that only certain rift basins invert during shortening, with strain localised in basin centres where crustal thinning enhanced ductile flow and buoyancy-driven folding. Together, these results emphasise that Proterozoic basin evolution reflects an interplay of obliquity, rheology, and inherited architecture, challenging conventional models of repeated orthogonal extension.

Numerical modelling demonstrates that Proterozoic basins cannot be interpreted through the lens of modern narrow-rift analogues alone. Simulations reveal that under hotter Proterozoic geotherms, extension developed as wide rifts, with strain distributed across broad zones of thinned lithosphere and expressed as laterally extensive, shallow basins. With time, progressive cooling strengthened the lithosphere, causing strain localisation, the formation of narrow rift geometries, and eventual continental breakup. This bimodal tectonic evolution provides a robust explanation for the geometry and longevity of basins such as McArthur, Birrindudu, and Roper, which preserve broad, shallow structures later overprinted by localisation and reactivation. The findings highlight that Proterozoic basins evolved under fundamentally different thermal and mechanical conditions than Phanerozoic rifts, and their architecture records the transition from wide to narrow rift modes driven by secular lithospheric cooling.

Geophysical modelling of gravity, magnetics, and seismic data provided a three-dimensional perspective on the crustal framework of the NAC. Forward models across key transects show that WNW-trending basement faults dip steeply to depths of 15–25 km, coinciding with isotopic

and geochronological boundaries, confirming their interpretation as fossil terrane sutures. Density contrasts between Archean and Paleoproterozoic blocks were resolved, highlighting the heterogeneous, polyphase assembly of the craton. The Ooradidgee half-graben is a striking example: forward modelling constrained its 20 km-wide, 14 km-deep geometry, linking potential-field anomalies with basin nucleation and fault-controlled subsidence. Integration with seismic reflectivity further demonstrated the role of inherited anisotropies in localising mafic intrusions and alteration zones. These results underline the predictive power of geophysics, bridging surface geology with concealed basement structures and showing how crustal inheritance governs both basin formation and mineral system fertility.

At the lithospheric scale, geophysical inversions and multiphysics workflows reveal new insights into mantle structure and rheology beneath the NAC. Gravity, seismic tomography, and magnetotelluric (MT) datasets consistently image vertically integrated anomalies that align with crustal sutures and basin boundaries. MT imaging highlights low-resistivity corridors interpreted as metasomatised, mantle-tapping structures that connect the deep lithosphere to the upper crust. These zones explain the spatial association of mineral belts such as Mount Isa, Tennant Creek, and Tanami with crustal discontinuities. Thermal–mechanical modelling further suggests that the NAC lithosphere is strongly heterogeneous, with Moho offsets, density contrasts, and zones of reduced elastic thickness (<20 km) promoting crust–mantle decoupling and long-lived reactivation. Together, these findings emphasise the central role of integrated geophysics in resolving concealed architecture, quantifying inheritance, and linking deep lithospheric structure to basin evolution and metallogenic fertility.

The implications of this work are twofold**.** For regional tectonic models, it highlights that Proterozoic basins must be interpreted in their own geodynamic context, shaped by hotter lithospheres and inherited fabrics, rather than through the lens of younger Phanerozoic analogues. For mineral exploration, it confirms that concealed crustal sutures and vertically integrated lithospheric corridors represent prime targets for world-class mineral systems. More broadly, it demonstrates that multidisciplinary integration—combining geophysical imaging, analogue experiments, numerical simulations, and isotopic mapping—is the key to understanding deep Earth processes and building predictive frameworks for exploration in covered terrains.

Table of Contents

Terms, Abbreviations and Acronyms

Abbreviation / Term	Full Form / Meaning
2D / 3D	Two-dimensional / Three-dimensional
AEM	Airborne Electromagnetic
ALE	Arnhem Land Event
ASO	Alice Springs Orogeny
AuSREM	Australian Seismological Reference Model
BDZ	Bruna Décollement Zone
CE	Cullen Event
DEM	Digital Elevation Model
DIC	Deformation Monitoring
DP	Data Point
EF	Exploring for the Future
EFG	Exploring for the Future Geoscience
ES	Envirospheres; Envirospheres®
ETF	Exploring for the Future (Geoscience Australia initiative)
GA	Geoscience Australia
Ga	Giga-annum (billion years ago)
GDF	Geodynamic Framework
GSE	Giddy Suite Event
GSSA	Geological Survey of South Australia
HCO	Halls Creek Orogen
HO1	Hooper Orogeny – First Phase
HO2	Hooper Orogeny – Second Phase
IF	Iron Fillings
ISB	Isa Superbasin

ISZ	Illogwa Shear Zone
LAB	Lithosphere–Asthenosphere Boundary
LC	Lower Crust
LE	Litchfield Event
LIP	Large Igneous Province
LM	Lithospheric Mantle
Ma	Mega-annum (million years ago)
MT	Magnetotellurics
MUE	Murchison Event
N / E / S / W	Compass directions: North, East, South, West
NAC	North Australian Craton
NE	Nimbuwah Event
NE / NW / SE / SW / WNW	Compass / structural orientations
NTGS	Northern Territory Geological Survey
OZ SEEBASE	Seismic Basement Mapping dataset (Geognostics proprietary model)
PDMS	Polydimethylsiloxane
pide	Petrophysical Interpretation tools for geodynamic Exploration
Pl	Colorific® Plasticine (black)
RGD	Ruby Gap Duplex
SE	Stafford Event
SPO	Shortening-related Preferred Orientation
TCE	Tennant Creek Event
TMI	Total Magnetic Intensity
TNE	Tanami Event
TWT	Two-Way Travel Time (seismic)
UC	Upper Crust

WA	Western Australia

Symbol / Term	**Definition / Description**	**Units**
A	Radiogenic heat production rate / Pre-exponential factor	$W\ m^{-3}$ (radiogenic); $MPa^{-n}\ s^{-1}$ (rheology)
Cp	Heat capacity	$J\cdot kg^{-1}\cdot K^{-1}$
E/Ea	Activation energy	$kJ\ mol^{-1}$
g	Gravity	m/s^2
L	Latent heat of fusion	$kJ\ kg^{-1}$
L_0	Initial length	m
n	Stress exponent	
T	Temperature	°C / K
t	Time	s
V	Activation volume	$m^3\ mol^{-1}$
Vp	P-wave velocity	$km\cdot s^{-1}$
Vs	Shear-wave velocity	$km\cdot s^{-1}$
α	Thermal expansivity/ Thermal diffusivity	$1/K$ / $m^2\ s^{-1}$
α, β, γ	Labels marking rifts in analogue models (figure captions)	–
ΔL	Length change	m
ΔL / L0	Normalised length change	–
ε_{xx}	Transverse strain	–
$\dot{\varepsilon}_{xx}$	Transverse strain rate	1/s
η	Viscosity	$Pa\cdot s$
θ	Obliquity angle	°
κ	Thermal diffusivity	$m^2\cdot s^{-1}$
ρ	Density	$kg\cdot m^3$
ρm	Mantle density	$kg\cdot m^{-3}$
$\sigma 1$	Maximum principal stress	Pa

ϕ	Melt fraction	
ρ	Density	kg m^{-3}
L_f	Latent heat of fusion	kJ kg^{-1}
n	Stress exponent	–
d	Grain size	m
p	Grain-size exponent	–
fH_2O	Water fugacity	MPa
r	Water fugacity exponent	–
E	Activation energy	$kJ\cdot mol^{-1}$
P	Pressure	MPa
V	Activation volume	$m^3\cdot mol^{-1}$
R	Gas constant	$J\cdot mol^{-1}\cdot K^{-1}$
$\sqrt{J_2}$	Second invariant of the deviatoric stress tensor	Pa
p	Pressure	Pa
v_i (v_x, v_y)	Displacement components in x and y directions	m
d_j (x, y)	Coordinate axes of the model domain	m
E_{xx}	Normal strain component in x-direction	–
E_{yy}	Normal strain component in y-direction	–
E_{xy}, E_{yx}	Shear strain components (x–y plane)	
μ_0	Bulk shear modulus	
X	Composition	
V_a	Activation volume	
ρcc	Crust Density	kg m^{-3}
ρm	Mantle Density	kg m^{-3}
ρa	Asthenosphere Density	kg m^{-3}
TP	Potential Temperature	K
zL	Lithospheric Thickness	m

List of Figures

List of Tables

1. Introduction

Proterozoic basins of northern Australia present a fundamental geodynamic paradox. Major depocentres such as the Birrindudu, Beetaloo, and South Nicholson basins preserve more than 10 km of sedimentary fill (Figure 1), yet seismic and gravity datasets demonstrate that the Moho beneath these regions remains relatively thick (Kennett et al., 2023). This contrasts with traditional models of basin formation, which emphasise either passive lithospheric extension, where the crust and mantle lithosphere are progressively thinned, or active asthenospheric upwelling, which drives thinning from below (Bott, 1976). In both cases, magmatism and sedimentary additions are expected to partially compensate for thinning, with isostatic adjustments maintaining balance over geological timescales (Aitken et al., 2013, 2015; Thybo & Nielsen, 2009). The North Australian Craton (NAC) basins, however, defy such simple explanations, suggesting that lithosphere-scale processes—including magmatic underplating, compositional thickening, and whole-lithosphere adjustments—were critical to their evolution.

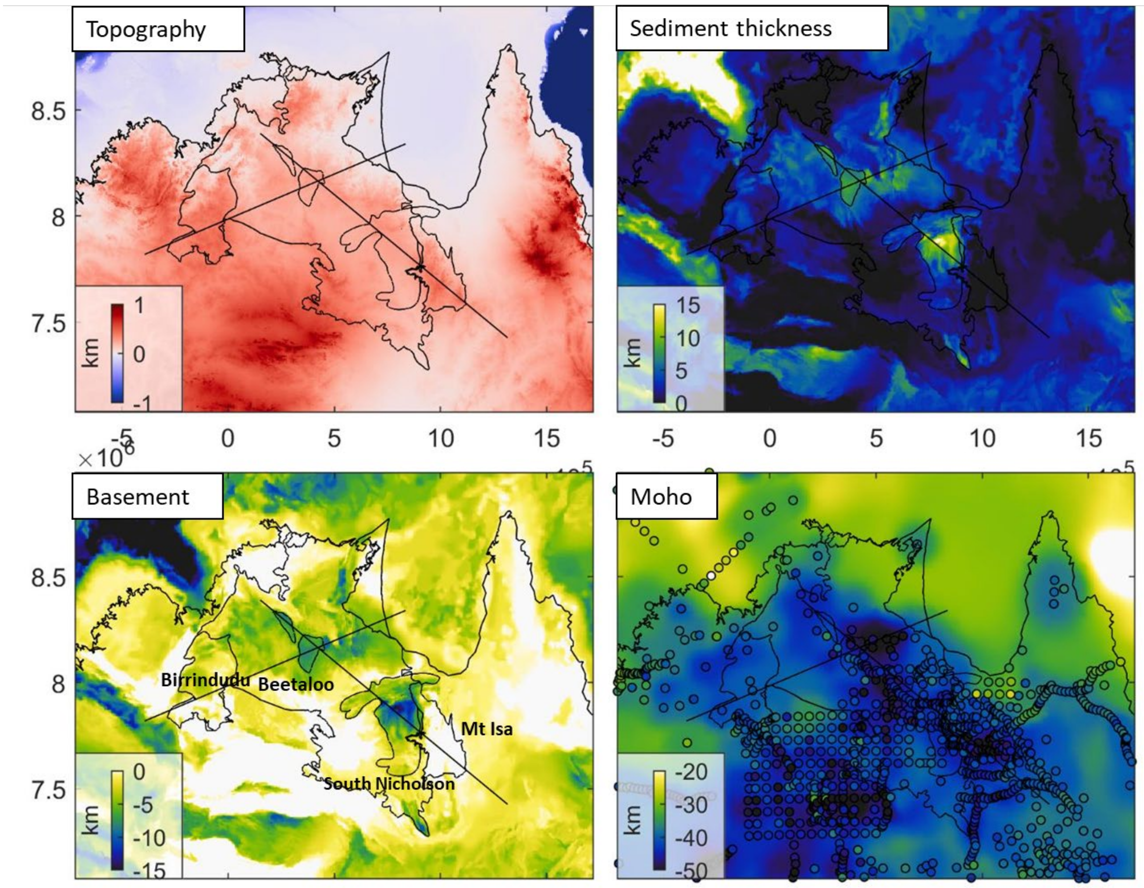

Figure 1. Regional characteristics of the North Australian Basins Region. Major basin depocenters, including Birrindudu, Beetaloo, and South Nicholson, are shown to have over 10 km of sedimentary strata (Geognostics, 2021). Notably, the Moho beneath these basins is relatively thick (Kennett et al., 2023) and suggests that the basin thickness is either not linked to net-crustal thinning, or that thinning was compensated by thickening e.g. through magmatic additions (Aitken et al., 2013, 2015; Thybo & Nielsen, 2009).

Understanding these processes requires a multi-technique modelling framework that can couple crustal and mantle dynamics. This study integrates three complementary approaches. First, geophysical imaging (seismic tomography, gravity–magnetic inversion, and deep seismic profiling) constrains crustal thickness, density, and inherited terrane boundaries, highlighting deep sutures and basement faults that governed basin initiation, subsidence, and later reactivation (Geognostics, 2021; Kennett et al., 2013; Korsch et al., 2012). Second, numerical thermo-mechanical modelling tests the consequences of elevated Proterozoic geotherms and radiogenic heat production. Simulations comparing cooler Moho conditions (~600 °C) with hotter Proterozoic-like states (~800 °C) show that warm, weak lithospheres promoted wide-rift basin development, which progressively evolved into narrower rifts as cooling and embrittlement occurred (Brun, 1999; Buck, 1991; Huismans & Beaumont, 2011). Third, analogue sandbox experiments physically replicate the interaction between brittle upper crust and ductile lower lithosphere under extension and inversion, demonstrating how inherited anisotropies and margin geometries produce segmented depocentres, selective inversion, and intracratonic orogens (Samsu et al., 2021, 2023; Zwaan & Schreurs, 2023).

Together, these approaches establish a process-based framework for understanding Proterozoic basin evolution in the NAC. They show that the basins developed under hotter, weaker lithospheric conditions than those typical of Phanerozoic analogues, with wide-rift modes of extension, lithosphere-scale compositional adjustments, and episodic inversion governing their long-term preservation. Importantly, these dynamics have direct metallogenic implications: wide-rift extension generated broad accommodation for thick stratigraphic packages, while subsequent inversion and fault reactivation localised deformation and fluid pathways, enhancing the fertility of mineral systems (Huston et al., 2020; Raimondo et al., 2021). By integrating geophysical, numerical, and analogue evidence, the study provides both a refined geodynamic model and a predictive framework for exploration in concealed Proterozoic terrains.

1.1. Minerals research/industry challenge and background

The minerals industry faces an escalating challenge: discovering new resources in frontier sedimentary basins that are deeply buried, structurally complex, and poorly defined. Many of Australia's Proterozoic basins host world-class ore deposits—including sedimentary- and volcanic-hosted Cu–Pb–Zn systems (e.g., Mount Isa, McArthur River, Century; Large et al., 2005; Huston et al., 2020), intrusion-related Cu–Au deposits (e.g., Broken Hill; Betts et al., 2016), and iron-oxide Cu–Au systems (e.g., Olympic Dam; Raimondo et al., 2021). Unlike young passive-margin basins, these Proterozoic successions preserve long-lived, multistage tectonic histories involving repeated rifting, inversion, magmatism, and interaction with deep-seated basement structures (Ahmad & Hollis, 2013; Betts & Giles, 2006). This architecture defies interpretation through modern analogues and requires models grounded in lithospheric inheritance and secular geodynamic change.

Exploration in these terrains is becoming increasingly costly and risky. As the search space extends beneath deep cover, traditional geological maps and first-order datasets provide limited predictive power. Sustaining the supply of critical and strategic metals therefore depends on developing new frameworks that link tectonic inheritance, lithospheric rheology, and thermal regimes to the fluid pathways and permeability networks that focus mineralisation (Champion, 2013; Huston et al., 2020).

This project addresses that need by using the NAC as a natural laboratory. We investigate how structural inheritance, lithospheric strength, mantle dynamics, and surface processes interact to shape basin evolution and mineral system development. By integrating analogue and numerical modelling with geophysical and geological datasets, the project develops predictive tools that reduce exploration risk, sharpen targeting strategies, and ultimately support more efficient, lower-impact exploration across Australia's resource-rich but underexplored sedimentary basins.

1.2. Objectives of the research

The overarching objective of this research is to develop a process-based and predictive framework for understanding the evolution of Proterozoic multistage rift basins and their control on mineral systems within the NAC. In contrast to younger, well-constrained rift systems, Proterozoic basins evolved under hotter, weaker lithospheres, where inherited crustal fabrics and thermal regimes exerted a dominant influence on basin geometry, inversion, and preservation (Betts et al., 2016; Aitken et al., 2013, 2015). This study therefore seeks to move beyond descriptive models and establish quantitative approaches that directly link lithospheric inheritance, tectonic processes, and mineralisation potential.

A first aim is to resolve the role of structural inheritance in governing basin development. Pre-existing basement sutures, terrane boundaries, and crustal-scale faults are hypothesised to have provided templates for subsequent rifting and reactivation (Champion, 2013; Betts et al., 2004). Understanding how these deep structures controlled basin initiation, compartmentalisation, and inversion is essential for reconstructing the tectonic evolution of the NAC and predicting mineralisation pathways (Crawford et al., 2010; Huston et al., 2020).

A second objective is to quantify the influence of thermal inheritance and Proterozoic geodynamic conditions on basin architecture. Elevated geotherms and enriched radiogenic heat budgets likely produced a lithosphere with markedly different strength profiles from those of younger tectonic settings (Aitken et al., 2013, 2015; Thybo & Nielsen, 2009). Testing how these conditions favoured wide-rift styles of extension, later transitioning into narrower rifts as the lithosphere cooled and strengthened, provides a new lens through which to interpret the distinctive geometries of Proterozoic depocentres (Kennett et al., 2023).

A third aim is to evaluate how surface processes interacted with deep lithospheric dynamics to shape basin evolution. Processes such as erosion, sediment loading, and dynamic topography redistributed stresses and influenced the activation or quiescence of crustal faults (Li et al., 2014; Cawood & Korsch, 2008). By linking mass redistribution at Earth's surface with lithospheric response, the study highlights the multi-scale coupling that underpins basin preservation and mineral system fertility.

To address these aims, the research integrates three complementary methodologies. Analogue modelling provides a physical means of reproducing lithospheric-scale extension and inversion, capturing the interaction between brittle upper crust and ductile lower lithosphere under controlled boundary conditions (Samsu at al.,2023). Numerical thermo-mechanical modelling simulates the effects of hotter Proterozoic geotherms, exploring how thermal state, rheology, and obliquity interact to produce the observed transition from wide to narrow rift modes (Samsu et al.,2023). Geophysical modelling of gravity, magnetics, seismic, and magnetotelluric data images the three-dimensional crustal and lithospheric framework of the NAC, resolving concealed sutures and quantifying density and conductivity contrasts between Archean and Proterozoic blocks (Heinson et al., 2006; Kumwenda et al., 2023). Together, these approaches establish a robust, multi-scale workflow for linking inherited lithospheric architecture to basin development and mineral system localisation.

Finally, the research is designed to deliver outcomes of direct relevance to the exploration industry. By combining analogue, numerical, and geophysical modelling with isotopic and geological datasets, the project generates predictive tools that reduce exploration risk in underexplored, covered terrains. These tools allow explorers to better anticipate basin geometries, fault reactivation histories, and the location of fertile fluid pathways, thereby focusing exploration efforts and supporting the discovery of the next generation of world-class mineral systems across Australia and other Proterozoic cratons worldwide (Huston et al., 2020; Wellman, 1988).

1.3. Scope

This project focuses on advancing the understanding of Proterozoic basin evolution and mineral system development within the NAC. Its scope is defined by three interrelated strands of investigation: (i) analogue modelling of lithospheric-scale deformation, (ii) numerical thermo-mechanical simulations of basin evolution under elevated Proterozoic thermal regimes, and (iii) geophysical modelling and data integration to image crustal and lithospheric architecture. Together, these approaches provide complementary insights into the processes that shaped basin initiation, growth, inversion, and long-term preservation.

The geographic scope is centred on the basins and basement terranes of northern Australia, including the McArthur, Birrindudu, Beetaloo, and South Nicholson basins, as well as the Tennant Creek, Pine Creek, and Litchfield regions. These basins are selected because they represent archetypal Proterozoic depocentres that host world-class mineral systems and because they provide an exceptional natural laboratory in which to evaluate the roles of structural inheritance, rheology, and mantle dynamics. While the focus is regional, the findings are designed to be transferable to other Proterozoic terranes worldwide.

Methodologically, the project integrates physical experiments, numerical simulations, and geophysical datasets in a multi-scale workflow. Analogue modelling explores how inherited structures, basin geometries, and margin obliquity control rifting and inversion. Numerical modelling tests the impacts of Proterozoic thermal states and rheological conditions on basin architecture. Geophysical datasets—including seismic, gravity, and magnetotelluric imaging—are inverted and interpreted to provide constraints on crustal thickness, lithospheric composition, and concealed structural boundaries. These complementary strands are used in tandem to produce testable, process-based models of basin development.

The scope does not extend to detailed stratigraphic reconstructions or resource inventory assessments. Instead, the emphasis is on lithospheric-scale processes and their implications for basin architecture and mineralisation pathways. Through this scope, the research bridges fundamental geodynamic understanding and applied exploration needs, aiming to reduce uncertainty in frontier basins by providing predictive insights into structural inheritance, basin preservation, and mineral system fertility.

2. Numerical Modelling

2.1. Numerical approach

We solve the problem of conservation of mass, momentum and energy for incompressible mantle flow and lithosphere deformation, using *Underworld2* - an open-source particle-in-cell finite-element code[*] - in conjunction with the *UWGeodynamics* library, an open-source python library for more user-friendly interaction with *Underworld2*. We assume a visco-plastic rheology depending on temperature, stress, strain, strain rate, and melt fraction. The densities of all rocks depend on temperature.

Table 1. Parameter values

Parameter	**Sediment**	**Upper Crust**	**Lower Crust**	**Mantle**
Thickness (km)	0-6	6-28	28-36	36-190
Reference density, ρ_r(kg m^{-3}) at 293.15 K	2600	2675-2725	2725-2825	3370
Thermal expansivity, α (K^{-1})	2.8e-5			
Heat capacity, C_p(J K^{-1} kg^{-1})	1000			
Thermal diffusivity, α(m^2 s^{-1})	0.9e-6			
Latent heat of fusion, L_f(kJ kg^{-1})	250			450
Radiogenic heat production, *A* (W m^{-3})	1.15e-6			0.02e-6
Mantle Heat Flow (W.m^{-3})	0.020 (Narrow Rift) / 0.040 (Wide Rift)			
Melt density change, $M_{\Delta\rho_r}$	0.13			
Liquidus term 1, a_0 (K)	1493			2013

---

[*] https://underworldcode.org

Parameter	Sediment	Upper Crust	Lower Crust	Mantle
Liquidus term 2, a_1 (K Pa^{-1})	-1.2e-7			6.15e-8
Liquidus term 3, a_2 (K Pa^{-2})	1.6e-16			3.12e-18
Solidus term 1, a_0 (K)	993			1393.661
Solidus term 2, a_1 (K Pa^{-1})	-1.2e-7			1.32899e-7
Solidus term 3, a_2 (K Pa^{-2})	1.2e-16			-5.104e-18
Friction coefficient	0.577			0.577
Softened friction coefficient	0.1154			0.0577
Cohesion, C (MPa)	20			20
Softened cohesion, C (MPa)	0.2			0.2
Pre-exponential factor, A (MPa^{-n} s^{-1})	6.60693e-8		10e-2	1600
Stress exponent, n	3.1		3.2	3.5
Activation energy, E (kJ mol^{-1})	135		244	520
Activation volume, V (m^3 mol^{-1})	0		0	23e-6
Water fugacity	0		0	1000
Water fugacity exponent	0		0	1.2
Melt viscous softening factor	1e-3		1e-3	1e-1
Melt fraction range for viscous softening	0.15 - 0.3		- 0.3	0.0- 0.2

2.1.1. Fundamental equations

Underworld solves the incompressible equations of continuity for momentum, energy, and mass as below:

$$\frac{\partial \tau_{ij}}{\partial x_j} - \frac{\partial \rho}{\partial x_i} = -\rho g \lambda_i$$

$$\frac{\partial T}{\partial t} + u_i \frac{\partial T}{\partial x_i} = \frac{\partial}{\partial x_i}\left(\kappa \frac{\partial T}{\partial x_i}\right) + Q$$

$$\frac{\partial u_i}{\partial x_i} = 0$$

Where x_i are the spatial coordinates, u_i is the velocity, T is temperature, ρ is density, *g* is gravity, λ_i is the unit vector in the direction of gravity, *t* is time, κ is thermal diffusivity, and *Q* is a source term for the energy equation. Summation on repeated indices is assumed.

Additional terms can be incorporated into the above equations. In the experiments presented, only radiogenic heating is added, unless explicitly mentioned otherwise - however, an additional experiment was run with partial melting, and so the associated terms and values are described below.

Both radiogenic heating and the thermal aspects of partial melting are incorporated into the energy equations as:

$$Q_{\text{radiogenic}} = \frac{A}{\rho C_p}$$

$$Q_{\text{partial melt}} = -1 \times \frac{L_f}{C_p}\frac{\delta M_f}{\delta t}$$

Where *A* is the rate of radiogenic heat production, $C_p$is heat capacity, L_f is latent heat of fusion, and $M_f$is the melt fraction.

The density of a material is defined via a function that depends on temperature and the melt fraction:

$$\rho = \rho_r \times (1 - \alpha(T - T_r) - (M_f \times M_{\Delta\rho_r}))$$

Where $\rho_r$is reference density, $\alpha$is thermal expansivity, $T_r$is reference temperature, and $M_{\Delta\rho_r}$is the fraction of density change when melted.

The melt fraction is calculated dynamically as part of the experiment, by using the super-solidus formula given by McKenzie and Bickle (1988):

$$T_{ss} = \frac{(T - T_{sol})}{(T_{liq} - T_{sol})} - 0.5$$

$$M_f = 0.5 + T_{SS} + (\mathrm{T}_{SS}^2 - 0.25) \cdot (0.4256 + 2.988 \cdot \mathrm{T}_{SS}^2)$$

Where T_{SS} is the normalised super-solidus temperature, T_s is the solidus, and T_l is the liquidus.

The solidus and liquidus are defined as:

$$T_{ss} = \mathrm{a}_0 + \mathrm{a}_1 P + \mathrm{a}_2 P^2$$

Where *P* is pressure, a_0, a_1, and a_2 are defined in Table 1. Parameter values.

The constitutive behaviour is assumed to be visco-plastic rheologies. For the viscous component, flow is computed using dislocation creep (Hirth and Kohlstedt, 2003):

$$\dot{\varepsilon}_{\text{disc}} = A\sigma^n d^{-p} f_{H_2O}^r \text{exp}\left(-\frac{E\ +\ PV}{nRT}\right)$$

Where $\dot{\varepsilon}$ is the effective strain-rate, *A* is the pre-exponential factor, *n* is the stress exponent, *d* is the grain-size, *p* is the grain-size exponent, f_{H2O} is the water fugacity, *r* is the water fugacity exponent, *E* is the activation energy, *P* is the pressure, *V* is the activation volume, *R* is the gas constant, and *T* is the temperature.

For the plastic component, failure is determined using the Drucker-Prager model:

$$\sqrt{J_2} = Ap\ + B$$

Where $\sqrt{J_2}$ is the second invariant of the deviatoric stress tensor, *p* is the pressure, and *A* and *B* are defined as:

$$A = \frac{2sin\phi}{\sqrt{3}(3 - sin\phi)}$$

$$B = \frac{6Ccos\phi}{\sqrt{3}(3 - sin\phi)}$$

Where *C* is the cohesion, and ϕ is the friction coefficient.

A linear strain-softening function is applied to the plastic component. As strain is accumulated from 0 to 20%, the material linearly weakens from its original cohesion and friction coefficient to their softened equivalents (defined in Table 1). Once fully weakened, the cohesion and friction coefficient remain constant at the softened values.

A stress limiter is applied to all rheologies, to limit the total strength of the lithosphere. The stress limiter is based on the workflow from Watremez et al. (2013), where a Von Mises criterion is applied, where:

$$\sqrt{J_2} = C$$

All materials are limited to 300 MPa in strength via this method, to account from pseudo-plastic processes, such as Peierls creep, and to ensure the lithosphere does not become artificially strong (Demouchy et al., 2013; Zhong & Watts, 2013). To ensure numerical stability, all rock materials also have a minimum and maximum viscosity range of 1e18 Pa·s to 5e23 Pa·s.

Partial melting has a mechanical effect, whereby material undergoing melt will reduce in viscosity, within a given melt fraction range (defined in Table 1), based on the following model:

$$\eta_{melted} = \eta \times (1 \times M_{f\%} + \eta_{factor} \times (1 - M_{f\%})$$

Where η_{melted} is the viscosity after melting, η is the viscosity calculated from the flow law, $M_{f\%}$ is a normalised linear interpolation of the melt fraction between the lower and upper limits of the melt fraction range, and η_{factor} is the melt viscous softening factor the material undergoes once fully melted.

2.1.2. Rheologies

The rheologies used are based on published work: the upper crust flow law is a wet quartzite from Paterson and Luan (1990); the lower crust flow law is a mafic granulite from Wang et Al. (2012); and the lithospheric mantle flow law is a wet olivine from Hirth and Kohlstedt (2003). Viscous flow laws that use 0 for the water fugacity exponent typically have this effect incorporated into the pre-exponential factor. Radiogenic heat production values are from Hasterok and Chapman (2011). Melt and other parameters are derived from Rey and Müller, (2010). The air material uses an isoviscous 1e18 Pa·s flow law, with a density of 1 kg m^{-3}, and a heat capacity of 1000 J K^{-1}. See Table 1 for detailed parameters values.

2.1.3. Boundary conditions

2.1.3.1. Isostatic basal condition

A constant pressure boundary condition is defined along the bottom wall to model isostatic equilibrium. The pressure applied is calculated at the beginning of the experiments by calculating the lithostatic pressure across the entire domain and using the average pressure from along the bottom wall. This value is then applied throughout the entire experiment.

Using a constant pressure boundary condition on the base of the model removes a significant constraint on the vertical position of the material in the domain, which can lead to instabilities and large artificial vertical velocities. To help stabilise the experiments, the vertical walls use a no-slip velocity boundary condition, and the top wall has a free-slip, no flux boundary condition (that is, no material can pass through the top wall).

2.1.3.2. Free surface and top wall boundary condition

To emulate a free surface, the experiments all use an air layer. The air material cannot be modelled at natural values of viscosity or thermal expansivity since it would be numerically very expensive and unstable. A common substitute is to use a “sticky-air” layer, which has unrealistically high viscosity, but is low enough to not interfere with underlying geodynamics. The isostatic criterion formula from Crameri et al, 2012 gives a criterion for determining the thickness and viscosity of a good sticky-air layer. Based on this, our experiments use an air-layer with a viscosity of 1e18 Pa·s, and a thickness of 20 km.

The top wall has a free slip, no flux boundary condition. The no flux condition helps stabilise the isostatic boundary condition on the wall, since it fixes the vertical position of the material in the domain. However, it also means that air material cannot flow in or out of the domain as topographic highs and lows form. Therefore, we give the air a high compressibility, so that it can expand, or contract as required.

2.1.3.3. Velocity boundary condition on vertical walls

To drive extensional deformation, we impose a horizontal velocity V_x of 1.073 cm/yr on both vertical walls, achieving an initial averaged strain rate of 1.5e-15 s^{-1}. Inversion is driven by inverting the sign of V_x applied to the vertical walls.

2.1.3.4. Thermal boundary conditions

The top wall of the model domain is held constant at 293.15 K (20 °C) along with any air material, and the bottom wall is held at 1623.15 K (1350 °C). Before the experiment is run, the asthenosphere has an additional boundary condition, so that it too is held at 1623.15 K (1350 °C). The model is then thermally equilibrated to achieve a steady state geotherm.

Once the experiment starts, the asthenospheric boundary condition is removed to let the thermal lithosphere evolve in a self-consistent manner.

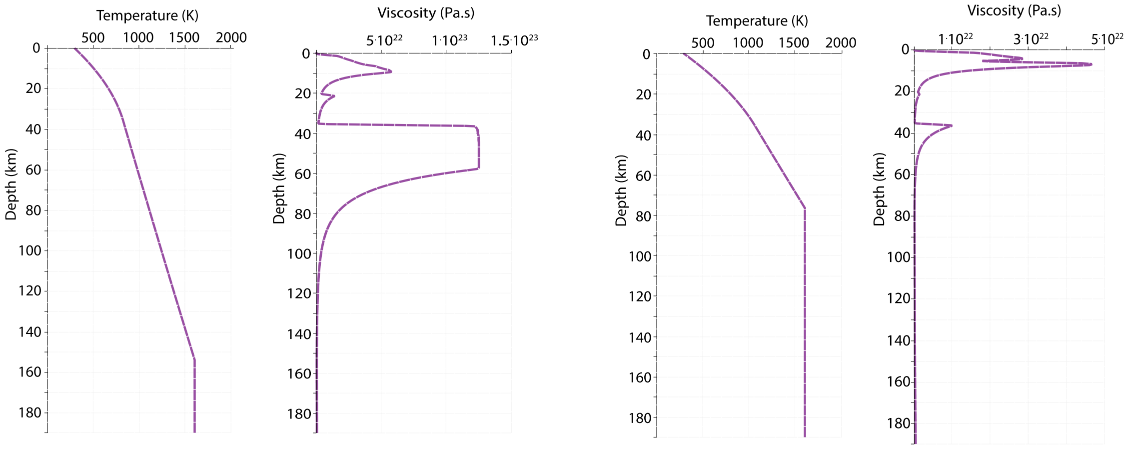

Figure 2. Temperature and viscosity profile (for a nominal strain rate of 1e-15 s^{-1}) for narrow rift model (left panel), and wide rift model (right panel).

2.1.4. Numerical parameters

2.1.4.1. Time stepping

Time stepping in Underworld uses the Courant-Friedrichs-Lewy (CFL) condition to ensure stable convergence. The CFL is a function of grid size, absolute maximum velocity, and maximum diffusivity. On top of this, to ensure a numerically efficient and temporally stable model run, the computed CFL timestep is multiplied by a factor of 0.1.

2.1.4.2. Solver parameters

The isostatic boundary condition used in these experiments is particularly sensitive to both the timestep size, and the solver parameters used. Underworld2 provides a tool called the penalty method, which is effective in solving difficult nonlinear problems - however, it is not compatible with compressible materials. Instead, we use stricter tolerances on the direct solver, with the nonlinear tolerance at 5e-4, and the linear solver tolerance at 1e-8. These parameters (along with the reduced CFL factor) produce very stable experiments, with very little velocity jumps and the associated strain-rate ‘oscillating’.

2.2. Modelling of Proterozoic continental extension

In northern Australia, Paleoproterozoic to Mesoproterozoic polyphase extension produced a complex system of stacked shallow intracontinental basins, including the Birrindudu, McArthur, South Nicholson, Fitzmaurice, Tomkinson, Davenport, and Lawn Hill basins (Rawlings, 1999). These basins record a long-lived history of tectonism, sedimentation, and magmatism extending over several hundred million years (Myers et al., 1996). Although some sub-basins accumulated impressive sedimentary and volcanic successions reaching up to 12 km in total thickness, this was not the product of a single extensional phase. Instead, multiple episodes of extension, separated by intervals of tectonic inversion and basin reactivation, each contributed only a few kilometres of additional fill (Soares et al., 2025). Well-documented successions such as the Tawallah, McArthur, and Roper groups of the McArthur Basin exemplify this episodic accumulation style, where lateral thickness variations point to strong growth-fault control and syn-depositional tectonism (Blaikie & Kunzmann, 2020).

This observation raises important questions about the nature of Proterozoic lithosphere and its response to extension. Owing to the strong temperature dependence of rock rheology, and the enhanced abundance of heat-producing radiogenic elements in the early Earth, we hypothesise that extensional processes during Proterozoic times may have been significantly different from those of the Phanerozoic (Giles et al., 2002). In particular, a warmer lithosphere would have been mechanically weaker, with lower effective viscosities and reduced strength contrasts between crust and mantle (Myers et al., 1996). To explore this idea, we employ coupled thermo-mechanical numerical experiments that compare extension of a modern-like lithosphere, characterised by a Moho temperature (TMoho) of ~600 °C, with that of a hypothesised Proterozoic lithosphere with TMoho elevated to ~800 °C.

Our modelling demonstrates that many Proterozoic basins likely developed under a wide-rift mode of extension, in contrast to the narrow-rift style often observed in present-day analogues. Under these warmer geotherms, deformation was distributed across broader regions rather than being localised into narrow rift valleys. At the same time, the elevated steady-state geotherm delivered a Moho that was persistently hotter and weaker, further promoting ductile flow and widespread subsidence (Soares et al., 2025). This combination of factors offers a plausible explanation for the geometry, longevity, and repeated reactivation of Proterozoic basins across northern Australia, and suggests that their tectonic inheritance played a key role in controlling subsequent basin evolution and metallogenic fertility (Large et al., 2005).

2.2.1. Methodology

Our model consists of a lithosphere standing above the asthenosphere. We include a 30 km layer of compressible air, which allows the development of topography. The continental has a thickness of 36 km. This model is mapped over a Cartesian grid of dimension 680 km (x-axis) by 220 km (y-axis) with 1 km grid cell resolution (Figure 3). An initial random plastic strain (up to 5%) is imposed in the crust to model existing damage and faulting.

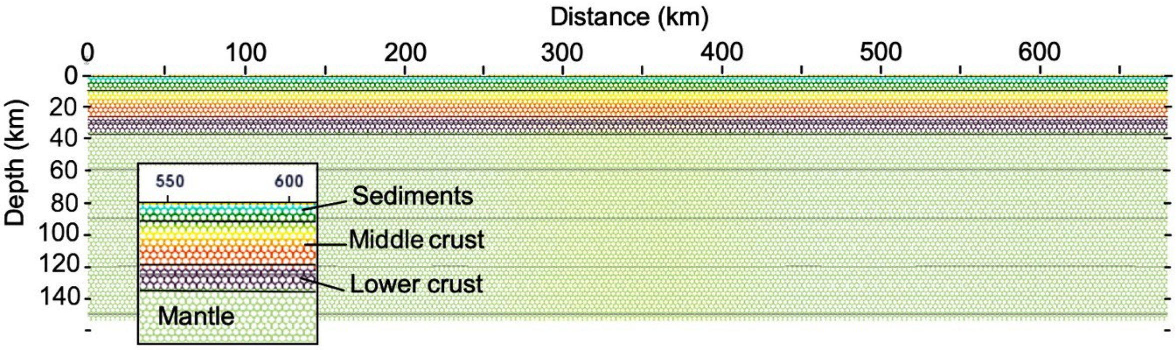

Figure 3. Initial lithosphere model. The crust is represented by sedimentary rocks (top 6 km), 22 km of mid-crust (6 to 28 km depth), and 8 km of lower crust (28 to 36 km depth). The crust stands above a lithospheric mantle the base of which corresponds to the isotherm 1300 °C.

2.2.2. Results and findings

Our coupled thermo-mechanical experiments highlight how lithospheric thermal state exerts a first-order control on rift style and basin evolution. In Model MT600 (T_{Moho} = 600 °C), representative of a modern-like lithosphere, extension is strongly localised into a narrow rift Figure 4, left panel). Here, high strain rates concentrate deformation into a limited zone, producing deep, asymmetric basins bounded by major normal faults. These features are consistent with Phanerozoic narrow-rift systems such as the East African Rift, where localised strain creates significant accommodation but limited lateral basin continuity.

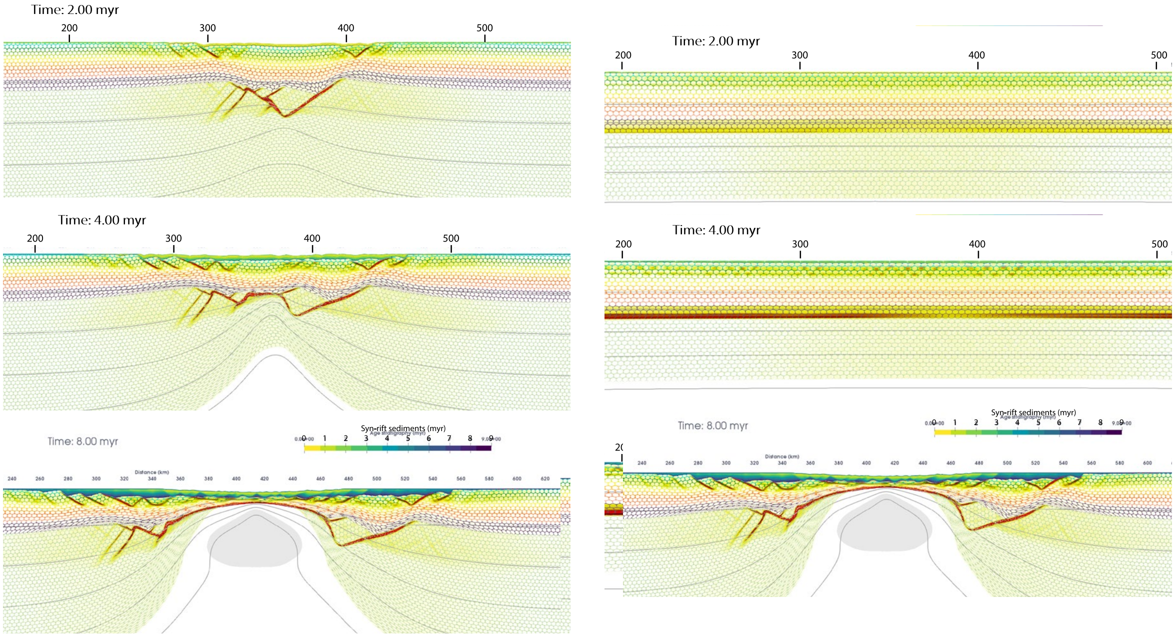

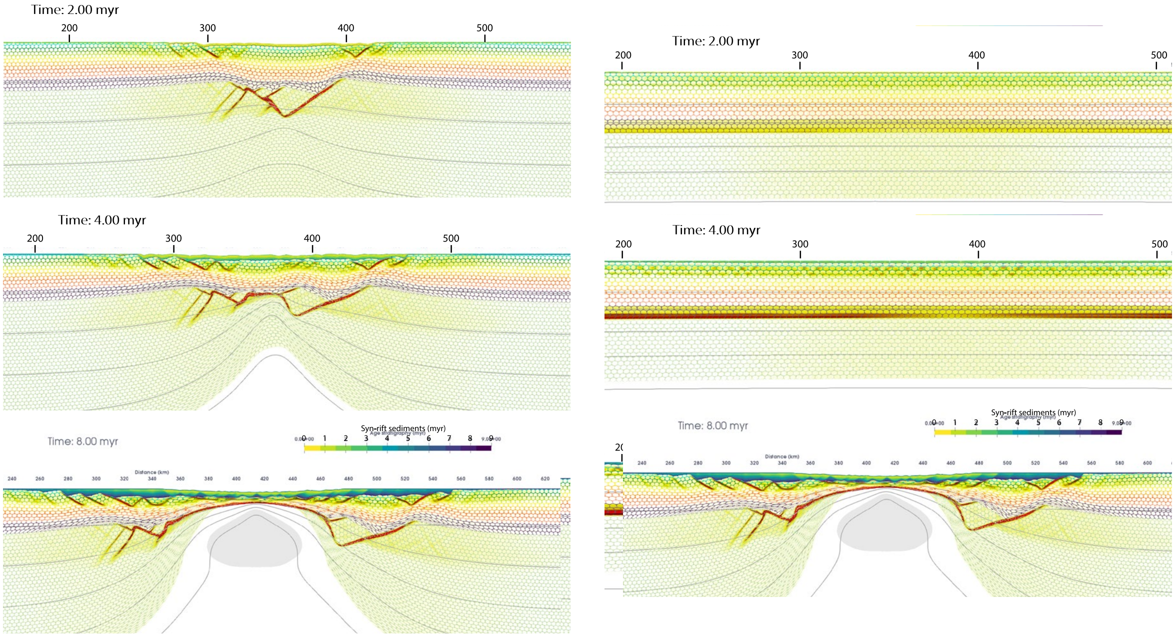

Figure 4. MT600 (TMoho=600 ºC, left panel) delivers a narrow rift, whereas Model MT800 (TMoho=800 ºC, right panel) delivers a wide rift. Zones of active deformation are mapped in red.

By contrast, Model MT800 (TMoho = 800 °C), representative of a hotter Proterozoic lithosphere, yields a wide rift geometry Figure 4, right panel). Extension is broadly distributed across a wide region of thinned lithosphere, with strain rates relatively low and faulting diffuse. This results in numerous shallow depocentres forming a mosaic of connected basins with only modest thickness variations. Such a configuration explains the architecture of northern Australian intracontinental basins, many of which extend laterally for hundreds of kilometres yet preserve relatively shallow stratigraphy punctuated by local growth-fault-controlled depocentres.

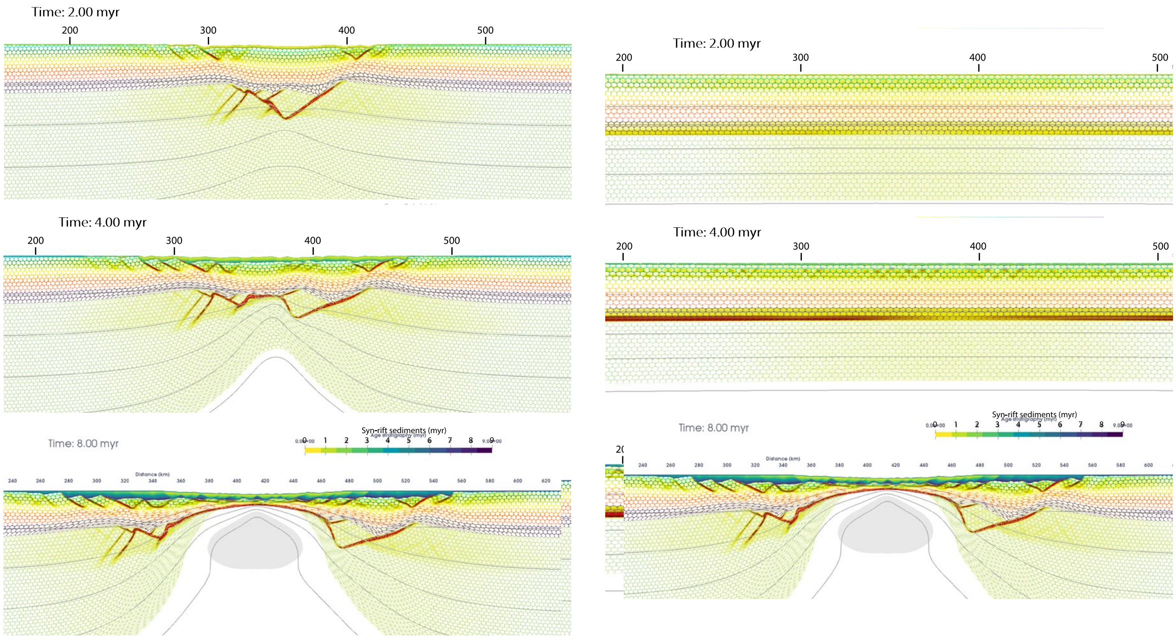

Importantly, the experiments also demonstrate that wide rifts are transient features. Even under warm geotherms, continued extension leads to progressive lithospheric thinning, asthenospheric cooling, and strengthening of the lower crust. As shown in Figure 5, after 20 Myr of extension (top panel) deformation is still broadly distributed, but by 27.5 Myr (bottom panel) strain becomes increasingly focused, leading to narrow-rift geometries and eventual continental breakup. This evolutionary pathway implies that Proterozoic basins may record multiple superimposed extensional events: early phases of wide-rift distributed subsidence followed by narrower, fault-controlled reactivations. Such polyphase behaviour aligns well with observed stratigraphic packages such as the Tawallah, McArthur, and Roper groups, where basin-wide sedimentation is overprinted by localised structural control.

a) 20 Myr of extension

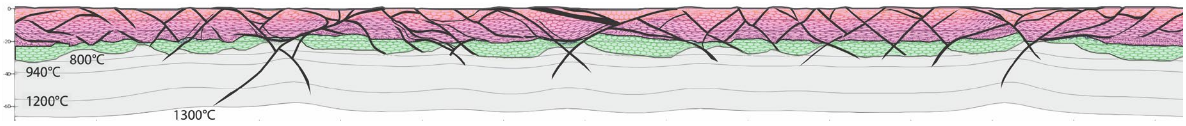

b) 27.5 Myr of extension

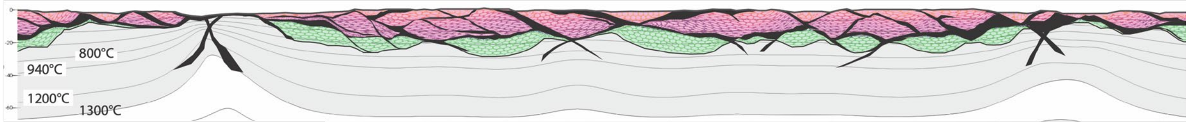

Figure 5. a) wide rift following 20 Myr of extension, b) following 27.5 Myr of extension (bottom). The pre-rifting lithospheric mantle is mapped in green. The mantle in grey corresponds to the syn-rifting cooling of the asthenosphere below 1300 ºC.

Together, these models suggest that Proterozoic extension was characterised by an initial wide-rift mode linked to high Moho temperatures, followed by a shift to narrow rifting as the lithosphere cooled and embrittled. This bimodal evolution provides a unifying explanation for the geometry, longevity, and repeated reactivation of northern Australian basins.

2.2.3. Discussion

Our numerical experiments reveal that under warmer Proterozoic geotherms, extension evolves through a bimodal tectonic cycle. During the initial phase, extension is accommodated by a long-lived wide rift with distributed deformation, low strain rates, and broadly connected shallow basins. With time, however, the system cools and strengthens: the lower crust becomes more rigid, leading to stronger mechanical coupling between the brittle upper crust and the upper mantle. This change drives a transition into a shorter-lived, high-strain-rate narrow rift stage that culminates in breakup. Similar dual-mode behaviour, where wide rifts evolve into narrow rifts with progressive cooling and strengthening of the lithosphere, has been recognised in both modern passive margins and the Australian North West Shelf (Gartrell, 2000) and is consistent with polyphase rift evolution recorded globally (Gartrell et al., 2022).

These results resonate with the geological record of northern Australia, where Paleoproterozoic to Mesoproterozoic polyphase extension produced stacked intracontinental basins such as McArthur, Birrindudu, Tomkinson, and Davenport. Many of these basins are broad, shallow, and laterally continuous, consistent with wide-rift development, yet they also preserve evidence of episodic localisation and tectonic reactivation, reflecting the narrowing stage observed in our models (Rawlings, 1999; Soares et al., 2025). The Daly Waters Fault Zone, for example, records multiple extensional and compressional phases, highlighting how tectonic inheritance repeatedly influenced basin reactivation (Soares et al., 2025).

From a geodynamic perspective, the findings align with predictions of secular Earth cooling. A hotter, more radiogenic Proterozoic lithosphere would have been mechanically weaker and more buoyant, favouring distributed extension and flat-lying basin systems (Myers et al., 1996; Giles et al., 2002). Over time, thermal re-equilibration and cooling promoted localisation, a pattern echoed in the inversion geometries of narrow versus wide rifts observed in nature (Blaikie & Kunzmann, 2020).

This transition from wide to narrow rifting helps explain why Proterozoic basins could accumulate thick sedimentary successions over long durations yet still preserve strong structural inheritance that guided subsequent basin evolution and inversion (Rawlings, 1999). Importantly, this tectonic inheritance also conditioned fluid flow, fault reactivation, and metallogenic systems. The world-class Zn–Pb–Ag deposits of northern Australia, such as McArthur River, occur in structurally controlled depocentres that developed during these multiphase rifting episodes (Large et al., 2005).

Our experiments support the hypothesis that many Proterozoic basins were fundamentally wide-rift systems, shaped by the hotter lithosphere of the time, and later narrowed during cooling and reactivation. This bimodal tectonic evolution provides a unifying framework for understanding the geometry, longevity, and metallogenic fertility of northern Australia's Proterozoic intracontinental basins.

2.3. Modelling of Proterozoic rift inversion

Rift inversion is a fundamental process that reworks basin architecture and controls the distribution of deformation, uplift, and fluid flow. In the Phanerozoic record, inverted rifts often reflect narrow-rift systems formed under relatively cool lithospheric conditions (TMoho < 650 °C). By contrast, Proterozoic rifts developed within a warmer lithosphere (TMoho > 750 °C), leading to wider rift geometries and potentially different inversion outcomes. Understanding these differences is essential for interpreting the architecture of Proterozoic orogens, such as those across northern and central Australia, and for evaluating how inherited structures control basin reactivation, fluid flow, and mineralisation.

Inversion behaviour is strongly dependent on rift mode. Wide rifts, typical of the Proterozoic, are underlain by distributed ductile deformation and broad zones of crustal thinning. During later compressional events, such rifts are more likely to show selective inversion, where only certain depocentres or basin segments are uplifted, while others subside due to competing thermal and flexural effects (Samsu et al., 2023). By contrast, narrow rifts with steep, well-developed normal faults tend to exhibit more direct and localised inversion along pre-existing fault systems (Gartrell et al., 2022).

The Australian record provides clear examples of both behaviours. In the southern Georgina Basin, Neoproterozoic rift faults were selectively reactivated during the Alice Springs Orogeny, producing high-angle reverse faults that inverted earlier extensional basins (Greene, 2010). Similarly, in the Mount Isa Inlier, the Isan Orogeny reworked earlier wide-rift basins, producing complex superimposed shortening and wrench geometries that reflect the mechanical inheritance of earlier extension (O'Dea et al., 1997).

Recent geodynamic models also emphasise that lithospheric thermal state plays a critical role. Inversion of wide rifts formed in warm lithosphere is influenced by the balance between tectonic shortening, post-rift thermal subsidence, and surface processes, meaning that some inverted rifts may paradoxically continue to subside in parts of their depocentres (Oravecz et al., 2024). This helps explain the persistence of long-lived, reactivated basins in northern Australia that preserve evidence of both inversion and renewed subsidence.

Here, we present a series of coupled thermo-mechanical experiments designed to test how inversion differs between narrow and wide rifts, and how the duration of post-rift cooling influences orogenic style. Our results build on analogues from the Browse and North West Shelf, where inversion style was shown to depend on inherited structural architecture, with low-angle detachment faults more prone to reactivation than steep, narrow-rift faults (O'Brien et al., 1999). These comparisons provide a framework for interpreting the Proterozoic inversion record and its implications for basin-hosted mineral systems.

2.3.1. Methodology

To investigate the inversion of narrow and wide rifts under contrasting thermal regimes, we carried out two suites of two-dimensional thermo-mechanical experiments using *Underworld 2*, an open-source finite-element geodynamic modelling framework. The model domain measured 680 km in length and 220 km in depth, discretised into a Cartesian grid with 1360 × 440 elements at 500 m resolution. Approximately 3.6×10^7 Lagrangian particles were employed to track the material properties, enabling high-resolution representation of lithospheric and asthenospheric deformation.

The experiments compared rift evolution under two thermal structures: a narrow rift configuration with a Moho temperature of 600 °C (MT600), representative of a cooler, modern-like lithosphere, and a wide rift configuration with a Moho temperature of 800 °C (MT800), representing a warmer Proterozoic lithosphere. In both cases, the lithosphere–asthenosphere boundary was defined by the 1300 °C isotherm.

The rheology of all materials followed viscoplastic behaviour governed by a Drucker–Prager yield criterion, with viscosity dependent on temperature, stress, strain, and melt fraction. Strain weakening was implemented to simulate fault evolution: cohesion was reduced by an order of magnitude and the friction coefficient by a factor of five in the crust as plastic strain accumulated, while in the mantle both parameters were reduced by a factor of ten. Partial melting was also included, reducing density by 13% and viscosity by up to three orders of magnitude in the crust and two orders in the mantle. Melt fractions were capped at 30% in the crust and 2% in the mantle.

The key material parameters used in the models are summarised in Table 2, which includes densities, viscosities, cohesion, and friction coefficients for the different lithospheric layers and sediments. These values are based on experimentally derived flow laws for wet quartz, wet olivine, and dry mafic granulite (Paterson & Luan, 1990; Hirth & Kohlstedt, 2004; Wang et al., 2012).

Table 2. Rheological parameters for numerical experiments. [a]All materials have a thermal expansivity of 2.8 × 10-5 K^{-1}. [b]The wet quartz, wet olivine, and dry mafic granulite rheologies used are of Paterson and Luan (1990), Hirth and Kohlstedt (2004), and Wang et al. (2012), respectively. [c]To enhance structural complexity of the experiments, the top kilometre of sediments employs an iso-viscous viscosity of 10^{20} Pa·s. This creates a 1 km thick décollement layer above which syn-tectonic sediments are deposited.

Material	**Density (kg m^{-3})[a]**	**Viscosity (Pa s)[b]**	**Cohesion (MPa)**	**Friction coefficient**
Sticky air	1	5×10^{18}	N.A.	N.A.

Material	**Density** (kg m^{-3})[a]	**Viscosity (Pa s)[b]**	**Cohesion (MPa)**	**Friction coefficient**
Syn-tectonic sediments	2300	0.1 x Wet Quartz	1 - 0.1	0.577 - 0.1154
Sediment[d]	2600	Wet Quartz	20 - 0.2	0.577 - 0.1154
Continental crust above 21 km depth	2675-2750	Wet Quartz	20 - 0.2	0.577 - 0.1154
Continental crust below 21 km depth	2775-2825	Dry Mafic Granulite	20 - 0.2	0.577 - 0.1154
Lithospheric mantle	3370	Wet Olivine	20 - 0.2	0.577 - 0.0577
Asthenosphere	3370	Wet Olivine	20 - 0.2	0.577 - 0.0577

2.3.2. Results and findings

In the narrow rift case, inversion is dominated by the reactivation of basin-bounding listric faults. As contraction proceeds, these structures are inverted to accommodate shortening, producing significant surface uplift of up to 3.8 km (Figure 6). The asymmetric orogenic belts that develop are associated with flexural foreland basins, created by the isostatic response to loading and underthrusting of extended margins. Deformation propagates outward into the foreland, producing a wide zone of crustal thickening. In the lower crust, convergence is accommodated by ductile folding, while the lithospheric mantle undergoes viscous flow and shear. Although the timing of inversion relative to extension influences sediment thickness and foreland basin development, the overall geometry of the inverted orogen is relatively consistent. Longer quiescence allows more sediment accumulation, which results in wider orogens with greater vertical relief, but the style of inversion remains focused and asymmetric.

The wide rift case produces a far more complex inversion history, highly sensitive to the thermal relaxation prior to contraction. If inversion follows immediately after extension, deformation is broadly distributed, with widespread reactivation of syn-extensional faults and ductile buckling of the crust. This produces a broad uplifted plateau with relatively subdued relief (Figure 7). However, with increasing post-rift quiescence and cooling, the inversion architecture changes dramatically. After ~20 Myr of cooling, only subtle damage zones develop near the Moho, but at ~40 Myr, cooling and embrittlement of the lithosphere strengthen the mantle, promoting the localisation of deformation into shear zones. These shear zones form symmetrical flower structures, while the crust continues to deform in a distributed manner.

Narrow rift inversion following extension

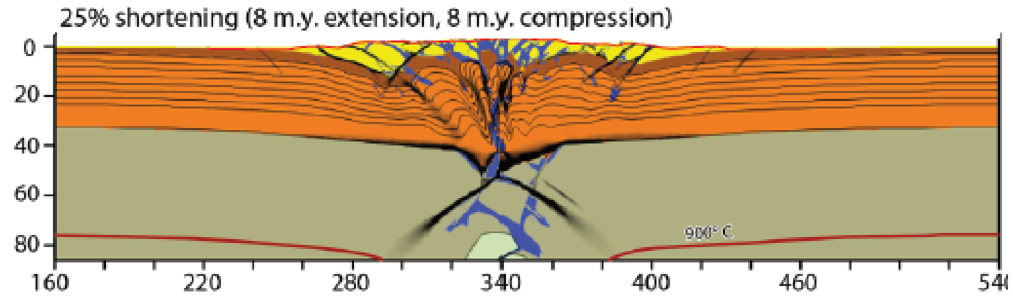

Narrow rift inversion after 60 myr of quiescence

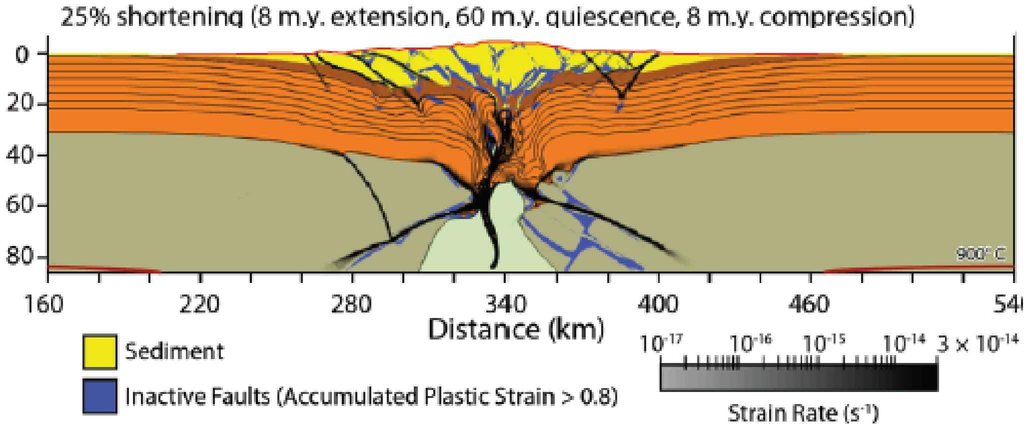

Figure 6. Inversion of narrow rift. In the top panel, inversion occurs soon after extension finishes. In the bottom panel inversion occurs following ~60 Myr of quiescence and cooling.

Wide rift inversion immediately following extension

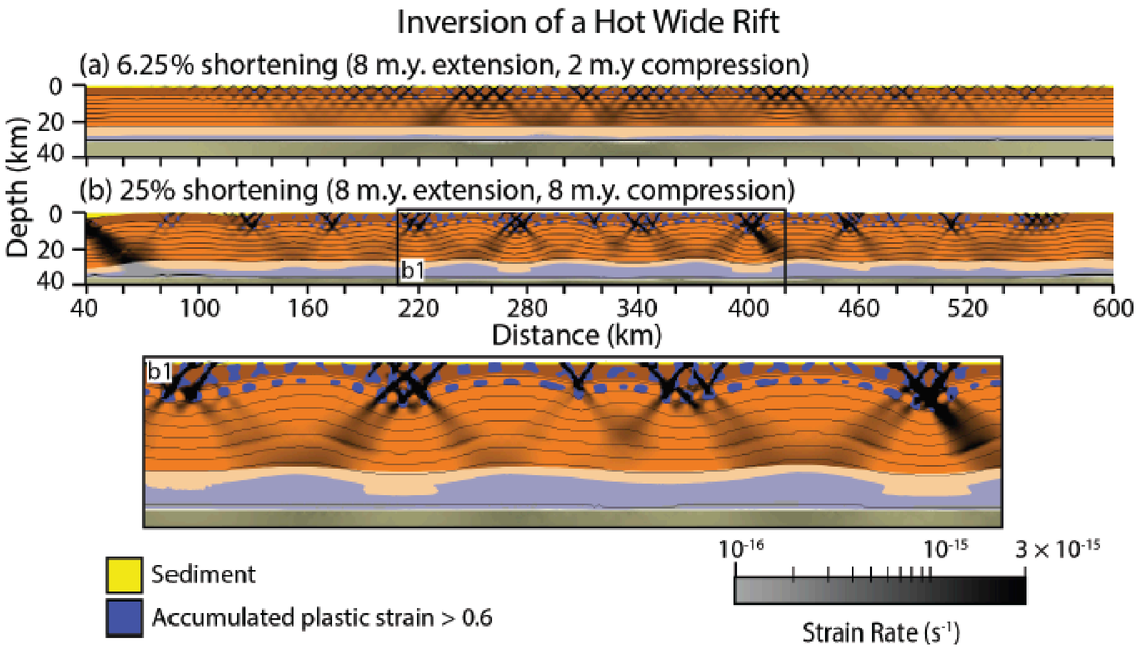

Figure 7. Inversion of wide rift soon after extension.

After ~60 Myr of quiescence, the inversion of a wide rift produces an architecture markedly different from both the narrow rift case and the hot wide rift case. Cooling strengthens the mantle to the extent that deformation becomes decoupled between the crust and mantle. Shear zones propagate through the mantle, forcing underthrusting of one rift margin beneath the other, while the deep crust undergoes significant buckling. The result is major offsets in the Moho, in some cases up to tens of kilometres, but relatively limited surface uplift (Figure 8). This architecture demonstrates that wide rifts, once thermally relaxed, are prone to developing deep-seated shear zones and crust–mantle decoupling, fundamentally different from the coherent deformation of hot wide rifts or the focused inversion of narrow rifts.

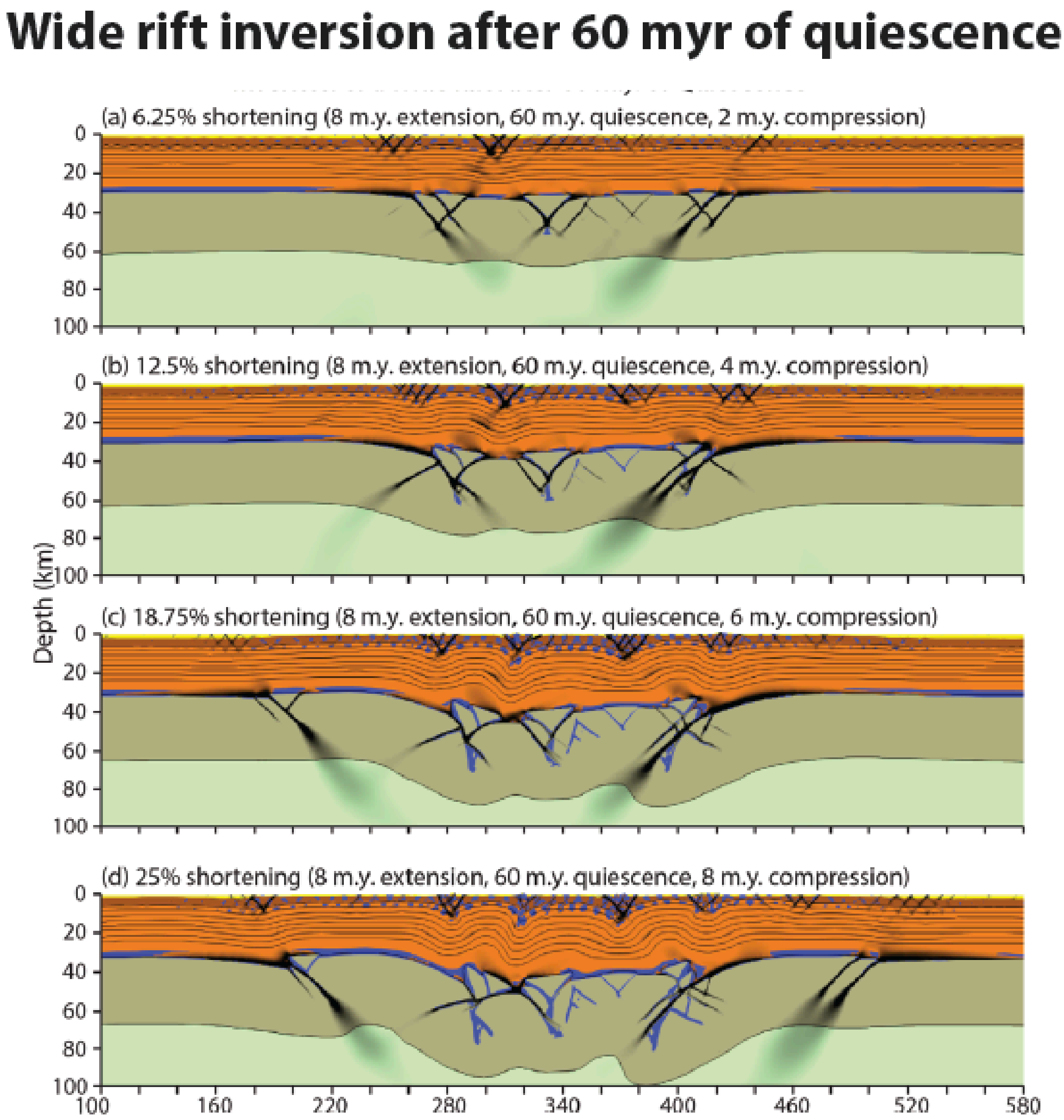

Figure 8. Inversion of wide rift following 60 Myr of quiescence and cooling.

These results demonstrate that the architecture of inverted rift orogens depends critically on both the initial mode of rifting and the thermal state of the lithosphere at the time of inversion. Narrow rifts consistently invert to form asymmetric, high-relief orogens with associated foreland basins, whereas wide rifts may produce either broad, low-relief plateaus (if hot) or structurally complex, Moho-offset orogens (if cooled). The thermal evolution of the lithosphere, particularly the duration of post-rift cooling, is therefore a key control on inversion style and long-term crustal architecture.

2.3.3. Discussion

The experiments demonstrate that the impact of post-rift quiescence on inversion style is strongly dependent on the initial rift mode. In narrow rifts, cooling intervals prior to contraction have relatively limited influence on the outcome. Inversion is consistently accommodated by the reactivation of listric basin-bounding faults, producing asymmetric orogenic belts with pronounced surface uplift and associated flexural foreland basins. Additional cooling time allows more sediments to accumulate, which enhances the vertical relief of the resulting orogen, but the overall style of inversion remains focused and localised. This relative insensitivity highlights the mechanical efficiency of narrow rift geometries in focusing contractional strain into pre-existing fault systems, regardless of thermal state (Hansen & Nielsen, 2003).

In wide rifts, however, the effect of cooling is profound. Immediately after extension, while the lithosphere remains hot and weak, inversion is distributed across the basin, producing broad plateaus with relatively subdued relief. With prolonged quiescence, cooling strengthens the mantle relative to the fault-weakened crust, creating strong mechanical stratification. As a result, deformation becomes decoupled: the crust continues to deform diffusely, while the mantle localises shortening into shear zones. These shear zones can propagate upward, offsetting the Moho and forcing underthrusting between rift margins. The consequence is a fundamental shift in orogenic style—from wide, low-relief plateaus in hot conditions to structurally complex, deep-seated shear zones and Moho offsets in cooled lithospheres. This highlights that lithospheric cooling, rather than the initial extension geometry alone, is the primary control on the evolution of wide rift inversion (Vasey et al., 2023; Oravecz et al., 2024).

These findings are consistent with analogue experiments by Samsu et al. (2023), which demonstrated that mantle strengthening relative to the crust drives folding and shear concentration in the lower crust, and with numerical models showing that post-rift cooling promotes strain localisation and polarity flips in inversion systems (Vasey et al., 2024). Together, these results underscore the importance of evolving rheology in shaping inversion architecture and demonstrate that Proterozoic orogens cannot be fully understood without accounting for the long-term cooling history of rifted lithosphere.

Natural examples reinforce the numerical predictions. The Araçuaí–West Congo Orogen represents the inversion of a 750 km-wide Tonian rift that accumulated extensive volcanic rocks. Inversion between ~630 and 530 Ma occurred under persistently high crustal temperatures sustained by radiogenic heating and mantle upwelling, resulting in small thrust nappes, flat orogenic bases, and distributed strain (Alkmim et al., 2006; Vauchez et al., 2019). This closely parallels our experimental results where hot lithospheres deform diffusely and produce broad, low-relief orogens.

The Centralian Superbasin of central Australia provides a contrasting example of wide rift inversion after prolonged cooling. Rifting began between ~1085 and 1040 Ma, creating a large intracratonic basin that accumulated up to 12 km of Neoproterozoic sediments (Walter et al., 1995). Following ~400 Myr of quiescence, inversion during the Petermann (570–530 Ma) and Alice Springs (450–300 Ma) Orogenies was accommodated by deep crustal shear zones that offset the Moho by as much as 25 km, while surface uplift remained modest. This pattern is consistent with the thermally relaxed wide rift inversion models, where deformation becomes concentrated at depth but produces muted topography (Gibson et al., 2016).

The Greater McArthur Basin of northern Australia also provides a natural analogue consistent with our experimental results. Seismic and structural studies reveal that its Paleoproterozoic successions record multiple episodes of extension and subsequent inversion, with basin-bounding normal faults reactivated during later orogenic events such as the Isan Orogeny (Blaikie et al., 2017; Soares et al., 2025). In particular, the Daly Waters Fault Zone demonstrates repeated reactivation under alternating extensional and compressional regimes, resulting in a complex superposition of structural fabrics. During inversion, strain was partitioned along deep-seated shear zones that connect through the crust into the lithospheric mantle, consistent with the thermally relaxed wide rift inversion style predicted by our models. Moreover, inversion structures in the McArthur Basin are closely tied to fluid pathways, providing conduits for mineralising systems such as the McArthur River (HYC) Pb–Zn deposit (Large et al., 2005).

Overall, the combination of modelling, analogue experiments, and natural case studies demonstrates that wide rift inversion is highly sensitive to thermal history, in contrast to narrow rift inversion which is largely geometry-controlled. This provides a unified explanation for the contrasting structural styles and topographic expressions of Proterozoic versus Phanerozoic rift-inversion orogens.

2.4. Contractional collapse of a hot rift basin: The curious evolution of the Irindina Basin

The Irindina Basin—more commonly referred to as the *Irindina Province*—is a Neoproterozoic to Cambrian fault-bounded sedimentary basin located in the Northern Territory, central Australia. It is widely regarded as the metamorphic equivalent of sedimentary successions within the larger Centralian Superbasin and is closely associated with igneous intrusions and the Harts Range Metamorphic Complex (Figure 9). The basin preserves an unusual thermal–tectonic history, characterised by high-temperature metamorphism, deep crustal flow, and complex structural reworking during the Alice Springs Orogeny (ASO, 450–300 Ma). Remarkably, the Irindina Basin records coeval development of two seemingly contrasting tectonic features: the Entia Dome to the north and the Ruby Gap Duplex (RGD) to the south. This study explores the dynamic link between these structures and proposes that their synchronous evolution reflects *convergent gravitational collapse* of a hot, deep rift basin.

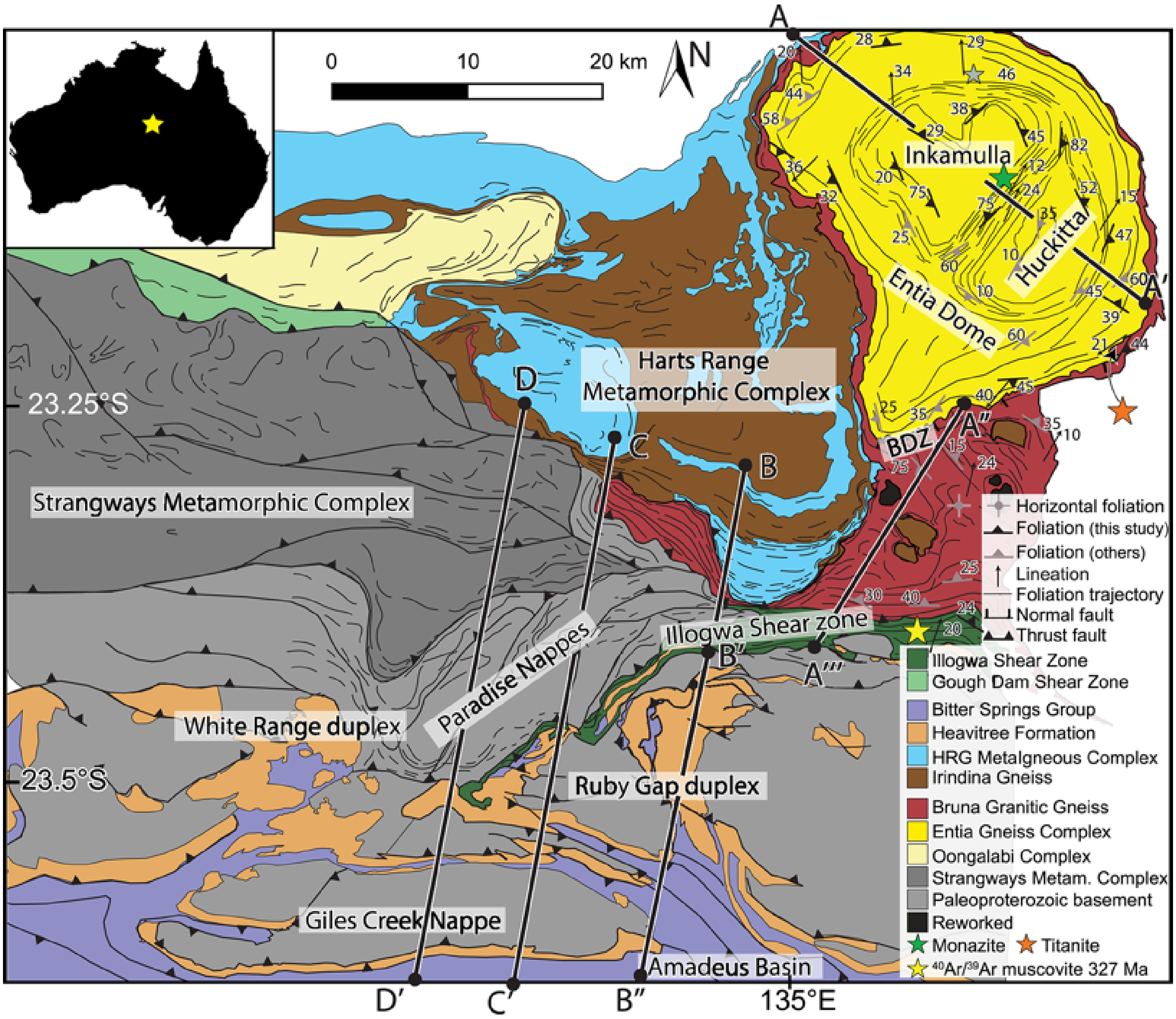

Figure 9. Harts Range - Entia Dome - Nappes Complex, central Australia, modified from Forman (1971), Shaw et al. (1984), Shaw and Freeman (1990), and Dunlap (1992). HRG—Harts Range Group.

2.4.1. Methodology

A multi-disciplinary approach was employed to unravel the tectonic evolution of the Entia Dome–RGD system. Field-based structural mapping was carried out along a north–south transect crossing the Entia Dome, the Bruna Décollement Zone (BDZ), the Illogwa Shear Zone (ISZ), and the RGD. Within this transect, key structural features—including shear fabrics, fold geometries, and kinematic indicators—were systematically documented.

Metamorphic and petrological analysis constrained the thermal gradient across the transect, revealing conditions ranging from upper amphibolite facies (>680 °C, 7–9 kbar) in the Entia Dome to greenschist facies (250–300 °C) in the RGD. Geochronology provided temporal control: U–Pb zircon and monazite dating, Sm–Nd isochron analysis, and Ar–Ar mica ages were combined to constrain the timing of deformation and metamorphism. These data demonstrated that the main tectono-metamorphic events were concentrated between 345 and 310 Ma.

Complementing the field evidence, numerical thermo-mechanical modelling was performed using the Underworld framework. Simulations tested the gravitational collapse of a 34 km-deep, hot rift basin filled with thermally weakened sediments. By applying temperature-dependent rheologies and varying velocity boundary conditions, the models successfully reproduced both dome exhumation and nappe thrusting, lending quantitative support to the gravitational collapse hypothesis.

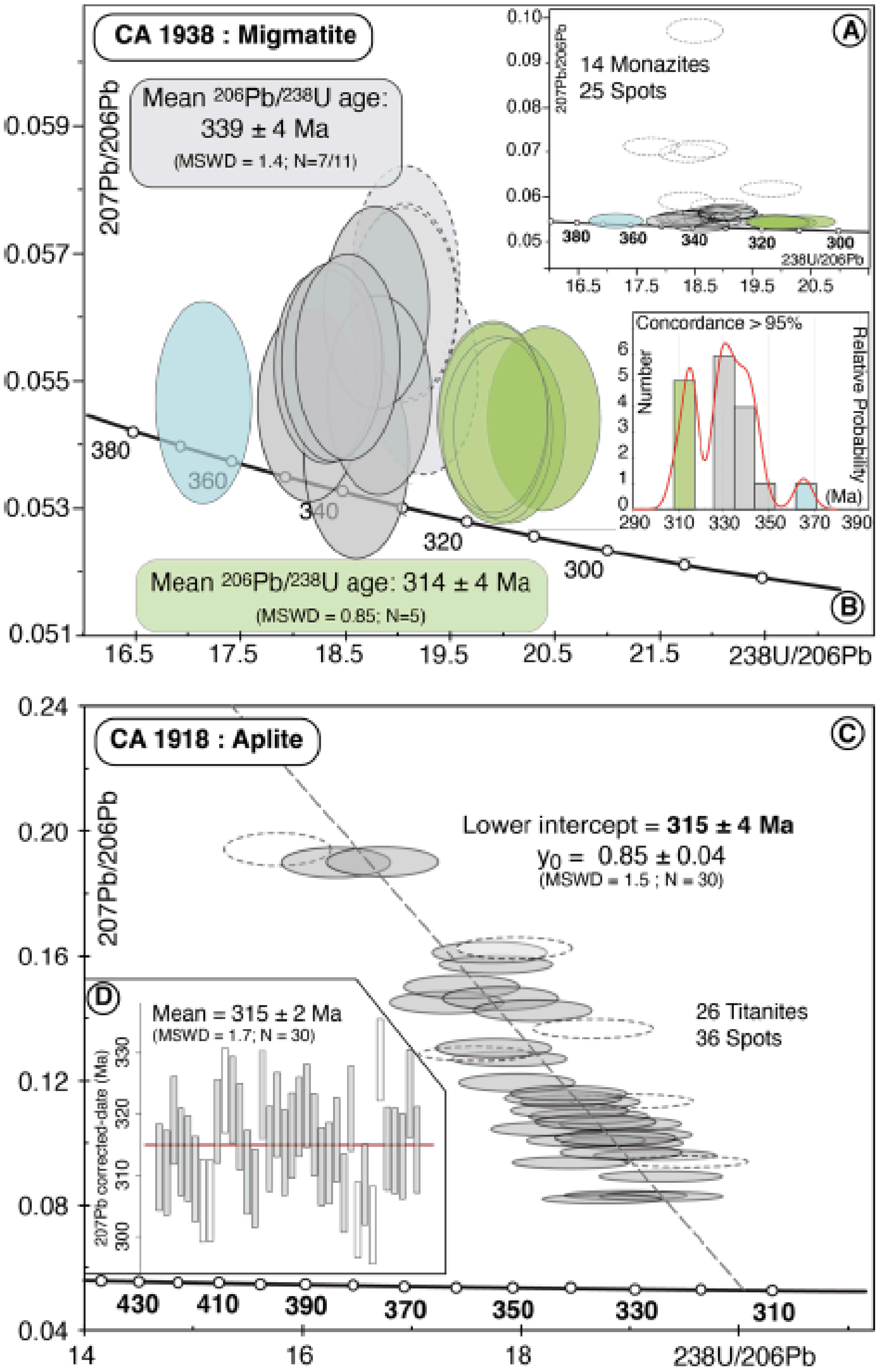

Figure 10. U-Pb monazite and titanite diagrams obtained by LA-ICPMS on thin section. A and B: Monazite U-Th-Pb Tera Wasserburg diagrams on the migmatite (sample CA1938) of the Median High strain zone. Error ellipses and uncertainties in ages are ± 2σ level. Dotted white ellipses are discordant data and are not considered in the histogram diagram (B) and for the age calculations, while dotted grey ellipses are not considered only when calculating the concordia age. C: Titanite U-Th-Pb Tera Wasserburg diagram from the aplite (CA1918). D: The weighted average of 207-corrected dates diagram. Error ellipses and uncertainties in ages are ± 2σ level. Dotted white ellipses and boxes are not taken into account for the age calculation.

2.4.2. Results and findings

The structural, metamorphic, and geochronological data reveal a coherent tectonometamorphic continuum across the Irindina Province, linking high-temperature dome exhumation in the north to contractional duplexing in the south. Regionally, the Irindina Basin (metamorphosed equivalent of Centralian Superbasin strata) lies adjacent to the Harts Range Metamorphic Complex and associated igneous rocks, defining a north–south transect from the Entia Dome through the Bruna Décollement Zone and Illogwa Shear Zone to the Ruby Gap Duplex (Figure 9, Forman, 1971; Shaw et al., 1984; Shaw & Freeman, 1990; Dunlap, 1992; Ibrahim et al., 2023).

At the core of this transect, the Entia Dome is a migmatitic double-dome structure, characterised by recumbent folds, melt-segregation features, and extensional shear fabrics. Peak metamorphic conditions of ~680–720 °C and 7–9 kbar indicate deformation at amphibolite- to granulite-facies conditions (Ibrahim et al., 2023). Geochronological data reveal two pulses of doming and melt extraction, at ~339 Ma and ~314 Ma, recorded by U–Pb monazite and zircon ages (Ibrahim et al., 2023; Dunlap, 1992). These results highlight the polyphase evolution of the dome during the Alice Springs Orogeny (Figure 10).

South of the dome, the BDZ represents a south-dipping normal shear zone separating Paleoproterozoic basement from Neoproterozoic–Paleozoic cover. Structural fabrics confirm top-to-the-southwest kinematics, while titanite U–Pb ages of ~315 Ma suggest that shearing was broadly synchronous with doming (Shaw et al., 1984; Ibrahim et al., 2023). The BDZ thus marks the transition from high-temperature domal exhumation to shear-dominated deformation (Figure 11).

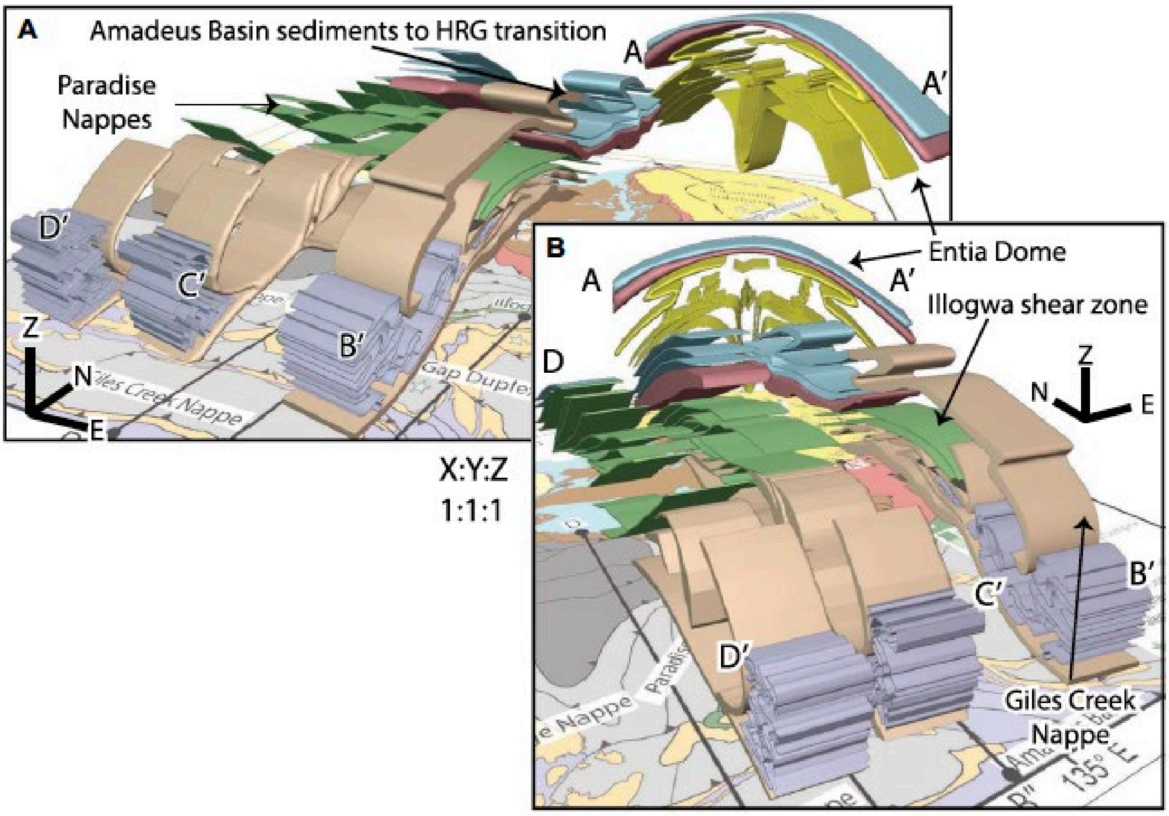

Figure 11. Structural architecture of the Entia Dome and Arltunga Nappe Complex.

The ISZ provides a transitional, high-strain corridor linking extension-related dome uplift to contractional deformation further south. It exhibits top-to-the-southwest shear, inverted metamorphic gradients, and the geometry of an axial planar fabric associated with large-scale fold nappes. These features suggest that the ISZ acted as the mechanical bridge between domal extension and the thrust duplex system of the RGD (Shaw & Freeman, 1990; Ibrahim et al., 2023).

Further south, the RGD is a south-directed duplex composed of thrust-imbricated sheets of Amadeus Basin cover sequences and Paleoproterozoic basement rocks. Deformation occurred under greenschist-facies conditions (~250–300 °C) at the brittle–ductile transition, with thrusting constrained between 336–311 Ma by U–Pb and Ar–Ar geochronology (Forman, 1971; Ibrahim et al., 2023). The regional cross-section (Figure 12) highlights the systematic north–south progression from high-temperature dome fabrics, through transitional shear zones, to contractional duplexing.

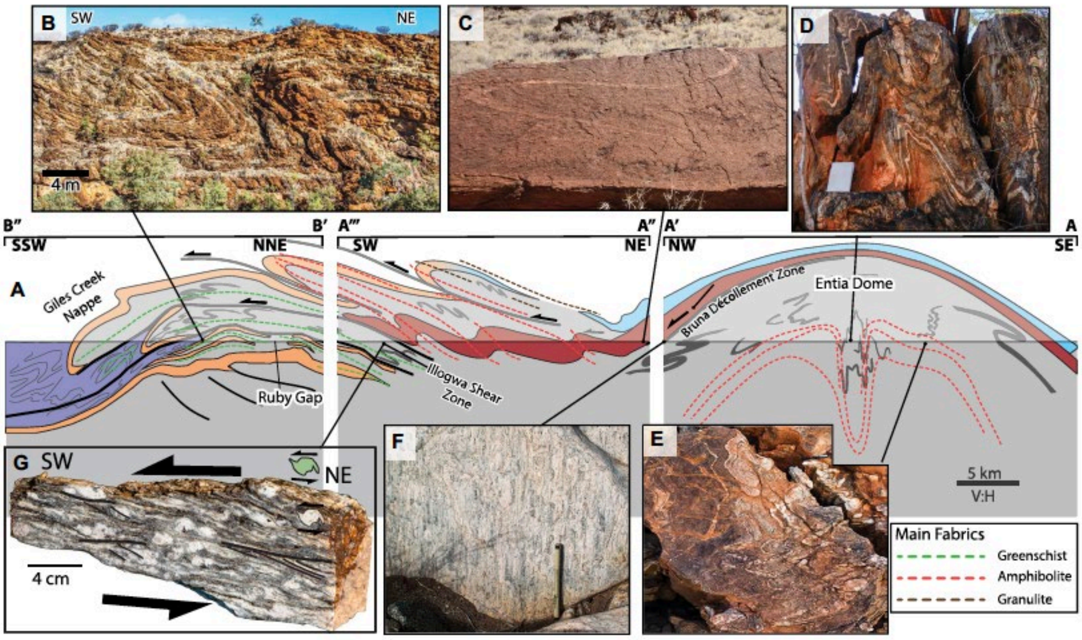

Figure 12. Composition cross-section from the Ruby Gap Duplex to the Entia Dome.

Taken together, the structural, metamorphic, and geochronological evidence shows that deformation across the Irindina Province was spatially continuous and temporally overlapping, concentrated between ~345–310 Ma. This spatiotemporal coherence argues for a single, dynamically coupled tectonic system, rather than isolated events.

Numerical thermo-mechanical models further support this interpretation. Simulations of a ~34 km-deep, hot rift basin filled with thermally weakened sediments reproduce the key features of the observed architecture. These experiments demonstrate that convergent gravitational collapse can drive synchronous dome exhumation and gravity-driven nappe emplacement. The resulting plateau-like uplift near the dome and contractional imbrication at the basin margin mirror the structural continuum observed in the field (Ibrahim et al., 2023, Figure 13). This provides a robust, process-based explanation for the dome–shear–duplex evolution during the ASO.

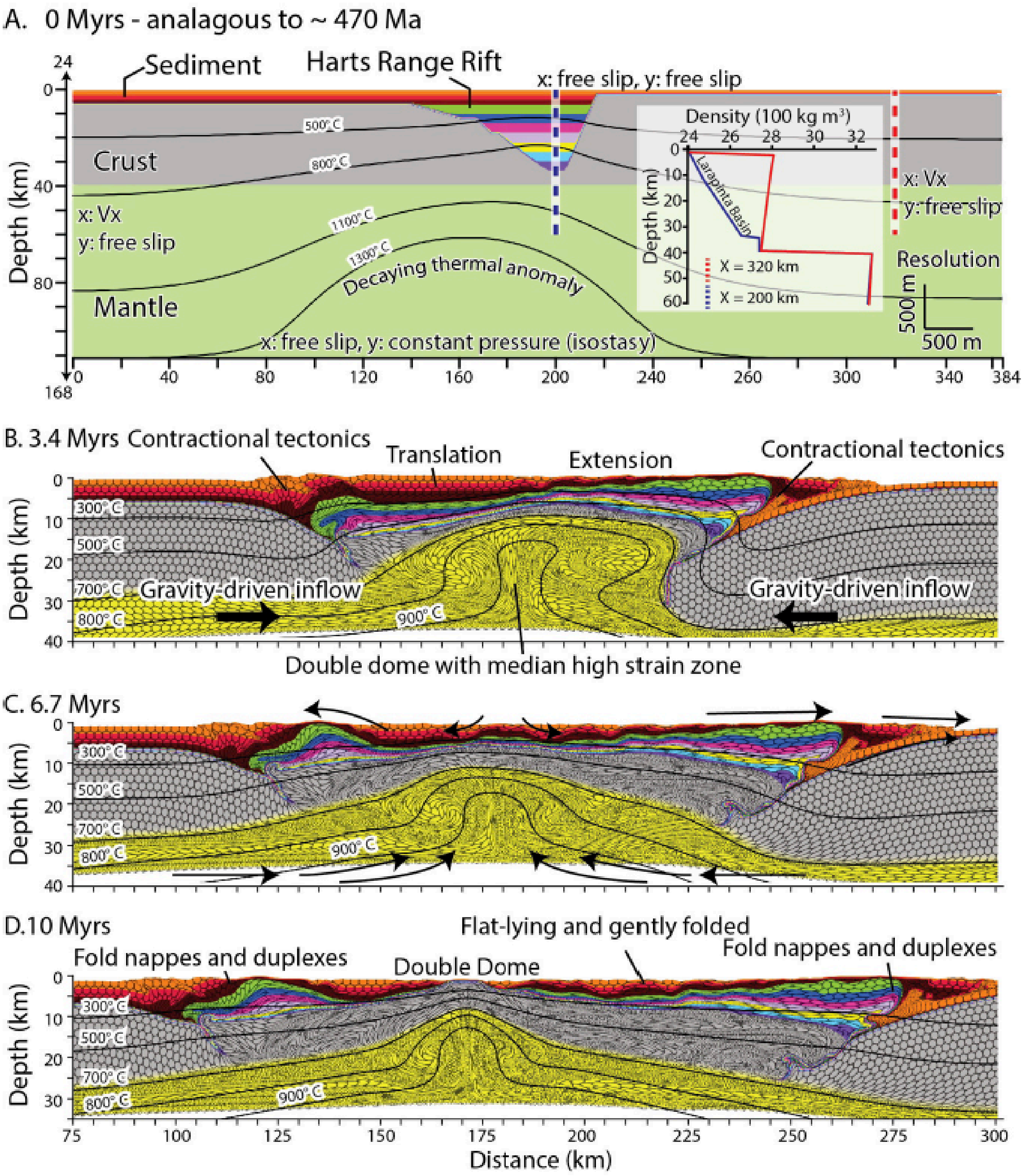

Figure 13. Numerical experiment showing contractional gravitational collapse of a deep and hot rift basin triggering the exhumation of a gneiss dome and associated gravity nappes.

2.4.3. Discussion

The results of this study support a tectonic model in which the Entia Dome and the Ruby Gap Duplex are genetically and dynamically linked through a continuum of extensional, translational, and contractional domains (Figure 11 - Figure 13). Rather than being isolated structural features, these elements represent different expressions of the same underlying process: the gravitational collapse of a deep, hot rift basin during the Alice Springs Orogeny.

The Harts Range Rift Basin, filled with thermally weakened Neoproterozoic sediments, played a pivotal role in this evolution. As the thickened crust began to collapse, a horizontal pressure gradient developed across the basin. This facilitated centripetal flow, driving both dome exhumation in the north and thrust stacking in the south. Gravitational forces therefore operated alongside far-field compressive stresses imposed by regional plate convergence, producing a hybrid tectonic regime that integrated both internal (gravitational) and external (plate boundary) drivers of deformation.

Within this system, the BDZ and ISZ served as key structural domains that accommodated strain transfer. The BDZ records amphibolite-facies shearing synchronous with dome exhumation, marking the transition from high-temperature migmatitic domes to shear-dominated mid-crustal deformation. The ISZ, in turn, represents a high-strain corridor with inverted metamorphic gradients and top-to-the-southwest shear sense. Its geometry is consistent with the axial planar fabric of a fold nappe, suggesting it mediated the transition from extensional doming to contractional nappe emplacement. Together, these shear zones form the kinematic and mechanical link between dome uplift and duplex thrusting, confirming their role as the structural “hinge” of the system.

The temporal gap between granulite-facies metamorphism (~470–450 Ma) and dome exhumation (~339–314 Ma) is particularly revealing. This delay likely reflects the balance between divergent rifting processes, which initially thinned and heated the crust, and subsequent convergent gravitational and plate-driven forces, which exploited this weakened lithosphere. Slow conductive heating during the intervening ~100 million years maintained high crustal temperatures, priming the crust for collapse and deformation once compressive stresses intensified.

This tectonic scenario explains the coeval development of high-temperature metamorphism, dome uplift, and nappe thrusting during the ASO. It provides a coherent framework for understanding why dome exhumation and duplex formation occurred synchronously, rather than sequentially. Moreover, it clarifies the structural and metamorphic architecture of the eastern Arunta region, where high-grade metamorphism, migmatite doming, and greenschist-facies thrusting appear juxtaposed but are in fact dynamically linked.

Numerical modelling further reinforces this interpretation. The Underworld thermo-mechanical simulations (Figure 13) reproduce the simultaneous exhumation of migmatitic domes and emplacement of gravity-driven nappes from a collapsing rift basin. The close agreement between model outputs and field observations suggests that gravitational instabilities in thermally weakened crust were the principal engine of deformation, with far-field compression acting as an amplifying factor.

In a broader context, this work highlights the importance of gravitational collapse in hot orogens as a mechanism for producing dome–nappe tectonic systems. The Irindina Basin case study demonstrates how deep rift basins, once weakened by heat and partial melt, may collapse under their own weight to generate dome exhumation and thrust duplexes. This mechanism likely operated in other intracratonic settings worldwide where thick sedimentary basins were inverted under high-temperature conditions, suggesting global parallels to the Australian record.

2.5. Discussion

Our thermo-mechanical experiments were designed to isolate the role of lithospheric thermal state in governing rift style, basin architecture, and subsequent inversion. The results highlight that the primary discriminator between “modern-like” and “Proterozoic-like” systems is the thermal–rheological state of the lithosphere, which controls whether extension evolves in a narrow or wide mode and how rifts respond to later contractional stresses.

2.5.1. Wide versus narrow rift evolution

In the “modern-like” configuration (TMoho ~600–650 °C), extension rapidly localises into narrow rifts. Deformation is focused along steep listric normal faults, strain rates are high, and the resulting basins are deep, asymmetric grabens with strongly fault-controlled architecture. This geometry is directly comparable to present-day narrow rift systems such as the East African Rift, the Baikal Rift, and the Basin and Range Province (Ebinger, 2005; Buck, 1991; Gartrell, 2000).

In the “Proterozoic-like” configuration (TMoho ≥ 750–800 °C), the same extensional forcing produces wide rifts with distributed strain, shallow laterally extensive depocentres, and a relatively flat Moho during the early phases of extension. Strain is accommodated diffusely across a broad zone of thinned lithosphere, and faulting is more distributed. As extension proceeds, progressive thinning and syn-rift cooling strengthen the lower crust and mantle, driving a transition from wide to narrow rifting. This bimodal evolution provides a robust explanation for why many northern Australian basins record both broad, regionally distributed subsidence and later, localised fault-controlled reactivations (Rawlings, 1999; Blaikie & Kunzmann, 2020; Soares et al., 2025).

This behaviour is consistent with secular changes in Earth’s thermal state. During the Paleoproterozoic–Mesoproterozoic, the mantle was hotter by ~150–250 °C, magmatism was more voluminous and diverse (from tholeiitic basalts to komatiites), and large igneous provinces were widespread (Herzberg et al., 2010; Ernst, 2014). Such magmatism elevated heat flow, modified lithospheric composition, and created long-lived permeability networks that focused later fluids and mineralising systems. In our experiments, these hotter geotherms manifest as low viscosities, reduced crust–mantle strength contrast, and distributed deformation—all conditions conducive to forming the wide, long-lived intracratonic basins characteristic of the Proterozoic (Myers et al., 1996; Giles et al., 2002).

2.5.2. High-temperature terranes and basin evolution

A second, equally important consequence of hot geotherms is the occurrence of high-grade metamorphism without major crustal thickening. Our models reproduce high temperatures at modest depths under extensional or near-neutral stress regimes, consistent with the development of amphibolite–granulite facies conditions in the absence of collisional crustal burial. This helps reconcile the widespread occurrence of Proterozoic high-T terranes and migmatitic domes with broadly extensional basin frameworks (Rey & Müller, 2010; Ibrahim et al., 2023). It also aligns with gravitational-collapse scenarios such as those documented in the Irindina Province, where hot, weak crust underwent lateral flow while far-field compressive stresses merely biased the collapse (Shaw & Freeman, 1990; Dunlap, 1992; Ibrahim et al., 2023).

2.5.3. Core complexes versus wide rift domes

A key contrast between narrow and wide rifting lies in the style of crustal exhumation. In Phanerozoic narrow rift systems such as the Basin and Range Province, strain localisation onto major low-angle detachment faults facilitates the formation of metamorphic core complexes (MCCs). These structures exhume mid- to lower-crustal rocks along ductile shear zones, producing dome-like culminations bounded by rolling-hinge detachments (Lister & Davis, 1989; Buck, 1991). MCCs reflect a lithosphere that is strong enough to localise strain, but weak enough to allow large-scale brittle–ductile coupling.

By contrast, our Proterozoic wide-rift experiments show that under elevated geotherms, strain remains broadly distributed. Instead of discrete detachment systems, deformation produces shallow depocentres and regional doming through distributed ductile flow. This explains why classic MCCs are rare in Precambrian terrains, despite abundant evidence for high-T deformation and dome structures (Rey & Müller, 2010). Instead, crustal flow in hot Precambrian lithosphere produced migmatitic domes and gneiss culminations such as the Entia Dome in the Irindina Province, which record gravitational collapse of weak rift basins rather than detachment-driven exhumation (Shaw & Freeman, 1990; Ibrahim et al., 2023). These domes may therefore be viewed as the wide-rift analogue of MCCs: both reflect crustal flow, but under contrasting thermal–mechanical regimes.

2.5.4. Inversion style and thermal memory

Our experiments also emphasise that rift inversion cannot be explained solely by initial rift geometry; it must be understood in the context of lithospheric thermal evolution.

In narrow rifts, inversion is consistently focused along basin-bounding listric faults, producing asymmetric orogens with flexural forelands. The style is relatively insensitive to quiescence duration, apart from enhanced relief where longer quiescence allows thicker sediment accumulation (Hansen & Nielsen, 2003; Gartrell et al., 2022).

In wide rifts, inversion is highly sensitive to cooling history. If contraction follows soon after extension, deformation is diffuse, yielding broad, low-relief plateaus. After tens of Myr of quiescence, however, mantle strengthening relative to the fault-damaged crust produces mechanical decoupling. Shear zones propagate through the mantle, offsetting the Moho and forcing margin underthrusting, while the crust continues to deform more diffusely (Samsu et al., 2023; Vasey et al., 2023; Oravecz et al., 2024). This geometry produces deep crustal shear zones with surprisingly muted surface relief, consistent with the Centralian Superbasin during the Petermann and Alice Springs Orogenies (Walter et al., 1995; Gibson et al., 2016).

The Greater McArthur Basin provides a complementary example. Its Paleoproterozoic successions preserve multiple episodes of extension and inversion, with reactivation of basin-bounding faults during the Isan Orogeny (Blaikie et al., 2017; Soares et al., 2025) . The Daly Waters Fault Zone in particular records alternating extensional and compressional regimes, consistent with our wide-rift inversion models where inherited structures remain mechanically weak and repeatedly exploited. Importantly, inversion structures in the McArthur Basin acted as fluid pathways that focused mineralising systems, providing a direct link between thermal inheritance, tectonic reactivation, and metallogenic fertility (Large et al., 2005).

2.5.5. Secular lithospheric evolution and basin systems

Finally, secular chemical differentiation is also critical. Extensive melt extraction during the Archean and Proterozoic left the lithospheric mantle more depleted and buoyant, stabilising thick cratonic keels (Jordan, 1988; Lee et al., 2011). Our wide-rift experiments over such buoyant lithosphere generate broad accommodation with slow thermal subsidence, ideal for preserving long-lived chemical sediments, organic-rich shales, and evaporites. This context also favours selective reactivation along inherited basement-rooted structures, consistent with the polyphase evolution of northern Australian basins (Rawlings, 1999; Blaikie & Kunzmann, 2020).

Taken together, the numerical experiments, analogue comparisons, and natural case studies demonstrate that the primary control on Proterozoic versus Phanerozoic rifting and inversion is lithospheric thermal–rheological state. Hot, weak, buoyant Proterozoic lithosphere favoured wide-rift initiation, gravitational collapse, distributed subsidence, and thermally modulated inversion styles. Cooler, stronger Phanerozoic lithosphere, by contrast, promoted narrow-rift localisation and fault-focused inversion. This provides a process-based template for interpreting the architecture and reactivation history of northern Australian basins, and for understanding how tectonic inheritance conditioned fluid flow and the localisation of world-class mineral systems.

3. Analogue Modelling

3.1. Analogue approach

Analogue modelling was employed to investigate the tectonic evolution of Proterozoic basins under varying boundary conditions and lithospheric architectures. Across three suites of experiments, we reproduced the coupled brittle–ductile behaviour of the lithosphere and its response to extension, inversion, and margin geometry. All experiments were conducted at lithospheric or crustal scale with mechanically scaled materials that capture contrasts between a brittle upper crust, a ductile lower crust, and a viscous lithospheric mantle over a glucose-syrup asthenosphere. The brittle layer comprised a calibrated quartz-sand–Envirospheres® mix (Coulomb behaviour; $\phi \approx 49°$, $C \approx 120$ Pa). Ductile layers used high-viscosity PDMS formulations (with plasticine and iron filings where required) to tune density/viscosity contrasts. Deformation was imposed by programmable linear actuators driving U-shaped sidewalls to deliver orthogonal or oblique extension followed by shortening, allowing controlled tests of obliquity, margin geometry, and rheology on rift segmentation and selective inversion. Scaling followed Ramberg (1967): a 44 × 40 × 2.8 cm model represents ~1100 × 1000 km × 70 km lithosphere; the time scale is ~7.1 Myr per experimental hour. Monitoring combined high-resolution imaging, and digital image correlation (DIC) with coffee-powder speckling to recover incremental/cumulative strain, displacement fields, and surface topography; data were post-processed in MATLAB for quantitative analyses.

This section outlines the common experimental framework used across the program. Experiment-specific configurations—including layer thicknesses, actuator kinematics (rates and obliquity), margin geometries, and any rheological variants—are detailed in the following subsections for each experimental set.

3.2. Selective inversion of rift basins in lithospheric-scale analogue experiments[†]

Ancient rift basins frequently record not only their initial extensional history but also evidence of subsequent tectonic events such as thermal relaxation or shifts in far-field plate dynamics (Morgan & Ramberg, 1987; Forsyth & Uyeda, 1975). In many continental interiors, aborted rifts persist as fossil basins that may later experience compressional overprint—a process termed "positive inversion", defined by Williams et al. (1989) as contraction over previously extended regions. Globally, basins often show evidence of this inversion, contributing to the structural architecture of later orogenic belts—examples include the NW Argentinian Andes, the Alps, and the Pyrenees (e.g., Carrera et al., 2006; Boutoux et al., 2014; Mencos et al., 2015).

While analogue modelling has traditionally focused on how pre-existing normal faults accommodate strain during inversion, our recent lithospheric-scale analogue experiments

---

[†] *Movies and GIS files are available in Appendix_1/Analogue_modelling3_2/*

introduce selective basin inversion: a scenario where only some rift basins are inverted under shortening. These experiments demonstrate that the rheology of lower crust and mantle, combined with the imposed bulk strain rate, regulate whether inversion affects all basins uniformly or only selected ones. This differentiation reflects the spatial distribution of ductile deformation—either homogenous stretching and thickening, which inverts all basins, or localised necking and folding, which leads to selective uplift of evenly spaced basins. Our findings are documented in Samsu et al. (2023), which shows that when ductile layers deform uniformly, all basins are inverted; when deformation localises, only certain basins are uplifted.

The experiments presented here mimic those conditions under structurally simplified—but tectonically relevant—boundary conditions, highlighting the importance of rheological and geometrical inheritance in determining which basins invert. This understanding is critical for interpreting complex basin systems such as those of the North Australian Craton, where mineral systems may be spatially linked to selectively reactivated basins.

3.2.1. Methodology

Analogue experiments were designed to investigate the selective inversion of rift basins in lithospheric-scale systems, inspired by the tectonic evolution of the North Australian Craton. The aim was to develop a reference experiment of wide rifting followed by shortening, against which future experimental series (e.g., those including pre-existing weaknesses or variable rheologies) can be compared. Models R4 and R5 (Table 3) were identified as the most appropriate reference experiments, representing wide rift development and subsequent inversion under NAC-like conditions (Samsu et al., 2023).

3.2.1.1. Experimental setup

Table 3. Summary of experimental parameters (UC is upper crust; LC is lower crust; LM is lithospheric mantle).

Model	***Layer thickness***			***Extension & shortening***		***Brittle–ductile thickness ration***	***Experimental strain rate***	***LC:LM strength ratio***	***Layer strength***	
	UC [cm]	*LC [cm]*	*LM [cm]*	*Velocity [mm h^{-1}]*	*Duration [h]*		*[s^{-1}]*		*LC [Pa]*	*LM [Pa]*
R1	*0.4*	*1.6*	*1.2*	*6.2*	*14*	*0.1*	*5.4 × 10−5*	*0.4*	*4.3*	*10.7*
R2	*0.4*	*1.6*	*1.2*	*6.2*	*14*	*0.1*	*5.4 × 10−5*	*0.4*	*4.3*	*10.7*
R3	*0.8*	*0.8*	*1.2*	*31*	*3*	*0.4*	*3.1 × 10−4*	*0.8*	*18.5*	*21.8*
R4	*0.8*	*0.8*	*1.2*	*28.3*	*3.1*	*0.4*	*2.8 × 10−4*	*0.2*	*11.23*	*68.51*
R5	*0.8*	*0.8*	*1.2*	*28.3*	*3.1*	*0.4*	*2.8 × 10−4*	*0.2*	*11.23*	*68.51*

The experiments used a three-layer lithosphere analogue (brittle upper crust, ductile lower crust, and ductile lithospheric mantle) isostatically supported on a liquid analogue asthenosphere (Figure 14). Extension was applied orthogonally by programmable moving sidewalls, followed by reversal into shortening at the same rate. Red arrows in Figure 14 illustrate the applied deformation directions, while Figure 14b–e compare natural and model strength profiles (after Brun, 1999).

Models R1 and R2 (Table 3) featured a thin upper crust relative to the ductile lower crust, whereas R3–R5 adopted a 50:50 thickness ratio between upper and lower crust, considered more representative of the NAC. R2 and R5 additionally included a pre-cut (45° dipping) in the lithospheric mantle to simulate pre-existing weaknesses, although these did not significantly localise strain during extension.

3.2.1.2. Boundary and initial conditions

The models were designed to mimic wide-rift behaviour typical of thick, post-orogenic lithosphere under higher-than-normal heat flow (Buck, 1991; Brun, 1999; Buck et al., 1999). Rheological layering was tuned to achieve broadly distributed extension, yielding multiple rift basins across the model rather than single narrow valleys. Crustal thickness ratios and extension rates were scaled from modern analogues such as the Basin and Range Province (Hamilton, 1987; Parsons, 2006; Gueydan et al., 2008).

Figure 14. a) Experimental setup. The red arrows indicate the imposed extension and shortening directions. b) Cross section of model layers. c) Natural strength profile of a thickened lithosphere (including a thickened crust) after orogenesis and thermal relaxation, which forms widely distributed grabens upon extension (Brun, 1999). d) Example of three-layer analogue model strength profile, showing that the strength of the ductile layer increases with strain rate (after Brun, 1999). e) Initial strength profiles of models in this study. UC is upper crust; LC is lower crust; LM is lithospheric mantle; ES is Envirospheres; PDMS is polydimethylsiloxane; Pl is plasticine; IF is iron filings.

Model dimensions were 44 × 40 cm in plan view and ~3 cm in thickness, corresponding to natural prototypes of ~1100 × 1000 km and 70–80 km thick lithosphere. Extension rates scaled to 1–2 cm/yr in nature, within estimates for the Basin and Range (Bennett et al., 1998; Snow & Wernicke, 2000; Hammond & Thatcher, 2004; Tetreault & Buiter, 2018). Each model underwent ~20% bulk extension before being shortened back to its original width.

3.2.1.3. Scaling and rheology of model materials

Scaling parameters followed Ramberg (1967) and Molnar et al. (2017). The brittle upper crust was modelled with a granular mixture of fine quartz sand and ~11% hollow ceramic Envirospheres®, calibrated to reproduce natural Mohr–Coulomb behaviour (ϕ≈49°, C≈120 Pa). The ductile lower crust and lithospheric mantle were simulated with PDMS-based mixtures, modified with plasticine and iron filings to adjust viscosity and density contrasts (Molnar et al., 2017; Samsu et al., 2021).

Different grain sizes of iron filings were tested, with ultrafine grains in R1–R3 (Table 3) doubling the viscosity unintentionally, while fine grains in R4–R5 (Table 3) provided a better balance. As a result, R3 had a relatively strong lower crust comparable to the lithospheric mantle, whereas R4–R5 (Table 3) achieved the expected weak lower crust relative to mantle (consistent with wide-rift strength profiles, Brun, 1999).

Density scaling factors ranged between 0.42 and 0.46, with viscosity scaling factors between 10^{-18} and 10^{-19}, producing time scaling factors of 1.5×10^{-11} to 1.5×10^{-10}. This yielded experimental strain rates of $\sim10^{-4}s^{-1}$, corresponding to natural rates of $\sim10^{-15}s^{-1}$.

3.2.1.4. Deformation monitoring and analysis

Deformation was tracked using digital image correlation (DIC) with two high-resolution cameras positioned obliquely above the model (Fig. 2a). Coffee powder was applied to the surface to generate high-contrast speckle patterns. Images were captured at 2–5 min intervals, depending on experiment length (3–14 h).

Strain maps were derived from displacement vector fields using DaVis v.8 (LaVision) software, providing incremental and cumulative strain tensors, vertical displacement fields, and topography. Post-processing in MATLAB removed spurious vectors, interpolated missing data, and corrected surface tilt (Garcia, 2011). Outputs include strain localisation patterns, rift spacing, surface uplift, and inversion geometries.

3.2.2. Results and findings

We report five lithospheric-scale analogue experiments (R1–R5; Table 3). Except for R1 (extension only), each experiment comprises an extension phase followed by shortening. Throughout, the imposed kinematics simulate orthogonal rifting and later orthogonal inversion; hence, basin long axes and fault strikes develop approximately perpendicular to the extension/shortening direction. Edge-parallel curvature near the western and eastern boundaries reflects friction with the confining U-walls, so interpretations focus on the central domain, away from boundary effects.

3.2.2.1. Extension: normal faulting and basin formation

Across all experiments, bulk extension produced an E–W–oriented horst–graben fabric consistent with wide-rift behaviour (e.g., Buck, 1991; Brun, 1999; Buck et al., 1999). We use “graben” and “basin” interchangeably for fault-bounded topographic lows (Reid et al., 1913; Peacock et al., 2000). The emergent patterns resemble natural wide-rift provinces—including the Proterozoic NAC (Allen et al., 2015; Betts et al., 2008), the Basin and Range (Wernicke et al., 1988), the Aegean (Doutsos & Kokkalas, 2001), and the East China Rift (Tian et al., 1992).

Rift evolution followed two stages: (1) basin nucleation and linkage, as normal faults initiated, grew, and connected; and (2) deepening then widening, as throw increased until down-dip propagation reached the base of the brittle upper crust, after which further strain was taken up by lateral widening. The timing is rheology- and rate-dependent (Figure 14e; Table 3): R4–R5 evolved fastest, followed by R3, then R1–R2. By 10% bulk extension, basin-bounding faults in R4–R5 had essentially reached final length, whereas R1–R3 were still in the nucleation/growth stage (compare Figure 15 for R1–R2 and Figure 16 for R3–R5).

By the end of extension (19–20% bulk), R1–R2 show evenly spaced, shallow, highly segmented grabens—consistent with their thin brittle lid—while R3–R5 develop clearer, longer fault traces and clusters of basins that define high-strain zones separated by low-strain zones (Figure 17d–f). R3 basins are narrower and more segmented than R4–R5; R4–R5 basins are more laterally continuous.

Mechanistically, these distributions reflect superposed periodic instabilities: crustal-scale boudinage (spacing ~initial crustal thickness) and lithosphere-scale boudinage (wavelength tied to viscous layer thickness and effective viscosity), as predicted by theory and prior experiments (Ramberg, 1955; Smith, 1977; Fletcher & Hallet, 1983; Benes & Davy, 1996). The faster imposed strain rates in R3–R5 strengthen the viscous layers (rate-dependent rheology), increasing mechanical coupling and promoting distinct high-/low-strain zoning (Brun, 1999; Zwaan et al., 2021). Conversely, slower rates in R1–R2 yield weak ductile layers, uniform thinning, and evenly spaced basins (Benes & Davy, 1996).

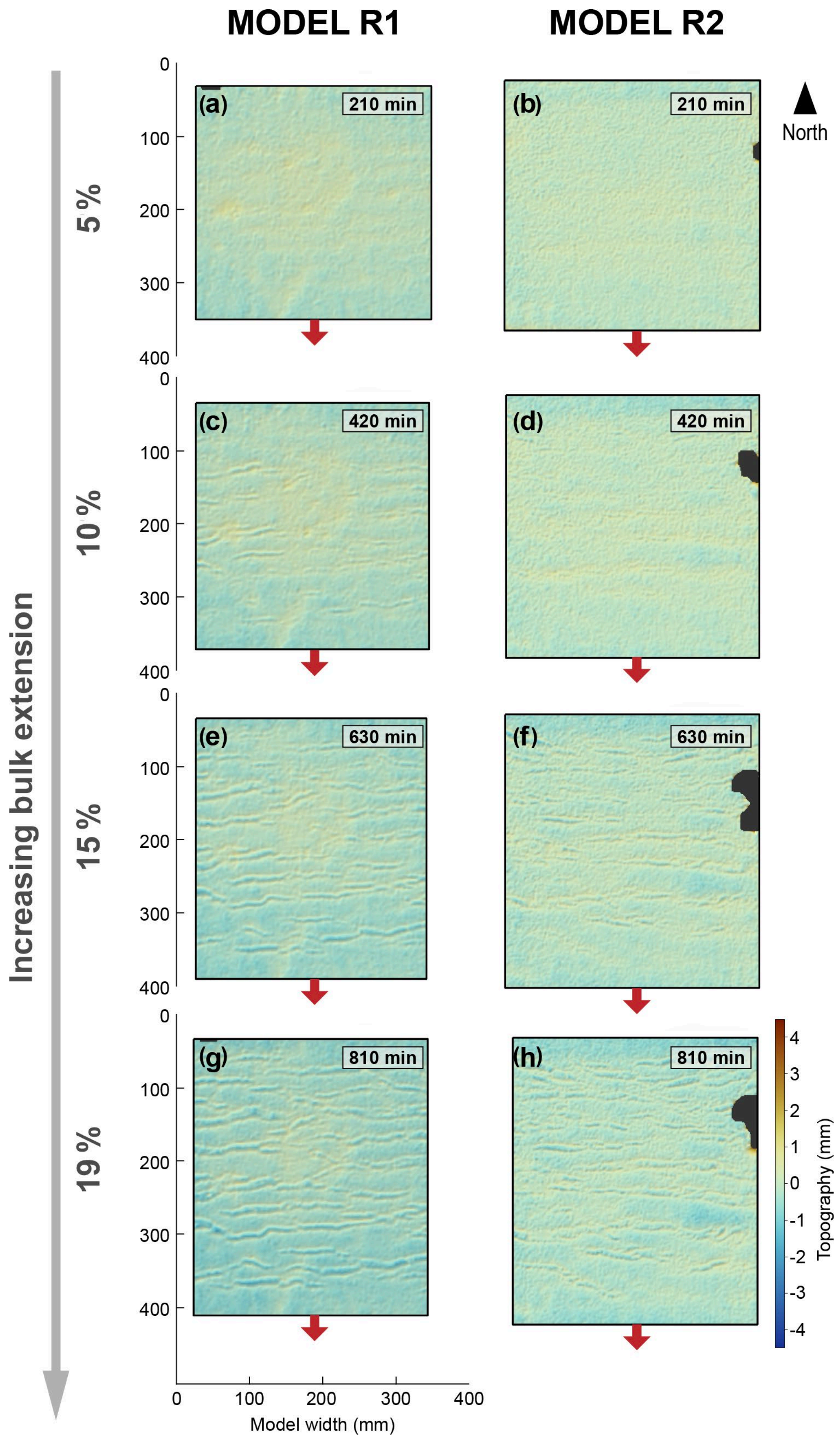

Figure 15. Topography of Models R1 and R2 at increasing durations and amounts of extension applied to the model (e.g. a and b correspond to 5% bulk extension, c and d correspond to 10% bulk extension, etc). Arrows show the direction of extension. The resulting rift basins are uniformly spaced along the y. See Movies and GIS files in Appendix_1/Analogue_modelling3_2/

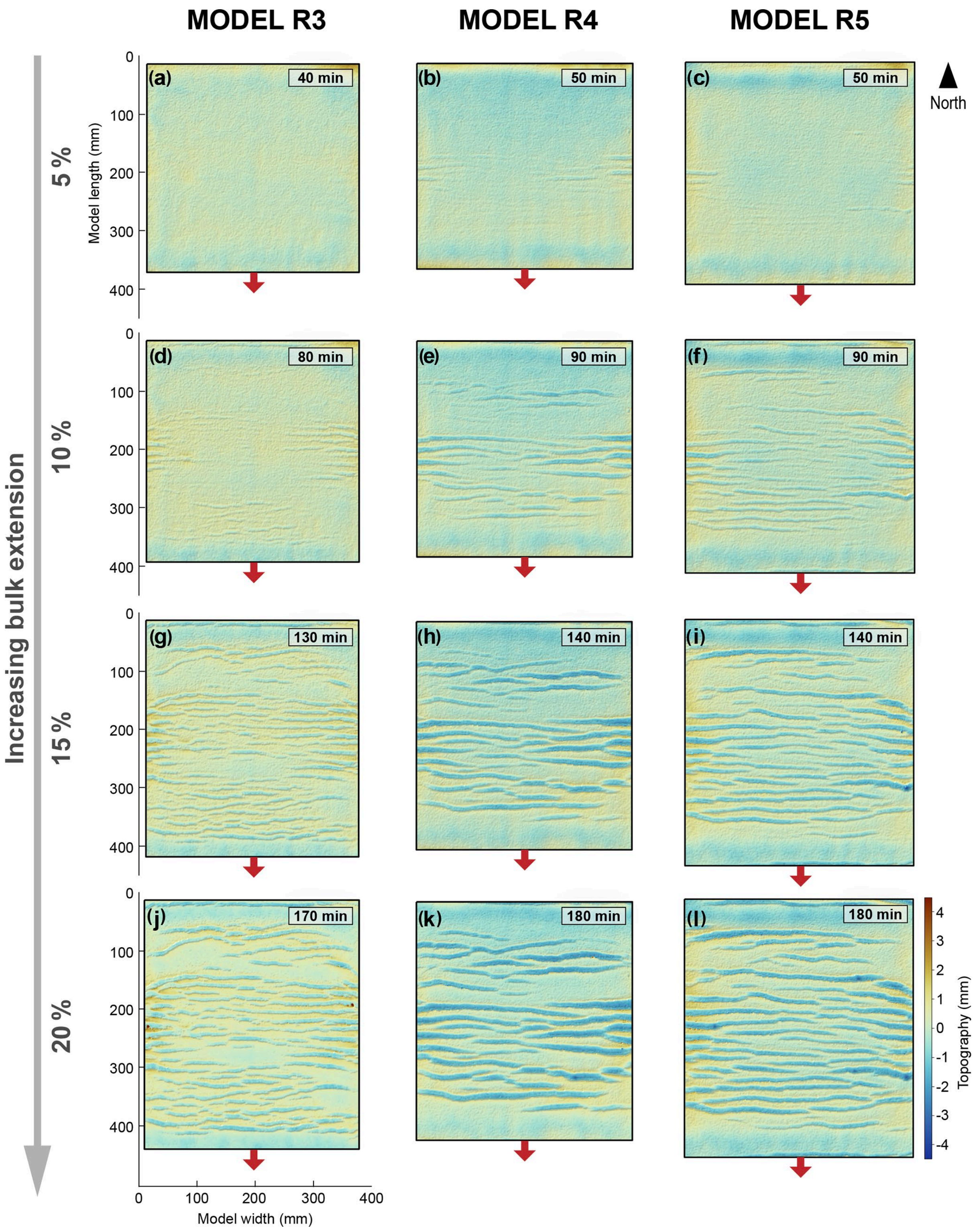

Figure 16. Topography of Models R3, R4, and R5 at increasing durations and amounts of extension applied to the model (e.g. a, b, and c correspond to 5% bulk extension, c, d, and e correspond to 10% bulk extension, etc). The rift basins are not uniformly spaced. Arrows show the direction of extension. See Movies and GIS files in Appendix_1/Analogue_modelling3_2/

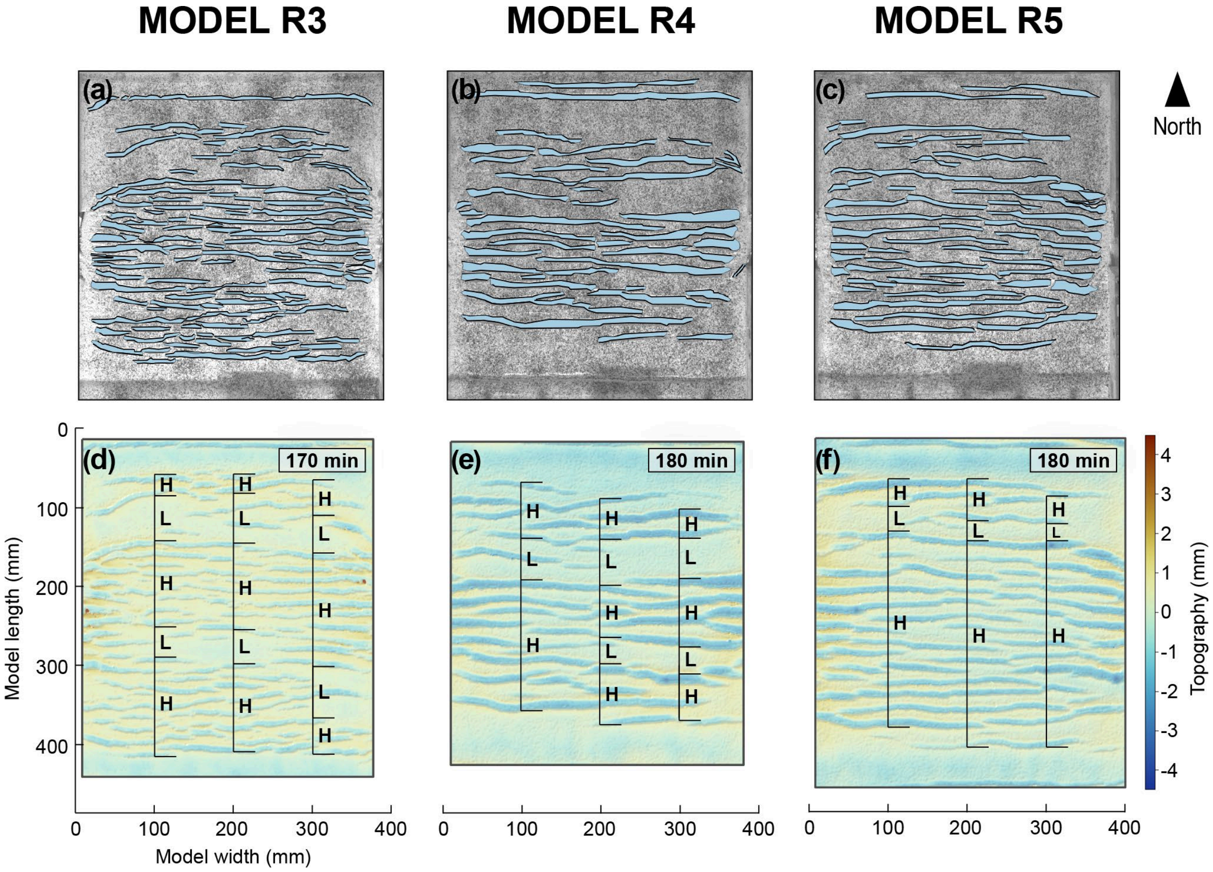

Figure 17. Orthorectified top-view photos of the surface of Models R3, R4, and R5 at the end of extension, with overlay of the interpreted. See Movies and GIS files in Appendix_1/Analogue_modelling3_2/

3.2.2.2. *Shortening: inversion and strain localisation*

Across all experiments, bulk shortening was accommodated by a combination of fault reactivation in the upper crust and viscous thickening or folding in the underlying ductile layers. Deformation patterns reflect the prior extensional architecture: horst–graben fabrics established during extension acted as primary loci for strain during contraction, producing selective basin inversion (Samsu et al., 2023). Inverted basins are defined here as former grabens that underwent surface uplift due to reverse reactivation of normal faults and/or upwelling of ductile material beneath them (cf. Buiter et al., 2009; Zwaan & Schreurs, 2023).

Shortening followed two principal stages: (1) initial reactivation of rift-bounding normal faults in reverse sense, generating local uplift of basin floors, and (2) progressive concentration of strain into a subset of basins, while others remained topographic lows. This selective inversion reflects the interplay between frictional reactivation in the brittle upper crust and folding or thickening in the ductile lower crust and lithospheric mantle (Figure 17).

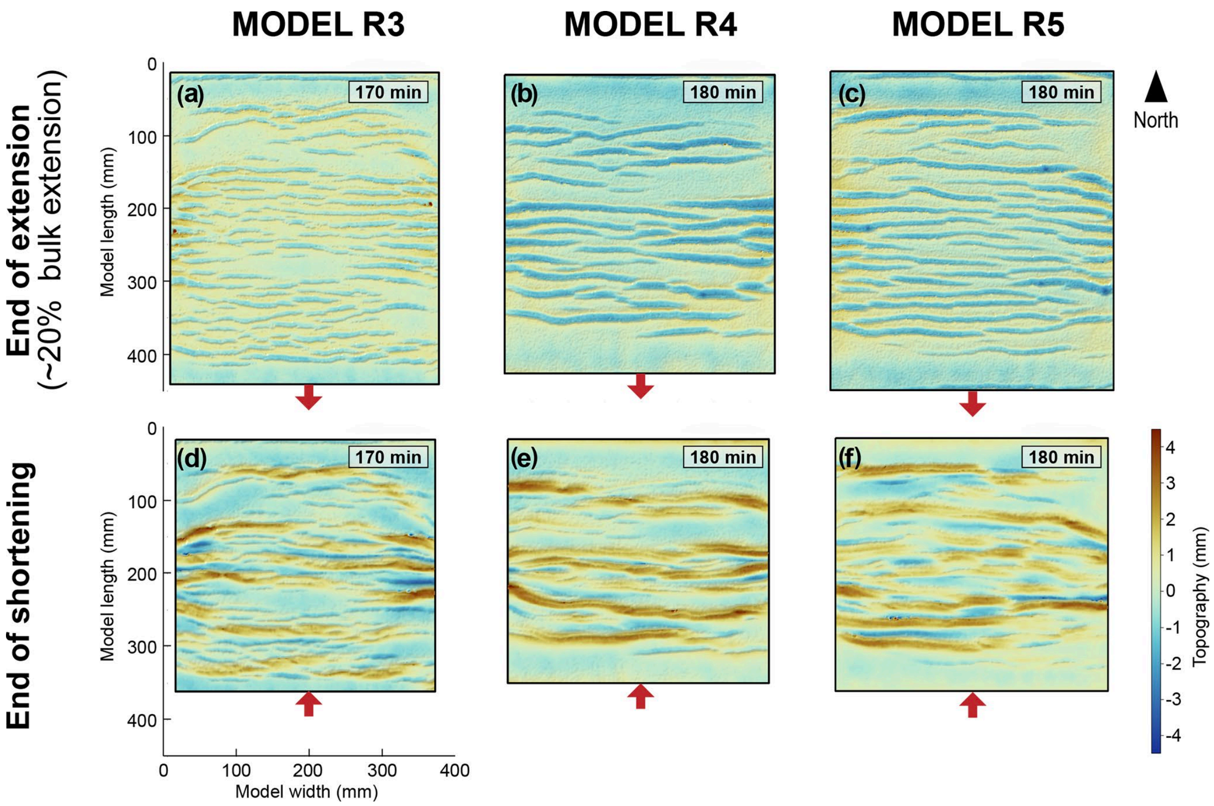

Figure 18. Topography of models R3, R4, and R5 at the end of extension and shortening. Highly segmented extensional basins correlate with highly segmented orogens (R3). In contrast, laterally continuous extensional basins appear to localise laterally continuous orogens (R5). See Movies in Appendix_1/Analogue_modelling3_2/

The style of inversion varied systematically with model rheology and strain rate. In Models R1–R2, characterised by a thin brittle lid and weak mantle, shortening was broadly distributed and largely accommodated by homogeneous layer thickening, with little localisation of uplift (Figure 15). By contrast, Models R3–R5 developed strongly segmented patterns: some basins inverted by >10 mm of uplift, while neighbouring basins continued to subside (Figure 19). These differences highlight how lithospheric strength distribution governs whether shortening produces evenly spaced orogens or highly selective inversion zones.

By the end of shortening, inverted basins consistently formed topographic highs, whereas non-inverted basins remained as depressions (Figure 20). This architecture has important thermal implications: in nature, subsiding, non-inverted basins would correspond to zones of higher geothermal gradients and amphibolite-facies metamorphism, whereas uplifted basins would be cooler and more likely to record greenschist-facies assemblages. The Mount Isa terrane preserves exactly this alternation of high- and low-grade metamorphic domains, consistent with selective basin inversion during regional contraction (Betts et al., 2006; Blaikie et al., 2017; Spence et al., 2021).

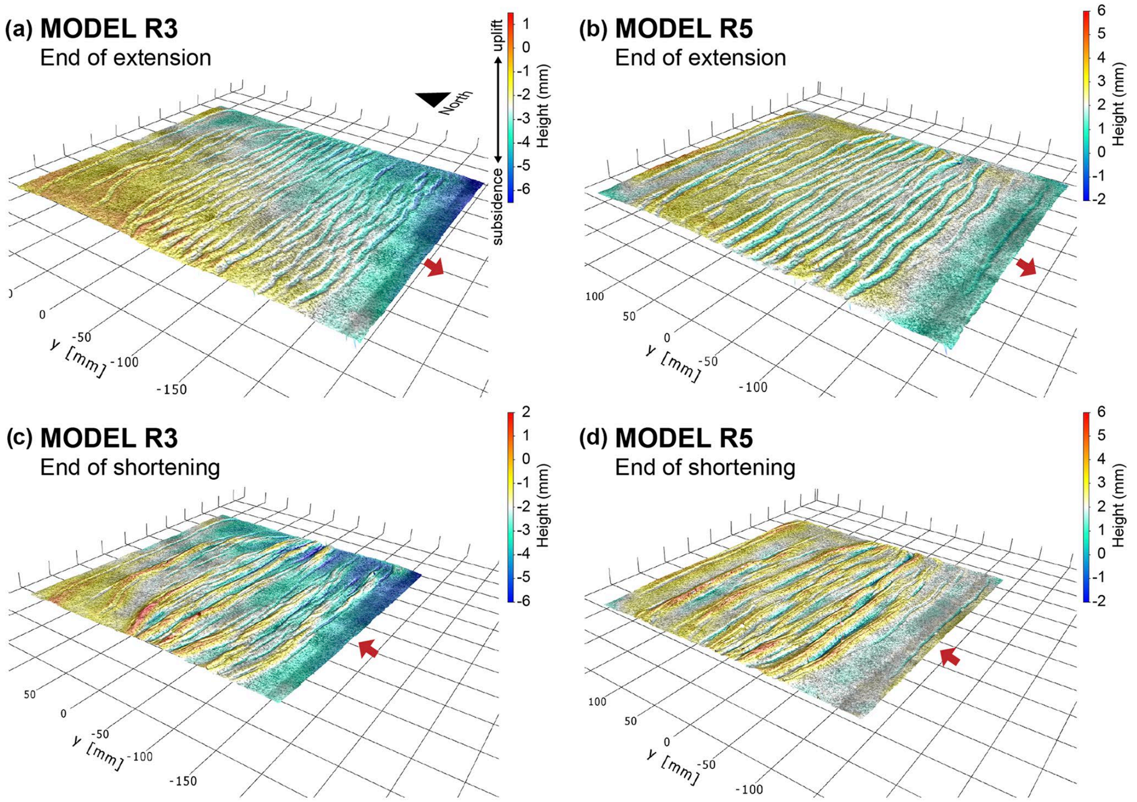

Figure 19. Oblique 3D view of topography of Models R3 and R5 at the end of the extension and shortening phases. This 3D visualisation was done in DaVis prior to the post-processing steps outlined in 3.2.1.4., see Movies in Appendix_1/Analogue_modelling3_2/

These results can be explained by superposed instabilities. Rift-scale boudinage generated during extension set the spacing of basins, while lithosphere-scale folding during shortening determined which basins inverted (Figure 20; Schmalholz et al., 2002; Benes & Davy, 1996). This dual control explains why inversion in natural wide rifts, such as the Proterozoic North Australian Craton, is often patchy rather than uniform.

(a) Topographic profile of Model R3 (x = 100 mm)

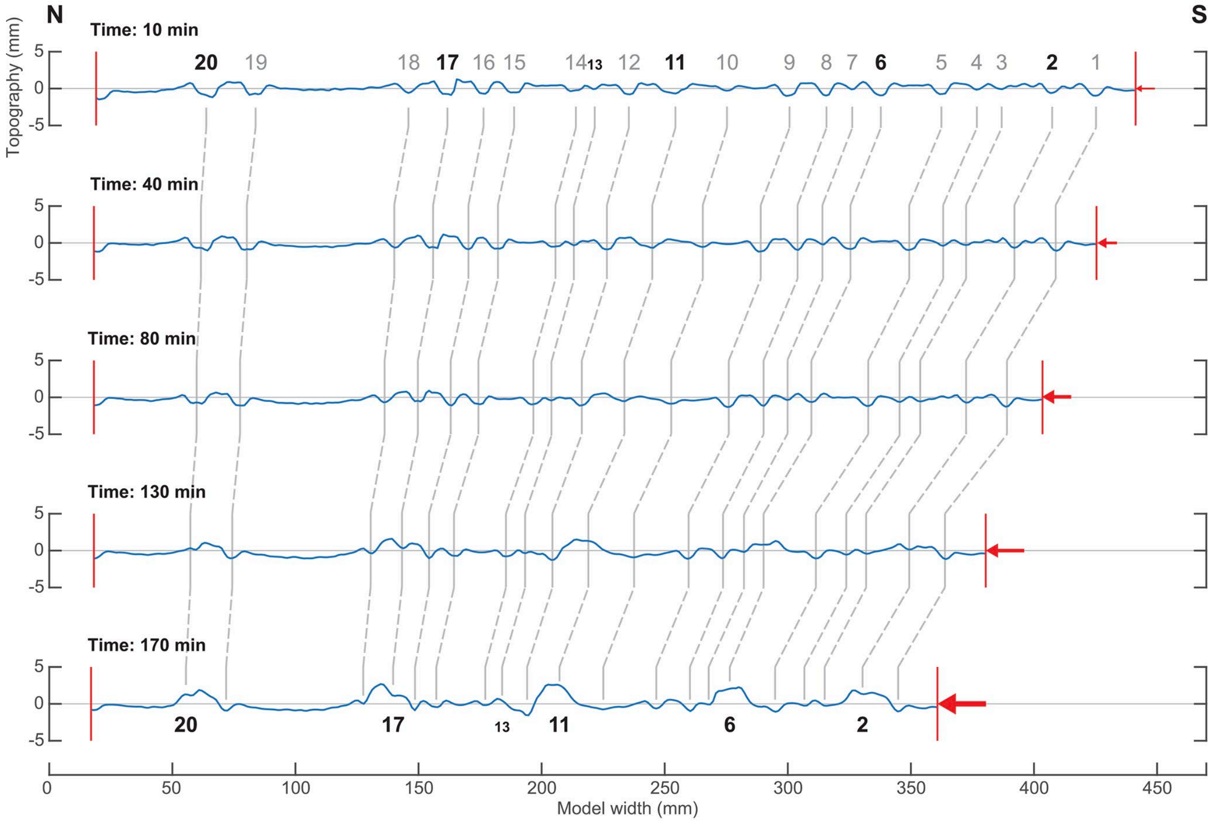

(b) Topographic profile of Model R5 (x = 100 mm)

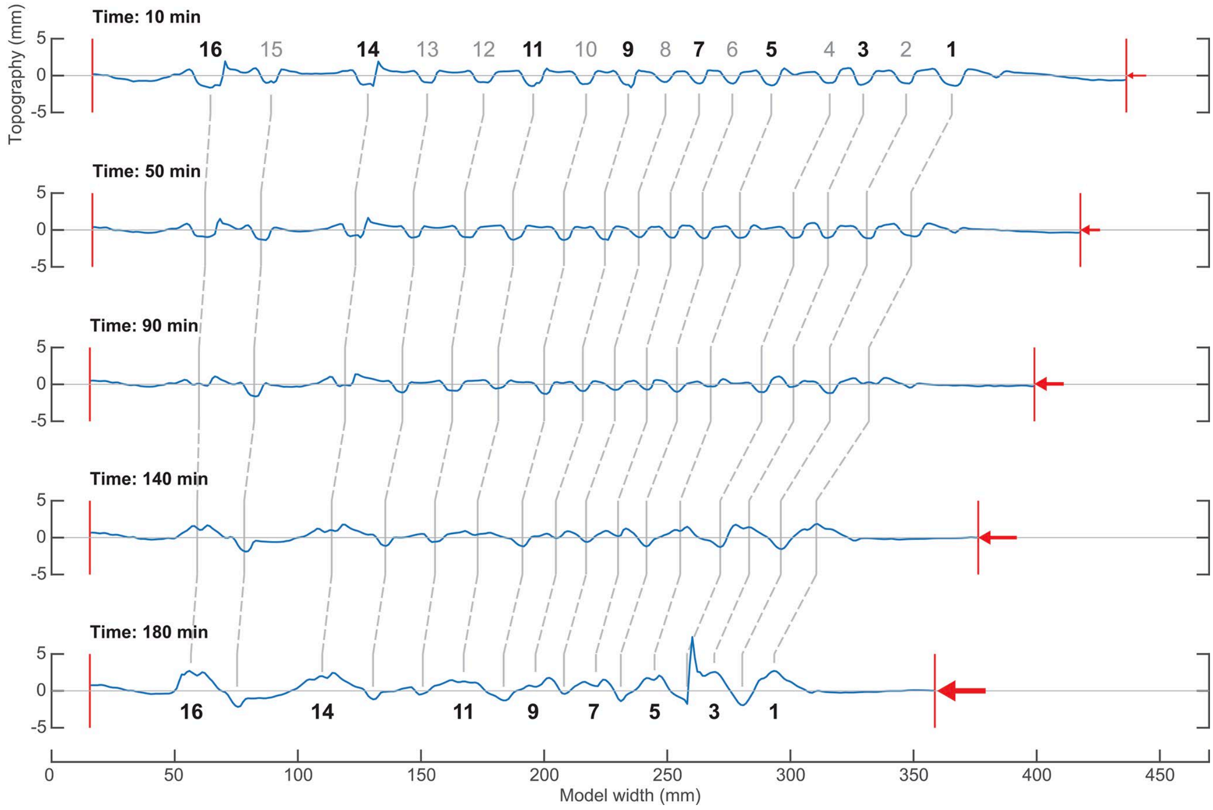

Figure 20. Evolution of the N–S topographic profiles of Models R3 and R5 during shortening, drawn along x D100mm (see location in Figure 16). The numbers denote basins which had formed by the end of the extensional

phase; numbers in bold correspond to basins that were uplifted during shortening. The red arrows represent the direction and cumulative amount of bulk shortening.

3.2.2.3. Selective uplift (inversion) of basins

A key outcome of the shortening experiments is that not all basins inverted uniformly; instead, uplift was strongly selective, affecting some depocentres while others continued to subside. This phenomenon—selective inversion—emerges naturally from the wide-rift initial conditions, where distributed extension produces multiple weak zones, but only a subset is mechanically optimally oriented or sufficiently cooled to be reactivated under compression (Samsu et al., 2023).

In the experiments, early inversion was expressed by small amounts of reverse slip on pre-existing basin-bounding faults, but uplift soon became concentrated into a few basins (Models R3 and R5 are presented in Figure 19). Neighbouring basins without favourable orientation or fault connectivity instead accommodated shortening by continued subsidence, viscous folding, or lower-crustal thickening (Figure 18). This partitioning resulted in alternating highs and lows across the experimental surface, producing an irregular, patchwork topography rather than uniform uplift.

The degree of selectivity increased with model strength and post-rift cooling. Hot, weak lithospheres (R1–R2) showed diffuse thickening and broad, non-selective uplift, whereas cooler or stronger lithospheres (R3–R5) produced pronounced differential behaviour, with up to 10 mm of relative relief between inverted and non-inverted basins (Figure 20). This finding agrees with numerical models and analogue experiments showing that lithospheric strengthening promotes strain localisation into narrow zones (Vasey et al., 2023; Samsu et al., 2023).

Natural examples support these results. In the southern Georgina Basin, Neoproterozoic grabens were selectively reactivated during the Alice Springs Orogeny, with only certain depocentres undergoing significant inversion (Greene, 2010). Similarly, in the McArthur Basin, inversion was strongly partitioned along the Daly Waters Fault Zone, where deep-seated shear zones provided the structural focus for uplift, while adjacent depocentres remained sites of continued accommodation (Soares et al., 2025). These cases echo the experimental outcome: selective uplift is the rule, not the exception, in wide-rift systems.

Routinely, selective inversion reflects the competition between brittle fault reactivation and ductile lower-crustal flow. Where rift-bounding faults remain mechanically weak, they invert directly, generating uplift. Where faults are unfavourably oriented or thermally overprinted, shortening is taken up by folding and subsidence, leading to paradoxical deepening of some depocentres during contraction (Oravecz et al., 2024). This duality explains why many Proterozoic basins in northern Australia preserve evidence of both uplift and continued sedimentation within the same tectonic episode (Blaikie et al., 2017; Betts et al., 2006).

3.2.3. Discussion

The analogue experiments highlight the fundamental control of rift mode and lithospheric thermal state on the subsequent style of shortening and inversion. In narrow-rift settings, deformation during contraction was consistently accommodated by the reactivation of basin-bounding faults, producing asymmetric orogenic belts with pronounced surface uplift and flexural foreland basins (Figure 21a–b). The outcome was relatively insensitive to the length of post-rift quiescence: sediment accumulation enhanced relief, but the geometry of inversion remained localised and fault focused. This underscores the mechanical efficiency of narrow rifts in focussing strain into pre-existing fault systems, consistent with observations from Phanerozoic orogens such as the Pyrenees (Beaumont et al., 2000) and North Sea (Badley et al., 1989).

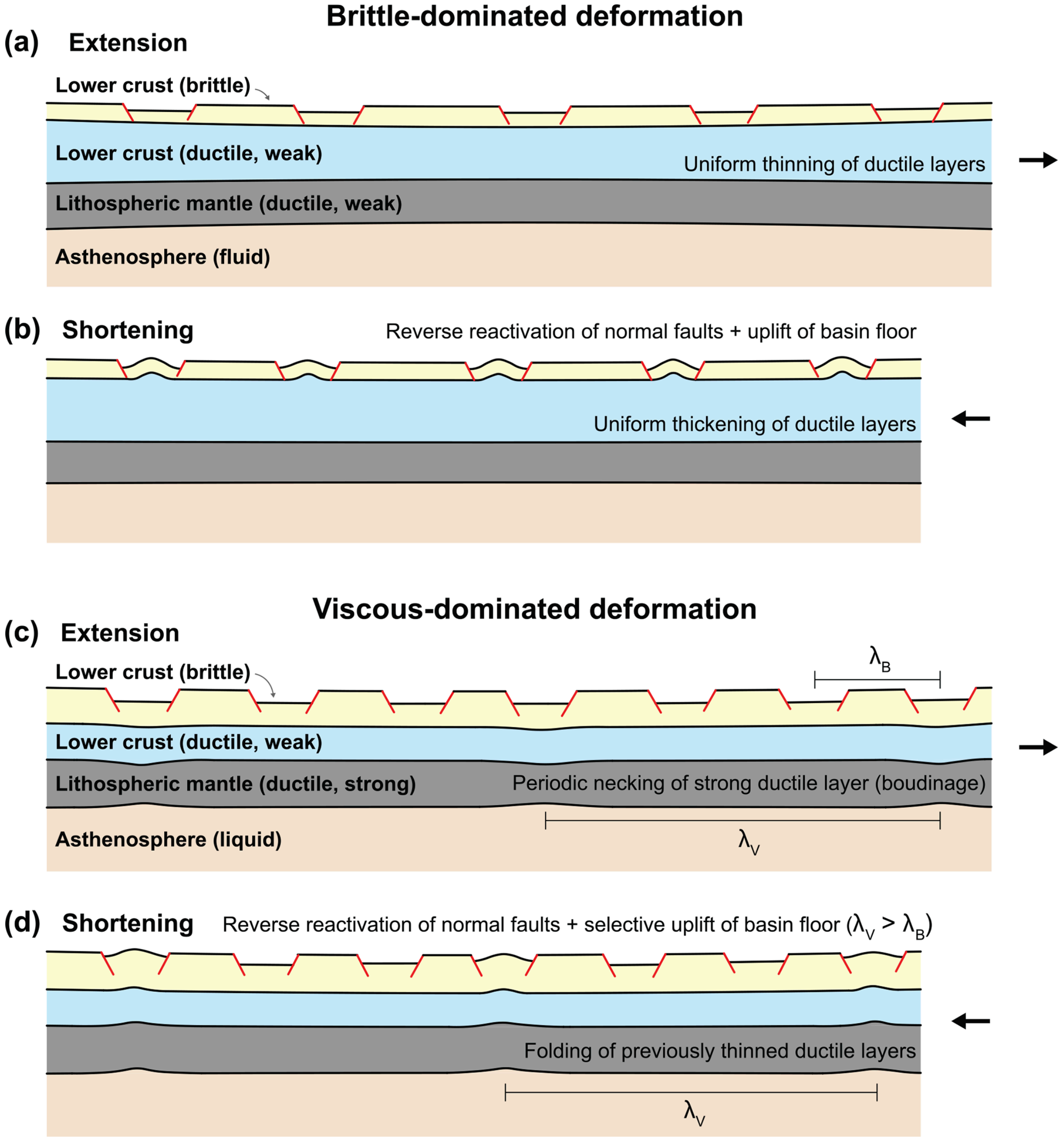

Figure 21. Conceptual illustration of brittle-dominated deformation (e.g. R2) and viscous-dominated deformation (e.g. R3, R4, and R5) during post-extension shortening. Upper crustal deformation is observed directly from photographs and PIV-derived topographic and strain maps. Deformation of the ductile and liquid layers are inferred from observations of the top of the lower crust after the upper crust has been removed and are also inspired by previous analogue experiments (Benes and Davy, 1996; Gartrell, 1997). Brittle-dominated deformation occurs at slow strain rates, as deformation localisation is controlled by the frictional properties of the brittle upper crust (a, b). Viscous-dominated deformation corresponds with faster strain rates: during extension (c), lithospheric-scale boudinage occurs due to periodic instabilities (with a characteristic wavelength λ) in the ductile lithosphere layers. B denotes characteristic wavelength of strain localisation in the upper crust (i.e. the spacing between basins).

When the lithosphere is shortened (d), the previously thinned ductile layers undergo folding and the basins above these areas are inverted. Folding of the ductile layers, with the characteristic wavelength λ, may also occur even without previous boudinage.

By contrast, wide-rift systems showed much more complex inversion behaviour. While the lithosphere remained hot and weak, shortening was broadly distributed, producing low-relief plateaus with diffuse strain. With progressive strengthening of the mantle relative to the fault-weakened crust, deformation became increasingly partitioned, leading to strong mechanical stratification and eventual crust–mantle decoupling. In this regime, shortening was accommodated by deep crustal folding and the development of lithospheric shear zones that offset the Moho by tens of kilometres, while surface uplift remained subdued (Figure 21c–d). These results emphasise that lithospheric rheology and strain partitioning, rather than post-rift cooling, are the primary controls on inversion style in wide rifts (Vasey et al., 2023; Oravecz et al., 2024).

The experiments also demonstrate the phenomenon of selective inversion, where only some basins or rift segments are uplifted while adjacent depocentres paradoxically continue to subside due to competing flexural and viscous effects (Figure 20). This selective behaviour is a hallmark of wide-rift inversion and aligns with field examples such as the southern Georgina Basin, where Alice Springs–age contraction inverted some Neoproterozoic depocentres while others remained sites of subsidence (Greene, 2010), and the Mount Isa Inlier, where the Isan Orogeny reactivated earlier rift fabrics in a complex, selective manner (O'Dea et al., 1997).

The progression from distributed to localised shortening, captured in the analogue cross-sections, illustrates how mantle strengthening relative to the crust drives folding and shear concentration (Figure 22a). This finding parallels analogue studies showing that mantle strengthening relative to the crust drives folding and shear concentration (Samsu et al., 2023), and numerical results that predict polarity flips and deep-seated shear zones under prolonged post-rift evolution (Vasey et al., 2024). Such insights stress the importance of evolving rheology in shaping inversion style and orogenic architecture.

Natural examples mirror these model behaviours. The Araçuaí–West Congo Orogen, formed during inversion of a Tonian wide rift, shows distributed deformation, flat orogenic bases and tops, and modest surface relief sustained by prolonged high temperatures (Alkmim et al., 2006; Vauchez et al., 2019) features consistent with hot wide-rift inversion. By contrast, the Centralian Superbasin experienced inversion after ~400 Myr of quiescence, with the Petermann and Alice Springs Orogenies driving crust–mantle decoupling, Moho offsets of >20 km, and muted surface relief (Walter et al., 1995; Gibson et al., 2016). The Greater McArthur Basin provides a further example, where Paleoproterozoic successions record multiple episodes of extension and inversion; seismic studies show that the Daly Waters Fault Zone repeatedly reactivated under alternating extensional and compressional regimes, with strain partitioned into deep-seated shear zones (Figure 22b; Blaikie et al., 2017; Soares et al., 2025). Importantly, inversion structures in the McArthur Basin also acted as fluid conduits, directly linking rift inheritance to the localisation of world-class Zn–Pb–Ag mineralisation such as the McArthur River deposit (Large et al., 2005).

Taken together, the results of the analogue experiments, supported by numerical modelling and natural case studies, reveal that narrow-rift inversion is largely geometry-controlled, whereas wide-rift inversion is highly sensitive to lithospheric rheology and strain partitioning. The selective uplift of basins (Figure 20), distributed deformation under weak lithospheric conditions, and Moho-offset shear zones under strengthened conditions (Figure 21c–d; Figure 22a–b) are diagnostic features of wide-rift inversion. These findings provide a unified framework for interpreting the contrasting inversion styles of Proterozoic versus Phanerozoic orogens and underscore the role of lithospheric architecture in shaping long-term basin evolution, tectonic inheritance, and mineral system development.

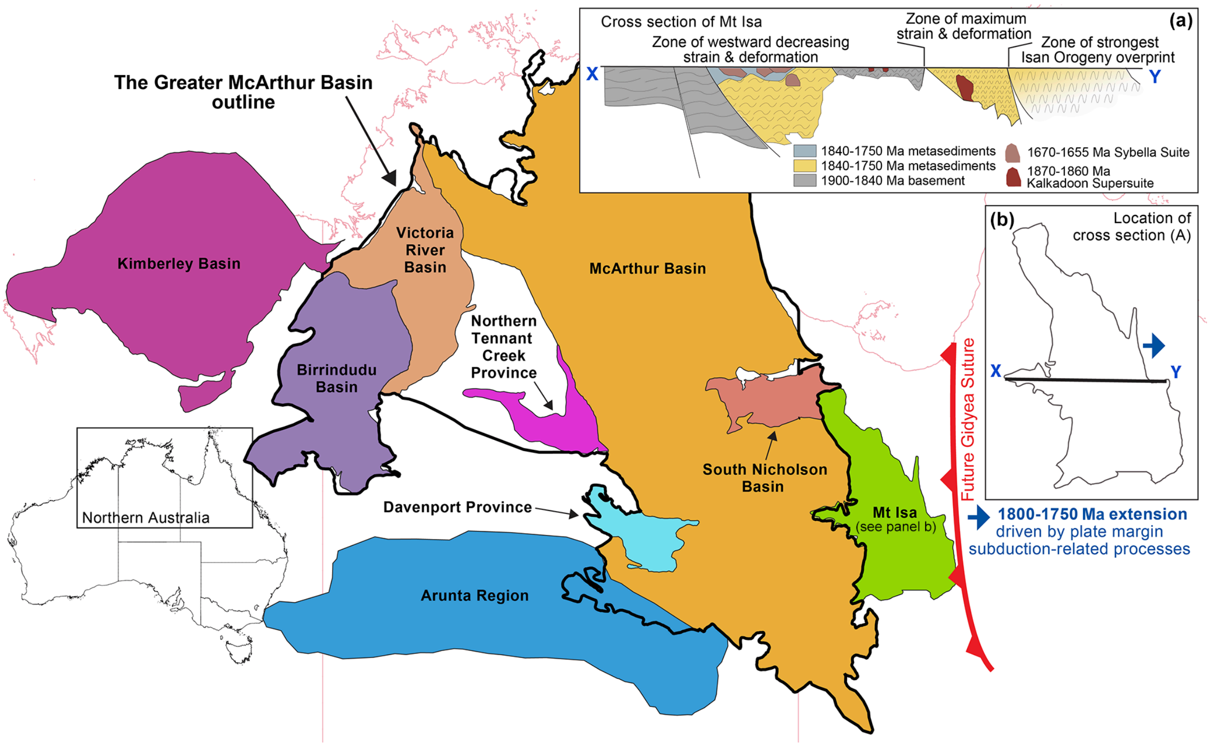

Figure 22. Map of Proterozoic basins in northern Australia (basin shapes obtained from [‡]*Geoscience Australia portal). (a) Cross section of 1800–1750 Ma showing strain and deformation intensity related to compression during the 1750–1710 Ma Wonga Orogeny (Spence et al., 2022) which followed the 1800–1750 Ma extension. (b) Outline of the Mt Isa terrane, showing the location of (a).*

3.3. Oblique extension and inversion[§]

Oblique rifting is a fundamental mode of lithospheric deformation in natural systems, reflecting the fact that extensional strain is rarely purely orthogonal to plate boundaries (Dewey, 1988; Withjack & Jamison, 1986). Analogue and numerical experiments consistently demonstrate that the degree of obliquity exerts a strong control on fault architecture, basin orientation, strain localisation, and the subsequent style of basin inversion (Tron & Brun, 1991; Clifton et al., 2000; Brune, 2014). In the NAC, Proterozoic basin systems show structural fabrics that are best explained by oblique rather than purely orthogonal extension (Betts et al., 2006; Spence et al., 2021). To investigate these processes, we designed lithospheric-scale analogue

---

[‡] *https://portal.ga.gov.au, last access: 28 October 2022*

[§] Movies for all the experiments are in Appendix_1_Analogue_modelling_3_3 experiments that imposed oblique extension followed by shortening, systematically varying the angle of obliquity (30°, 45°, 60°, 90°).

3.3.1. Methodology

3.3.1.1. Experimental setup

All experiments described here consist of a 44 × 40 × 2.8 cm three–layer brittle–ductile model lithosphere that floats isostatically on a fluid model asthenosphere contained within a 65 × 65 × 20 cm acrylic tank (Figure 23). The model lithosphere is confined by two U–shaped walls, one of which is fixed to the side of the acrylic tank and the other attached to a moving wall pulled by two linear actuators. These actuators can operate independently and at right angles to one another, allowing the imposition of both orthogonal and oblique extension and inversion boundary conditions. Their programmability ensures precise control of velocity and direction, enabling simulations of kinematics ranging from pure orthogonal extension ($\theta = 0°$) to high-obliquity ($\theta = 90°$) strike-slip.

The model lithospheric layers were carefully constructed within the U–shaped walls and attached to the north and south railing arms (Figure 23a). Ductile layers were prepared separately in a rigid frame to achieve the desired thickness and extent, then placed gently onto the underlying glucose-syrup asthenosphere to reach isostatic equilibrium and allow air bubbles to dissipate. The brittle upper crust was sifted onto the ductile lower crust from a height of ~30 cm to avoid compaction artefacts and to produce a mechanically consistent granular layer. Once all layers were in equilibrium with the asthenosphere, the railing arms were fastened to the confining walls.

To allow for digital image correlation (DIC) analysis, a thin layer of dark coffee powder was sifted onto the light-coloured model surface, producing a high-contrast speckle pattern without altering surface mechanics. After the extension phase, additional powder was applied to improve surface contrast within the newly formed rift basins. The lateral gaps between the U-walls and model layers were lubricated before each experiment to minimise boundary drag.

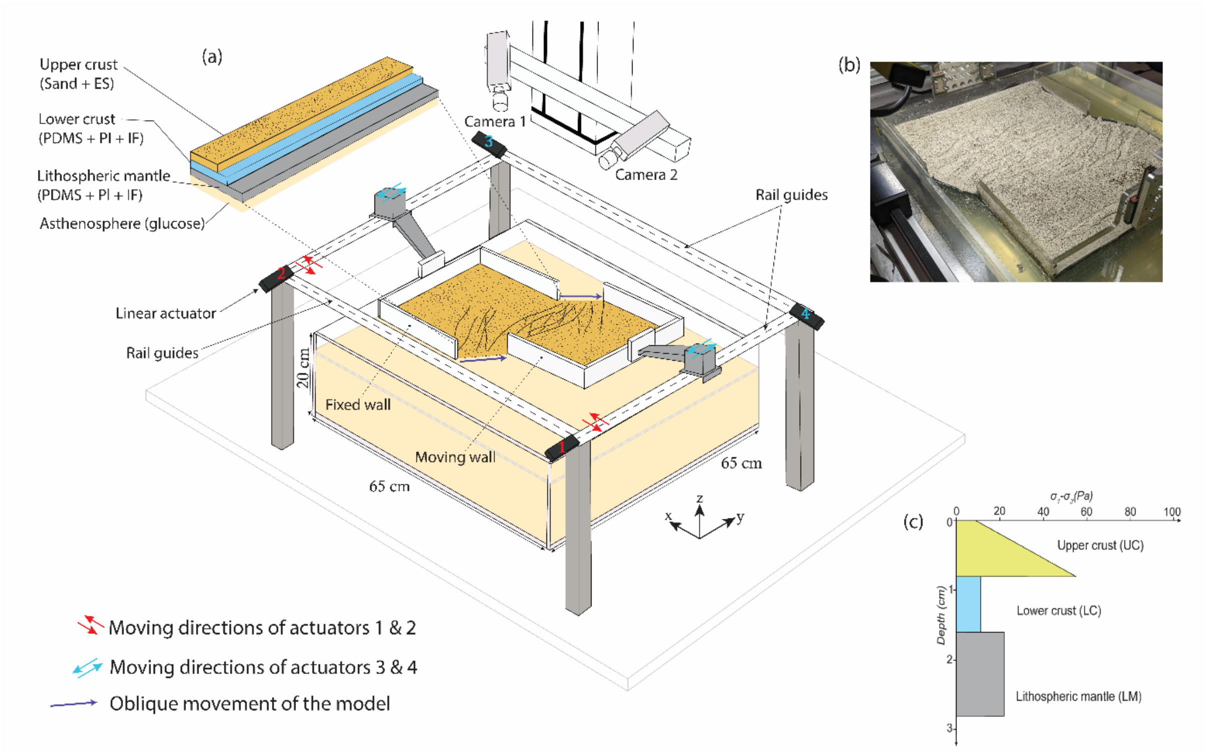

Figure 23. Experimental setup. (a). A 3-D sketch of how the laboratory experiments were constructed. Using a stereoscopic setup, particle image velocimetry (PIV) cameras 1 and 2 captured the deformation of the model surface. The oblique movement of the moving wall was obtained by the simultaneous movement of actuators 1 and 4 which provide the orthogonal and right-angle movements, respectively. (b) Oblique view photo of the analogue model (Obl 1 after 20% extension). (c) Initial strength profile of model in this study. Abbreviations: ES = Envirospheres®, PDMS = Polydimethylsiloxane, PI = Colorific® Plasticine (black), IF = Iron filings.

3.3.1.2. Boundary and initial conditions

The boundary and initial conditions were designed to reproduce wide-rift behaviour under oblique extension and subsequent inversion, conditions thought to characterise Proterozoic intracontinental basins in the NAC (e.g., Buck, 1991; Brun, 1999; Buck et al., 1999). Five experiments were carried out by varying the degree of obliquity (θ) from 0° (pure orthogonal) to 90° (pure strike-slip), with intermediate values of 30°, 45°, and 60° (Figure 24). Each experiment consisted of an "extension" phase followed by an "inversion" phase at the same obliquity. Orthogonal experiments (θ = 0°) serve as reference models (see section 2.2) and here we focus primarily on the four oblique experiments.

In plan view, the upper edge of the model corresponds to "north" and the moving wall displaced the lithosphere toward the "south" or "south-west," depending on the obliquity imposed. To reduce boundary artefacts from wall friction, analyses were confined to the central portion of the models. The symmetry and reproducibility of the imposed kinematics were validated by three repeat experiments, which yielded similar first-order deformation patterns and strain partitioning.

Prior to deformation, the lithosphere was allowed to equilibrate isostatically with the fluid asthenosphere, with density contrasts scaled to natural lithosphere–asthenosphere systems (Schellart, 2011; Molnar et al., 2017). The imposed wall velocities generated extension and shortening at natural equivalents of ~1–2 cm/yr, consistent with Phanerozoic intracontinental rifting rates observed in the Basin and Range Province (Bennett et al., 1998; Snow & Wernicke, 2000; Hammond & Thatcher, 2004).

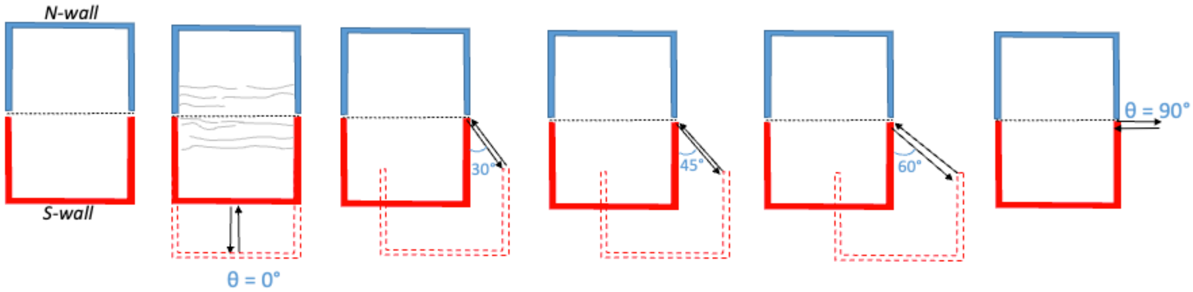

Figure 24. Experimental plan showing the systematic variation of extension and shortening of the south wall (S-wall) from pure orthogonal (Θ = 0°) to pure strike-slip with a fixed north wall (N-wall).

Initial strength profiles of the models (Figure 23c) were tuned to mimic post-orogenic lithosphere after thermal relaxation, favourable to wide-rift formation (Brun, 1999). The brittle upper crust was set mechanically stronger than the underlying ductile lower crust, which in turn overlay a relatively stronger lithospheric mantle. These contrasts ensured that extension resulted in distributed faulting and multiple rift basins rather than single, narrow grabens, consistent with theoretical predictions of lithospheric-scale instabilities (Benes & Davy, 1996; Brun, 1999). The imposition of obliquity rotated the principal stress field, promoting transfer faults, oblique grabens, and rotated fault blocks comparable to natural oblique rift provinces such as the Aegean (Doutsos & Kokkalas, 2001) and East African Rift (Ebinger, 2005).

3.3.1.3. Scaling parameters and model materials

We use scaling parameters of Ramberg (1967) and Molnar et al. (2027) to appropriately scale down lengths, time and forces to a model that behaves in a mechanically similar way to nature, over a desired period of time. All experiments reported here comprise a simplified multi–layer brittle ductile lithosphere with a brittle upper crust, ductile lower crust and a lithospheric mantle, overlaying a model asthenosphere (Figure 23a). These layers were created using granular and viscous materials similar to those previously used by Molnar et al. (2017) and Samsu et al. (2021, 2023).

For all experiments, the length scaling factor, L^*, was fixed by setting the model lithospheric thickness, $L_m = 2.8$ cm to represent natural thickness, $L_p = 70$ km, resulting in $L^* = L_m/L_p = 4 \times 10^{-7}$, where subscript m and p refer to model and natural prototype, respectively. Therefore, the model surface area of 44 × 40 cm corresponds to 1100 × 1000 km in nature. The density scaling factor, $\rho^* = \rho_m/\rho_p = 0.42$ was obtained from the density ratio between the model asthenosphere material (Queen glucose syrup, Schellart, 2011) and natural asthenosphere densities estimated between 3100 and 3400 kg m^{-3}, consistent with previous lithospheric-scale analogue models (e.g., Molnar et al., 2017; Santimano and Pysklywec, 2020; Samsu et al., 2021, 2023). All the experiments were carried out under normal field of gravity (1 g), therefore the gravity scaling factor is $g^* = g_m/g_p = 1$. Similarly, the viscosity scaling factor, $\mu^* = \mu_m/\mu_p = 2.7 \times 10^{-18}$ was determined using the ratio between the effective viscosity of the model asthenosphere (520 Pa s) and that of natural asthenosphere (1.9×10^{19} Pa s). The time scaling factor can then be defined as $t^* = \mu^*/\rho^* \times g^* \times L^* = t_m/t_p = 1.61 \times 10^{-11}$, meaning that 1 hour in the model corresponds to ~7.1 Ma in nature. The list of experimental and natural material properties and scaling parameters of all experiments are summarised in Table 4.

Mixtures of polydimethylsiloxane (PDMS) were used to model the ductile lower crust and lithospheric mantle. PDMS is an optically clear, high viscosity Newtonian viscous fluid with a power law component of $n \sim 1$ at our experimental strain rate ($2.8 \times 10^{-4}\ s^{-1}$). The brittle upper crust was modelled using a granular mixture that is similar to one described in section 2.3.1. The mixture comprises of 89 % dry quartz sand (Rocla 90 Fine Sand, Hanson Australia) and 11 % of hollow ceramic Envirospheres®. Samsu et al. (2023) determined the angle of internal friction of this mixture to be $\phi \sim 49°$ with a cohesion $C \sim 120$ Pa which is suitable to model brittle upper crust with a Mohr–Coulomb behaviour (e.g., Byerlee, 1978; Schellart, 2000).

Table 4. Scaling and experimental parameters for all analogue models. Abbreviations of modelling materials: ES is Envirospheres, BPL is black plasticine, IF is iron filings.

Oblique models		**Thickness**		**Density**		**Viscosity**		
		Model (mm)	Nature (km)	Model (kg/m^3)	Nature (kg/m^3)	Model (Pa s)	Nature (Pa s)	Material
Upper crust	Brittle	0.8	20	1136	2700	-		Sand + ES
Lower crust	ductile	0.8	20	1199	2850	1.1×10^{22}	3.0×10^{4}	PDMS + IF
Lithospheric mantle	ductile	1.2	30	1304	3100	9×10^{22}	2.4×10^{5}	PDMS + BPL + IF
Asthenosphere	fluid	-	-	1430	3400	1.9×10^{20}	5.2×10^{2}	Glucose
Scaling factors		$L^* = 4.0 \times 10^{-7}$		$\rho^* = 4.2 \times 10^{-1}$		$\eta^* = 2.7 \times 10^{-18}$		
		$t^* = 1.61 \times 10^{-11}$		$g^* = 1$		1 hr in model ~ 7.1Myr in nature 28 mm/hr ~ 10 mm/yr in nature		
		$v^* = 2.48 \times 10^{4}$		$\sigma^* = 1.68 \times 10^{-7}$				

3.3.1.4. Deformation monitoring and analysis

The digital image correlation (DIC) method was used to monitor and record the deformation of the model surface. The image acquisition and DIC analysis workflow are similar to that outlined in Molnar et al. (2017) and Samsu et al. (2021, 2023). The DIC system is equipped with two high-speed cameras with spatial resolution of >0.1 mm and a temporal resolution of >0.1 s. The two cameras at oblique angles to the model surface were used to record images at 2 min interval over 2 – 4 hr range for each extension and shortening phase of an experiment. These images allowed us to compute strain and topographic evolution of the models using the StrainMaster module of the commercial software DaVis (version 10.1.2, LaVision). The software uses stereo cross correlation to obtain precise spatio-temporal measurements of incremental and cumulative deformation (e.g., Boutelier and Cruden, 2013; Schrank et al., 2008). Cumulative strain data are calculated as the sum of incremental data. We computed displacement vectors based on the strain tensor,

$$E_{ij} = \frac{dv_i}{d_j} \text{ with } i,j = x,\ y,\ z$$

Where v_i are the displacement components in the x and y direction (i.e., v_x and v_y) and d_j refer to the x and y axis of the coordinate system. We calculate the gradient in the vector component *i* (x,y) along the *j (x,y)* axis. We consider the 2-D strain matrix in order to calculate the maximum normal strain on the surface;

$$\begin{vmatrix} E_{xx} & E_{xy} \\ E_{yx} & E_{yy} \end{vmatrix}$$

And define the maximum normal strain, E_{max}, on the surface as the largest eigenvalue of the matrix;

$$E_{max} = \frac{(E_{xx} + E_{yy})}{2} + \sqrt{\left| \frac{(E_{xx} + E_{yy})^2}{4} + \frac{(E_{xy} + E_{yx})^2}{4} \right|}$$

The incremental and cumulative displacement data computed by DaVis were imported to MATLAB to improve visualisation and post processing. Post-processing of data includes interpolation of missing data and slight height adjustment of model surface (i.e., initially uneven surfaces).

Surface strain and topography data were exported from DaVis for further processing steps in MATLAB. Postprocessing including routines to correct and level topographic data and detection and removal of spurious displacement vectors.

We use the principal strains E_{max} and E_{min} to quantify deformation during extension (i.e., rifting) and shortening (i.e., inversion) phases in our models, respectively. Incremental strain values (given DIC increments of 2 min) are within the range [0, 3] % and [-3, 0] % for rifting and inversion phases, respectively. To compare finite deformation in the models, we normalise strain values within each model domain between [0, 1] for rifting and [-1, 0] for inversion phases. For each conducted experiment, we provide profiles parallel to the direction of motion for topography, incremental as well as (normalised) finite deformation values.

3.3.2. Results and findings

Five lithospheric-scale analogue experiments were conducted to investigate the influence of obliquity (θ) on extension and subsequent inversion, ranging from pure orthogonal (θ = 0°) to pure strike-slip (θ = 90°). Orthogonal experiments are treated as reference cases (Samsu et al., 2023, section 3.2.2) and are not repeated in detail here; instead, the focus is on the four oblique configurations (θ = 30°, 45°, 60°, and 90°). Each experiment progressed through an extension phase followed by shortening at the same imposed obliquity. Analyses concentrate on the central domain of the models to minimise boundary effects caused by friction with the U-shaped sidewalls.

3.3.2.1. Low obliquity experiment (θ = 30°)

During the early stage of extension (5% bulk strain, ~0.9 h), no faults were visible on the surface, but incremental strain maps already showed strong localisation (~2%) perpendicular to the imposed obliquity at the northern and southern model margins (Figure 25b). Additional moderate strain patches appeared in the centre of the model (yellow–green in Figure 25b), though these did not immediately correspond to topographic expression. Profiles across section A confirm this lag, showing incipient strain spikes in the absence of discernible relief (Figure 25c).

By 10% extension (~1.9 h), two first-order fault systems had developed: (i) SE–NW trending normal faults approximately perpendicular to the oblique extension direction, and (ii) N–S trending normal faults that curved toward NW–SE orientations in the model centre, coinciding with earlier incremental strain hotspots (Figure 25a). At this stage, topographic depressions became established as rift basins, aligned with strain spikes exceeding the ~2% incremental strain threshold, here defined as the onset of active faulting (Figure 25c).

At 12.5% extension (~2.4 h), both fault systems remained active, producing wider and deeper basins with increasing throw. NW–SE trending linking faults emerged to connect N–S rifts, generating composite grabens (Figure 25a). Continued extension to 15% (~2.8 h) and 20% (~3.8 h) resulted in the stabilisation of early-formed basins: strain remained concentrated within the deepest rifts, but no new major faults developed. By the end of extension, basin-bounding faults had reached final length, with inactive linking structures preserved in the rift network.

Shortening initially concentrated strain within basin interiors (Figure 26b). At 7.5% bulk shortening (~1.7 h), the deepest extensional basins (Figure 26c) inverted via reverse reactivation of basin-bounding faults, while basin shoulders remained intact. With further shortening (~12.5%), NW–SE linking faults rotated clockwise and closed, merging with adjacent N–S rifts. By the final stage of shortening (15%), six of ten basins along profile A were inverted, highlighting the selective reactivation of pre-existing extensional structures (Figure 26c).

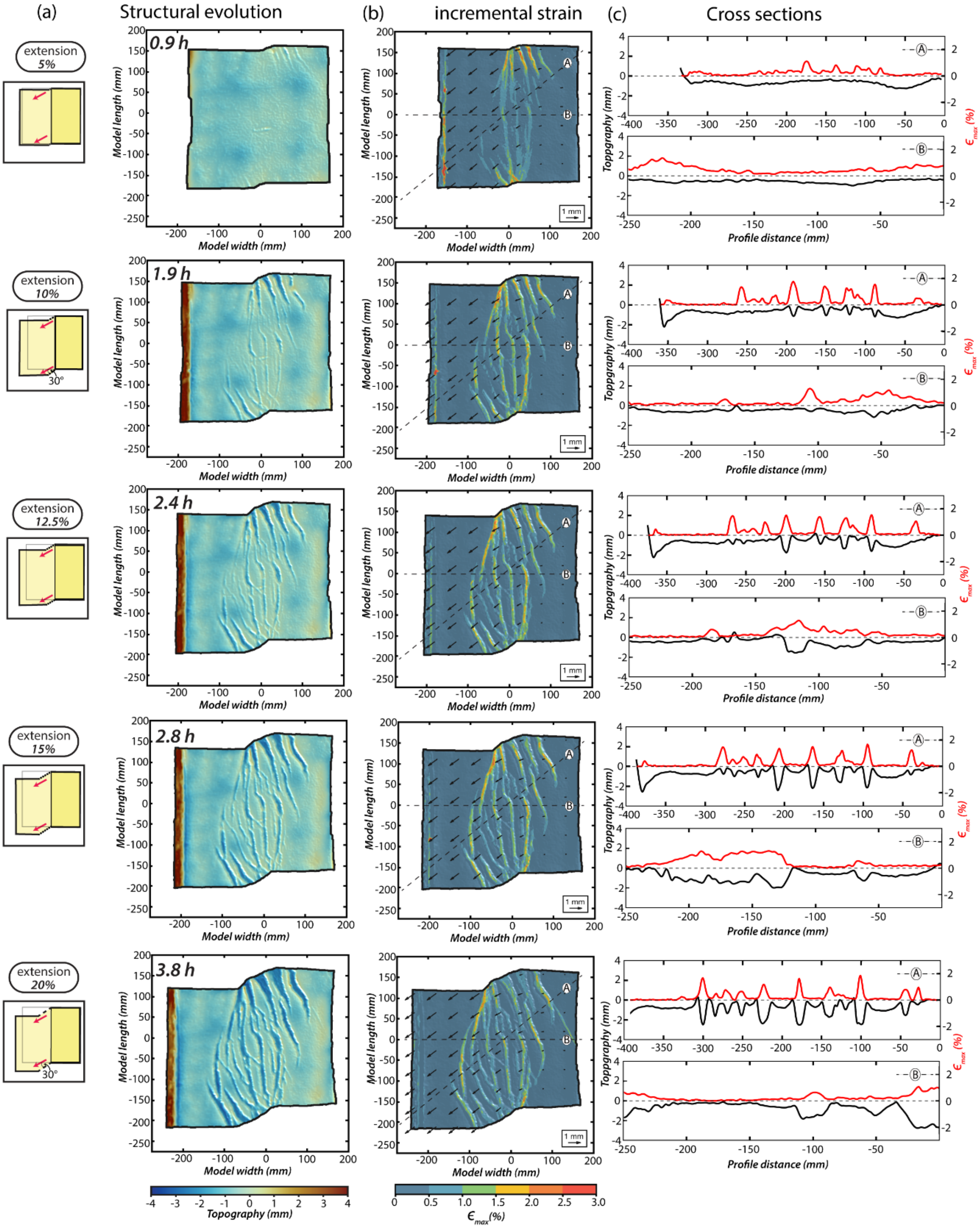

Figure 25. Evolution of deformation during the extension phase with a low obliquity (ϴ = 30°) model. (on the left) Schematic drawings showing the extension direction for different bulk extension ratios. (a) Topography (2D) and the structural evolution with respect to each bulk extension ratio presented in top-view DEMs. (b) Maps of incremental normal strain (E_{max}) on the surface for each stage. Location profiles of A and B shown in column c are indicated by black dotted lines. Black arrows are vectors showing the displacement magnitude and the direction of model surface. (c) Surface elevation (black) and incremental normal strain (red) profiles. see Movies in Appendix_1/Analogue_modelling3_3/.

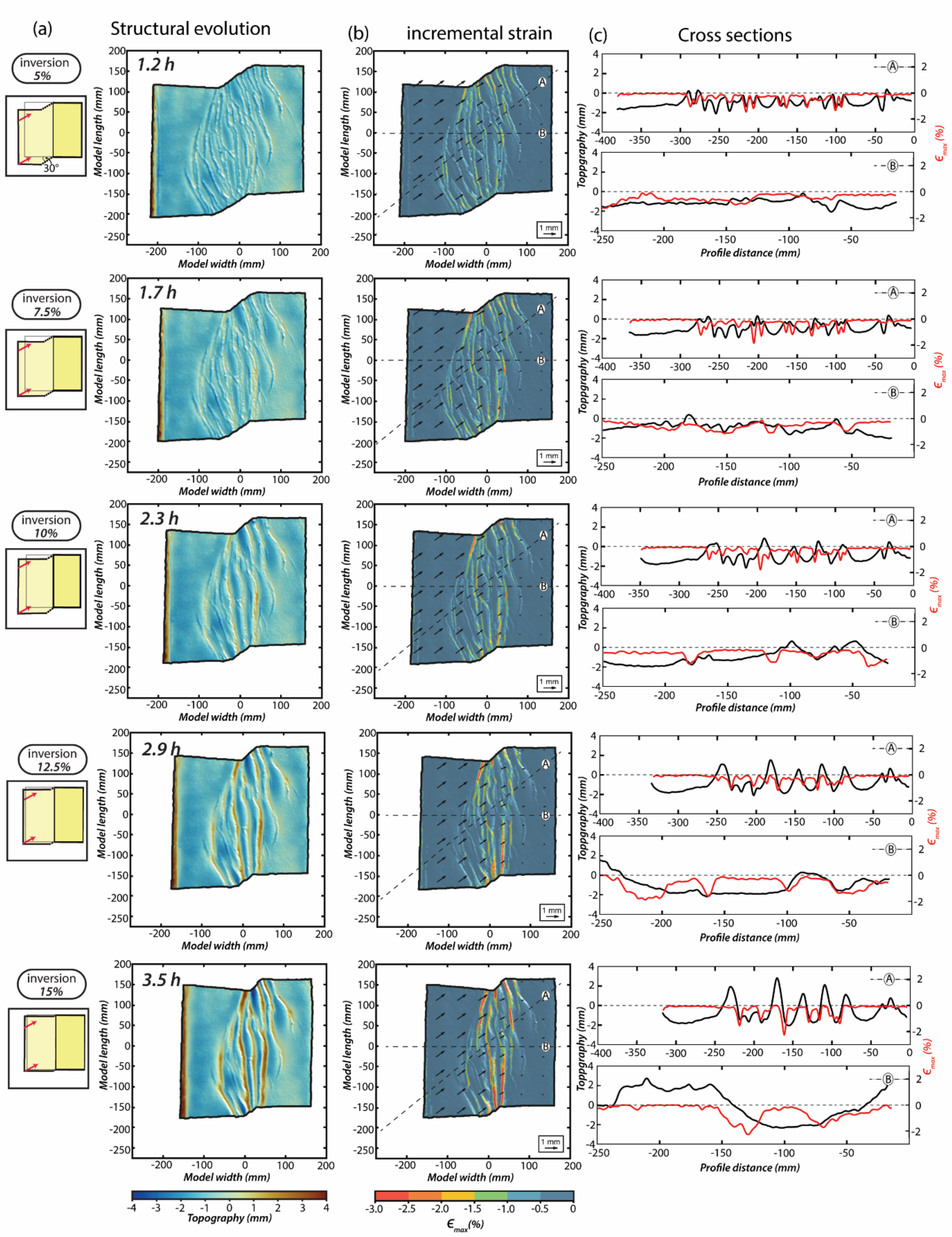

Figure 26. Evolution of deformation during the inversion phase with a low obliquity (ϴ = 30°) model. (on the left) Schematic drawings showing the extension direction for different bulk inversion ratios. (a) Topography (2D) and the structural evolution with respect to each bulk extension ratio presented in top-view DEMs. (b) Maps of incremental normal strain (E_{max}) on the surface for each stage. Location profiles of A and B shown in column c are indicated by black dotted lines. Black arrows are vectors showing the displacement magnitude and the direction of model surface. (c) Surface elevation (black) and incremental normal strain (red) profiles. see Movies in Appendix_1/Analogue_modelling3_3/.

3.3.2.2. Moderate obliquity experiment (θ = 45°)

At 5% (~0.9 h) bulk extension (ϴ = 45°), faults had not formed even though the incremental strain map shows strong strain localisation in the middle of the model at the N-S direction and a few towards the NW-SE directions (Figure 27b, c). After 10% extension, at about 2% incremental strain, two distinct first order faults had formed trending NS and NW-SE (Figure 27a, b, 4c). At this stage, strain became highly localised in the centre of the rift depressions and extension was consequently accommodated by increasing the width and the depth of the rift basins (Figure 27b, 4). At 15% bulk extension, both first order rift systems were still active, and they became deeper. At this stage, a few linking faults (i.e. transfer faults) were formed with a trend of NW-SE mainly connecting NS trending first-order normal faults. Towards the final stage of the extension (i.e., 20%, ~3.8 h), most of the early formed first-order basins and linking faults were inactive and basins became fully established as the basin-bounding normal faults reached their final length

At early stage of the shortening (5%, ~1.7 h), structural evolution remained similar to that of the preceding extensional phase. The incremental strain map shows that strain is highly and slightly localised within NS and NW-SE trending rift basins, respectively. Regardless of the incremental strain signature, the topography profile along the line A (Figure 28c) shows that the deepest and widest of both NS and NW-SE trending rift basins that were formed at the end of the extension phase had already started to invert by decreasing their basin depths and widths. At about 12.5% shortening, incremental strain is strongly localised mainly in the centre of the NS trending rift basins, and NW-SE trending linking faults appear to close up and merge with NS trending first order rifts after rotating clockwise. Towards the final stage of shortening (15%), 6 out of 11 basins (along the profile line A; Figure 28c) that were formed at the end of the extension were inverted showing NS orientation.

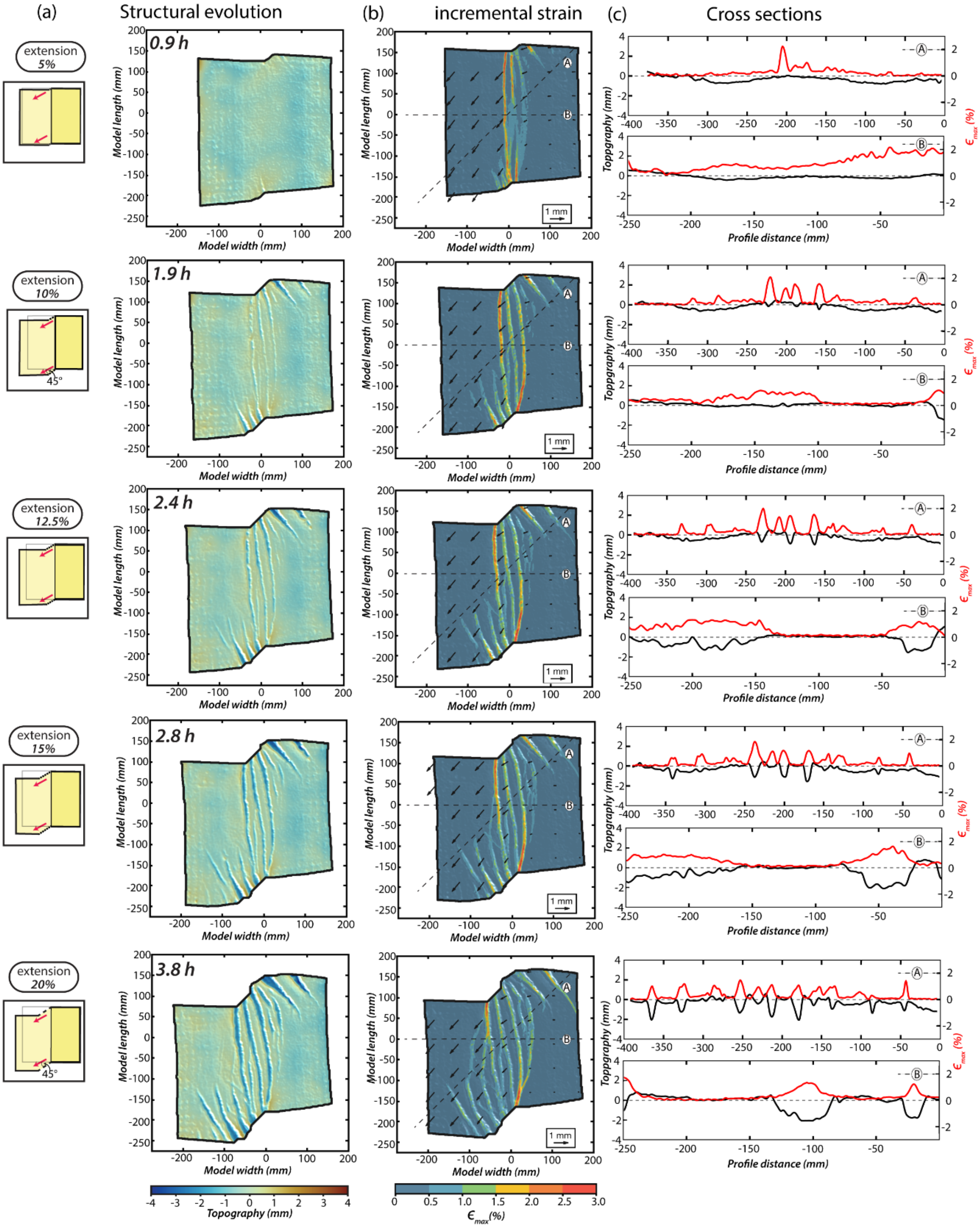

Figure 27. Evolution of deformation during the extension phase with a moderate obliquity (ϴ = 45°) model. (on the left) Schematic drawings showing the extension direction for different bulk extension ratios. (a) Topography (2D) and the structural evolution with respect to each bulk extension ratio presented in top-view DEMs. (b) Maps of incremental normal strain (E_{max}) on the surface for each stage. Location profiles of A and B shown in column c are indicated by black dotted lines. Black arrows are vectors showing the displacement magnitude and the direction of model surface. (c) Surface elevation (black) and incremental normal strain (red) profiles. see Movies in Appendix_1/Analogue_modelling3_3/.

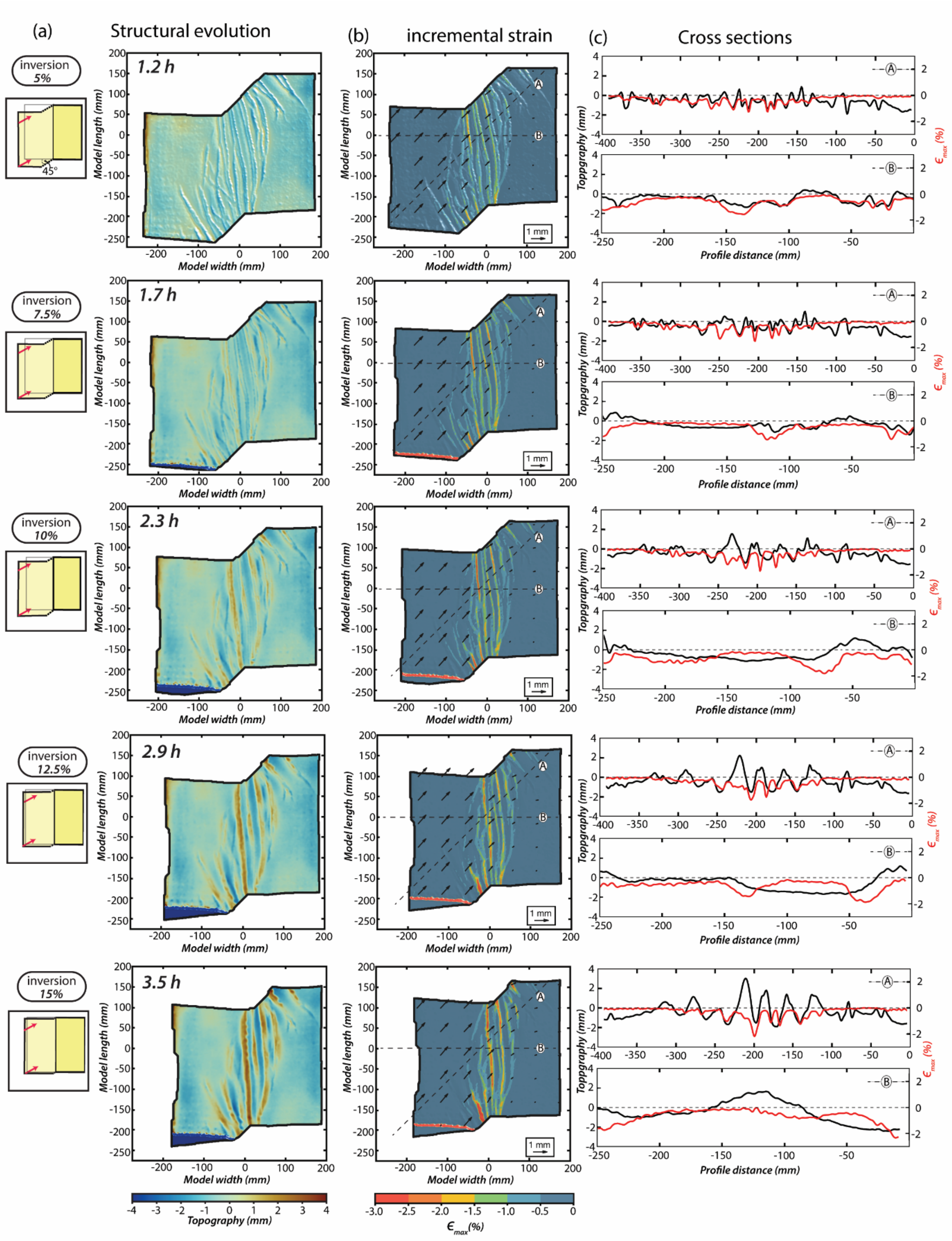

Figure 28. Evolution of deformation during the inversion phase with a moderate obliquity (Θ = 45°) model. (on the left) Schematic drawings showing the extension direction for different bulk inversion ratios. (a) Topography (2D) and the structural evolution with respect to each bulk extension ratio presented in top-view DEMs. (b) Maps of incremental normal strain (E_{max}) on the surface for each stage. Location profiles of A and B shown in column c are indicated by black dotted lines. Black arrows are vectors showing the displacement magnitude and the direction of model surface. (c) Surface elevation (black) and incremental normal strain (red) profiles. see Movies in Appendix_1/Analogue_modelling3_3/.

3.3.2.3. *High obliquity experiment (θ = 60°)*

At 5% (~0.9 h) oblique extension (Ɵ = 60°), despite the absence of any surface structures (Figure 29a), the incremental strain was strongly localised and propagated southward in the centre of the model (Figure 29b, c). At 10% extension, the topography map shows the presence of two almost parallel linear normal faults trending N-S, and the incremental strain is highly localised within these two fault segments. Cross sections of surface elevation and incremental strain at 12.5% indicate that the N-S trending boundary faults towards the East of the model started to form a basin at a strain threshold of 2% (Figure 29c). Moreover, linking faults that are perpendicular to the obliquity started to form at this stage in between two main N-S trending normal faults. With ongoing extension (at ~15 %), four active normal faults which are subparallel to each other and trending almost N-S were established in the center of the model. The basin that formed during the previous stage of extension is now deeper and wider with localised strain in the rift interior. During the advanced stage of extension (~15%, 3.8 h), rift basins stabilised when basin widening and strain localisation in the rift interiors was observed.

During the early stage of shortening (~5%, 1.2 h), the deformation and incremental strain is highly localised in the N-S trending rift basins that were formed at the end of the extension. However, the linking faults that connected the main N-S trending rift basins in the preceding extensional phase are inactive at this stage. Continued shortening (~7.5%, 1.8 h) causes the reverse reactivation of basin bounding faults and the basins become narrower and shallower together with the onset of basin inversion. At about 12.5% shortening, two N-S trending small magnitude basins start to merge with large magnitude rift basins with the same orientation, which are active at this stage. Towards the final stage of shortening (15%), 3 out of 6 basins (along the profile line A; Figure 30c) that were formed at the end of the extension were inverted showing nearly NS orientation.

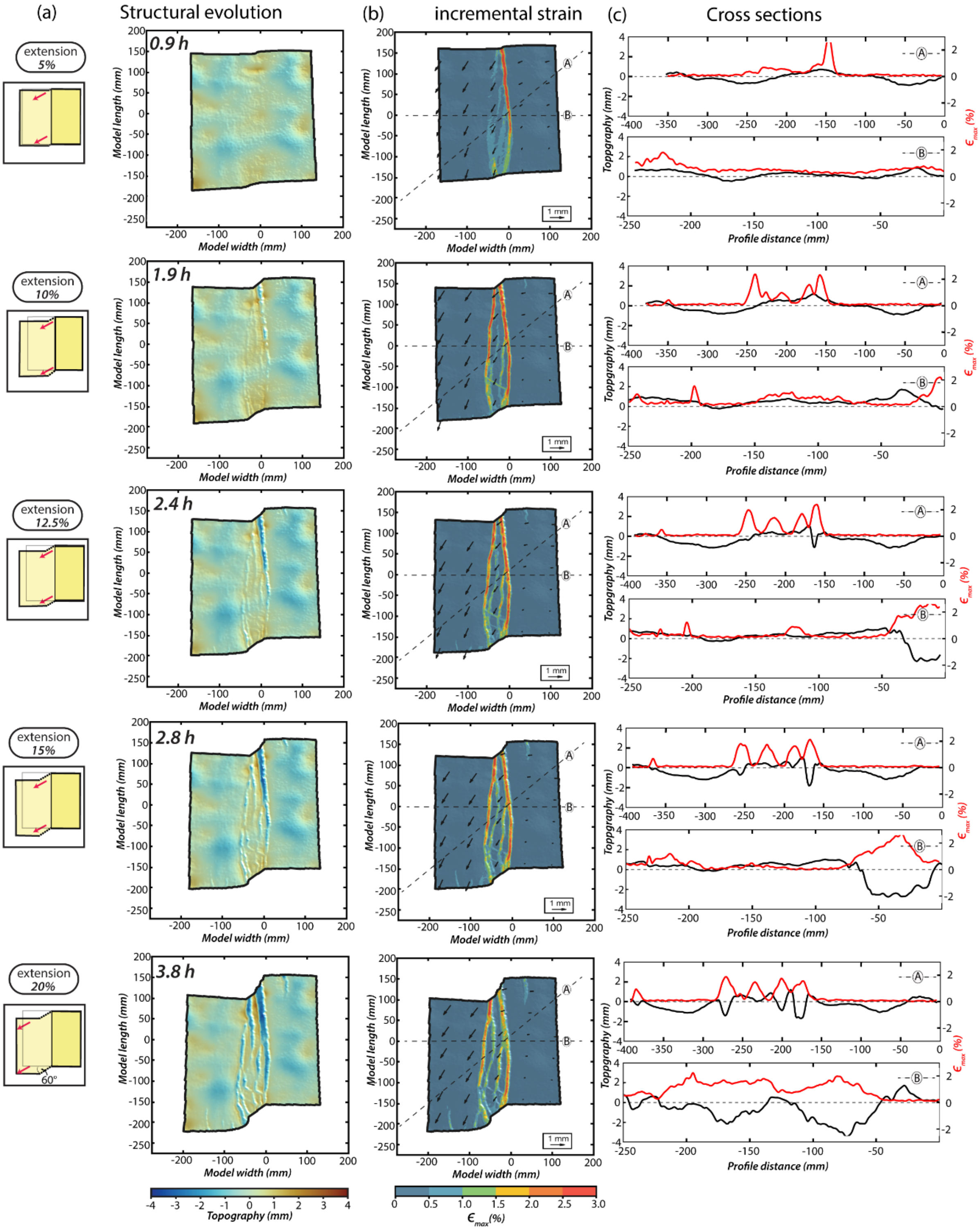

Figure 29. Evolution of deformation during the extension phase with a high obliquity (Θ = 60°) model. (on the left) Schematic drawings showing the extension direction for different bulk extension ratios. (a) Topography (2D) and the structural evolution with respect to each bulk extension ratio presented in top-view DEMs. (b) Maps of incremental normal strain (E_{max}) on the surface for each stage. Location profiles of A and B shown in column c are indicated by black dotted lines. Black arrows are vectors showing the displacement magnitude and the direction of model surface. (c) Surface elevation (black) and incremental normal strain (red) profiles. see Movies in Appendix_1/Analogue_modelling3_3/.

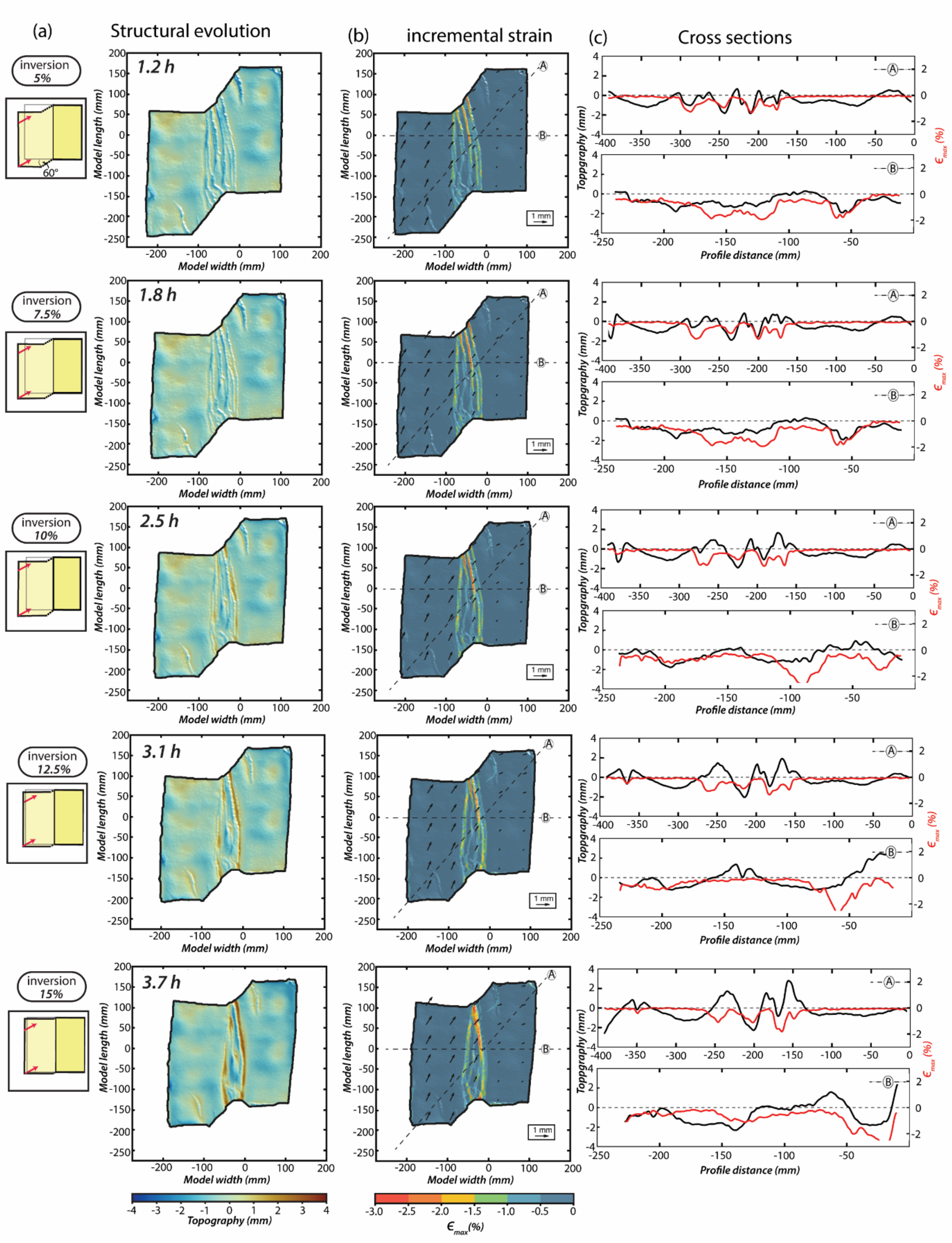

Figure 30. Evolution of deformation during the inversion phase with a high obliquity (Θ = 60°) model. (on the left) Schematic drawings showing the extension direction for different bulk inversion ratios. (a) Topography (2D) and the structural evolution with respect to each bulk extension ratio presented in top-view DEMs. (b) Maps of incremental normal strain (E_{max}) on the surface for each stage. Location profiles of A and B shown in column c are indicated by black dotted lines. Black arrows are vectors showing the displacement magnitude and the direction of

model surface. (c) Surface elevation (black) and incremental normal strain (red) profiles. see Movies in Appendix_1/Analogue_modelling3_3/.

3.3.2.4. Pure strike-slip experiment (θ = 90°)

In contrast to all other models, at the early stage of bulk strike-slip displacement (~5%, 0.7 h), the incremental strain is weakly localised in a N-S trending zone at the centre of the model with no corresponding development of topography (Figure 31a, b). At 10% (~1.3 h) strike-slip (Ɵ = 90°), the incremental strain is highly localised in the centre of the model, forming an active almost linear N-S trending fault. With continued extension (12.5% - 15%), this fault starts to curve outwards from the centre at the northern and southern boundaries of the model. Moreover, it breaks into two separate fault segments at the centre of the model where the south-ward and north-ward orienting fault segments change directions towards SW and NE, respectively (15%, Figure 31b). During the advance stage of strike-slip displacement (20%, 2.7 h), previously segmented faults are still active with high strain localisation at the centre of the model. However, a completely new and active fault which connects the N and S boundaries of the model curves outwards from the centre (Figure 31b).

During the early stage of shortening (~10%, 1.3 h), reactivation of basin bounding faults appear in the southern boundary of the model with weak strain localisation. At about 15% shortening (2.0h), this reactivated fault curves outward (NE-SW trend, Figure 32b) from the centre of the model showing that its incremental strain gradually propagates from south to north. At late stages of shortening (~20%, 2.7 h), both major faults that were formed during initial strike-slip deformation are now inverted forming a large basin in between them.

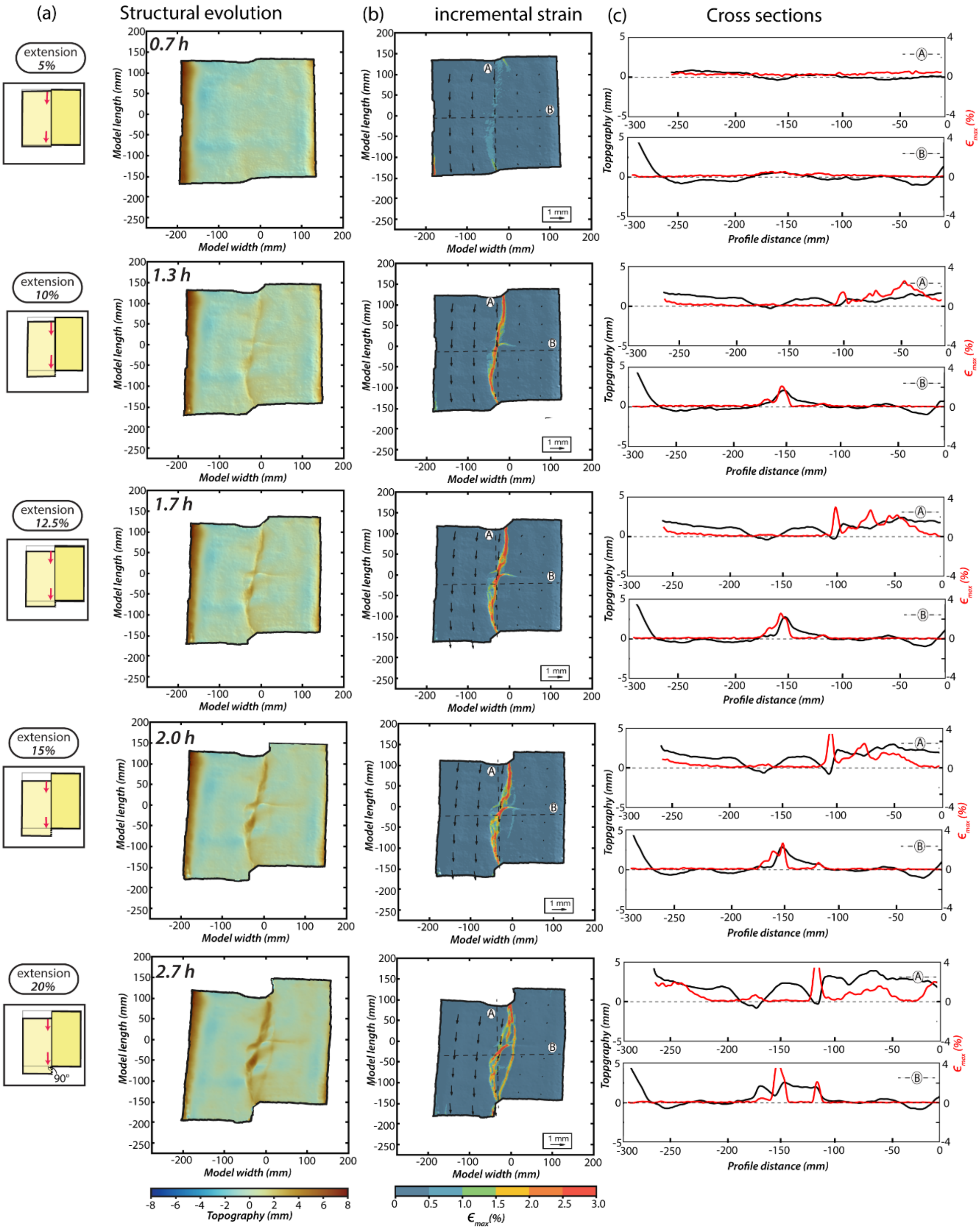

Figure 31. Evolution of deformation during the extension phase with a moderate obliquity (Ɵ = 60°) model. (on the left) Schematic drawings showing the extension direction for different bulk extension ratios. (a) Topography (2D) and the structural evolution with respect to each bulk extension ratio presented in top-view DEMs. (b) Maps of incremental normal strain (E_{max}) on the surface for each stage. Location profiles of A and B shown in column c are indicated by black dotted lines. Black arrows are vectors showing the displacement magnitude and the direction of model surface. (c) Surface elevation (black) and incremental normal strain (red) profiles. see Movies in Appendix_1/Analogue_modelling3_3/

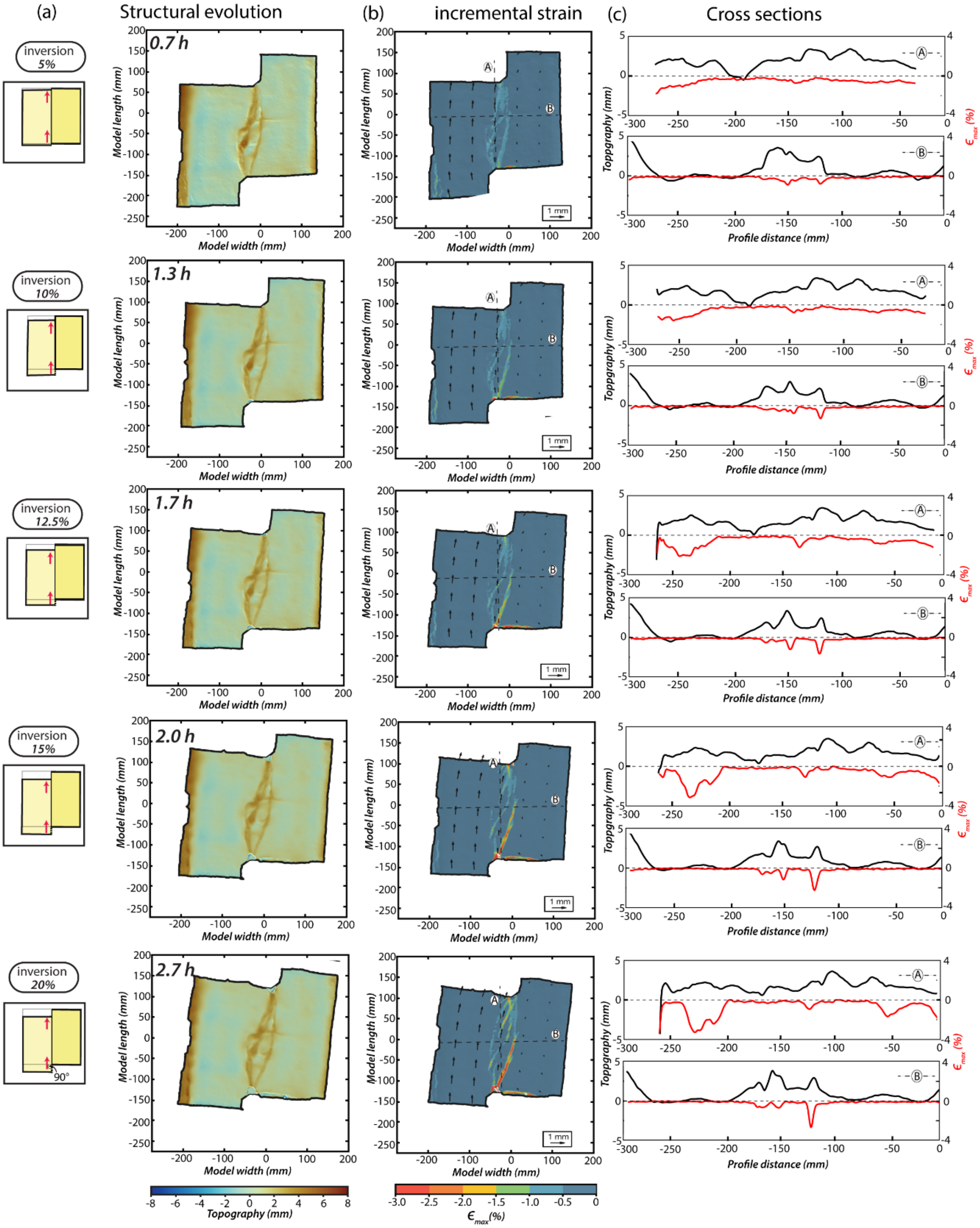

Figure 32. Evolution of deformation during the inversion phase with a low obliquity (ϴ = 90°) model. (on the left) Schematic drawings showing the extension direction for different bulk inversion ratios. (a) Topography (2D) and the structural evolution with respect to each bulk extension ratio presented in top-view DEMs. (b) Maps of incremental normal strain (E_{max}) on the surface for each stage. Location profiles of A and B shown in column c are indicated by black dotted lines. Black arrows are vectors showing the displacement magnitude and the direction of model surface. (c) Surface elevation (black) and incremental normal strain (red) profiles. see Movies in Appendix_1/Analogue_modelling3_3/

3.3.3. Discussion

The oblique extension and inversion analogue experiments demonstrate that the evolution of strain localisation, rift geometries, and basin inversion is highly sensitive to the degree of obliquity in applied boundary conditions. With all other parameters held constant, the systematic variation from orthogonal (0°) through low to high obliquity (30–90°) allows direct assessment of how fault orientation, basin segmentation, and inversion style evolve. Three end-member categories emerge: low obliquity (30°), medium obliquity (45°), and high obliquity (60°), while the pure orthogonal and strike-slip cases represent kinematic extremes. The comparative strain maps (Figure 33) and summary diagrams (Figure 34) highlight how low obliquity promotes distributed, complex fault networks and linkage structures, whereas higher obliquity focuses strain into narrower, more linear rifts. These findings are consistent with previous analogue and numerical studies, which show that increasing obliquity reduces fault diversity, promotes rift-parallel faulting, and limits transfer fault development (Autin et al., 2010; Corti et al., 2013; Autin et al., 2017; Richetti et al., 2023).

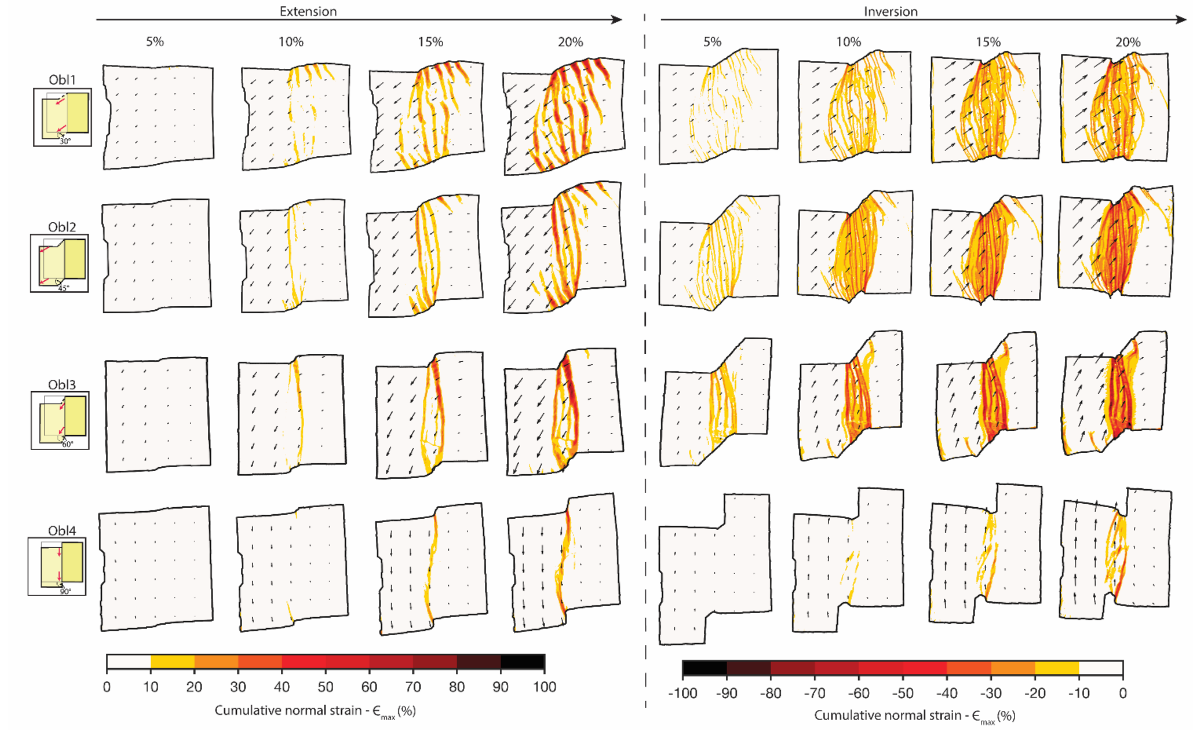

Figure 33. Cumulative strain maps for each experiment after 5%, 10%, 15% and 20% during extension and inversion phases. Colour scale indicates cumulative normal strain on surface (E_{max}). Black arrows indicate the displacement vectors in each phase. For cumulative strain evolution, see Movies in Appendix_1/Analogue_modelling3_3/cumulative strain

In the low-obliquity models (30°–45°), extension produced dual fault sets—orthogonal to extension and oblique N–S trending systems—linked by NW–SE transfer faults (Figure 25 - Figure 28). These zones of fault linkage were also hotspots of cumulative strain (Figure 33), suggesting that such transfer structures may serve as long-lived fluid pathways, consistent with natural systems where oblique rifts focus hydrothermal circulation and mineralisation (Sandiford et al., 2006; Ebinger, 2005; Autin et al., 2009). As extension progressed, strain localisation thresholds (Emax ≈ 2%) governed the onset of visible rift topography, with a reproducible lag between strain build-up and surface expression. This delay echoes natural examples in the NAC, where rift initiation is recorded by distributed subsidence prior to the localisation of major fault systems (Betts et al., 2006).

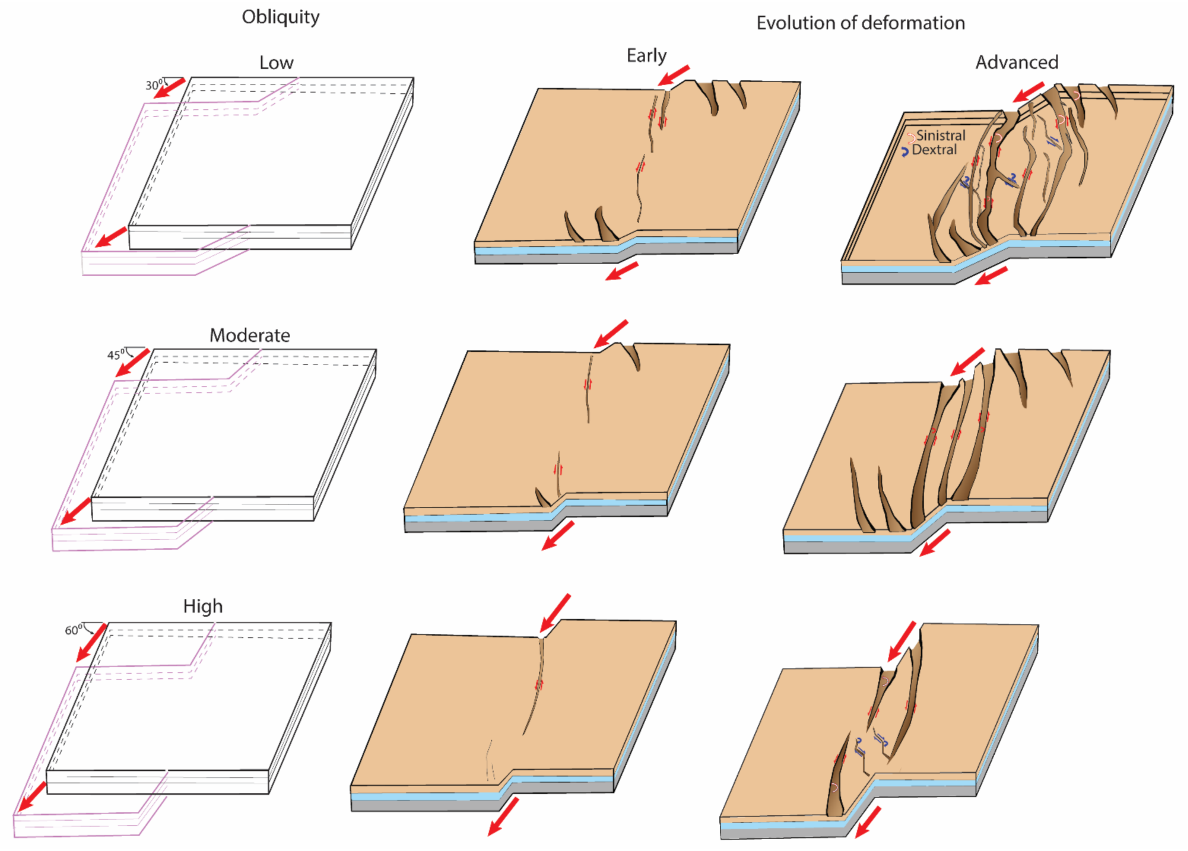

Figure 34. Summary of experimental findings in terms of evolution of deformations as a function of the degree of obliquity. The red and blue arrows along the rifts indicate the shear directions during the extension and the red and the blue curve arrows show their vorticity (i.e. sense of shearing).

By contrast, the high-obliquity (60°) and strike-slip (90°) experiments showed simpler geometries: predominantly N–S parallel rifts with limited linking faults and little strain dispersion (Figure 27 - Figure 30). This narrowing of deformation zones aligns with observations from natural oblique margins such as the Gulf of Aden, where oblique extension results in en-échelon fault sets that eventually evolve into rift-parallel structures (Autin et al., 2010, 2013). During inversion, reactivation was largely confined to basin-bounding faults, producing relatively linear and narrow uplift zones compared to the broader, distributed inversion seen in the low-obliquity models. Comparative profiles through the inversion phases (Figure 35) clearly illustrate this trend: low-obliquity models show selective uplift across multiple basins, whereas higher obliquity models produce inversion focused along a few major structures, with the pure strike-slip case (90°) forming highly linear, fault-controlled inversion geometries.

A key insight of these experiments is the vertical partitioning of deformation between upper and lower crust. Crustal deformation was concentrated in the brittle upper crust, which carried the load and exhibited the highest sensitivity to boundary conditions, while the ductile lower crust responded primarily to gravitational forces and buoyancy (Figure 36a). This mechanical decoupling promoted crustal necking during extension, generating periodic instabilities that set the wavelength of rift basins. During shortening, these thinned zones of upper crust acted as natural sites of inversion, where ductile folding of the lower crust beneath previously necked regions drove selective uplift (Figure 36b). Thickening of the ductile layer further weakened the system, enhancing its tendency to invert. Such behaviour contrasts with earlier models that tied crustal necking primarily to lithospheric mantle topography and strain rates (e.g., Brun, 1999; Huismans, 2010) and instead emphasises the interplay between upper crustal weakening and lower crustal flow.

Figure 35. a-c) Evolution of the obliquity parallel topographic profiles of models Obl1 ($\Theta = 30°$), Obl2 ($\Theta = 45°$), Obl3 ($\Theta = 60°$) and Obl4 ($\Theta = 90°$) during inversion, drawn along the profile A line (see locations in Figure 26c, Figure 28c, Figure 30c, Figure 32c).

This coupling explains why inversion was most pronounced at basin centres, where crustal thinning had been greatest and ductile flow could most effectively drive uplift (Figure 26, Figure 28, Figure 30, Figure 32). Our observations are consistent with thermomechanical predictions that inversion localises where thermal gradients and ductile flow are maximised beneath rift centres (Sandiford et al., 2006; Chenin et al., 2018). The vorticity changes and selective localisation also highlight the potential for focused fluid migration along reactivated faults, an issue of direct significance for metallogenesis in Proterozoic basins (Large et al., 2005).

The complex fault and basin patterns generated in the oblique experiments—particularly the 30° experiment—reproduce the N–S faults, linkage structures, and basin geometries observed in the NAC (Figure 26, Figure 37). Previous interpretations invoked multiphase orthogonal extension—NW–SE followed by NE–SW—to explain the Calvert and Isa superbasins (Betts et al., 2006). Our results show that a single oblique dextral kinematic event can generate comparable architectures, eliminating the need to postulate multiple extension phases. This reinforces obliquity as a first-order control on basin geometry and fault orientation, consistent with evidence from modern oblique rifts such as the Aegean and East African Rift systems (Doutsos & Kokkalas, 2001; Ebinger, 2005).

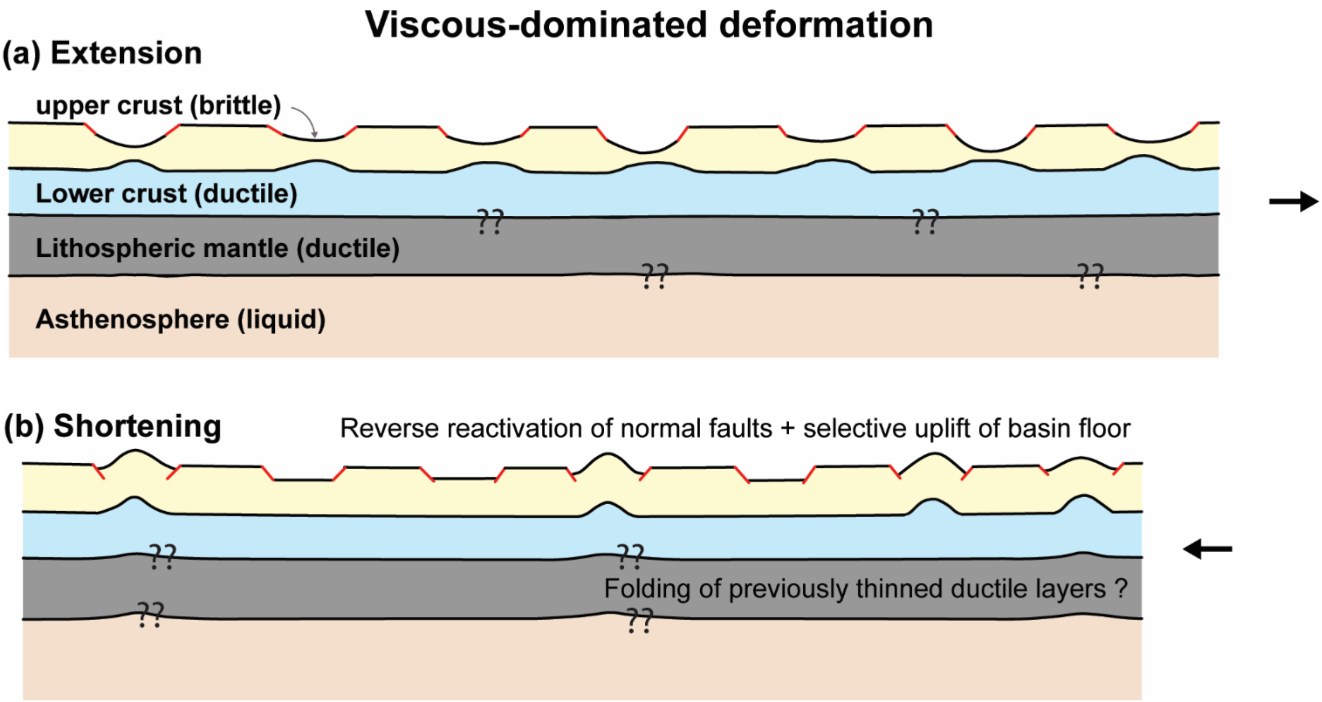

Figure 36. Conceptual illustration of viscous-dominated deformation of lithospheric layers during extension and extension shortening. Upper crustal deformation is observed directly from photographs and PIV-derived topographic and strain maps. Deformation of the upper (brittle) crust inferred from observations of the top of the lower crust after the upper crust has been removed. Top surface of the lower crust (ductile) inferred from observations after removing the upper crust at the end of the extension (test model) and also inspired by previous analogue experiments (Benes and Davy, 1996; Gartrell, 1997). During extension (a), upper crustal - scale boudinage occurs due to changes in upper crustal strength as a result of extension of the layers. (b) During shortening, previously thinned upper crust (i.e. rift basins) undergoes folding and the basins above these areas are inverted (i.e. basin inversion). Question marks along the crust-mantle and lithosphere-asthenosphere boundaries refer to an experimental limitation where the data are not available using the current setup.

Thermomechanical analysis of basin inversion by Sandiford et al. (2006) has shown that inversion is commonly localised along the central basin axis, reflecting the higher-than-average thermal and mechanical gradients beneath the basin centre. Our experiments reproduce this pattern: strain consistently localised in the centre of rift basins, and inversion was most pronounced at these locations, as indicated by incremental strain maps (Figure 25b, Figure 26b) and cumulative vertical displacement (Figure 25a, Figure 26a, Figure 35). Although our models are isothermal, the geometry of deformation provides an analogue for thermal-mechanical feedbacks in nature. At the end of extension, basin centres overlie regions of pronounced upper crustal necking, where thinning reduces lithospheric strength and potentially creates a pathway for asthenospheric upwelling (Figure 36). This crustal necking amplifies thermal gradients (Chenin et al., 2018), increasing the potential for ductile weakening and focused inversion.

The coupling of upper crustal thinning and lower crustal ductile flow promotes buoyancy-driven folding beneath the basin axis, further focusing uplift during shortening. Similar mechanisms have been described in analogue experiments where isostatic adjustments and ductile underplating drove selective basin inversion (Allemand & Brun, 1991; Zwaan & Schreurs, 2023), and in geodynamic models where post-rift heating and weakening dictated strain localisation (Huismans & Beaumont, 2011). In our experiments, this interplay is visible in the anticlinal folding of the ductile layer beneath thinned basins, which facilitated reverse reactivation of basin-bounding faults (Figure 36).

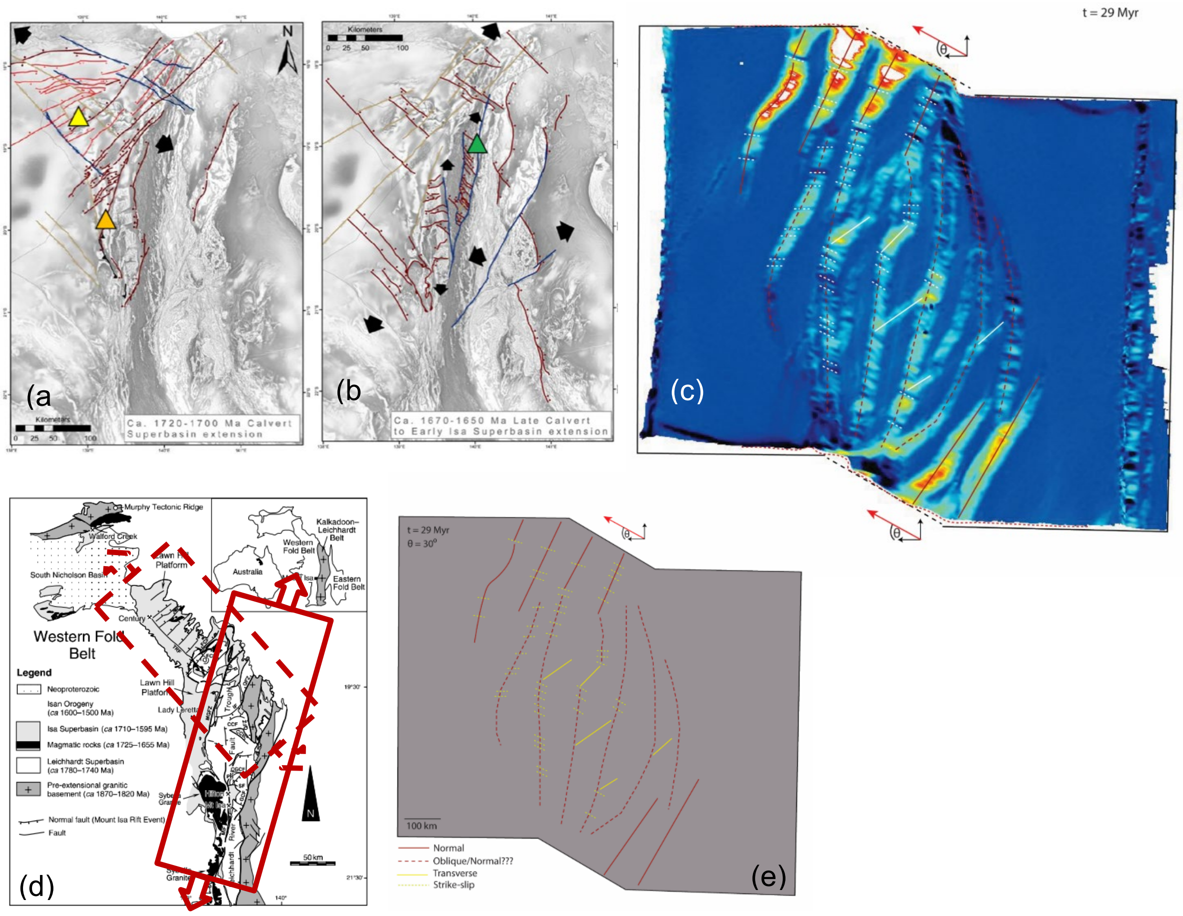

Figure 37. Comparison of basin architecture of NAC and the model with 30° obliquity. (a) Calvert super basin extension and (b) Early Isa super basin extension. (c) Maximum normal shear strain map at the end of the extension with interpreted faults. (d) Map of the Western Fold Belt interpreted by Betts et al. (2006) showing multi-phase

orthogonal extension (NW-SE, NE-SW). (e) Fault orientation map interpreted from the 30° obliquity model during the extension.

We therefore suggest that natural basin inversion reflects the combined influence of mechanical inheritance (fault-bounded basin geometries) and thermo-mechanical feedbacks (lithospheric thinning and asthenospheric upwelling). This helps explain why Proterozoic basins, which developed under warmer geotherms, often show broad, distributed inversion, while younger, cooler lithosphere favours more localised reactivation along discrete fault systems (Brun & Nalpas, 1996; Buiter et al., 2009; Oravecz et al., 2024). In both cases, however, the key control is lithospheric weakening at basin centres, making them persistent sites of strain localisation during both extension and inversion.

Shortening phases reinforce this interpretation: inherited oblique rift fabrics directly control inversion style. In low-obliquity systems, distributed reactivation produces selective uplift of multiple basins, while in higher obliquity models, inversion is linear and confined to major basin-bounding faults. This contrast aligns with analogue and numerical experiments showing that the style of inversion depends not only on fault geometry but also on whether ductile layers deform by distributed thickening or by localised folding, which in turn dictates whether inversion is broad or selective (Samsu et al., 2023; Hansen & Nielsen, 2003). Numerical geodynamic models further demonstrate that inherited thermo-rheological heterogeneities exert a strong control on whether uplift or even renewed subsidence dominates during inversion, depending on the interplay between contractional uplift, post-rift thermal subsidence, and sedimentary loading (Oravecz et al., 2024). Case studies of natural basins such as the Fundy Basin (Withjack et al., 2010) and Browse Basin (Lawrence & Thompson, 2014) show that the geometry of pre-existing rift fabrics governs partitioning of deformation, with shallow inversion expressed as distributed folding while deep-seated basin-bounding faults focus strain into linear belts. These experimental and natural insights provide a plausible explanation for the duality observed in Proterozoic basins: in some cases (e.g., McArthur, Isa) broad inversion reactivated multiple depocentres, whereas in others, inversion was strongly fault-controlled and localised (Rawlings, 1999; Blaikie & Kunzmann, 2020). This duality can thus be understood as the outcome of how obliquity, pre-existing structures, and lithospheric rheology interact to partition strain during contraction (Lowell, 1995; Mora et al., 2009).

Overall, the experiments highlight the complex interplay between tectonic forcing, crustal rheology, and boundary obliquity in shaping rift–inversion systems. They demonstrate that crustal necking, ductile thickening, and oblique kinematics are sufficient to generate the complex geometries of Proterozoic basins, without requiring multiple deformation phases. Moreover, they show that inversion is not simply a matter of reactivating pre-existing faults, but also involves distributed ductile flow beneath thinned crust, which drives uplift and basin inversion. This integrated framework offers a powerful analogue for understanding the architecture, reactivation, and metallogenic fertility of the NAC and other ancient intracontinental basins.

3.4. Crustal scale craton margin experiments

3.4.1. Methodology

3.4.1.1. Experimental setup

A third series of analogue experiments was conducted to investigate how inherited craton margin geometry influences subsequent crustal extension and inversion. Unlike the lithospheric-scale orthogonal and oblique extension and inversion models described previously, these experiments simulated deformation within the brittle upper and ductile lower crust only. Accordingly, the models excluded a lithospheric mantle layer and underlying asthenosphere and were therefore not in full isostatic equilibrium.

The experimental apparatus and configuration are illustrated in Figure 38. The 30 × 30 cm model domain was deformed using a moving wall and base plate driven by a computer-controlled linear actuator at a prescribed extensional or compressional rate. The static side and back walls were lubricated to minimise boundary friction. Transparent, removable sidewalls constrained the model's east and west edges, with additional lubricants applied at wall–lithosphere contacts. Analyses were restricted to the central portion of the model to avoid sidewall drag effects (Figure 38c). In map view, the upper edge of the model is referred to as "north," with extension directed toward the "west" or "southwest," depending on the imposed obliquity.

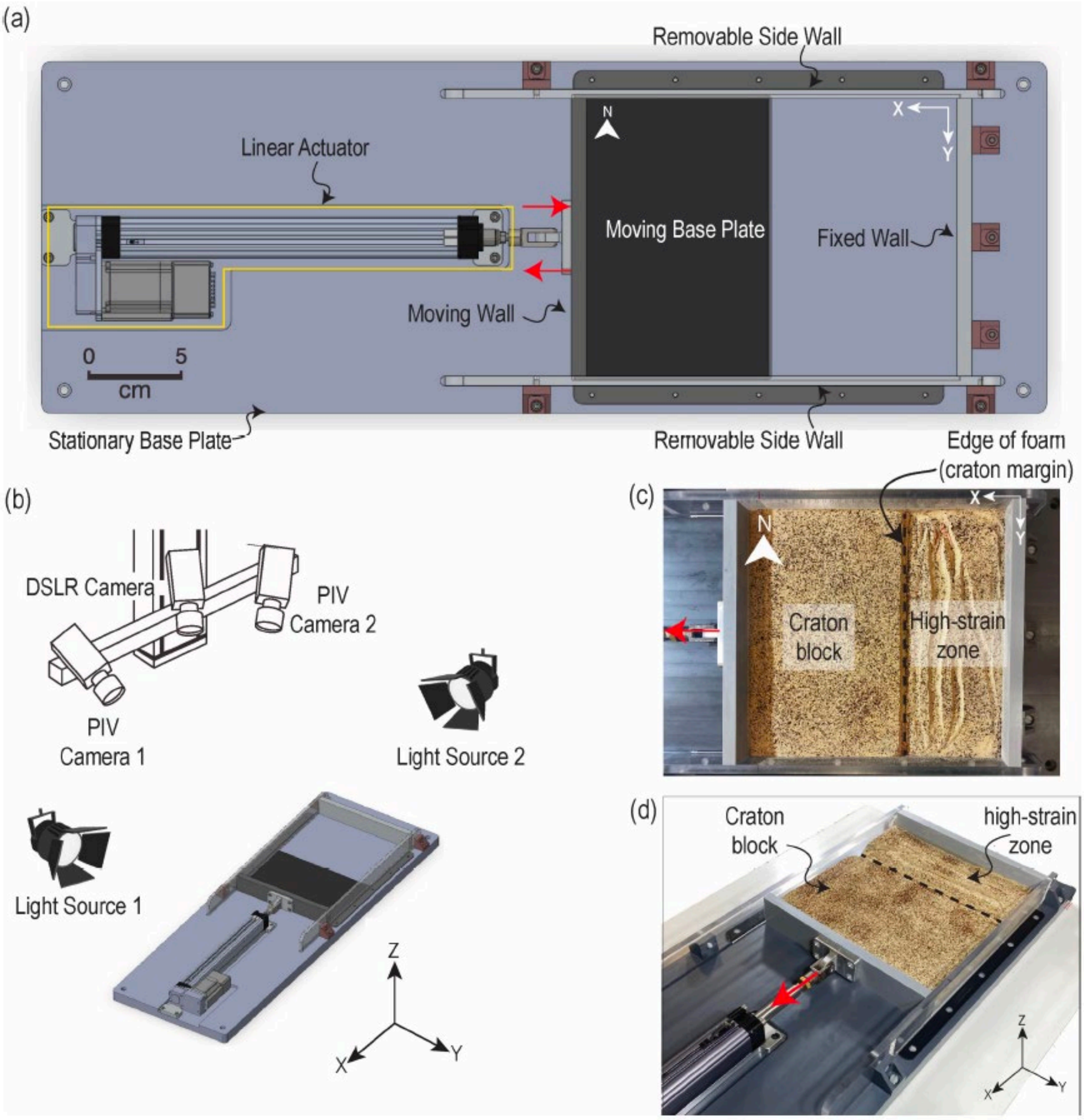

Figure 38. Experimental setup. (a) The top view of the experimental setup shows the fixed wall, moving wall, moving base plate, transparent and removable side walls, linear actuator, and stationary base plate. Red arrows show the direction of movement of the moving wall. The white arrow indicates what we consider to be the north direction while describing the experiment results. Additionally, the x-coordinates follow the east-west direction, while the y-coordinates correspond to the north-south direction. The z-coordinates represent the vertical direction, as depicted in other panels. (b) 3-D sketch of the experimental setup. Inclined stereoscopic particle imaging velocimetry (PIV) cameras 1 and 2 were used to monitor the deformation of the model surface. A downward-facing DSLR camera captured top-view images. Oblique lighting was used to increase contrast and improve the visualisation of deformation patterns. (c) Top view of an experiment after extension. The craton block is positioned on the west side of the model, adjacent to the moving wall, while the high-strain zone is situated on the east side of the model, next to the fixed wall. The dashed line indicates the edge of the block of foam that is used to simulate the cratonic lower crust; this edge coincides with the edge of the moving base plate in (a) and is analogous to the craton margin. (c) A 3-D view of the same experiment after extension.

Initial conditions were designed to approximate isostatic equilibrium between the model lithosphere and a viscous asthenospheric base. To reproduce natural lithospheric strength contrasts, the western side of the model incorporated a high-strength foam block representing the cratonic lower crust, while the eastern side consisted of a weaker, layered crustal block with brittle upper and ductile lower crustal analogues (Figure 39a). This configuration introduced a first-order mechanical heterogeneity equivalent to a natural craton margin. The interface between the cratonic and non-cratonic domains was aligned with the moving base plate and acted as a persistent structural boundary throughout deformation.

The cratonic lower crust was represented by a rigid foam block (30 × 20 × 1 cm) affixed to the moving base plate with double-sided tape. The lower crust of the high-strain zone consisted of a 30 × 10 × 1 cm layer of viscous PDMS mixed with iron filings (PDMS–IF). A uniform 30 × 30 × 1 cm layer of brittle sand–Envirospheres mixture was then sieved across both lower crustal blocks, completing the crustal-scale model. The rheological layering and strength contrasts were scaled to reflect natural conditions at the margins of the North Australian Craton (Figure 39a–b).

Surface deformation was monitored in real time using a stereoscopic digital image correlation (DIC) system comprising two inclined cameras and a downward-facing DSLR camera for top-view imaging (Figure 38b). Oblique lighting enhanced surface contrast, enabling accurate detection of faulting and strain localisation. These imaging techniques allowed quantitative analysis of both incremental and cumulative surface strain and topographic evolution throughout the experiments.

Because this was the first series of experiments using the apparatus, pilot runs were performed to identify and minimise boundary effects. Early trials exhibited strain localisation adjacent to the moving wall, producing curved rift geometries influenced by boundary friction (Figure 38c). These effects were progressively reduced in later experiments by adjusting material thicknesses and applying lubricants along the sidewall–model interfaces.

3.4.1.2. Boundary and initial conditions

The model domain was prepared to minimise boundary effects. Transparent, removable sidewalls constrained the north and south edges of the model, and lubricants were applied at all wall–lithosphere contacts to reduce friction. Analyses were restricted to the central area of the model to avoid sidewall drag (Figure 38c). In plan view, the upper model edge corresponds to “north,” with extension directed “west” or “southwest” depending on the imposed obliquity.

Initial conditions ensured near-isostatic equilibrium between the model lithosphere and viscous asthenosphere. The western margin contained a rigid foam block representing a cratonic buttress, while the eastern margin consisted of a weaker, rheologically modified lithosphere designed to accommodate distributed extension and subsequent inversion. This configuration produced a first-order strength contrast equivalent to a natural craton margin (Figure 38c; Figure 39a–b). The interface between the two domains coincided with the moving base plate and functioned as a pre-defined structural discontinuity throughout deformation.

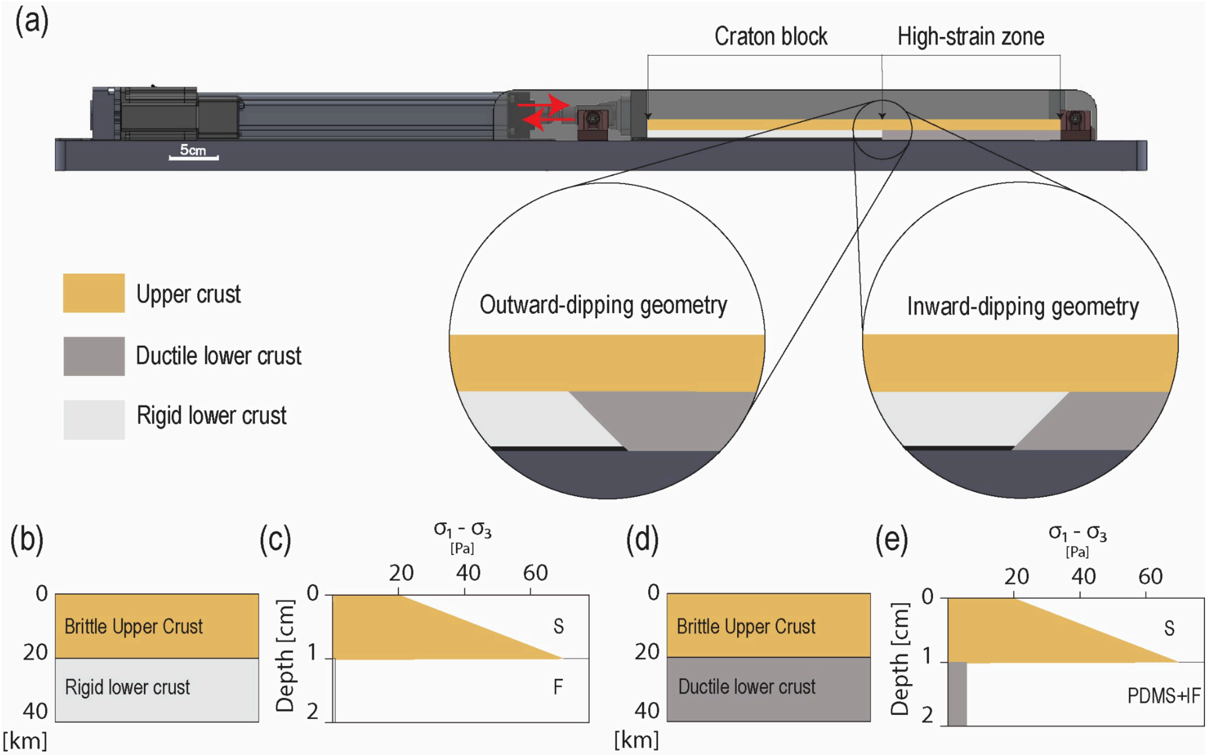

Figure 39. Schematic illustration of the rheological layering of the crustal-scale analogue models and strength profiles of the model craton block and high-strain zone. (a) E-W cross-section through the centre of the model shows how the model layers are constructed and the approximate geometry of the inward and outward dipping craton margins. (b) Natural prototype and scaled-down thicknesses for carton block. (c) Representative strength profile of the model craton crust. (d) Natural prototype and scaled-down thicknesses for the high-strain zone. (e) Representative strength profile of the high-strain zone crust. Abbreviations: S = Fine quartz sand, F = Rigid foam, PDMS = Polydimethylsiloxane, IF = Iron Fillings.

The upper crust was represented by a fine, homogeneous granular mixture sieved from ~30 cm height to ensure low initial cohesion. Prior to deformation, a thin layer of dark powder was applied to the surface to enhance DIC tracking and improve contrast. After the extension phase, additional powder was used to maintain visibility of deformation features within the developing rift basins.

The imposed displacement rates correspond to natural lithospheric strain rates of approximately 10^{-14}–10^{-15} s^{-1}, equivalent to extension or shortening at 1–2 cm/yr (cf. Bennett et al., 1998; Snow & Wernicke, 2000; Hammond & Thatcher, 2004). These rates maintained isostatic balance between the cratonic block and the high-strain zone, consistent with their relative strength profiles (Figure 39c–e).

The experimental design ensured reproducibility: repeated runs with identical initial and boundary conditions produced consistent first-order strain geometries. This confirmed that the observed deformation patterns were governed by obliquity and rheological configuration rather than experimental noise.

3.4.1.3. Scaling and rheology of model materials

Scaling followed Ramberg (1967), with similarity conditions applied to lengths, forces, and times (see section 3.2.1.3). The upper crustal brittle sand–Envirosphere mixture yielded a model density of ~1142 kg/m³, corresponding to ~2570 kg/m³ in nature. Direct shear tests indicated a friction angle (ϕ) of ~38° and negligible cohesion (~9 Pa), within the range reported by Molnar et al. (2017) and Montanari et al. (2017).

The lower crustal PDMS–IF mixture had a density of ~1200 kg/m³, scaling to ~2700 kg/m³ in nature, and a viscosity of $\sim 3 \times 10^4$ Pa·s at experimental strain rates. This corresponds to $\sim 10^{21}$ Pa·s in nature, consistent with previous analogue modelling studies (Benes & Davy, 1996; Davy & Cobbold, 1991). Time scaling was $t^* = \eta^*/(\rho g L^*)$, giving $\sim 1.4 \times 10^{10}$; thus, 1 hour of laboratory deformation equates to ~0.82 Myr in nature. Velocity scaling corresponds to ~20 mm/yr for the 6 mm/hr applied in the experiments.

3.4.1.4. Deformation monitoring and analyses

Deformation monitoring followed protocols described in section 3.2.1.4. High-contrast markers (coffee powder) seeded the model surface for digital image correlation (DIC). Images were captured every 2–5 minutes, and incremental/cumulative strain fields were derived using DaVis v. 10 software, with post-processing in MATLAB.

Cross-sections of surface topography and strain were extracted along fixed profile lines (e.g., A–A′, B–B′), enabling comparison between experiments. In selected runs, the brittle upper crust was removed at the end of deformation to expose the ductile layer, revealing wavelengths of boudinage and folding inferred during active deformation (Figure 40d).

3.4.2. Results and findings

The analogue experiments demonstrate that the geometry of craton margins exerts a first-order control on deformation style during both extension and subsequent inversion. While all models produced faulting, folding, and strain localisation, the degree of partitioning, efficiency of reactivation, and distribution of shortening varied systematically with margin type.

The inward-dipping margin experiments consistently showed that margin geometry exerts a dominant control on deformation localisation. During the extension phase, faults nucleated immediately adjacent to the craton block and propagated basin-ward, producing asymmetric rift geometries dominated by normal faults that detached along a mid-crustal analogue horizon (Figure 40a). Extension was accommodated within narrow half-grabens, with strain concentrated at the craton margin rather than distributed across the basin interior. These depocentres progressively deepened with continued extension, generating curved, margin-parallel fault networks that confined subsidence to the immediate footwall domain (Figure 40b–c).

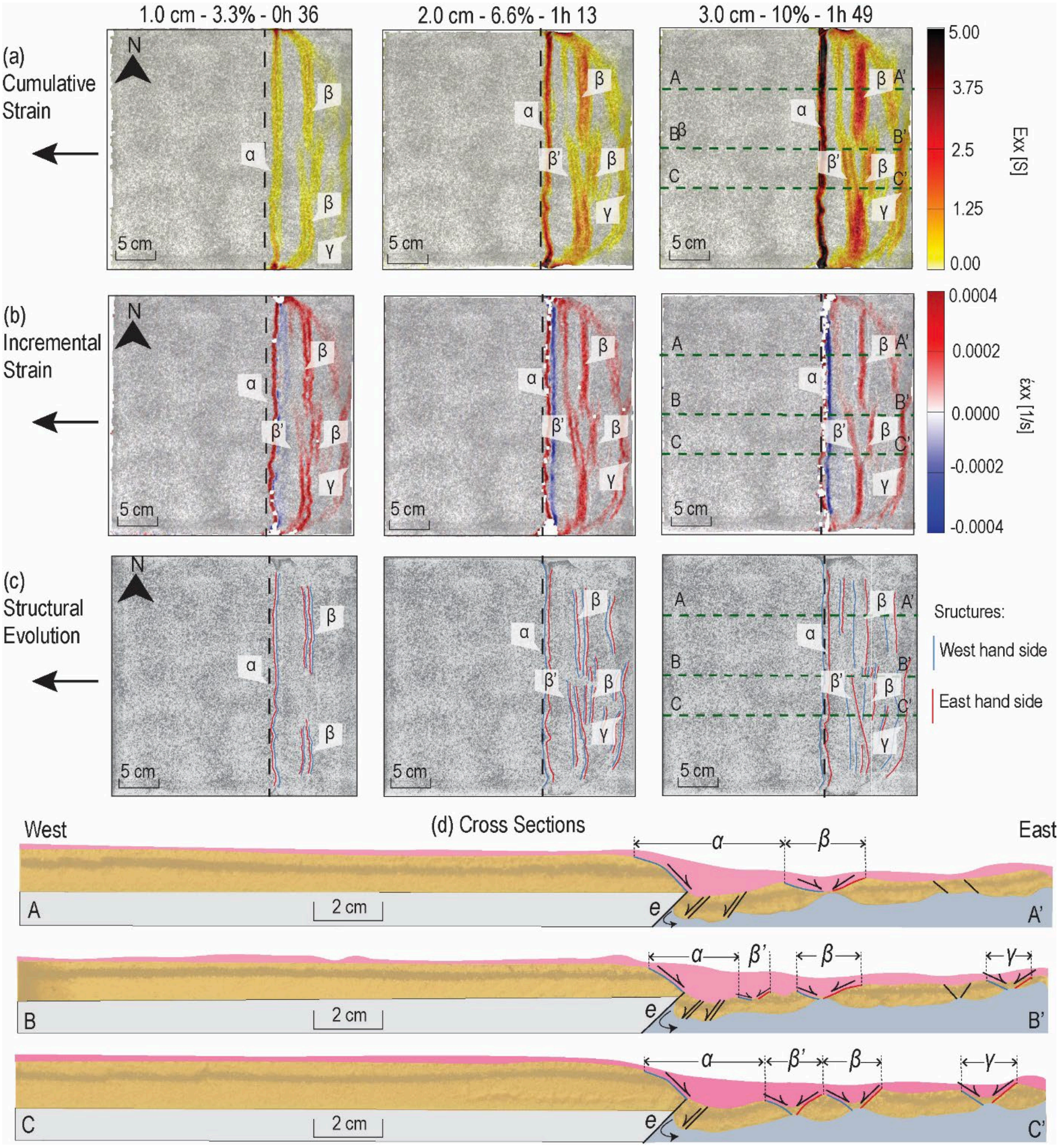

Figure 40. Inward dipping craton margin experiment – Extension of the model with inward dipping craton margin (IE4.1): (a) Maps of cumulative transverse strain (Exx) over time. The text above the panels indicates the "length change - percentage of extension – time (duration)". Please note that [S] is not a unit of measurement but rather an abbreviation for the term "strain". Labels α, β, β', and γ highlight the main rifts formed during extension. The black dashed line indicates the edge of the rigid foam block (aka craton margin). Green dashed lines indicate the location of cross sections. (b) Maps of incremental transverse strain rate (ἐxx) with units [1/s]. (c) Maps of structural interpretation presented in top-view DSLR camera images – red and blue lines indicate the east and west-hand side structures, respectively. (d) Cross sections across the model (green dashed lines shown on maps) showing structural interpretation – Cross sections along lines AA', BB', and CC' as indicated in the maps of the 10% extension panel (a to c). The pink polygon indicates the infill sediments added to the model after the extension. The "e" is the abbreviation for foam edge. Additionally, the black arrows along the interpreted structures show the sense of movement. An Exx value of 1 corresponds to an elongation of 2.

The surface deformation patterns captured by digital image correlation and top-view imaging confirm that brittle strain was tightly focused into these fault zones, while subsurface cross-sections reveal that ductile flow was channelled into the thinned margin domain (Figure 40d).

This partitioning between brittle upper crust and ductile lower crust is a key feature of inward-dipping geometries: crustal thinning in the brittle layer directly guided strain into ductile shear zones below, establishing a mechanically coupled system that promoted efficient inheritance.

During shortening, these inherited detachments acted as pre-defined weakness zones that were readily reactivated in reverse sense. Faults that had originally accommodated extension inverted to form steep reverse faults, producing uplift and surface topography tightly confined to the basin margin (Figure 41a–c). Incremental strain maps show that deformation during inversion was strongly partitioned along these inherited detachments, with very limited nucleation of new faults away from the margin (Figure 41b). Cross-sections confirm that uplift was accommodated almost entirely by reactivation of pre-existing faults, generating asymmetric inversion structures (Figure 41d).

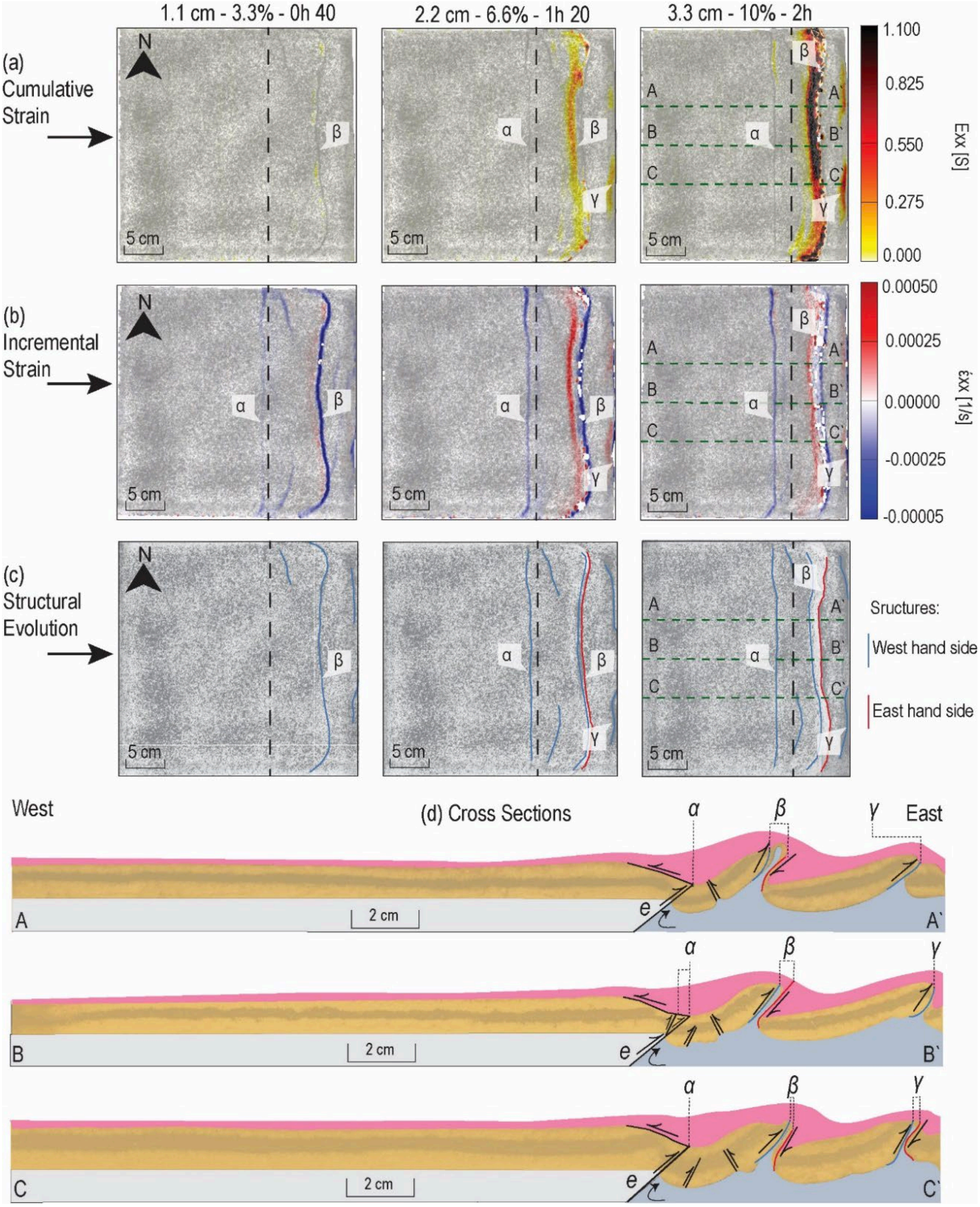

Figure 41. Inward dipping craton margin experiment – 10% Extension followed by shortening of the model with inward dipping craton margin (IE4.2): (a) Maps of cumulative transverse strain (Exx) over time. The text above the panels indicates the "length change - percentage of extension – time (duration)". Please note that [S] is not a unit of measurement but rather an abbreviation for the term "strain". Labels α, β, and γ highlight reactivated zones formed during shortening. The black dashed line indicates the edge of the rigid foam block (aka craton margin). Green dashed lines indicate the location of cross sections. (b) Maps of incremental transverse strain rate (ἐxx) with units [1/s]. (c) Maps of structural interpretation presented in top-view DSLR camera images – red and blue lines indicate the east and west-hand side structures, respectively. (d) Cross sections across the model (green dashed lines shown on maps) showing structural interpretation – Cross sections along lines AA', BB', and CC' as indicated in the maps of the 10% extension panel (a to c). The pink polygon indicates the infill sediments added to the model after the extension before shortening. The "e" is the abbreviation for foam edge. Additionally, the black arrows

along the interpreted structures show the sense of movement. An Exx value of 1 corresponds to an elongation of 2.

The inward-dipping margin experiments highlight the mechanical efficiency of this geometry in localising both extension and inversion. The coupling between brittle detachments and lower crustal ductile flow created focused deformation zones that were repeatedly exploited through multiple tectonic phases. In natural systems, this behaviour helps to explain why inward-facing craton margins such as those in the McArthur Basin or along the Tanami margin show narrow depocentres, efficient inversion, and long-lived reactivation of the same crustal-scale faults across successive tectonic events.

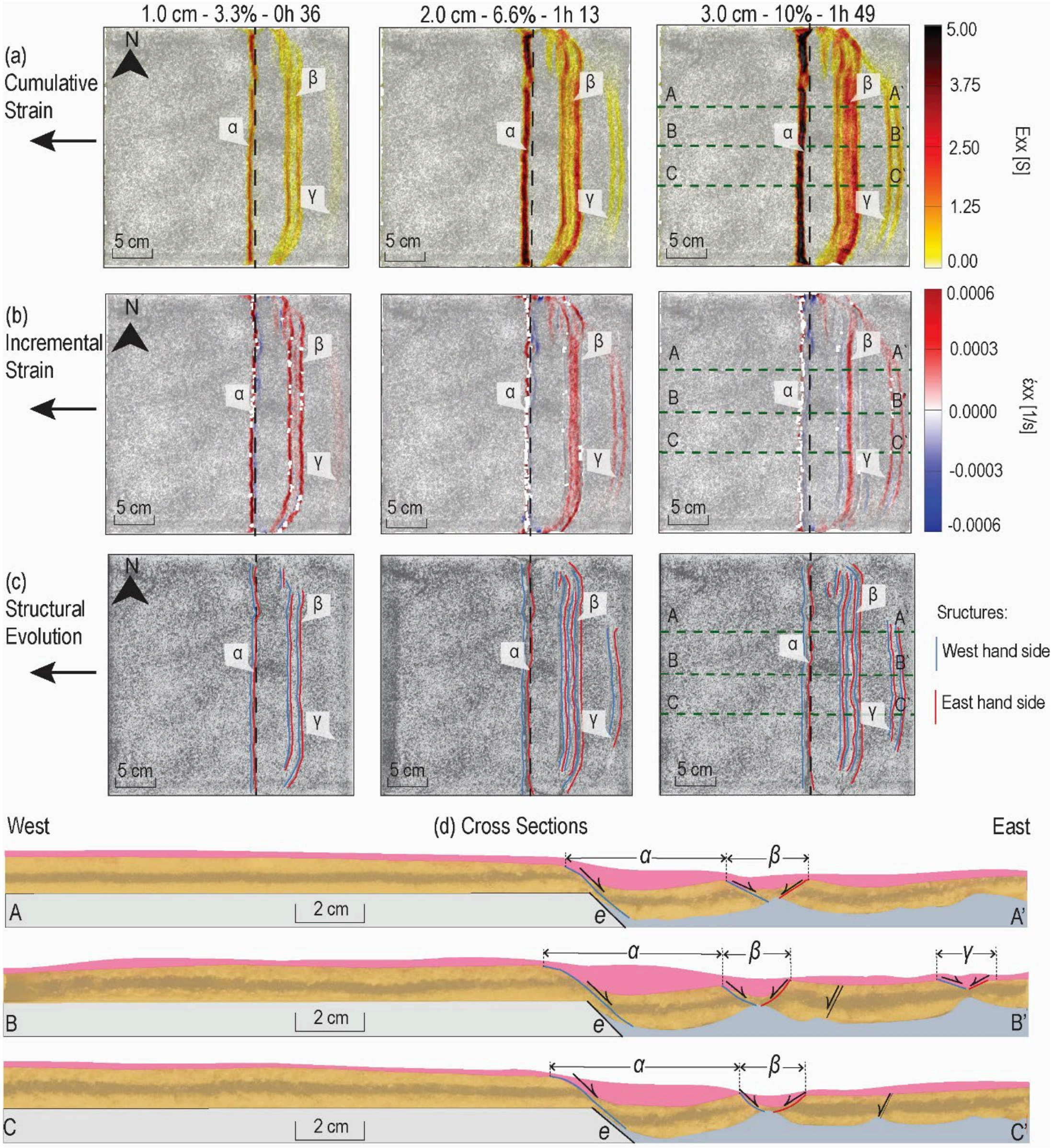

Figure 42. Outward dipping craton margin Experiment – Extension of the model with outward dipping craton margin: (a) Maps of cumulative transverse strain (Exx) over time. The text above the panels indicates the "length change - percentage of extension – time (duration)". Please note that [S] is not a unit of measurement but rather an abbreviation for the term "strain". Labels α, β, and γ highlight the main rifts formed during extension. The black dashed line indicates the edge of the rigid foam block (aka craton margin). Green dashed lines indicate the location

of cross sections. (b) Maps of incremental transverse strain rate ($\dot{\varepsilon}xx$) with units [1/s]. (c) Maps of structural interpretation presented in top-view DSLR camera images – red and blue lines indicate the east and west-hand side structures, respectively. (d) Cross sections across the model (green dashed lines shown on maps) showing structural interpretation – Cross sections along lines AA', BB', and CC' as indicated in the maps of the 10% extension panel (a to c). The pink polygon indicates the infill sediments added to the model after the extension. The "e" is the abbreviation for foam edge. Additionally, the black arrows along the interpreted structures show the sense of movement. An Exx value of 1 corresponds to an elongation of 2.

The outward-dipping margin experiments produced a very different style of deformation compared to the inward-dipping case. During extension, strain was broadly distributed across the model interior rather than being strongly focused along the margin. Normal faults nucleated throughout the basin and propagated steeply downward, producing planar, through-going geometries that cut across the entire brittle layer (Figure 42a–b). Unlike the asymmetric, margin-focused half-grabens of the inward-dipping models, the outward-facing margins generated wider, more symmetrical rift basins with multiple depocentres spread across the basin floor (Figure 42c–d).

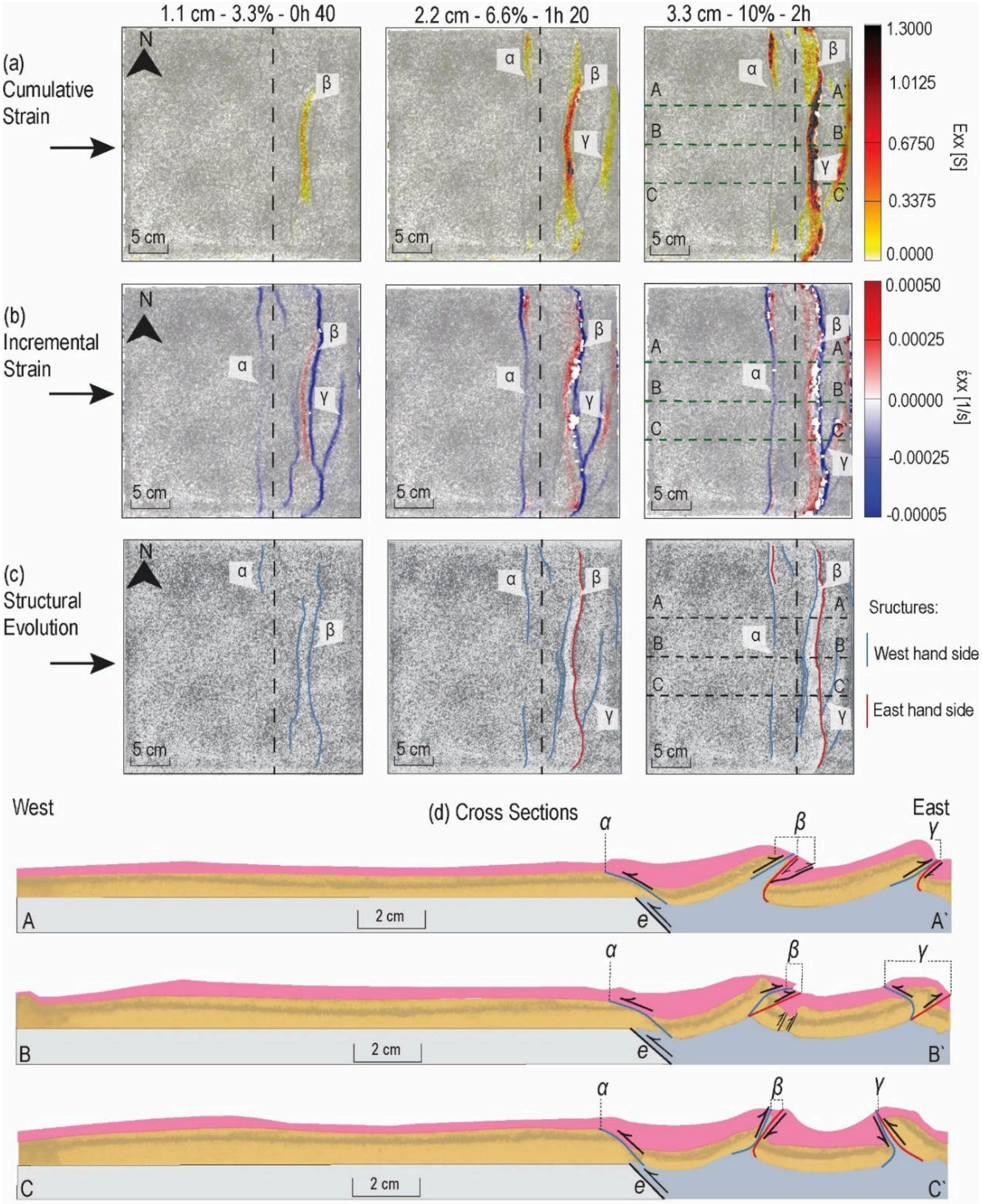

Figure 43. Outward dipping craton margin Experiment – 10% Extension followed by shortening of the model with outward dipping craton margin: (a) Maps of cumulative transverse strain (Exx) over time. The text above the panels indicates the "length change - percentage of extension – time (duration)". Please note that [S] is not a unit of measurement but rather an abbreviation for the term "strain". Labels α, β, and γ highlight the reactivated zones formed during shortening. The black dashed line indicates the edge of the rigid foam block (aka craton margin). Green dashed lines indicate the location of cross sections. (b) Maps of incremental transverse strain rate (ε̇xx) with units [1/s]. (c) Maps of structural interpretation presented in top-view DSLR camera images – red and blue lines indicate the east and west-hand side structures, respectively. (d) Cross sections across the model (green dashed lines shown on maps) showing structural interpretation – Cross sections along lines AA', BB', and CC' as indicated in the maps of the 10% extension panel (a to c). The pink polygon indicates the infill sediments added to the model after the extension before shortening. The "e" is the abbreviation for foam edge. Additionally, the black arrows along the interpreted structures show the sense of movement. An Exx value of 1 corresponds to an elongation of 2.

Surface strain maps show that deformation during extension was more evenly partitioned across the basin, with incremental strain accumulating along several parallel, high-angle faults rather than concentrating into a single margin-bound detachment. Subsurface cross-sections confirm that ductile deformation beneath the brittle layer was also more diffuse: flow was distributed across a broad zone of thinned crust, with limited evidence for channelisation or strong coupling to surface structures (Figure 42d).

During shortening, inversion behaviour contrasted sharply with the inward-dipping experiments. Instead of efficiently reactivating extensional detachments, most of the previously formed normal faults remained inactive. Deformation was instead accommodated by the nucleation of new high-angle reverse faults that overprinted earlier extensional fabrics (Figure 43a–c). Incremental strain maps show that these reverse faults were widely spaced, producing distributed zones of contraction with no single dominant inversion structure (Figure 43b). Cross-sections illustrate that deformation penetrated deeper into the model crust, with uplift distributed across the basin interior rather than tightly focused at the margin (Figure 43d).

The inefficiency of inheritance in outward-dipping systems highlights the weaker mechanical coupling between brittle and ductile layers under this geometry. Without inward-facing detachments to act as weak zones, inversion required the development of entirely new fault systems, leading to broader, more diffuse shortening and less pronounced surface relief.

In natural settings, this behaviour provides an analogue for outward-facing craton margins such as those in the southern Georgina Basin, where contractional events produced broad, distributed deformation with limited reactivation of earlier rift structures. The experiments emphasise that outward-dipping margins are poor candidates for efficient fault inheritance and instead favour complex superpositions of extensional and compressional fabrics that may obscure earlier basin geometries.

The experiments demonstrate that margin geometry controls fault style, strain distribution, and inversion efficiency. Inward-dipping margins favoured focused deformation and efficient reactivation of extensional faults; outward-dipping margins produced diffuse faulting and poor inheritance; and dual-suture systems generated structurally complex, partitioned strain corridors. These findings highlight the predictive value of analogue experiments in understanding the role of inherited lithospheric geometry in basin evolution and orogenic reactivation.

3.4.3. Discussion

The craton margin analogue experiments highlight the fundamental control exerted by craton margin geometry on rift style, inheritance, and inversion efficiency. Inward- and outward-dipping configurations produced systematically different patterns of strain localisation, fault reactivation, and brittle–ductile coupling, with direct implications for interpreting Proterozoic basins and orogens in the NAC.

Inward-dipping margins were mechanically efficient systems in which extension and inversion structures were both localised along inherited detachments. During extension, fault nucleation and subsidence were confined to narrow half-grabens at the margin, producing strongly asymmetric rift geometries (Figure 40a–c). Surface strain maps confirm that brittle deformation was concentrated within these margin-parallel fault zones, while subsurface cross-sections show that ductile flow beneath the thinned crust channelled into the same domain (Figure 40d). The mechanical coupling between brittle detachments and ductile shear zones meant that the same structures were repeatedly exploited during shortening, resulting in efficient reactivation and tightly focused uplift (Figure 41a–d). This behaviour is consistent with earlier analogue work showing that margin geometry strongly conditions fault reactivation (Benes & Davy, 1996; Gartrell, 1997), and mirrors natural examples from the McArthur Basin and Tanami Province where crustal-scale faults have remained active across multiple Proterozoic tectonic events (O'Dea et al., 1997; Blaikie et al., 2017).

By contrast, outward-dipping margins were mechanically inefficient. Extension was broadly distributed across the basin interior, generating steep, planar normal faults and wide, symmetric depocentres (Figure 42a–d). Incremental strain maps and cross-sections confirm that deformation was partitioned across multiple faults and that ductile flow beneath the brittle layer was diffuse, lacking the strong coupling observed in inward-dipping systems. During shortening, earlier normal faults were rarely reactivated; instead, new high-angle reverse faults developed across the basin interior, producing distributed uplift (Figure 43a–d). This inefficiency of inheritance reflects the absence of inward-dipping detachments, requiring new structures to nucleate under compression. Comparable behaviour has been reported in the southern Georgina Basin, where broad contractional strain produced complex overprinting relationships with limited reactivation of earlier extensional fabrics (Greene, 2010).

The experiments also highlight the importance of brittle–ductile interactions. In both geometries, brittle faulting dominated surface deformation, but ductile layers beneath exerted a strong influence on how strain localised. In inward-dipping margins, the ductile crust flowed into the thinned margin beneath brittle half-grabens, enhancing the likelihood of fault reactivation during inversion (Figure 40d; Figure 41b). In outward-dipping margins, ductile flow was spread across the basin floor, preventing efficient coupling between surface faults and deeper shear zones (Figure 42d). This finding resonates with numerical and analogue studies showing that lithospheric rheology and thermal state exert first-order control on deformation style and the potential for crust–mantle decoupling (Burov, 2011; Samsu et al., 2023).

Taken together, these results emphasise that craton margin geometry dictates whether extension and inversion will be localised or diffuse. Inward-dipping margins promote focused inheritance, producing asymmetric basins that are easily inverted along pre-existing detachments. Outward-dipping margins, in contrast, promote distributed rifting and require the nucleation of new faults during contraction, leading to structurally complex overprints. These contrasting behaviours provide a useful framework for interpreting Proterozoic basins of northern Australia: narrow depocentres and long-lived reactivation in the McArthur and Isa basins can be explained by inward-facing geometries, whereas broader, symmetric depocentres with complex inversion histories, such as parts of the Georgina Basin, may reflect outward-facing margins.

3.5. Discussion

The analogue experiments demonstrate that craton margin geometry exerts a fundamental control on deformation style during both extension and inversion. Inward-dipping margins consistently promoted strain localisation, producing narrow, asymmetric half-grabens bounded by listric faults that detached along mid-crustal horizons (Figure 40). These inherited detachments were subsequently reactivated in reverse sense during contraction, leading to efficient inversion and tightly focused uplift zones (Figure 41). The partitioning of deformation between brittle upper-crustal faults and ductile lower-crustal shear zones highlights the mechanical efficiency of inward-dipping geometries in focussing both extension and shortening.

Natural examples from the NAC provide direct support for these experimental findings. In the McArthur Basin, seismic reflection profiles across the Daly Waters Fault Zone show steeply dipping faults that penetrate the crust and repeatedly reactivated during multiple tectonic events (Blaikie et al., 2017; Soares et al., 2025). Similarly, along the Tanami margin, crustal-scale fault zones were active across both extensional and contractional regimes, producing narrow depocentres that were later inverted during the North Australian Orogeny (O'Dea et al., 1997). These behaviours are consistent with the analogue models in which inward-dipping margins localised strain into margin-proximal zones and repeatedly exploited the same fault systems through successive deformation phases. Such efficiency of inheritance explains why these regions became prime structural traps and fluid conduits, ultimately localising giant mineral systems such as McArthur River Zn–Pb–Ag (Large et al., 2005).

By contrast, the outward-dipping margin experiments revealed distributed extension and inefficient inheritance. Extension produced wider, more symmetric rift basins with multiple depocentres bounded by steep, through-going faults (Figure 42). During shortening, these extensional structures were rarely reactivated; instead, new reverse faults nucleated, producing distributed contraction and limited preservation of earlier rift geometries (Figure 43). This behaviour mirrors observations from the southern Georgina Basin, where Alice Springs–age contraction generated broad, low-relief inversion with only weak reactivation of earlier Neoproterozoic rift fabrics (Greene, 2010). Seismic data confirm that much of the deformation was accommodated by newly formed contractional structures, leaving the extensional architecture poorly preserved. The experiments therefore provide a mechanical explanation for why outward-dipping craton margins typically lack long-lived structural inheritance: without inward-dipping detachments to guide reactivation, inversion must rely on newly nucleated faults, producing diffuse and poorly focused deformation.

The broader experimental series also captures the importance of wide-rift inheritance and thermal evolution. The progression from distributed, plateau-like uplift in hot lithospheres to strongly localised Moho-offset shear zones under cooler conditions (Figure 21and Figure 22) provides a compelling analogue for the Centralian Superbasin, where prolonged post-rift cooling allowed the Petermann and Alice Springs Orogenies to drive crust–mantle decoupling, >20 km Moho offsets, and muted surface relief (Walter et al., 1995; Gibson et al., 2016). These natural features are directly replicated in the wide-rift analogue experiments, where the ductile lower crust thickened beneath basins and later folded under shortening, leaving surface relief subdued but deep-seated deformation strongly partitioned.

Finally, the obliquity experiments (Figure 23 - Figure 37) provide a framework for understanding the structural complexity of the Isa and Calvert superbasins. At low obliquity (30°–45°), experiments produced en-echelon rifts, transfer faults, and structurally complex linkages that closely match the observed geometries of these basins (Betts et al., 2006; Spence et al., 2021). During shortening, these oblique fabrics focussed inversion into selected corridors, paralleling natural strain localisation along the Leichhardt River Fault Trough and other transfer zones in the Isa Inlier. These findings demonstrate that a single oblique rifting event can generate fault patterns previously interpreted as evidence for multiple orogenic phases, an interpretation that requires reconsideration of long-standing tectonic models for northern Australia.

Taken together, these experiments confirm that Proterozoic basin evolution in the NAC was shaped by the interplay of lithospheric inheritance, thermal state, and tectonic obliquity. Inward-dipping margins and oblique transfer zones emerge as mechanically efficient features, repeatedly reactivated to focus deformation and mineralising fluids. Outward-dipping margins, by contrast, preserved distributed strain and limited inheritance, obscuring early extensional geometries. These insights not only reconcile analogue results with natural case studies across the NAC but also provide a predictive framework for assessing which craton margins are most likely to preserve long-lived structural inheritance and host world-class mineral systems.

4. Geophysical Modelling

4.1. Lithospheric scale modelling

The evolution of the NAC has previously been investigated using regional-scale geophysical data, with most studies focusing on its tectonic history within the context of supercontinent cycles. However, constraints on the present-day thermal and compositional structure of the NAC remain limited. Furthermore, the temporal evolution of these properties through time and their influence on sedimentary basin formation and preservation are not well understood.

This study addressed the following questions:

1. What are the temperature and compositional characteristics of the North Australian Craton lithosphere?
2. Which tectonic processes may account for the observed variations in the thermal and compositional architecture of the NAC?
3. How does thermal and compositional heterogeneity influence the formation and preservation of sedimentary basins?

Our current understanding of the lithospheric architecture of the NAC is primarily derived from continent-scale studies utilising early-stage seismic tomographic imaging. The Australian Seismological Reference Model (AuSREM, (Kennett et al., 2013)) provides a first-order constraint on the seismological structure of the modern-day lithospheric mantle in the NAC. Shear wave velocities (Vs) within the NAC are notably fast, exhibiting a NE–SW-trending high-velocity anomaly beneath Tennant creek (Figure 44).

Building on seismic tomography and gravity data, (Tesauro, Kaban & Aitken, 2020a) resolved thermal and compositional anomalies in the Australian upper mantle. Their results indicate that the NAC is relatively cold and depleted, characterised by elevated magnesium numbers (#Mg ≈ 91.1), indicative of mantle depletion. This depletion is spatially variable, with Tennant Creek exhibiting the most depleted mantle, while the mantle beneath the McArthur Basin appears more fertile (#Mg ≈ 89-90).

To further investigate the rheological properties of the crust and mantle, the resolved thermal and compositional structure was integrated with surface heat flow data (Tesauro, Kaban, Petrunin et al., 2020). The resulting vertical strength profiles suggest a fully decoupled crust-mantle system in the NAC, with low effective elastic thickness (<20 km). The combination of high crustal temperatures—driven by elevated surface heat flow and low mantle temperatures—implies the potential for lower crustal flow in this region.

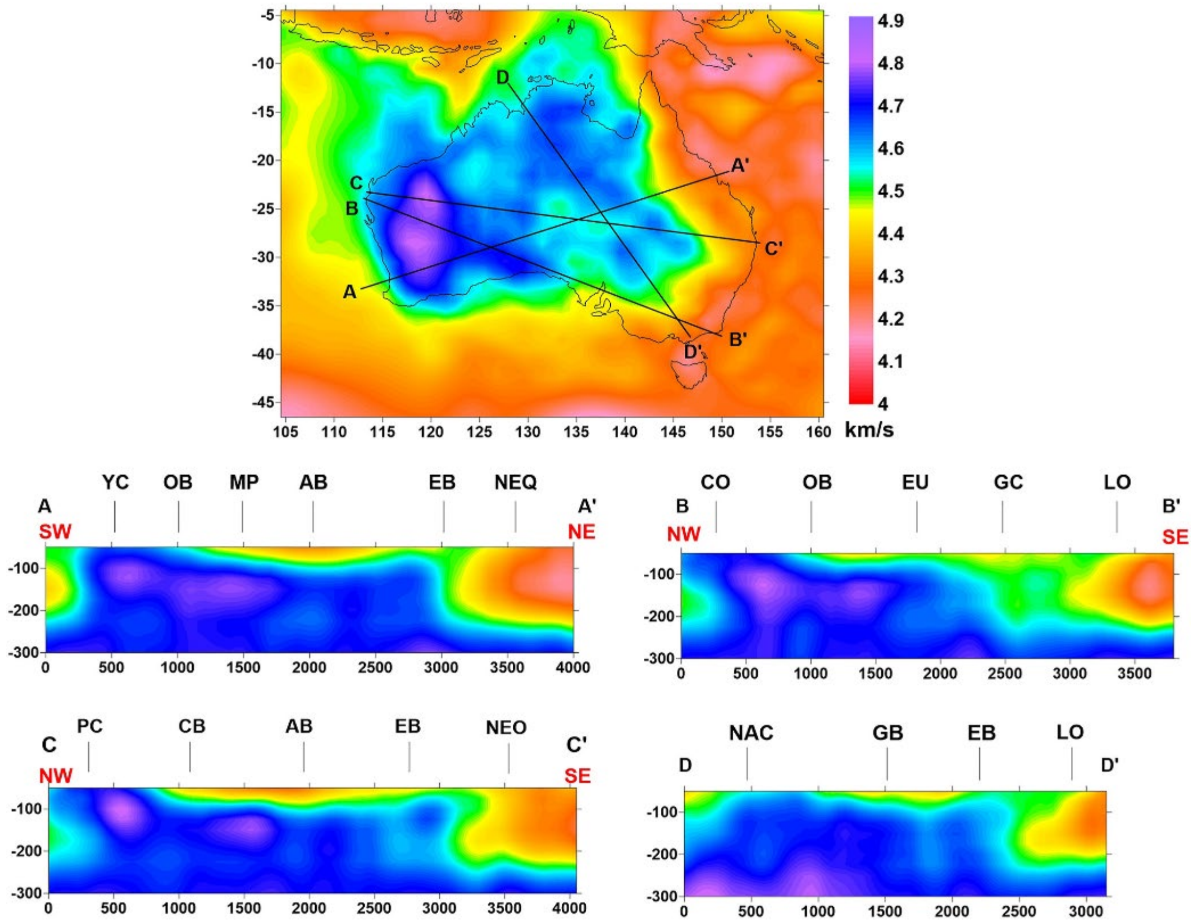

Figure 44. Shear wave velocity structure at 100 km depth from the AuSREM model (Bennet, 2013), with selected cross sections highlighting lateral variations across the Australian continent (Adapted from Tesauro, Kaban, & Aitken, 2020b). The Yilgarn and Pilbara cratons in Western Australia exhibit consistently fast velocities. In contrast, the eastern margin of the continent shows markedly lower velocities, indicative of a warmer and more tectonically active lithosphere. These variations delineate the contrast between ancient cratonic interiors and younger, reworked terranes along the east coast. Vs within the NAC are notably fast, exhibiting a NE–SW-trending high-velocity anomaly.

While previous models (Kennett et al., 2013; Tesauro, Kaban & Aitken, 2020a) provide valuable insights into large-scale mantle structure, resolving absolute mantle temperatures and fine scale variations remains challenging (Haeger et al., 2022). This limitation is partly due to the resolution of seismic tomography model, with horizontal resolution >100 km. In addition, discrepancies between Vs values in seismic tomography and mineral physics parameters cause additional processes (e.g. temperature shift) to be required to resolve the true mantle temperature (Haeger et al., 2022). Moreover, seismic attenuation causes seismic speed to dramatically decrease in the high temperature region. As the lithosphere and asthenosphere boundary has usually been defined as a temperature isosurface, a small uncertainty due to the previously mentioned factors would accumulate to cause significant implications for estimates of lithospheric thickness (Hoggard et al., 2020).

In this project component, we leverage the accumulation of geophysical observations over the decade since the publication of AuSREM, incorporating the recently developed Australian shear wave velocity model (AU22, (de Laat et al., 2023)), improved constraints from mantle xenoliths (Sudholz et al., 2022; Sudholz, Jaques et al., 2023; Sudholz, Reddicliffe et al., 2023), and advances in effectively solving large scale gravity inversion (Codd et al., 2021). These developments enable lithospheric mantle modelling at sub 100 km resolution. We present a new method for mapping the thermal and compositional structure of the lithosphere and investigate the spatial heterogeneity of the upper mantle beneath the NAC.

4.1.1. Methodology

Although this study focuses on the NAC, it is necessary to model the lithosphere across the entire Australian continent. This is required to robustly estimate the relationship between shear wave velocity, temperature, density, and composition, which relies on a continent-scale dataset.

The modelling of lithospheric mantle is applied used a three-stage method (following Li et al., 2025). In the first stage, mantle xenolith and xenocryst constraints were used to establish an optimised relationship between shear wave velocity, temperature, and composition within a Bayesian inversion framework. This constrained relationship was then applied to convert shear wave velocity into initial estimates of mantle temperature and density, assuming a uniform initial composition (#Mg = 91). In the second stage, gravity inversion was used to solve the density distribution to fit gravity data. This resolved mantle density separates the thermal and compositional contributions to shear wave velocity (Figure 45), as multiple temperature-composition combinations can cause similar velocities (e.g., blue dashed line in Figure 45) but result in distinct mantle densities. Finally, a grid search was used to select the best-fitting temperature and composition that fulfill both the shear wave velocity and mantle density in this self-consistent framework.

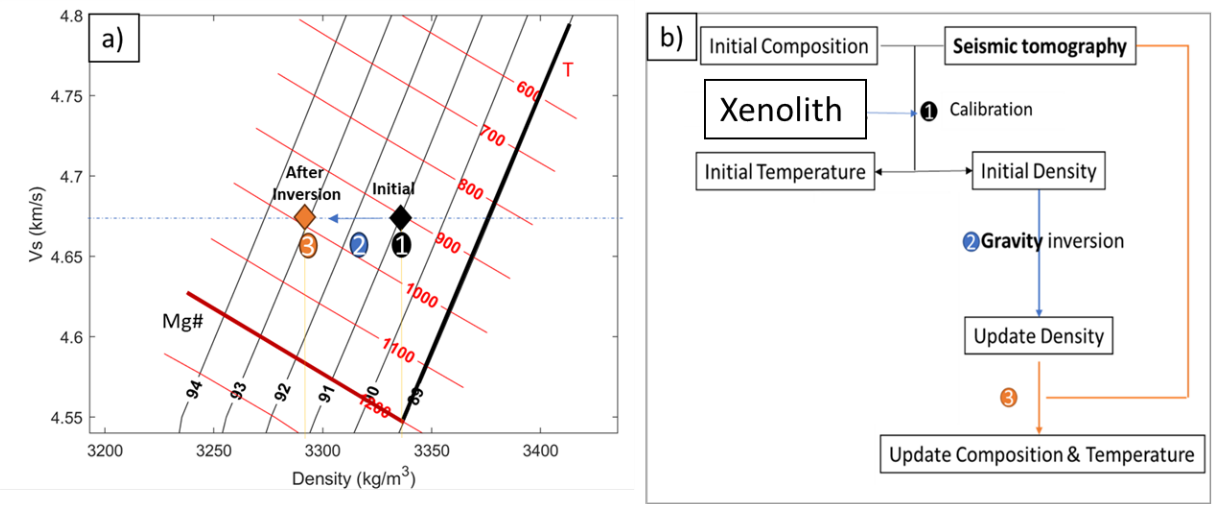

Figure 45. Modelling concept: seismic velocity and density vary with changing composition and temperature. (a) Variation in shear-wave velocity corresponding to changes in temperature and mantle composition; note the difference in resolved density changes. (b) Workflow for estimating composition, density, and temperature changes in Australia. Step 1: Estimate a Vs-temperature-density-composition relationship and generate an initial density and temperature field based on an initial mantle composition. Step 2: Use gravity inversion to resolve the mantle density distribution and update the density field. Step 3: Use the updated density field and seismic velocity to update the temperature and composition.

4.1.1.1. *Mantle xenolith and xenocryst*

Mantle xenoliths and xenocrysts offer a rare opportunity for direct sampling of the mantle and provide critical constraints on lithospheric structure and mantle conditions. To date, more than

60 mantle xenolith and xenocryst samples have been documented across Australia. Detailed compositional data for these samples are available in Hoggard et al. (2024).

Paleotemperature and paleopressure estimates were derived using thermobarometric relationships from an enstatite-in-clinopyroxene thermometer (Nimis & Taylor, 2000) and Cr-in-clinopyroxene barometer (Sudholz, Yaxley, Jaques, & Brey, 2021). Further details on data processing are provided in Hoggard et al., 2024.

In addition to thermal and pressure constraints, the presence of garnet in mantle xenocrysts provides further insight into mantle composition. We applied the Fe–Mg exchange geothermometer from O'Neill & Wood (1979) to calculate the magnesium number (#Mg) in olivine. Paleotemperature estimates were obtained using a Ni-in-garnet geothermometer (Sudholz, Yaxley, Jaques, & Chen, 2021), and paleopressure was calculated by projecting these temperatures onto the paleogeotherm inventory (Hoggard et al., 2024).

In total, 15 samples were selected for location-preserved garnet and have reliable paleogeotherm estimations. A paleogeotherm and composition example is shown in Figure 46. The paleogeotherm is estimated by fitting a conductive geotherm through mantle xenolith calculated paleopressure and paleotemperature. Calculated mantle compositional data were spatially binned at 10 km intervals used for Bayesian inversion.

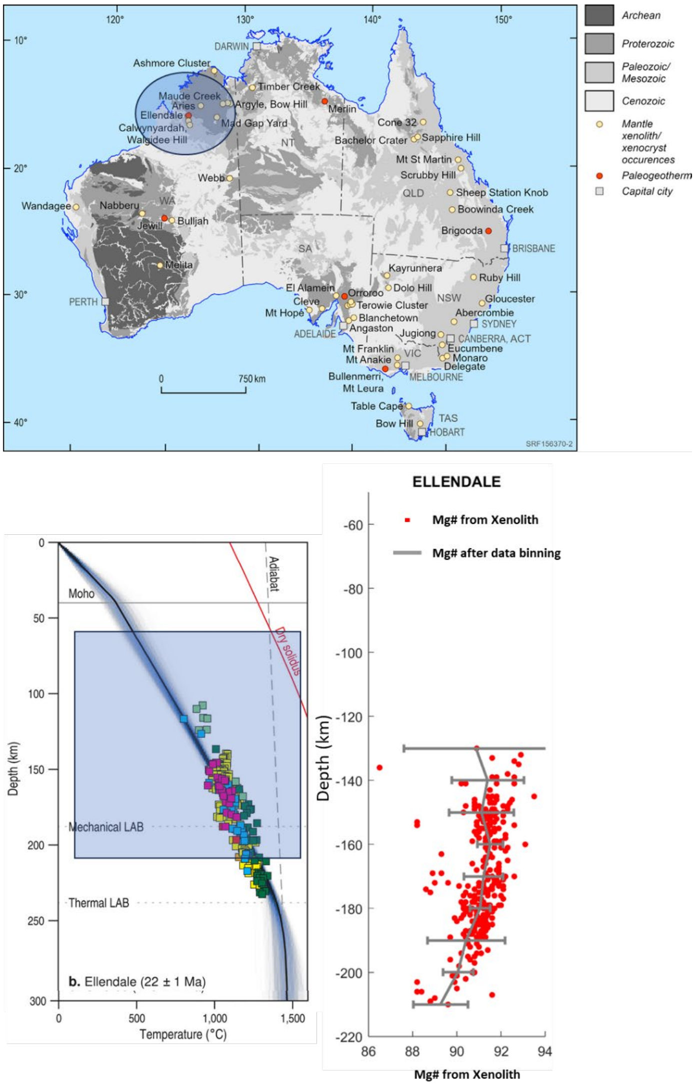

Figure 46. Mantle xenolith and xenocryst information across Australia continent (Hoggard et al., 2024). A representative mantle xenocryst is also shown in here (Ellendale). The paleogeotherm is calculated by fitting P-T estimates (Square) obtained from single-clinopyroxene thermobarometry. The red dot shows the Mg# in olivine calculated by Fe–Mg exchange geothermometer. The Mg# in olivine is subsequently binned into 10 km interval for the MCMC process.

4.1.1.2. MCMC relationship

The relationships between seismic velocity, density, temperature, and composition are estimated using paleotemperature, pressure, and compositional data derived from mantle xenoliths and xenocrysts, within a Bayesian inversion framework (Hazzard et al., 2023; Li et al., 2025). This approach enables calibration of key elastic parameters (e.g., shear modulus and its dependence on temperature, pressure, and composition), anelastic properties (e.g., reference viscosity, activation energy, and solidus gradient), and compositional controls on density (Figure 47).

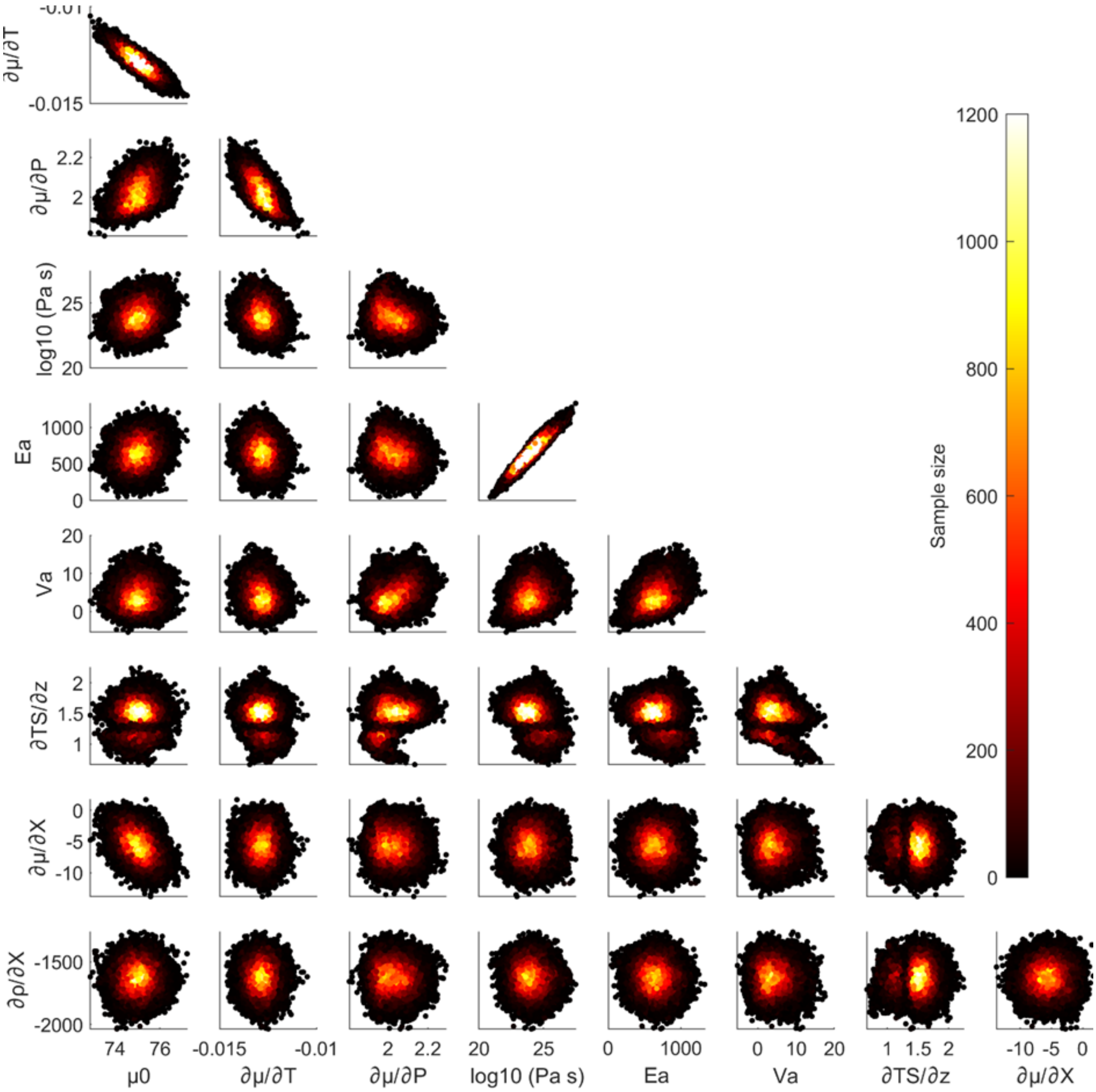

Figure 47. Posterior sampling of each combination of model parameters, highlighting physical trade-offs between parameters. μ_0 represents bulk shear modulus, while ∂μ/∂T, ∂μ/∂P, ∂μ/∂X show how bulk shear modulus deviates with temperature, pressure, and composition. Other parameters include mantle viscosity (log10 (Pa s)), activation energy (Ea), activation volume (Va), the depth gradient of the solidus temperature (∂T_S/∂z), and how density varies with composition (∂ρ/∂X).

A key advantage of the Bayesian framework is its ability to incorporate multiple xenolith-derived constraints into a joint inversion without imposing subjective weighting across different locations. Hyperparameter tuning allows for flexible integration of diverse datasets. Further details on the implementation are provided in Hazzard et al. (2023); Li et al. (2025).

4.1.1.3. Gravity inversion

Gravity inversion was performed in a spherical coordinate system using a finite element method implemented in esys-escript (Gross et al., 2007). High-performance parallel computation was achieved using a preconditioned conjugate gradient solver (Codd et al., 2021), enabling efficient resolution of large-scale geophysical models. The detailed mathematical formulation and implementation are described in Codd et al. (2021; Li et al. (2025).

The inversion requires an initial density model to account for variations within the lithosphere and asthenosphere. The gravity inversion then solves for density corrections, which are subsequently combined with the initial model to produce the final density distribution.

Accurately resolving the density distribution of the lithospheric mantle requires a robust account of both crustal and mantle contributions. For topographic constraints, we used the ETOPO global relief model (MacFerrin et al., 2025), and sediment thickness variations were incorporated from the OzSeebase (Geognostics, 2021). Given the significant influence of the crust on the observed gravity field, we employed the AUCrust shear wave velocity (Chen et al., 2023) model, which integrates both synchronous and asynchronous ambient noise tomography. It enhances seismic ray-path density compared to traditional methods, thereby providing improved resolution of the Australian crustal structure.

To convert Vs to density, we applied an empirical relationship calibrated for lithospheric conditions. Moho depth was constrained using the AUSMOHO 2023 model (Kennett et al., 2023), which incorporates additional seismic-derived Moho estimates and significantly reduces data gaps across the NAC.

Initial estimates of mantle density were derived from the AU22 model (de Laat et al., 2023) using the xenolith-calibrated Vs-to-density conversion relationship. AU22 is an azimuthally anisotropic S-wave tomographic model of the Australian Plate, constructed from over 9,000 seismic stations and more than 26,000 events recorded between 1994 and 2018 (de Laat et al., 2023). This extensive dataset enables improved resolution of upper mantle structure across the continent, providing more detailed information for the Australian lithosphere.

4.1.2. Results and findings

Here we show the inverted mantle composition, and lithosphere thickness across the whole Australian continent, and a focused view of NAC.

4.1.2.1. Continental result

Mantle composition and lithospheric thickness across Australia are shown in Figure 48. A general trend is observed, with mantle fertility increasing from west to east, reflected by a decrease in magnesium number (#Mg) and an increase in lithospheric thickness. This pattern broadly corresponds to geological age, with Archean cratons located in Western Australia and progressively younger terranes toward the east.

Several regions exhibit distinctly depleted mantle signatures. The Yilgarn and Pilbara cratons show elevated #Mg values, indicating preservation of Archean mantle domains. In contrast, although the NAC and Gawler Craton retain Archean crustal components at the surface, geophysical evidence suggests that their underlying mantle has been modified and no longer retains a clear Archean signature in bulk composition.

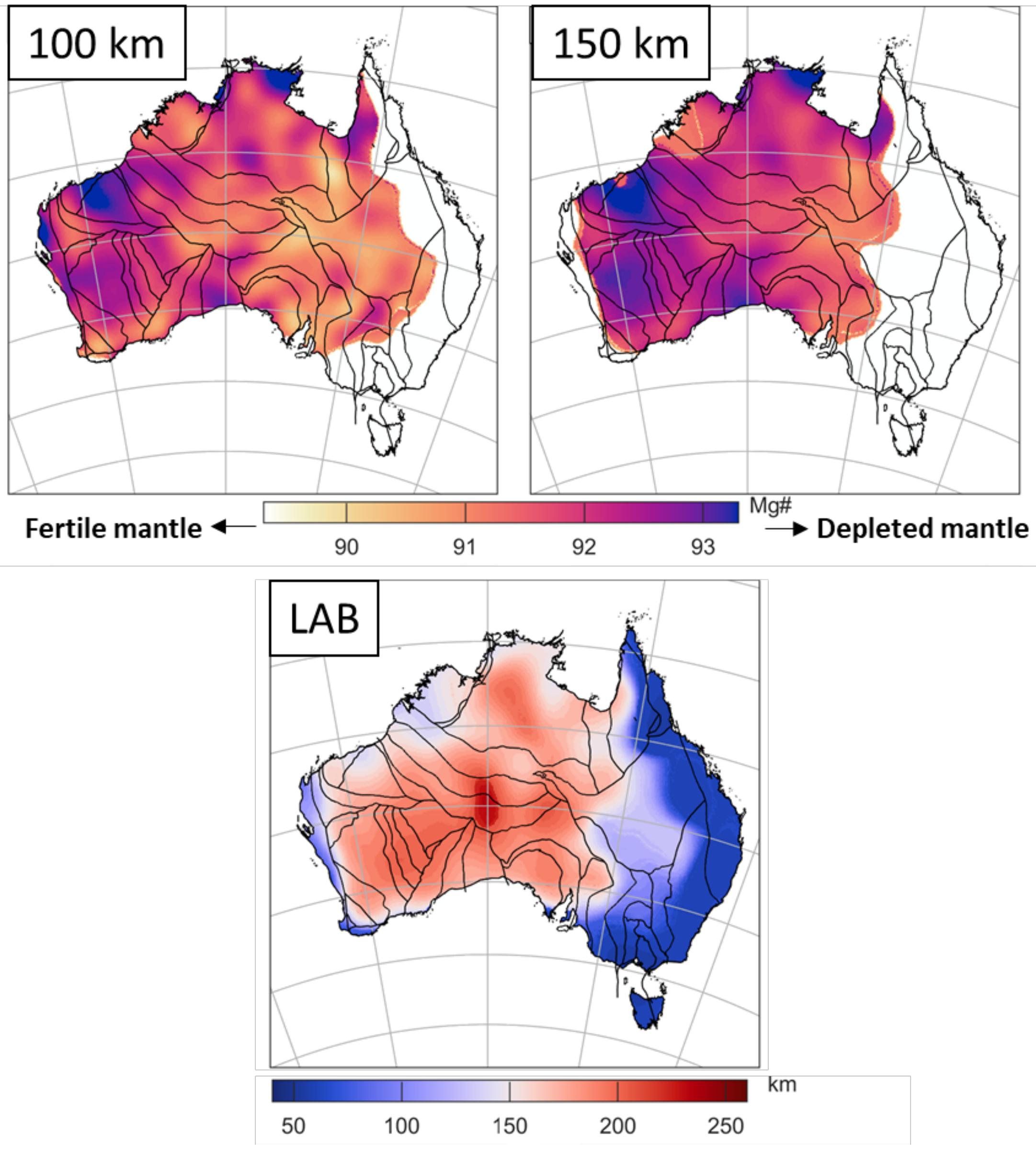

Figure 48: *Lithospheric thickness and mantle composition across the Australian continent, derived from integrated geophysical models derived in the project. The distribution highlights significant regional variations, with thick, depleted lithosphere beneath the Yilgarn and Pilbara cratons, contrasting with thinner and more fertile lithosphere along the eastern margin.*

Unexpectedly, a few regions show anomalously high #Mg values despite surface geology suggesting oceanic crustal origins (e.g., Eucla Basin). These anomalies are primarily derived from fast shear wave velocities, which were not apparent in earlier continental- or global-scale models. Recent full-waveform inversion tomography for Australia reveals similar high-velocity features, lending support to the reliability of these observations (Holzschuh et al., 2024).

In addition, the Kimberley Craton appears unusually fertile and thin in our model. This result misaligns with geodynamic interpretations based on mantle xenolith data (Sudholz, Jaques et al., 2023). This discrepancy arises from the AU22 model (de Laat et al., 2023), where the removal of data from seismic station FITZ—which previously indicated fast mantle velocities—has significantly influenced the resolved thermal and compositional structure. This highlights the sensitivity of lithospheric models to initial seismic tomography inputs.

Lithospheric thickness exceeds 250 km in central Australia, forming a distinct thick domain. Interestingly, major cratonic regions are not situated within the thickest lithospheric zones but rather along their margins.

4.1.2.2. NAC result

A more focused view of the NAC is presented in Figure 49, where mantle composition and lithospheric thickness are overlain with major tectonic boundaries and basin depocenters. The mantle beneath the NAC is relatively fertile, with an average #Mg of 90.5. Notably, the major basin depocenters are located above more fertile mantle domains. The NAC has undergone multiple phases of rifting and shorting though time (Kumwenda et al., 2023). The heterogeneous mantle composition that we see today indicates potential tectonic activities have modified NAC mantle composition through time.

In contrast, the mantle beneath the area between Tanami and Tennant Creek appears significantly depleted, suggesting preservation of the Archean core of the NAC in this region. Lithospheric thickness reveals several distinct domains, with a prominent NW–SE-trending thick lithospheric corridor in the central NAC. Major sedimentary basins, including the Beetaloo and Birrindudu basins, are located along the margins of this thick lithospheric zone.

In the Mt Isa region, lithospheric thickness shows a thick-thin-thick structure from south to north. The thinnest mantle in the centre of Mt Isa also shows fertile mantle compositions. This pattern may reflect a paleosubduction related signature associated with the Laurentian.

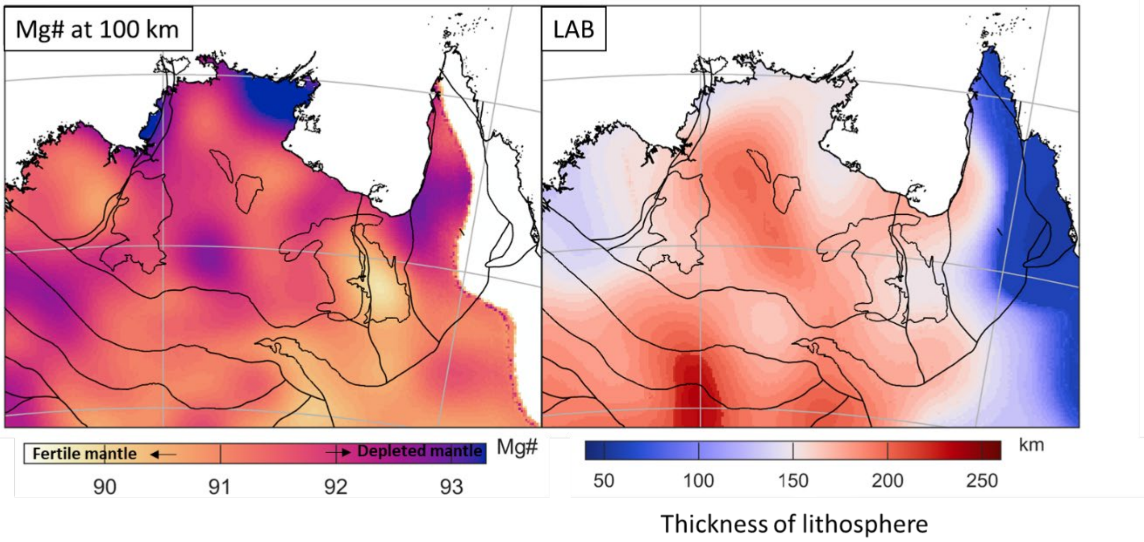

Figure 49. A focused view of lithospheric thickness and mantle composition across the NAC.

4.1.3. Discussion

4.1.3.1. Linking mantle architecture with Large Igneous Provinces (LIPs)

Significant variation in lithospheric thickness and mantle composition across the NAC indicates that large-scale geodynamic processes have modified the lithospheric mantle over time. One of the primary candidates for this modification is the extensive mafic–ultramafic magmatism associated with large igneous provinces (LIPs) emplaced across the region.

Several LIP (Claoué-Long & Hoatson, 2009) events have been proposed in the NAC (Figure 50). These include a prolonged mafic–ultramafic magmatic phase between 1870–1750 Ma, followed by another phase from 1720–1530 Ma. Although there is no discernible hiatus between these two events, the locus of magmatic activity appears to have shifted spatially over time. After the 1590 Ma event, magmatic activity in the NAC diminished until the intrusion of the Derim Derim Dolerite at ~1300 Ma, which affected the greater McArthur Basin in northern Australia. Subsequently, the Mordor event occurred at ~1135 Ma along the southern margin of the NAC and the Mt Isa region. Major magmatism resumed at ~510 Ma with the emplacement of the Kalkarindji LIP, which covered large portions of the NAC and the Canning Basin.

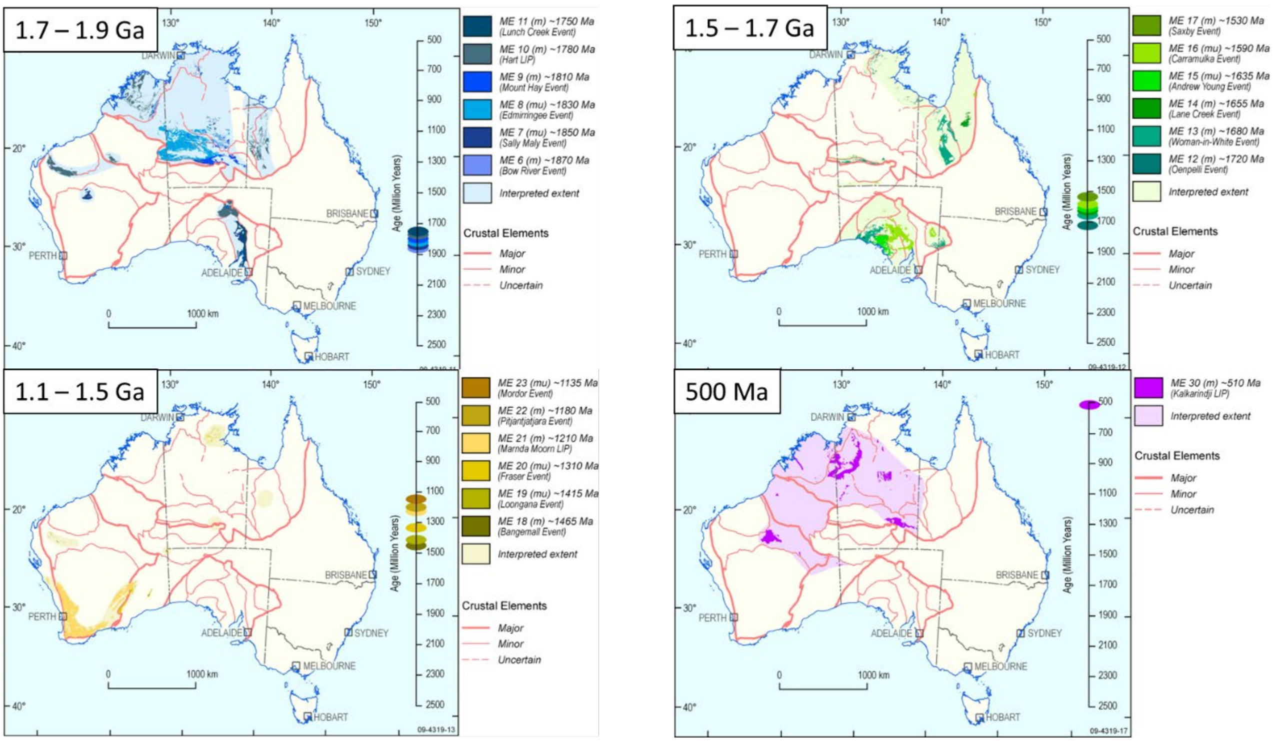

Figure 50. Spatial and temporal distribution of Large Igneous Provinces (LIPs) across the Australian continent (Claoué-Long & Hoatson, 2009). The compilation highlights episodic magmatic events from the Proterozoic to the Phanerozoic, with spatial clustering in both cratonic and marginal settings.

4.1.3.2. Impact for sedimentary basin forming and preservation

The widespread emplacement of LIPs across the NAC suggests that associated mafic to ultramafic magmatism has potentially significantly modified the lithospheric mantle. Changes in mantle composition resulting from LIP-related processes may exert a strong influence on basin formation and preservation, due to the impact on buoyancy, rheology and thermal structure.

Global datasets reveal a consistent trend of increasing modern-day lithospheric thickness with time since LIP eruptions, before the trend flattens at ~250 Ma (Stephenson et al., 2023). This pattern can be interpreted as initial lithospheric thinning due to magmatic intrusion during LIP emplacement, followed by gradual thickening as thermal perturbations dissipate over time. If mantle composition remains unaltered, and if extension is not significant the lithosphere may reform close to its original state (Figure 51). However, interaction between mantle material and magmatic fluids can lead to compositional changes. In such cases, mantle depletion of the partial melting zone occurs via melt extraction, reducing iron content and increasing magnesium, thereby lowering mantle density. This buoyant mantle condition can result in surface uplift relative to pre-LIP elevation.

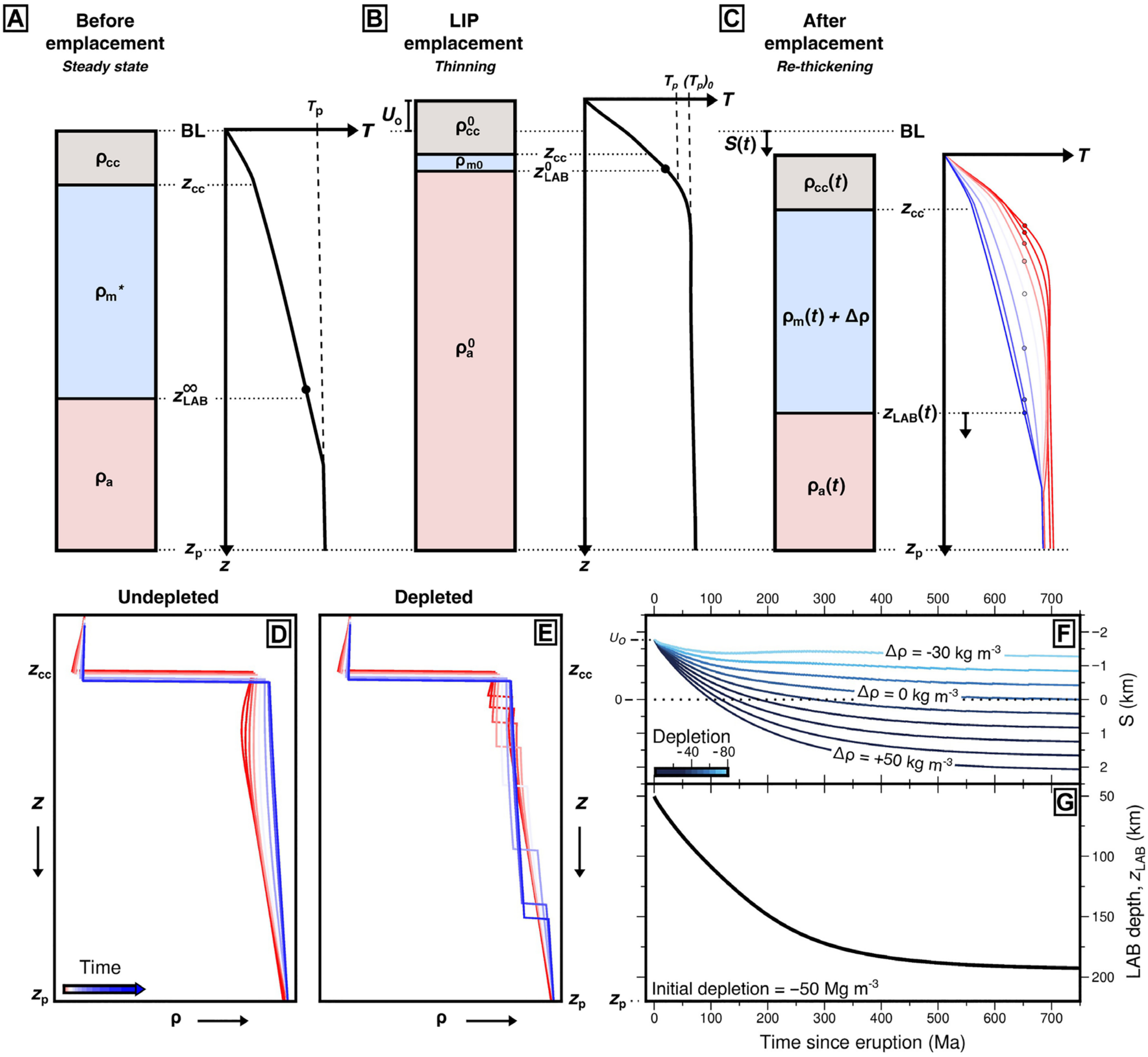

Figure 51. Changing mantle composition (density) lead to surface subsidence or uplift. a) Pre-LIP steady-state lithosphere with defined LAB depth (1175 °C isotherm), crustal thickness (zcc), plate thickness (zp), and density structure (ρcc crust density, ρm mantle density, ρa asthenosphere density).b) At t = 0, lithospheric thinning and elevated mantle potential temperature causes transient uplift. c) As thermal decay progresses, LAB deepens, and time-dependent densities (ρcc(t), ρm(t), ρa(t)) evolve, driving net subsidence (S(t)). d–e) Density-depth profiles for undepleted and depleted lithospheric mantle, showing effects of depletion (Δρ). f) Air-loaded subsidence curves for varying Δρ values, illustrating long-term uplift or subsidence outcomes. If rethickening lithosphere is more

depleted than original lithosphere net uplift is generated, in turn, if the mantle refertilisation causes net subsidence. g) LAB depth evolution over time post-eruption (zLAB(t)). (Figure adapted from Stephenson et al. (2023).

Conversely, regions experiencing mantle fertilisation through magmatic addition of iron-rich rocks (e.g., pyroxenite sills and dykes) exhibit increased mantle density. This denser mantle induces negative buoyancy, leading to surface subsidence over time. The evolution of the Earth surface is highly sensitive to this balance between thermal and compositional drivers. For example, if the melt-zone (where depletion occurs) and the emplacement zone (where refertilisation occurs) are offset, then a 'new' topographic gradient will be induced. Such processes can generate both surface uplifts and accommodation space for sediment accumulation, leading to basin formation. Inverse modelling of mafic trace element composition suggests that lithospheric thickness in the NAC was less than 80 km between 1.9 and 1.7 Ga (Klöcking et al., 2020), coinciding with inferred LIP activity and indicating substantial mantle modification during this interval and subsequent thickening since that time (Figure 52).

The episodic nature of LIP events from 1.9 Ga to 500 Ma—including the Mount Hay Event and the most recent Kalkarindji LIP—suggests potential for repeated modification of lithospheric thickness and composition in the NAC. Major basins formed between 1.9 Ga and 1.6 Ga, including the Leichhardt (ca. 1800–1740 Ma), Calvert (ca. 1740–1650 Ma), and Isa (ca. 1650–1595 Ma) superbasins (Jackson et al., 2000). These basins may have formed associated with the earliest LIP events in the NAC. Later-stage LIPs episodically modified lithospheric thickness and composition, lowering the isostatic base level. These refertilisation events likely contributed to long-term surface subsidence, reducing erosional potential and promoting basin preservation.

In addition to modifying buoyancy and lithospheric strength, LIPs can directly impact sedimentary basins through the emplacement of intrusive complexes. Seismic data from the Exmouth Plateau, for example, reveal a vast network of sills emplaced into sedimentary successions during LIP activity, where melt was arrested within the basin fill rather than erupting at the surface. This process not only altered basin thermal regimes but also influenced density distributions and subsidence patterns, reinforcing the role of LIPs as active controls on basin geometry and accommodation space (Rohrman, 2013). Similarly, in the Canning Basin, mantle refertilisation linked to the Warakurna, Gairdner, and Kalkarindji LIPs generated anomalously Fe-rich lithospheric mantle. This fertilisation created negative buoyancy conditions, promoting long-lived basin subsidence and preservation of thick sedimentary packages (Moro et al., 2024).

Thermal effects of sill emplacement into sedimentary basins also drive extensive contact metamorphism, releasing large volumes of thermogenic volatiles such as CO_2 and CH_4. These processes not only contribute to global environmental change but also accelerate maturation of organic-rich source rocks, influence hydrocarbon system development, and further modify basin preservation potential (Svensen et al., 2023). Together, these lines of evidence indicate that LIPs act as powerful, multi-stage drivers of basin evolution—first by thinning and heating the lithosphere, then by compositional modification that alters long-term subsidence, and finally by intrusive and thermal effects that shape basin stratigraphy and preservation over hundreds of millions of years.

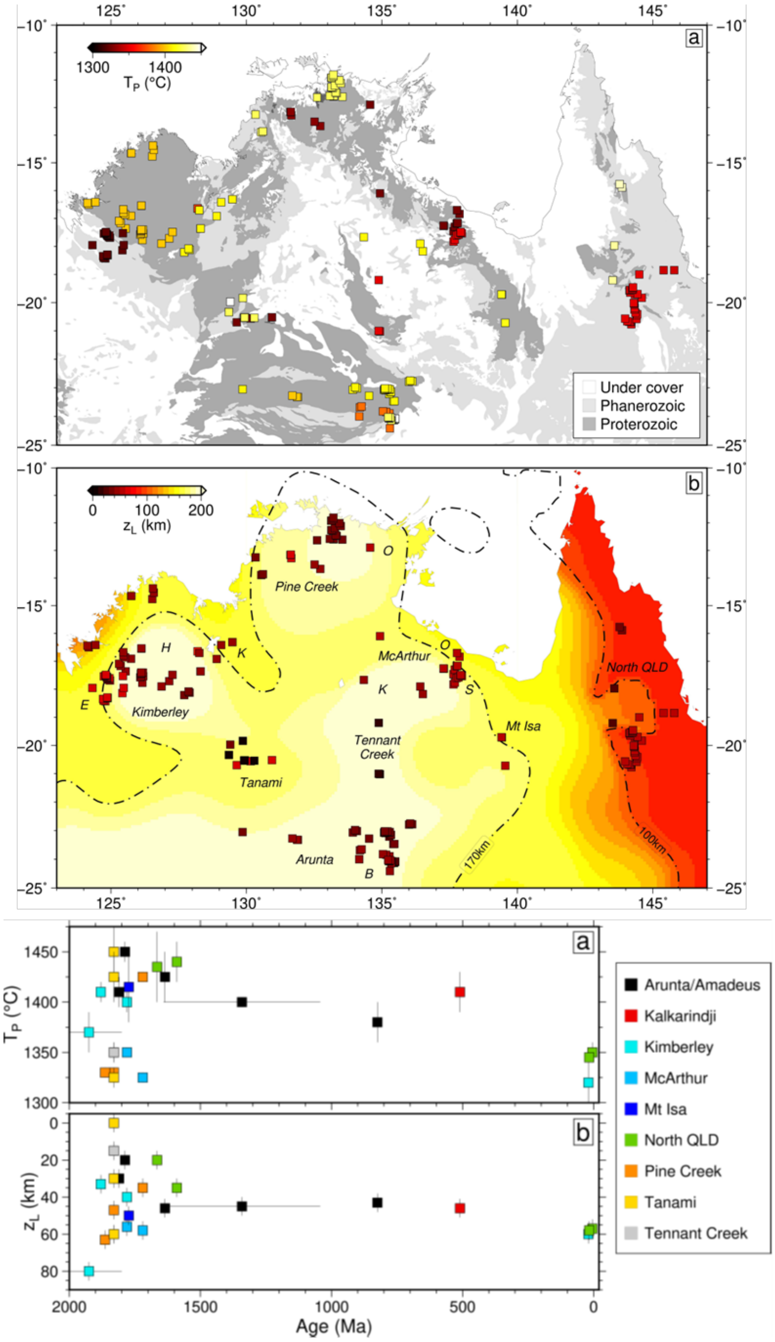

Figure 52: Results from inverse modelling of mafic trace element compositions in the NAC. (a) Igneous samples coloured by calculated potential temperature (TP). Dark/light grey polygons show Proterozoic/Phanerozoic outcrop geology (Raymond et al., 2012). (b) Samples coloured by calculated lithospheric thickness (zL). Background colours and black dashed lines show present-day lithospheric thickness (Hoggard et al., 2020). Bottom panel shows modelled potential temperature and lithospheric thickness with time. Figure adapted from Klöcking et al. (2020).

4.2. Crustal scale modelling

The thickness and properties of Australian crust have been investigated through several continental-scale to region-scale investigations. A continent-scale density model was modelled using a gravity inversion constrained by seismic Moho depth. This large-scale analysis reveals that a thick and dense crust is required to fit regions of deep Moho with Bouguer gravity highs (Aitken et al., 2013). At the regional scale, receiver function studies and deep seismic reflection profiles provide additional insights into crustal architecture; however, these datasets remain spatially limited (Jiang et al., 2019; Kennett et al., 2023; Sippl, 2016).

In mineral-rich regions such as Mt Isa, targeted surveys including seismic and magnetotelluric transects have offered further constraints on crustal structure and major boundaries (Jiang et al., 2019). These localised studies highlight the importance of integrating high-resolution geophysical data to refine interpretations of crustal composition and geometry (Figure 53).

There is a clear need to leverage these regional datasets to improve understanding of how crustal structure influences basin formation and evolution through rheology, thermal structure and composition. Enhanced resolution of crustal architecture will contribute to more accurate models of lithospheric dynamics and basin preservation mechanisms.

The main questions we would like to address are:

1. What is the crustal structure, and particularly the density and magnetic susceptibility distribution in the crust?
2. The impact of crustal heterogeneity on sedimentary basin forming and preservation.

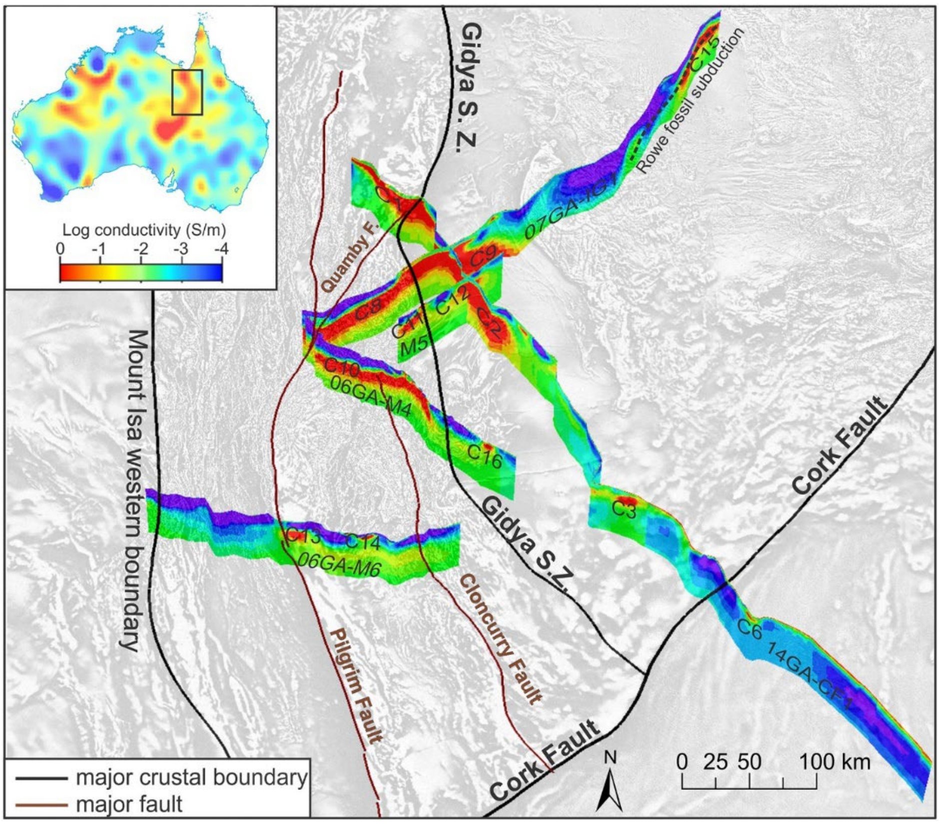

Figure 53: Focused seismic and MT transects help identify major crustal boundaries in Mt Isa (Jiang et al., 2019).

4.2.1. Methodology

To investigate crustal architecture, we employed a multiphysics joint inversion framework implemented in JIF3D (Moorkamp et al., 2011). This approach couples density and magnetic susceptibility using variation of information to constrain the coupling. Rather than seeking a smooth solution that independently fits gravity and magnetic data, the inversion assumes that an unknown statistical relationship exists between density and magnetic susceptibility. Solutions with low mutual information (Figure 54) are penalised by minimising information entropy, thereby enhancing structural coherence between datasets.

This inversion framework has been applied in several regions, with results demonstrating good agreement with known geological structures (Lösing et al., 2023). The mutual information coupling imposes a strong data-driven petrophysical coupling, which may yield structural models that differ from those derived through individual inversions or those coupled via structural similarity constraints (e.g., cross-gradient).

In this study, we incorporate SEEBASE and AUSMoho2023 as structural inputs and apply a joint inversion framework to resolve coupled density and magnetic susceptibility within the crystalline crust. We calculate residual gravity by removing the density effects of sedimentary basins and Moho undulations, using a reference model with a reference Moho as 40 km, crustal and mantle densities of 2800 kg/m³ and 3300 kg/m³, respectively. Density within the sedimentary layer is defined by an exponential compaction law (Aitken et al., 2015) with quartz grain density (2650 kg/m³) and saline water fluid density (1030 kg/m³). The porosity exponentially decreases with increased depth ($\varphi = 0.40\mathrm{e}^{0.3(\mathrm{h}-2.5)}$). The residual gravity field thus reflects deviations from the reference density model, enabling improved understanding of crustal density and susceptibility variations. This approach aims to enhances our understanding of how crustal structure influences basin development.

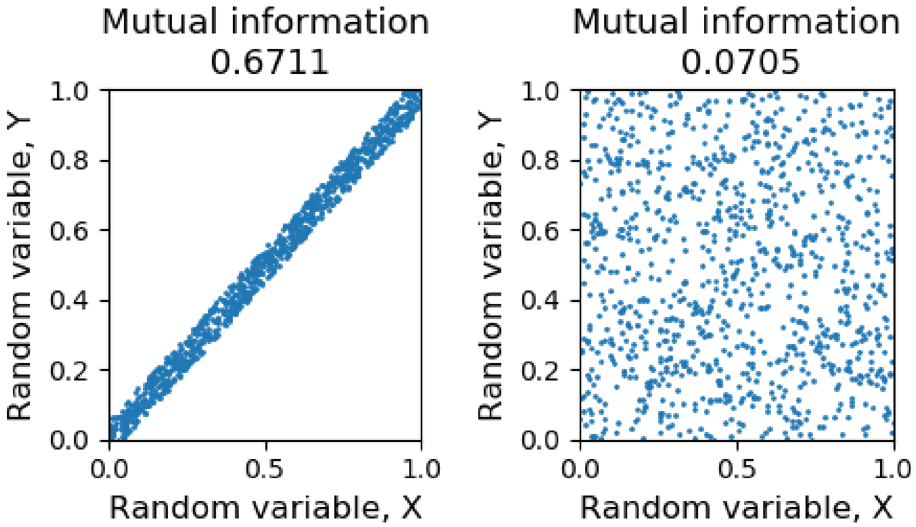

Figure 54: Example of mutual information illustrating the relationship between two variables. When a strong relationship exists, the mutual information value is high. In contrast, when the variables show no apparent relationship, the mutual information value is low. In the inversion the latter case will be penalised, seeking to promote the former.

4.2.2. Result and findings

The modelled crustal density and magnetic susceptibility are presented in Figure 55. The resolved structures show strong spatial correlation between density and susceptibility.

At the upper to lower crustal levels, several low-density felsic domains are observed in the Tanami region and along the western margin of the South Nicholson Basin. Multiple magnetic highs in these regions suggest intense intrusive activity, consistent with both mafic and felsic intrusions. Major basin depocenters—including the Birrindudu, Beetaloo, South Nicholson, and Mt Isa—are associated with mafic crustal compositions beneath, in agreement with previous continent-scale studies (Aitken et al., 2013).

In the lower crust, dense material is required to simultaneously fit the gravity anomalies given the thick Moho depths. These features are interpreted as mafic underplates. However, their distribution is not uniform across the NAC. For example, while the Birrindudu Basin exhibits thick crust, it does not require an extremely dense mafic underplate to match gravity observations. In contrast, the Beetaloo Basin, South Nicholson Basin, and Mt Isa region do require dense mafic material at the base of the crust. This spatial variability in mafic crustal distribution likely reflects differences in the timing and location of lower-crustal magmatic addition events across the NAC.

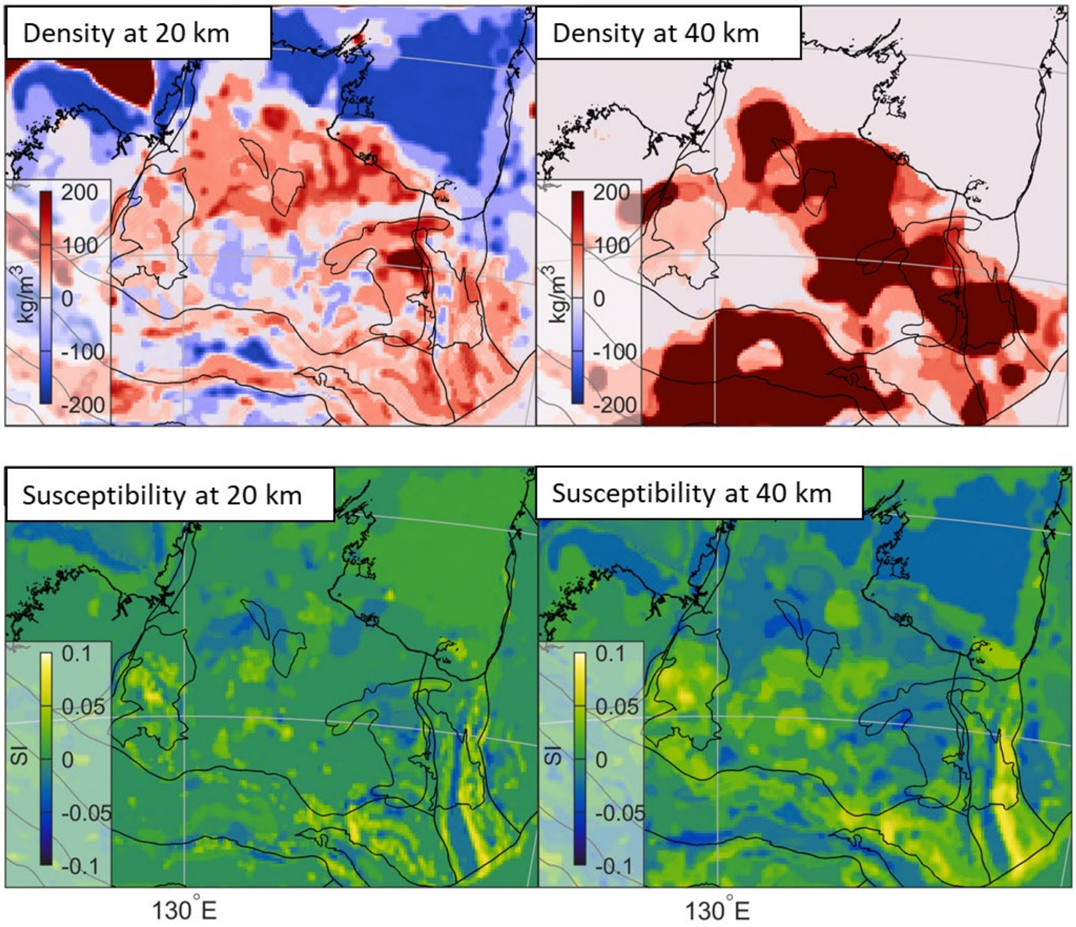

Figure 55: Density and magnetic susceptibility distributions derived from joint inversion results. The model highlights spatial correlations between density zones and magnetic susceptibility, reflecting coupled geological domains.

4.2.3. Discussion

Joint inversion results suggest the presence of extensive dense material in the crust, which can be interpreted as mafic crust beneath the NAC. Based on the modelled crustal density distribution, the mid-to lower crust of the NAC can be broadly classified into two major domains: a mafic domain extending across the Beetaloo, South Nicholson, and Mt Isa regions, oriented NW–SE; and a felsic domain encompassing the Tanami region and extending south of the South Nicholson Basin.

The widespread spatial distribution of the mafic domain is likely driven by the emplacement of large volumes of magma, with LIP being a primary candidate. In the NAC, multiple LIP events are recorded by extensive mafic dike swarms spanning from 1.9 Ga to 510 Ma. Although the precise timing of mafic domain formation remains difficult to constrain, the mapped present-day mafic domains are likely the cumulative result of multiple LIP emplacements through geological time. Several LIPs show strong spatial correlation with the mapped mafic domains. For example, the 1330–1295 Ma Derim Derim LIP, which intrudes the middle and upper Roper Group formation of McArthur Basin, overlaps significantly with the modelled mafic underplate (Nixon et al., 2022). The morphology of the Derim Derim Dolerite intrusion within the greater McArthur Basin suggests a deep-seated magma plumbing system (>3 km), implying that significant exhumation and erosion have occurred to expose the intrusions at their present-day depths (Hall et al., 2024). Other mafic underplates may be associated with younger events, such as the 510 Ma Kalkarindji LIP (Claoué-Long & Hoatson, 2009). The Kalkarindji LIP spans a vast area across the NAC, with preserved basaltic flows and intrusive dykes extending into regions such as the Canning Basin (Bradshaw et al., 2021). Its emplacement has been linked to significant thermal events and caused the long term stability of Canning Basin (Moro et al., 2024).

There is a strong spatial correlation between the mapped mafic domains and known occurrences of mafic volcanism (Figure 56). Major volcanic centres, such as those in the Arunta Province and McArthur Basin, are located within the mafic domain. Trace element modelling of mafic igneous rocks from these regions suggests that 3% to 27% partial melting of the mantle is required to reproduce the observed compositions (Klöcking et al., 2020). These large melt volumes might cause the crustal thickening by forming mafic underplates inferred from our models. In contrast, the felsic domain—particularly the region between Tanami and Tennant Creek—shows no evidence of preserved mafic volcanism. While this absence may reflect preservation bias, it is notable that this region also exhibits highly depleted mantle signatures and a thick lithospheric root (Figure 49). These features suggest that the felsic domain may have remained largely unaffected by significant magmatic modification over geological time.

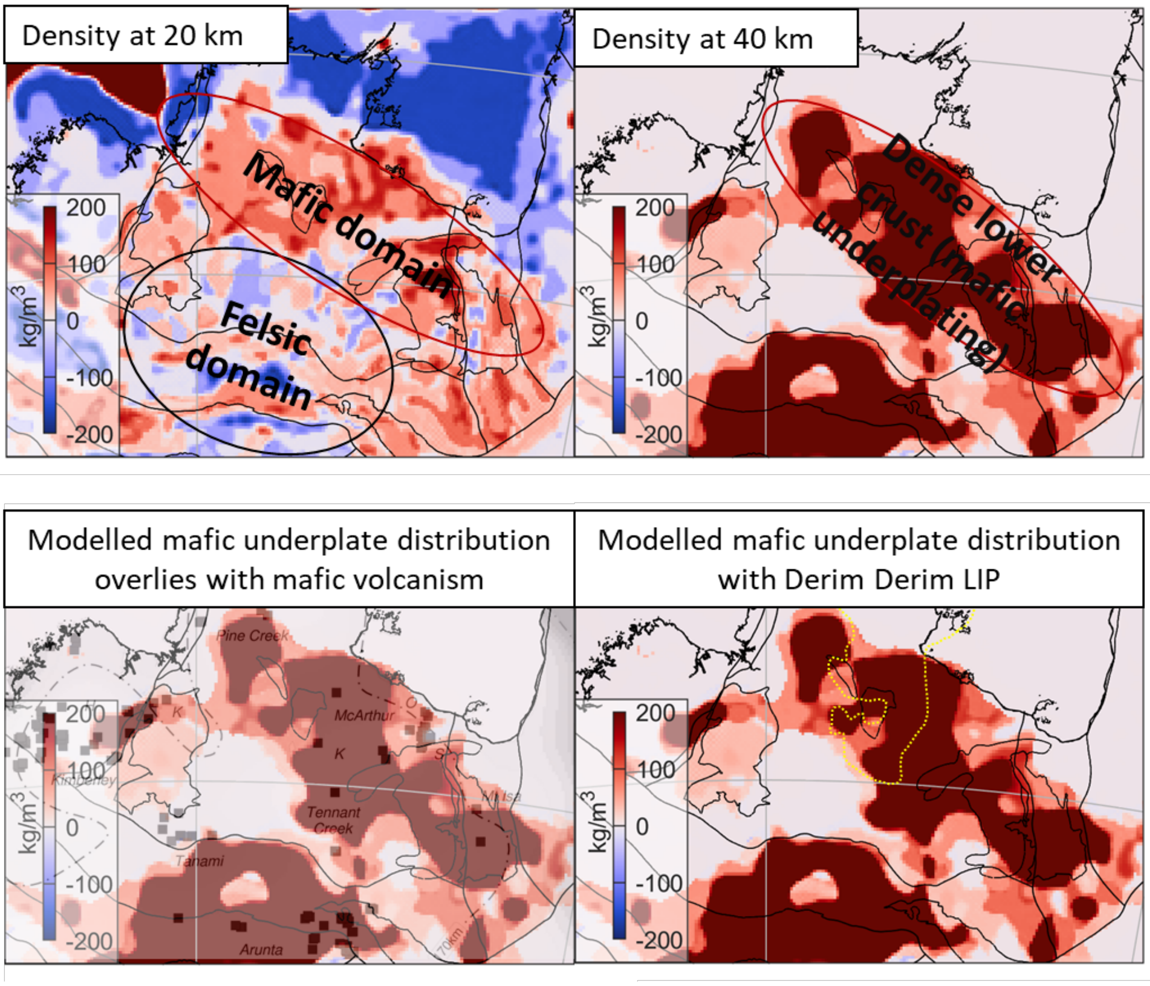

Figure 56: Classification of mafic and felsic domains in the NAC based on density distribution. The modelled mafic update shows substantial overlap with known mafic volcanism (Klöcking et al., 2020) in the region and partially coincides with the inferred Derim Derim LIP (yellow dashed line, (Nixon et al., 2022)).

The emplacement of mafic material into the crust results in a higher average crustal density compared to typical felsic crust. While crustal thickening replaces less dense crust with denser mantle, generating positive buoyancy that can promote surface uplift and erosion, the dense mafic crust contributes less buoyancy than a thick felsic crust. Thus, mafic crust influences isostasy in two opposing ways: in the middle and upper crust, its higher density relative to reference crust generates negative buoyancy, promoting subsidence; meanwhile, crustal thickening contributes positive buoyancy, but the mafic composition partially offsets the buoyancy of the underlying mantle. The long-term isostasy is governed by the combined effects of crustal density variation and mantle buoyancy compensation, and it varies both spatially and temporally. Over geological timescales, this overall mechanism is moderated by the slow pace of thermal decay. Driven by episodic magmatic activity, this gradual process may have maintained basin surfaces near paleo–sea level for extended periods, enabling continuous sediment accumulation at relatively low sedimentation rates.

4.3. Discussion

In this study, we present a framework for more accurately modelling the thermal and compositional structure of the upper mantle, conditioned by input from seismic tomography models and geological constraints such as mantle xenoliths and mapped geology. While our focus is on the regional lithospheric architecture of the NAC, continent-scale modelling is essential to account for mantle heterogeneity at the basin scale.

Sedimentary basins form through the development of accommodation space into which sediments can accumulate. Basin formation is typically driven by subsidence of the underlying crust relative to surrounding regions. While this is classically assumed to involve extension, either passively or actively driven, an alternative mechanism for such subsidence is the large-scale replacement of low-density, depleted lithospheric mantle with higher-density more fertile material. This compositional transformation increases lithospheric density, enhances negative buoyancy, and promotes surface subsidence. This subsidence will be realised over long time frames as the lithopshere cools. As such, mantle refertilisation processes may play a critical role in both basin formation and long-term preservation. The major basin depocenters in NAC are located above fertile mantle (Figure 49) indicating that mantle referitlisation has occurred beneath them and may be partly responsible for their formation.

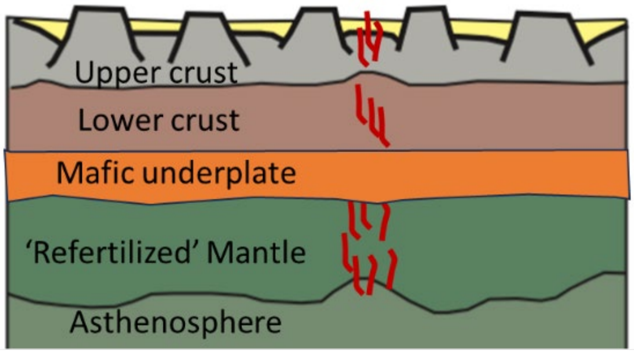

Figure 57: *Conceptual model illustrating the link between basin formation and preservation with negative buoyancy induced by dense mafic underplates and refertilised lithospheric mantle. Magmatic activity associated with LIPs contributes to mantle compositional changes, increasing lithospheric density and promoting surface subsidence. This subsidence enhances accommodation space, favouring long-term sediment accumulation and basin preservation.*

Some of the major basin depocenters in NAC are located above dense, mafic underplates identified in the northern half of the craton. Our modelling suggests that the original crust in these regions was substantially thinned, subsequently intruded and thickened by magmatic activity, resulting in the formation of mafic underplates and a mafic middle-to-lower crust. Mafic additions to the crust exert a two-fold influence on isostatic compensation. First, the replacement of felsic crust with denser mafic material generates negative buoyancy. Second, the emplacement of mafic underplates that extend into the mantle contributes positive buoyancy—though significantly less than would be produced by a felsic crust. During the initial stages of thermomagmatic events, transient thermal uplift and lithospheric thinning elevate surface topography. However, as thermal energy decays over time, the mafic additions increasingly contribute to negative buoyancy, favouring sustained surface subsidence. Thus, magmatic processes contribute not only to basin formation but also to their long-term preservation.

Our results demonstrate a strong link between basin evolution and deep-seated lithospheric architecture. While local Airy isostasy is commonly treating Moho as the compensation surface, in reality crustal and mantle heterogeneity often deviates from this assumption. Instead, a whole-lithosphere compensation framework is required to accurately represent isostatic compensation, including buoyancy forces from depleted and fertile mantle layers, underplated and/or magmatically intruded crusts and sedimentary basins (Figure 57).

Given the widespread emplacement of magmatic activity associated with LIPs in the NAC, the Proterozoic basin formation and preservation may be partly driven by magmatically induced negative buoyancy. While it is not possible to 'date' the geophysically-resolved mantle chemistries directly, we may infer from geochemistry analyses that the thick and fertile mantle formed since the Paleoproterozoic, and may be tied to interlinked LIP and basin forming processes that comprehensively modified the crust and lithospheric mantle. This has implications for understanding the drivers of basin formation in a more nuanced mode including these local buoyancy forces alongside extensional drivers of basin formation.

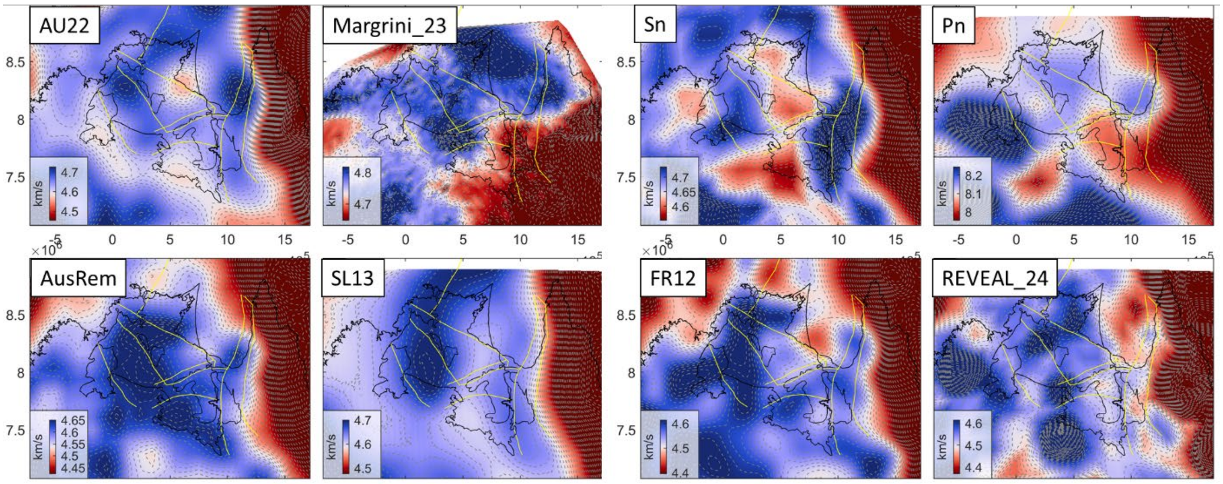

Figure 58: Seismic tomography model at 100 km depth across the NAC, illustrating large-scale consistency in velocity structure and small-scale variations (de Laat et al., 2023; Fishwick & Rawlinson, 2012; Kennett et al., 2013; Magrini et al., 2023; Schaeffer & Lebedev, 2013; Sun & Kennett, 2016; Thrastarson et al., 2024; Wei et al., 2018). The overall pattern reveals a coherent high-velocity signature characteristic of cratonic lithosphere. However, localised differences in velocity are evident, reflecting variations in input datasets, inversion techniques, and model resolution.

5. Geophysical Imaging of Thermomechanical Models

5.1. pide: Petrophysical Interpretation tools for geoDynamic Exploration

The integration of geodynamic simulations with geophysical observations is a major challenge in understanding the structure and evolution of Earth's lithosphere. Traditional geophysical surveys such as magnetotellurics (MT), gravity, and seismic tomography provide critical constraints on crustal and mantle properties but translating these signals into meaningful geological interpretations often suffers from ambiguity and non-uniqueness. Recent advances in numerical modelling now allow realistic simulations of lithospheric deformation, yet these models rarely produce outputs that can be directly compared with geophysical datasets.

The open-source Python library pide (*Petrophysical Interpretation tools for geoDynamic Exploration*) was developed to close this gap (Özaydın et al., 2025). By integrating experimental petrology, mineral and rock physics, and forward geophysical modelling, pide enables the transformation of thermomechanical model outputs into observable geophysical properties such as seismic velocity, electrical conductivity, magnetic anomalies, and gravity fields. This allows researchers to bridge the divide between geodynamic theory and field-based observations, providing a new pathway to interpret Earth's lithospheric architecture.

5.1.1. Methodology

pide is structured around three core classes that interact to generate synthetic geophysical models from thermomechanical simulations.

The pide class computes electrical conductivity and seismic velocities, incorporating key petrophysical parameters such as mineral composition, water content, porosity, and mineral interconnectivity. Calculations of seismic velocities are performed using the external SAnTex library, ensuring robust and efficient computation.

The material class represents Earth materials with customisable mineralogical and physical properties. Users can define modal proportions of olivine, pyroxenes, garnet and other phases, as well as water distribution and connectivity, allowing tailored modelling of crustal and mantle domains.

The model class organises material objects in three dimensions and calculates magnetic and gravity anomalies via the Harmonica library. This provides a seamless interface between lithospheric models and forward geophysical calculations.

Two supporting modules enhance pide's capabilities. The model_modifier converts thermomechanical outputs into conductivity grids suitable for MT modelling, while the inversion module enables single-parameter optimisation to infer input variables (e.g., composition, melt content) from geophysical outputs. Although the inversion capability is currently limited, future development will incorporate probabilistic ensemble inversion to better quantify uncertainty.

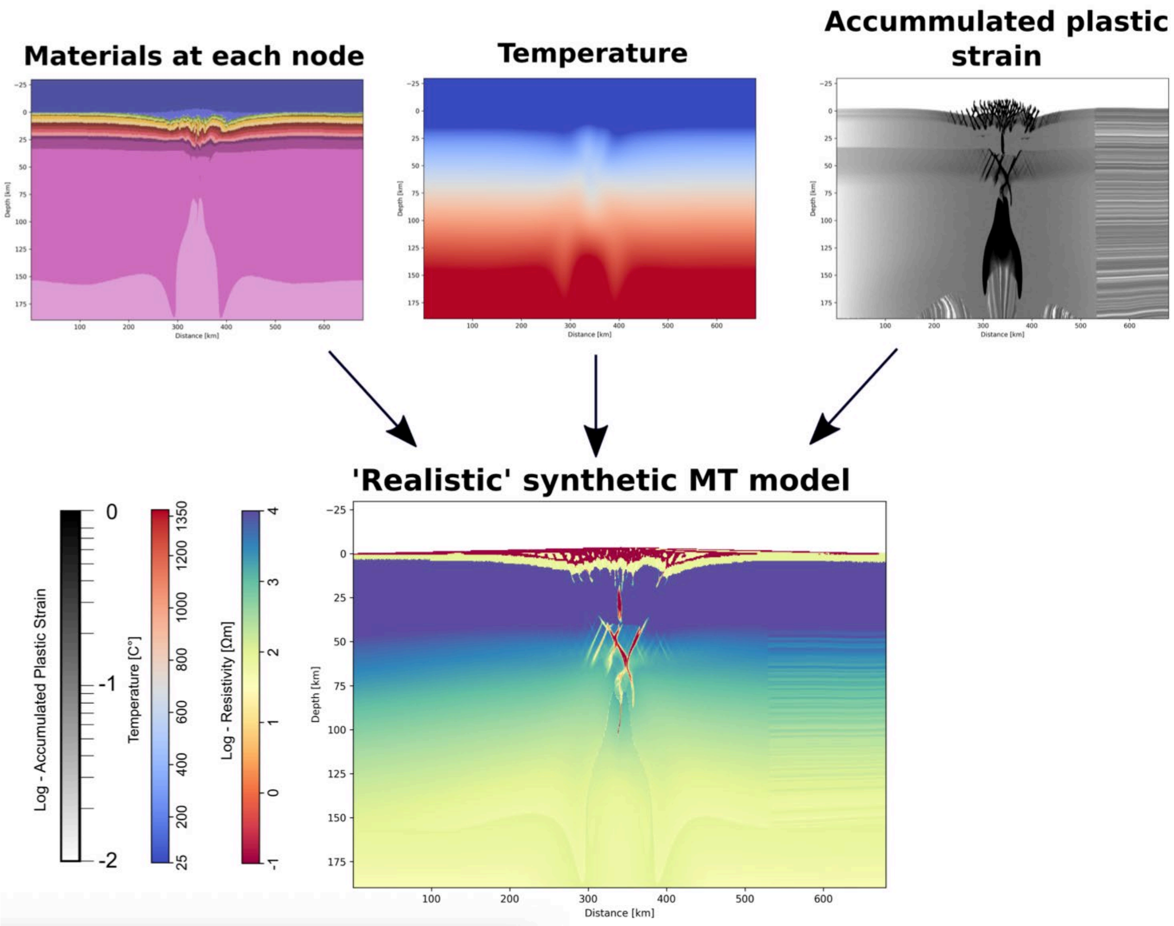

Figure 59. Example of pide being used for conversion of a thermoemchanical model into a synthetic MT model.

5.1.2. Results and findings

Initial applications of pide demonstrate its versatility and scientific value. The software has successfully computed theoretical conductivity and seismic velocities across a wide range of Earth materials, and converted lithospheric-scale thermomechanical models into synthetic MT, gravity, and magnetic data (Özaydın et al., 2025). These synthetic outputs can be readily integrated with established inversion platforms such as ModEM and Mare2DEM, allowing direct comparison with field datasets.

One of the clearest demonstrations is provided in Figure 59 where pide converts a 2D thermomechanical simulation into a synthetic MT model. This example illustrates how complex geodynamic simulations—typically output as temperature, pressure, and composition fields—can be made directly comparable with observed geophysical signals. The modular and extensible design of pide means it can be customised for diverse tectonic settings, from subduction zones to intracratonic basins.

5.1.3. Discussion

The development of pide directly addresses the long-standing problem of linking geophysical anomalies to geological processes. Conventional tomography often provides broad-scale velocity or conductivity anomalies but rarely constrains their underlying mineralogical or petrological causes. By embedding experimental petrology and mineral physics directly into its computational framework, pide provides a pathway to resolve these ambiguities and offer geologically meaningful interpretations.

Compared to existing tools such as MATE and SIGMELTS, pide stands out for its broader functionality and deeper integration with geodynamic workflows. The incorporation of external libraries such as SAnTex (seismic velocities) and Harmonica (gravity and magnetic fields) ensures that calculations are both physically robust and computationally efficient. Importantly, the ability to generate synthetic observables that can be inverted using standard geophysical software makes pide an invaluable tool for testing hypotheses about lithospheric structure.

The future development of probabilistic inversion modules will extend its scope even further, enabling uncertainty analysis and ensemble modelling for complex geological scenarios. For Proterozoic basins, where geophysical data often provide the only window into concealed crustal domains, pide offers a powerful approach to integrate geophysical imaging with numerical and analogue modelling. In this way, it strengthens predictive frameworks for understanding basin evolution and metallogenic fertility across northern Australia.

5.2. pide application: Does strain control the electrical conductivity anomalies in the lithosphere

5.2.1. Methodology

The methodology of this study was designed to address the challenges of interpreting magnetotelluric surveys at the lithospheric scale, where conductivity anomalies are often ambiguous and difficult to resolve. To achieve this, we compared field-based MT data on the Marmara Sea region with a synthetic MT model generated from a three-dimensional thermo-mechanical model of pull-apart basin. The synthetic MT model is based on laboratory constraints on the electrical properties of minerals, fluids, and melts. By incorporating strain fields into the conductivity models, we were able to test the hypothesis that deformation enhances the connectivity of conductive phases, thereby producing anomalies that MT surveys can detect. Laboratory measurements of conductivity under varying pressure, temperature, and fluid conditions were used to constrain the physical plausibility of the modelled anomalies. This integrated approach allowed us to move beyond descriptive imaging and toward a process-based interpretation of MT signals at the lithospheric scale.

5.2.1.1. Thermo-mechanical model

We use underworld to simulate the development of a 3D strain field associated with the development of a pull-apart basin (Figure 60). The internal and boundary conditions (velocity boundary condition, crustal thickness, geotherm, etc.) are guided by the geology of the Marmara Sea region. We employ similar rheological parameters to those listed in Table 1, but with a geotherm leading to a temperature at the Moho of 540 ºC.

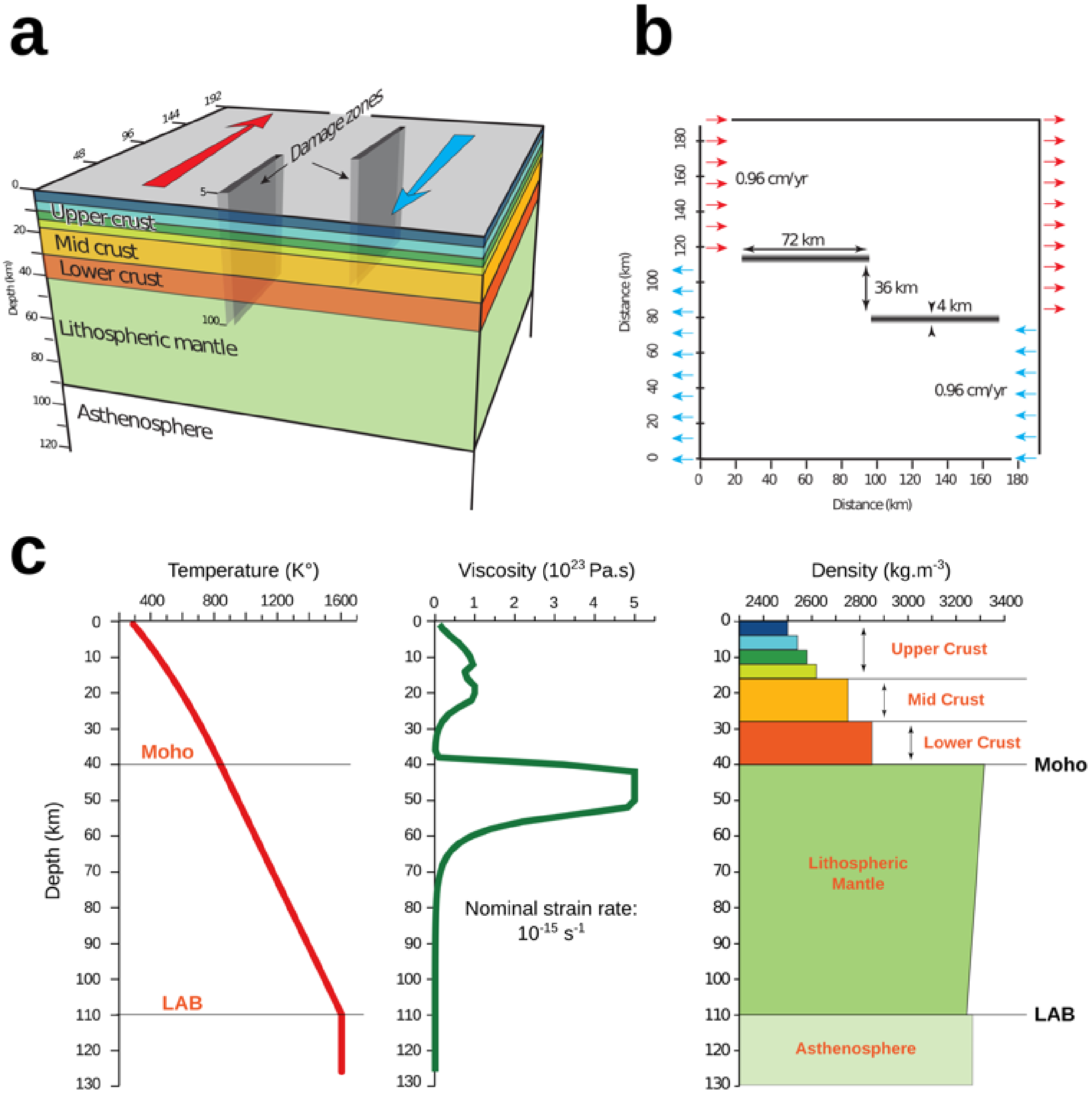

Figure 60. a) Initial state of the 3D thermo-mechanical model depicting the distribution of layers and damage zones. b) Velocity boundary conditions. c) Vertical profile of temperature, viscosity and density structure of the initial state of the model

5.2.1.2. Electrical conductivity model

The accumulated plastic strain, as well as the temperature and pressure fields are then used to derive a model of electrical conductivity. Using the value of plastic strain, this model combines a background conductivity with a maximum conductivity model (Figure 61).

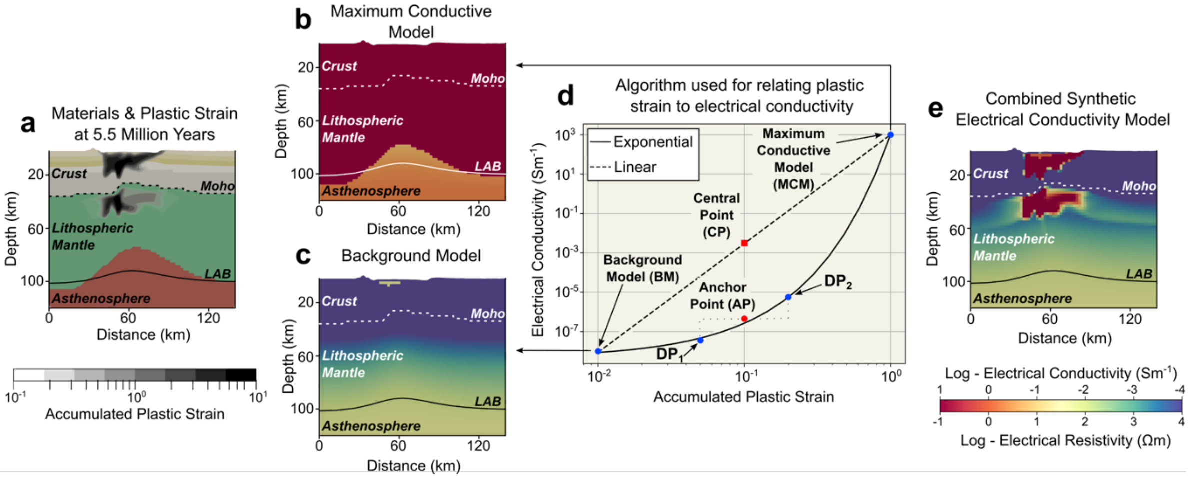

Figure 61. Graphical representation of synthetic conductivity model creation from thermo-mechanical models. a) Materials at 5.5 million years of development, b) maximum conductivity model, c) background conductivity model, d) graph representing the algorithm to combine the two models via accumulated plastic strain, e) combined conductivity model. DP: Data Point. LAB: Lithosphere Asthenosphere Boundary.

5.2.1.3. *MT model*

To translate our 3D synthetic conductivity models into 3D MT models, we first simulate MT responses at the surface using forward modelling. These synthetic responses are then used to run MT inversions, generating a 3D conductivity distribution that represents what an actual MT survey would observe. We use the ModEM algorithm (Kelber et al., 2014) for both forward and inverse MT modelling purposes. Cross-sections from the resulting MT models are shown alongside the corresponding thermomechanical simulations at 0.5, 2.5, 4.5, and 5.5 million years (

Figure 62).

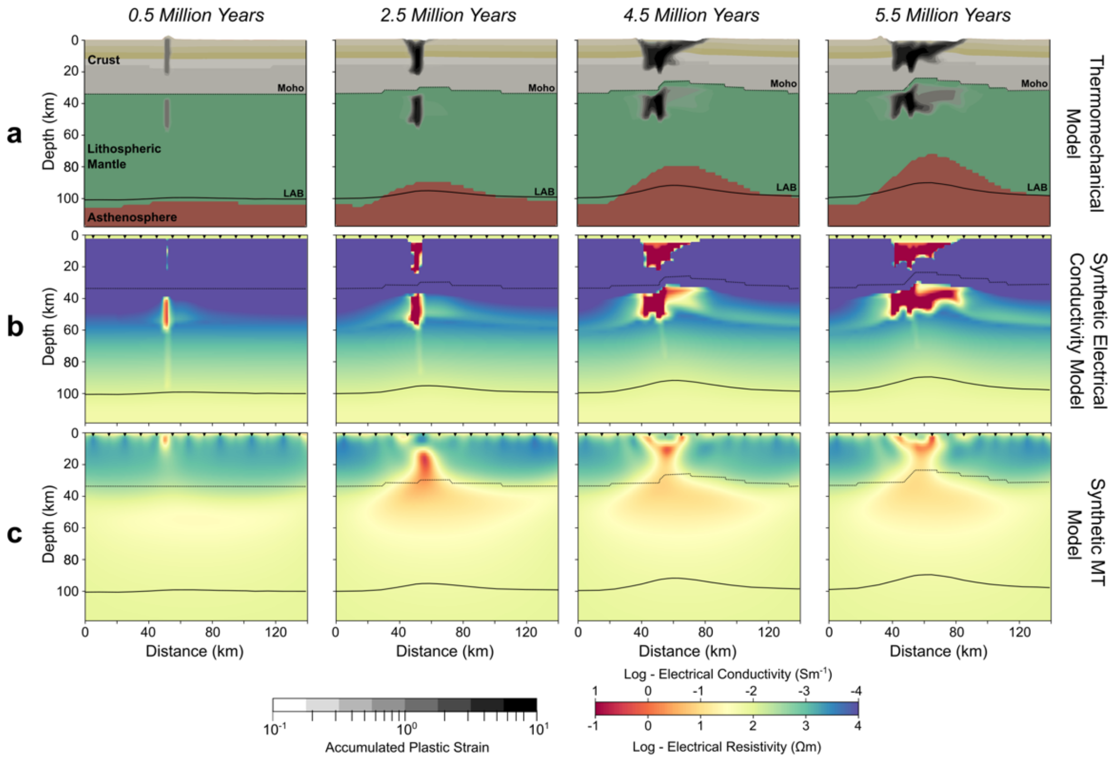

Figure 62. a) Evolution of thermomechanical model from 0.5 to 5.5 million years alongside b) the synthetic conductivity models, and c) corresponding MT inversion models.

5.2.2. Results and findings

Models that excluded the effects of strain (Figure 63a) produced conductivity patterns that were diffuse and inconsistent with the observed MT data. In contrast, synthetic models that incorporated strain-controlled conductivity distributions successfully reproduced the sub-vertical conductive anomalies observed in the Marmara region (Figure 63). These anomalies extended from the upper crust into the upper mantle, suggesting that deformation creates vertically integrated pathways for fluid and melt migration. These results demonstrate that the geometry and continuity of conductivity anomalies imaged by MT surveys are strongly influenced by strain localisation within the lithosphere. The findings suggest that conductivity anomalies are not diffuse but instead align with zones of tectonic weakness, such as shear zones and fault strands. This alignment supports the interpretation that MT surveys are imaging the structural memory of deformation, preserved as interconnected networks of conductive phases. The results highlight the importance of considering deformation processes when interpreting lithospheric-scale MT data, as they provide a unifying explanation for the geometry and persistence of conductivity anomalies.

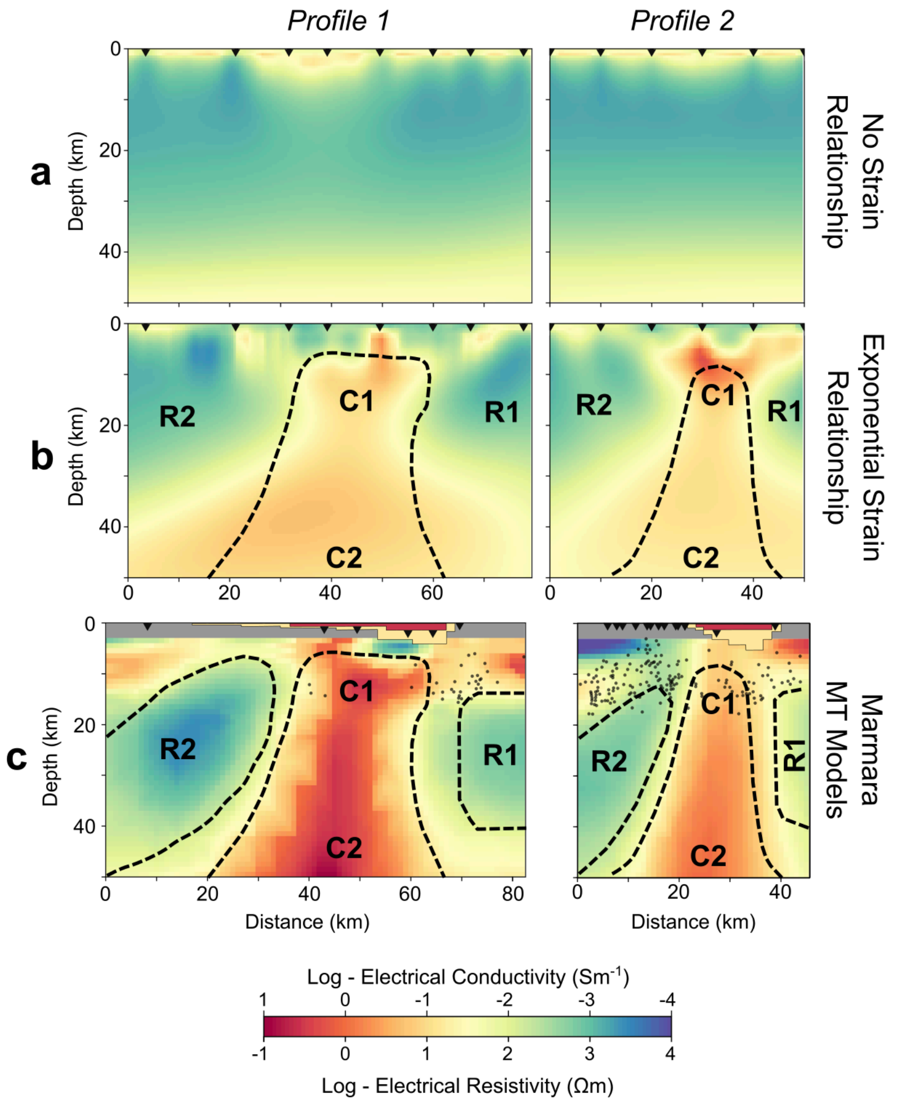

Figure 63. a) Synthetic MT model excluding the effect of strain on electrical conductivity, b) Synthetic MT model including an exponential strain-conductivity relationship, c) Marmara MT models digitised and replotted after Kaya et. al (2013). Black dots are earthquake hypocentres.

5.2.3. Discussion

The interpretation of MT surveys at the lithospheric scale has long been complicated by two fundamental issues: the limited resolution of inversion techniques and the ambiguity of the conductive phases responsible for the anomalies. Conductivity anomalies may arise from a variety of sources, including interconnected fluids, partial melts, graphite films, or hydrous minerals, and distinguishing between these possibilities has often been problematic. Our study suggests that these difficulties can be mitigated by recognising the central role of strain in organising conductive pathways (Figure 64). Strain localisation enhances porosity, promotes fluid migration, and facilitates the precipitation of conductive minerals, thereby creating networks that surpass the percolation threshold required for MT detectability.

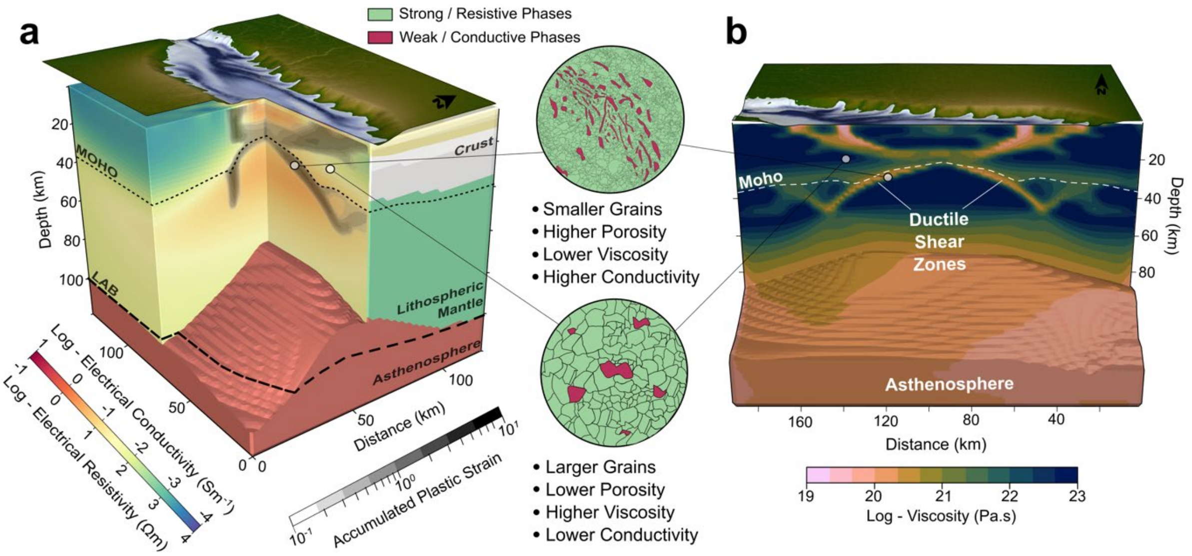

Figure 64. a) 3D depiction of the MT model at 5.5 million years of development alongside b) the viscosity distribution showing high-strain zones as low-viscosity corridors.

In this framework, conductivity anomalies are not simply indicators of present-day fluids or melts but are also records of past tectonic processes. They represent the scars of deformation, preserved as lithosphere-scale shear zones that continue to influence the mechanical and thermal evolution of the lithosphere. This interpretation reframes MT surveys as tools for reconstructing the tectonic history of a region, providing insights into both active processes and long-lived structural inheritance. The significance of MT surveys, therefore, lies not only in their ability to map conductive phases but also in their capacity to reveal the deep architecture of the lithosphere and its tectonic evolution.

6. Multi-disciplinary investigation on the North Australian Craton

6.1. Basement architecture of the North Australian Craton basins

The NAC represents one of the most extensive and mineral-rich crustal provinces in Australia, with a geological record spanning from Archean to Mesoproterozoic time. Much of its interior basement is concealed beneath thick sedimentary basins, yet scattered exposures at Pine Creek, Tennant Creek, Tanami, Arnhem, Halls Creek, and Mount Isa provide critical windows into its architecture. Understanding the composition, age, and tectonic configuration of these basement domains is essential for refining models of continental assembly, unravelling the history of Proterozoic basin formation, and predicting metallogenic fertility (Figure 1 and Figure 65).

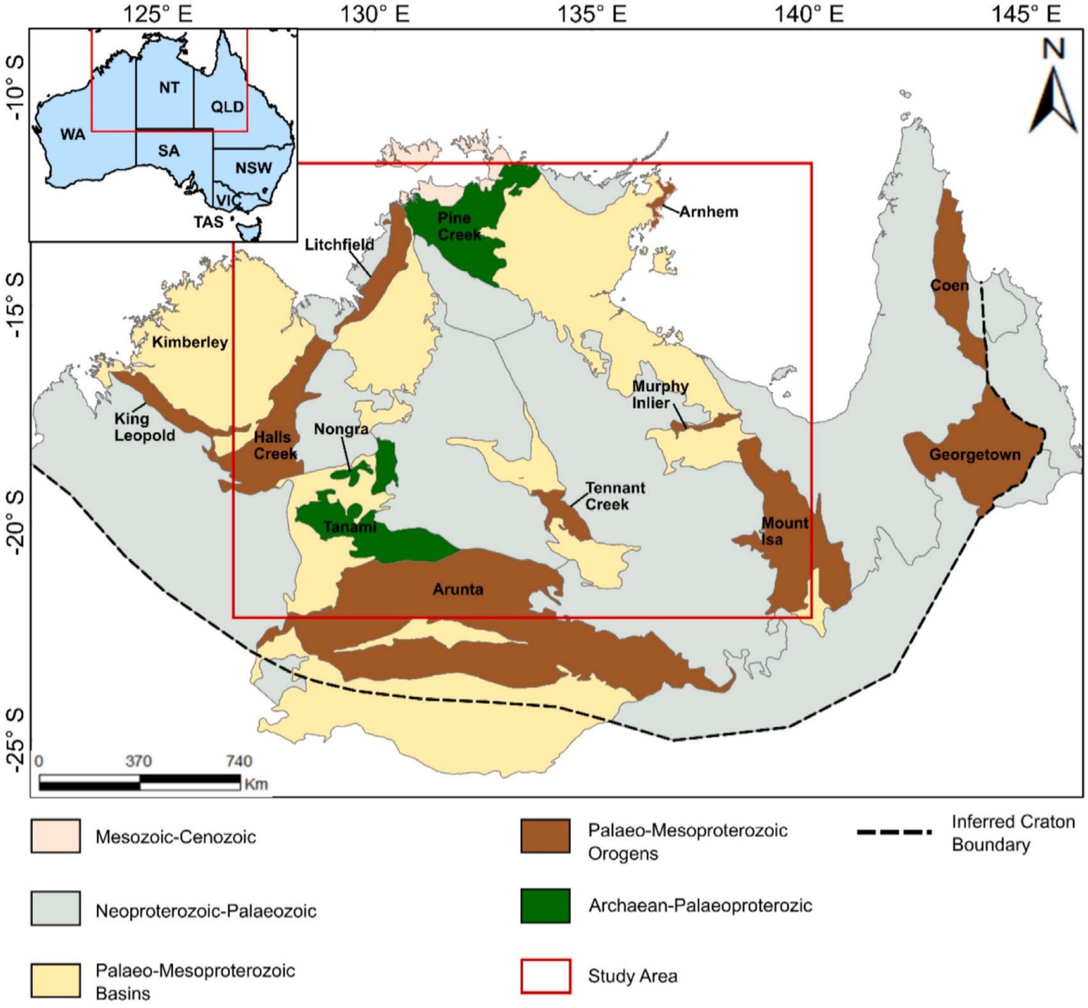

Figure 65. Regional map of the NAC showing basement provinces and Proterozoic basins.

This study investigates the concealed basement geology of the NAC, focusing on the integration of isotopic, geochronological, and geophysical datasets to reveal its crustal architecture. The aim is to delineate basement domains, reconstruct their tectonic histories, and assess the broader implications of their evolution, with particular attention to the Barramundi Orogeny (~1870–1850 Ma), a pivotal event in craton amalgamation.

The study set out four interconnected objectives. First, to identify and delineate the extent of major basement provinces beneath younger cover sequences using geophysical and isotopic data. Second, to integrate whole-rock neodymium (Nd) isotope compositions with zircon U–Pb geochronology and regional geophysical datasets in order to constrain crustal formation ages and model ages (T_DM). Third, to develop a tectonic framework for crustal assembly during the Barramundi Orogeny, establishing how Archean protoliths were reworked and amalgamated with juvenile additions. Finally, to place the NAC within a broader continental context, assessing the significance of its crustal domains for the assembly of northern Australia and its relationship to global Paleoproterozoic orogenic systems (Figure 66).

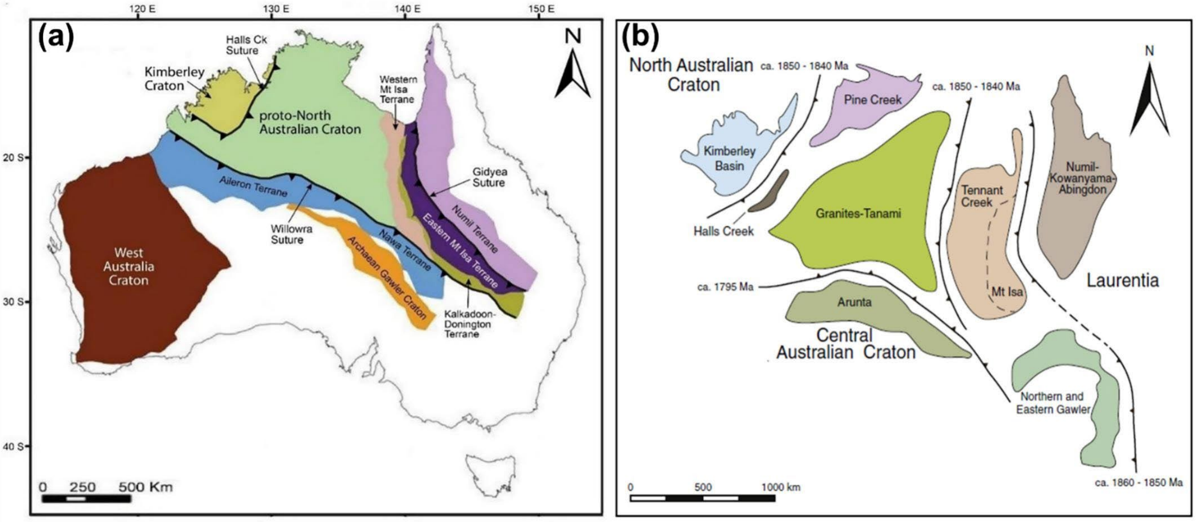

Figure 66. Contrasting proposed models for the evolution of the North Australian Craton by (a) Betts et al. (2016) and (b) Li et al. (2014).

6.1.1. Methodology

The investigation combined aeromagnetic and gravity data with whole-rock Nd isotope compositions and zircon U–Pb ages from across the NAC. Lineament extraction from geophysical data was used to identify crustal boundaries and reactivated fabrics, particularly in the Tennant Creek region (Figure 67). These structural features were compared with isotopic signatures to distinguish reworked Archean crust (negative εNd(t), old T_DM ages) from juvenile Paleoproterozoic additions (positive εNd(t), young T_DM ages). By correlating isotopic domains with mapped geology in Pine Creek, Tanami and Halls Creek (Figure 68, Figure 70, Figure 71), a regionally consistent picture of crustal provinces was established. Building on this framework, zircon U–Pb datasets were compiled from Neoarchean to Paleoproterozoic basement rocks to establish magmatic pulses and inheritance patterns across the craton. For example, the distribution of inherited zircon ages older than 1900 Ma in pre-1800 Ma magmatic rocks (e.g., Cullen Supersuite, Sally Downs Supersuite, and Giddy Suite) was used to trace assimilation of older crust and distinguish isotopically evolved provinces. Nd isotope model ages were integrated to quantify the balance between crustal reworking and mantle additions, with strongly non-radiogenic signatures ($\varepsilon Nd < -2.9$) marking reworked Archean sources and radiogenic signatures (εNd > 0) denoting Paleoproterozoic juvenile input.

Geophysical interpretation further refined these isotopic domains. Potential field anomalies in aeromagnetic and Bouguer gravity data revealed deep-seated fault systems and terrane boundaries that correlate with isotopic contrasts. For example, the Pine Creek and Tanami blocks record Neoarchean granitoids with steep rare earth element (REE) depletion patterns and εNd values down to –6.3, while the Halls Creek Block hosts suites with younger U–Pb zircon ages and more radiogenic Nd signatures.

This multi-proxy methodology therefore allowed integration of isotopic datasets with structural and geophysical interpretations. By comparing isotopic provinces to mapped geology and potential-field anomalies, crustal growth and reworking patterns were constrained across the NAC. These results underpin regional correlations between Pine Creek, Tanami, Halls Creek, and Tennant Creek terranes, forming the basis for reconstructing the Paleoproterozoic tectonic architecture of northern Australia.

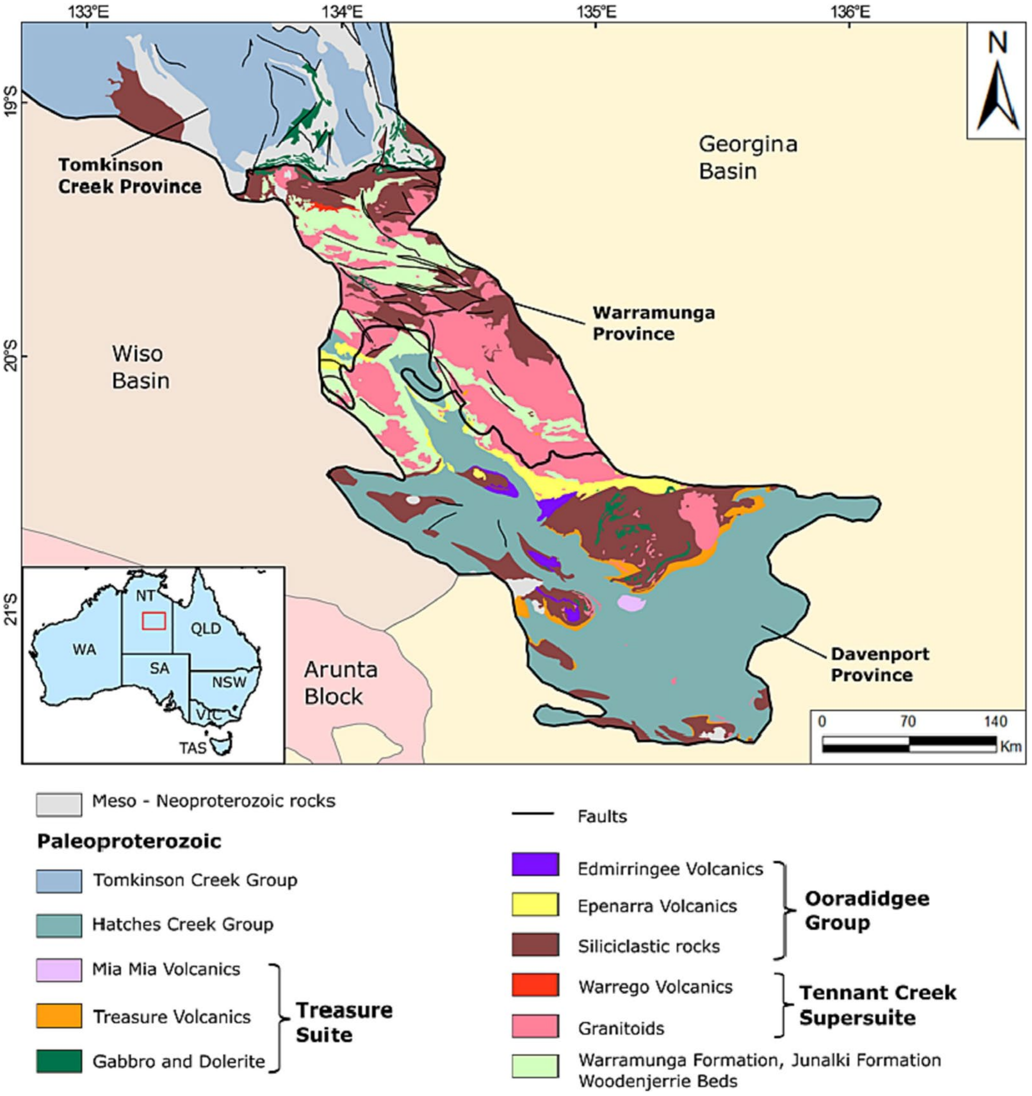

Figure 67. Geology map of the Tennant Creek region showing main basement lithologies and faults based on synthesis of GIS from the solid geology of the North Australian Craton (Stewart et al., 2020).

6.1.2. Results and findings

The NAC preserves a composite crustal record, anchored by a major phase of crustal growth around 2.5 Ga. This Archean basement provided the protolith for later reworking and amalgamation during Paleoproterozoic time. Between ~1900 and 1800 Ma, extensive tectonism, magmatism and deformation during the Barramundi Orogeny reshaped these Archean foundations, incorporating juvenile additions and stitching together disparate blocks into a more coherent, though internally complex, cratonic framework (McDonald et al., 1997; Champion, 2013; NTGS, 2019).

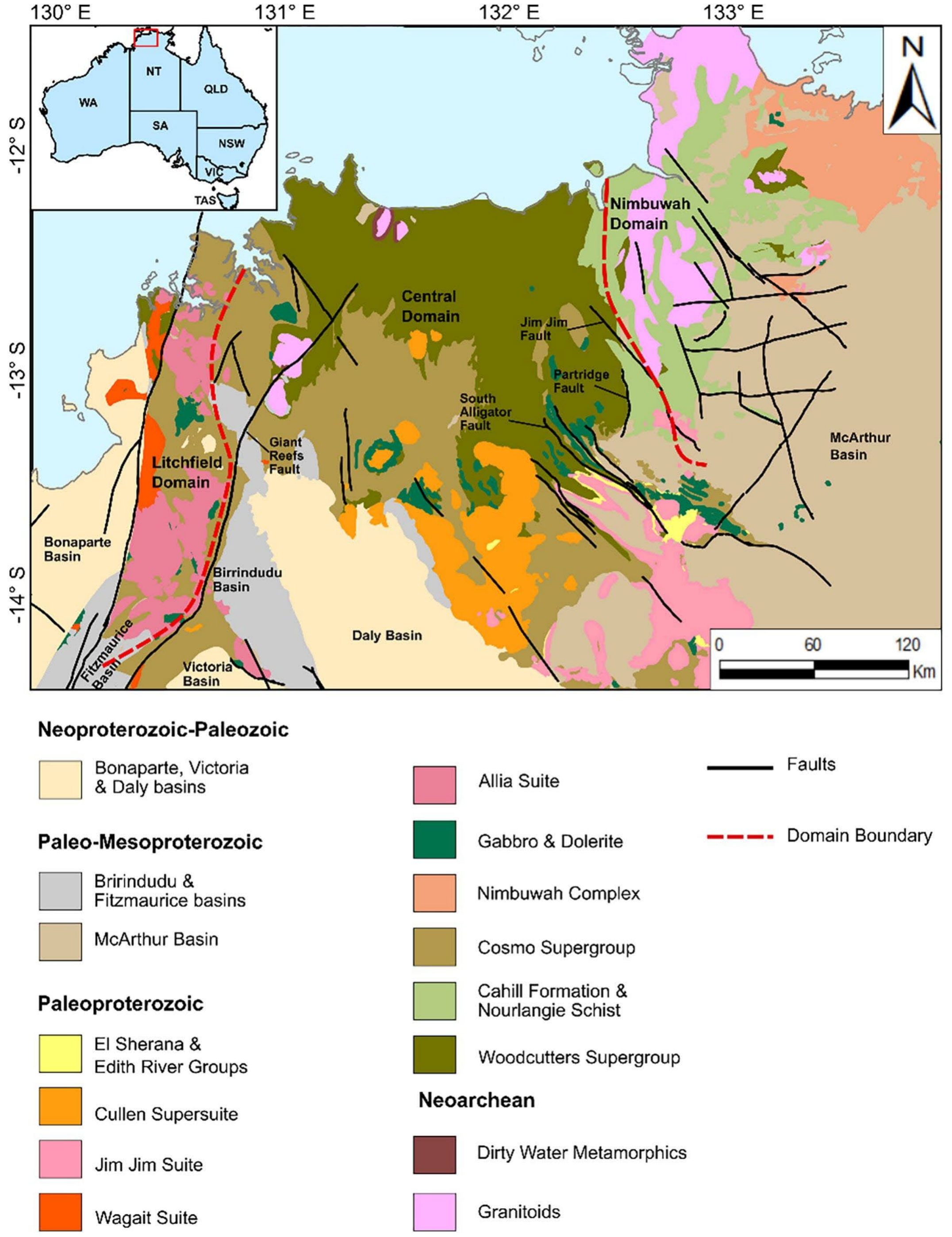

Figure 68. Geology map of the Pine Creek Orogen showing primary basement lithologies, basement domains and faults, based on the synthesis of GIS from the Solid Geology of the North Australian Craton (Stewart et al., 2020).

A synthesis of Nd isotopic values (εNd(t)) and model ages (T_DM, T2DM), integrated with zircon U–Pb crystallisation ages, provides spatial and temporal insights into mantle extraction and crustal growth across the NAC. Negative εNd(t) values and older model ages identify terranes dominated by reworked ancient crust, while positive εNd(t) values point to juvenile mantle-derived additions. Mapping the distribution of these isotopic parameters, cross-validated with structural and geochronological data, enabled the delineation of distinct crustal provinces and the recognition of concealed suture zones beneath basin cover. This integrative dataset facilitated the correlation of basement blocks across structural discontinuities and sedimentary basins, refining the tectonic model for the Barramundi Orogeny and its role in continental assembly.

In the Pine Creek Orogen (Figure 68), isotopic and geochronological data confirm Archean inheritance intruded by ca. 1870–1840 Ma granitoids of the Nimbuwah Event, associated with amphibolite- to greenschist-facies metamorphism and felsic volcanism. Detrital zircon and Hf isotopes further suggest crustal boundaries between the Central and Nimbuwah domains, coinciding with major geophysical features such as the Partridge Thrust and Jim Jim Fault (Figure 69), implying Paleoproterozoic rifting and subsequent re-amalgamation.

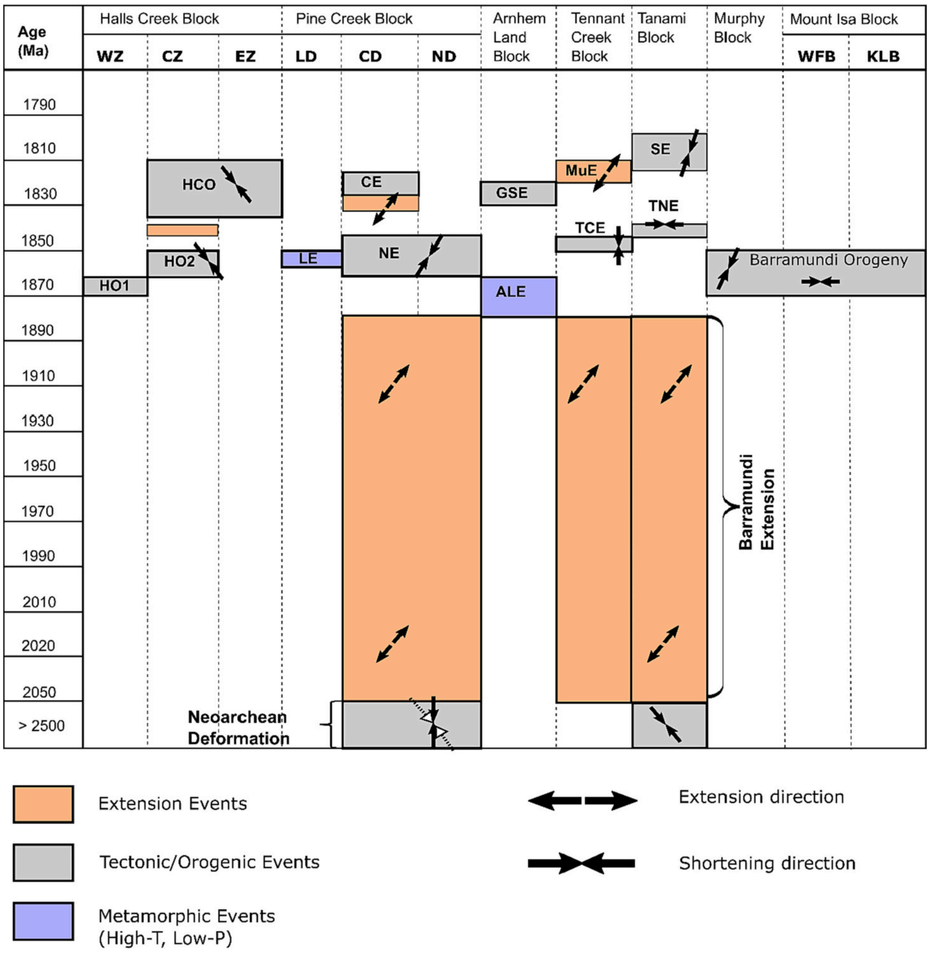

Figure 69. Pre-1800 Ma deformation events in North Australian Craton. HCO (Halls Creek Orogeny), HO1 (Hooper Orogeny-first phase); HO2 (Hooper Orogeny-second phase); LE (Litchfield Event); CE (Cullen Event); NE (Nimbuwah Event); ALE (Arnhem Land Event); GSE (Giddy Suite Event); MuE (Murchson Event); TCE (Tennant Creek Event); SE (Stafford Event); TNE (Tanami Event) (Korsch et al., 2011; Compston, 1995; Fraser et al., 2008; Maidment et al., 2013; Blake, 1987; Donnellan, 2013a, 2013b; Kruse et al., 2010; Myers et al., 1996; de Vries et al., 2008; Whelan et al., 2017; Kraus et al., 2015; Kositcin et al., 2018; Iaccheri, 2017; Joly et al., 2010; Maidment

et al., 2020; Goleby et al., 2009; Crispe et al., 2007; Blake et al., 1979; Ahmad et al., 2013b,a; Li et al., 2014; Dean, 2001; Bagas et al., 2014; Griffin et al., 2000; Phillips et al., 2016; Tyler et al., 1995; Kohanpour et al., 2020; Kohanpour et al., 2018; Lindsey et al., 2016; Bodorkos et al., 1999; Sheppard et al., 2001; Tyler et al., 2012; Withnall and Hutton, 2013; Betts et al., 2016; Page and Williams, 1988; Ahmad and Wygralak, 1989; Gardner, 1978; Ahmad et al., 2013b,a; Ahmad and McCready, 2001; Lally, 2002; Ahmad and Hollis, 2013; Ahmad and Lally, 2003; Doyle and Lally, 2004; Hollis et al., 2011; Hollis et al., 2009a,b; Needham et al., 1988; Sener, 2004; Glass et al., 2010; Stuart-Smith et al., 1993; Carson et al., 2008; Hendrickx et al., 2000).

The Tennant Creek Block (Figure 67) preserves polydeformed turbidites (Warramunga Formation) intruded by 1860–1840 Ma granitoids of the Tennant Creek Supersuite, whose isotopic signatures show clear mixing between evolved crust and mantle-derived components. Nd isotopic contrasts coincide with geophysical lineaments, highlighting major crustal breaks and supporting interpretations of reactivated fabrics as suture-related structures.

In the Tanami Block (Figure 70), inherited zircon ages (~2500 Ma) and negative εNd values point to Archean foundations reworked during multiple Paleoproterozoic events, including the Tanami and Stafford orogenies. However, seismic and isotopic data suggest a major south-dipping suture along its margin with the Arunta Block, consistent with Nuna assembly models

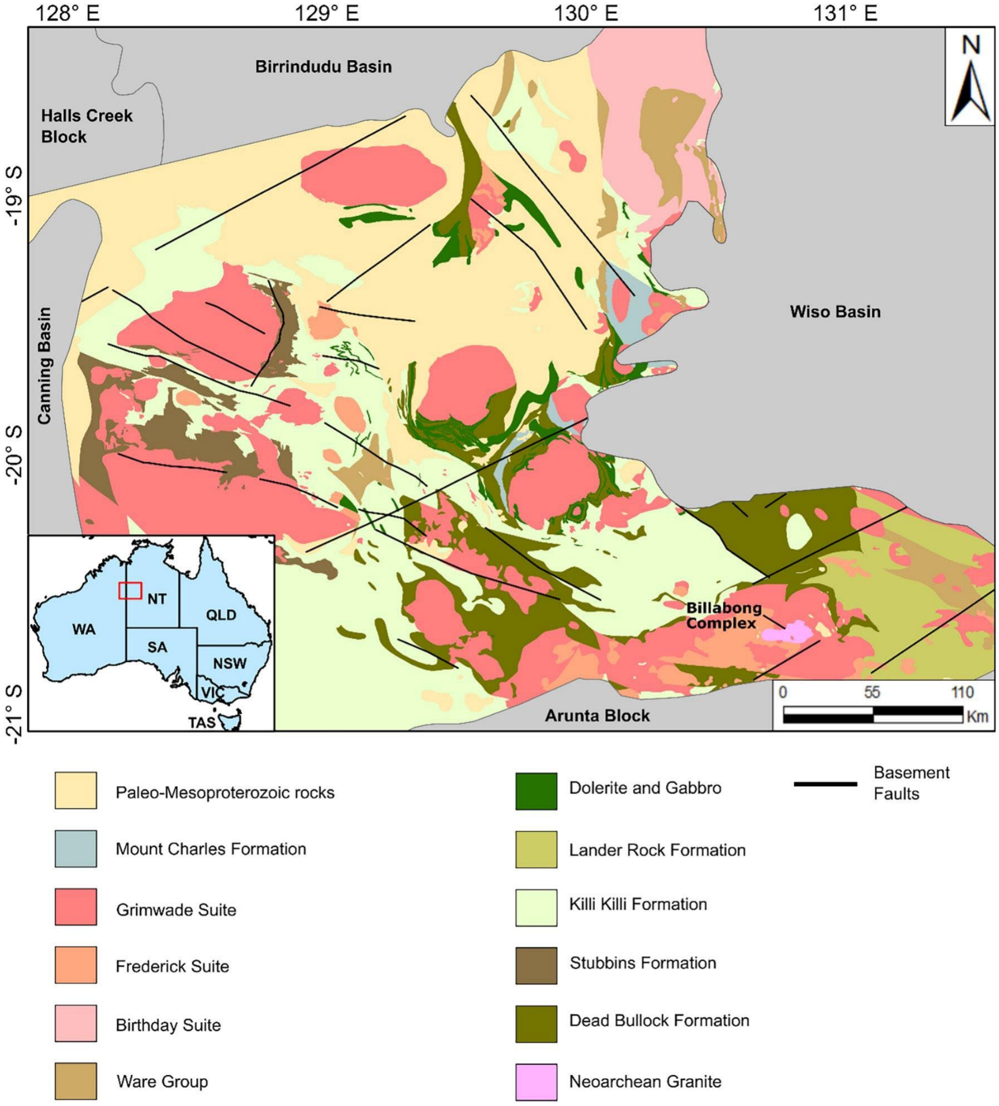

Figure 70. Geology map of the Tanami Block showing basement Archean to Paleoproterozoic rocks and faults based on the synthesis of GIS from the Solid Geology of the North Australian Craton (Stewart et al., 2020).

Along the craton margin, the Halls Creek Orogen (Figure 71) records Paleoproterozoic accretion with isotopically radiogenic granitoids (εNd +1.4 to –0.9) of the Sally Downs and Marble Downs suites, reflecting significant mantle contributions. These were emplaced synchronously with the Hooper Orogeny (ca. 1864–1845 Ma), and their geochemistry implies subduction-related magmatism. Together with aligned geophysical fabrics, these isotopic domains mark a first-order suture zone, where previously disparate terranes were stitched during final cratonisation.

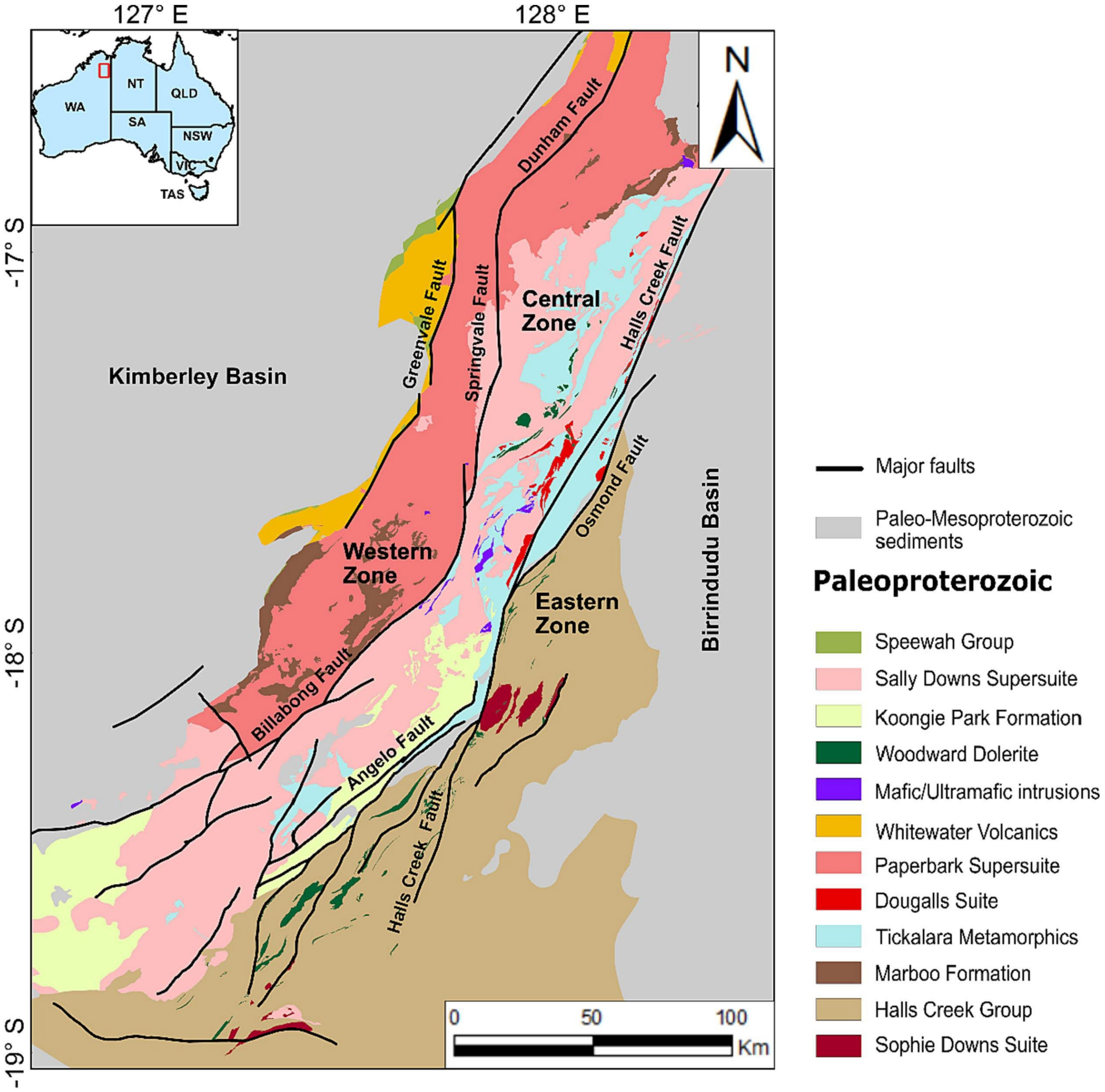

Figure 71. Geology map of the Halls Creek Block showing Paleoproterozoic lithologies and major terrane boundary faults based on a GIS synthesis of the North Australian Craton (Stewart et al., 2020).

These findings demonstrate that, while isotopically homogeneous at craton scale, the NAC is cut by cryptic discontinuities that reflect a complex assembly history. The Barramundi Orogeny (~1870–1850 Ma) was confirmed as a major crust-forming and reworking event, significantly contributing to the present configuration of the NAC (Page & Williams, 1988). Isotopic and geochronological datasets highlight the amalgamation of Archean basement domains with juvenile Paleoproterozoic additions, producing a composite lithosphere that preserved both ancient signatures and evidence of large-scale reworking (Kumwenda et al., 2023).

The recognition of Archean protoliths stitched together with Paleoproterozoic juvenile additions underscores the importance of inherited basement architecture. These boundaries acted as zones of mechanical weakness that were repeatedly reactivated during subsequent tectonic events, such as the Tanami and Stafford orogenies, influencing basin initiation and structural compartmentalisation (Li et al., 2014). Crustal-scale isotopic contrasts between blocks like Pine Creek, Tanami, and Tennant Creek reveal that these terranes were not simply coherent Archean nuclei but mosaics of domains with different mantle extraction ages, stitched along cryptic suture zones now masked beneath basin cover.

These inherited discontinuities exerted first-order controls on the location and development of Proterozoic basins such as McArthur, Isa and Tanami (Jackson et al., 2000; Rawlings, 1999). Their influence extended beyond simply providing accommodation space: pre-existing structural fabrics focused magmatism, fluid pathways, and sediment dispersal networks. For example, Nd–Hf isotopic signatures and zircon U–Pb ages from the Mount Isa and Pine Creek regions demonstrate that basin development was closely tied to the reactivation of crustal-scale faults, where mantle-derived magmas exploited isotopically juvenile corridors, while older, evolved crust promoted recycling and preservation (Bierlein et al., 2011).

The composite nature of the NAC also explains spatial variations in basin longevity and mineral prospectivity. Areas underlain by isotopically juvenile crust, such as those modified during the Barramundi Orogeny, often record enhanced subsidence histories and are associated with world-class base metal systems in the Isa Superbasin (Betts et al., 2006). In contrast, more evolved Archean domains appear to have acted as stable buttresses, localising deformation and influencing basin margins, as observed in the Pine Creek and Halls Creek regions.

6.1.3. Discussion

The synthesis of isotopic, geochronological and geophysical evidence refines the tectonic model for the NAC. It demonstrates that Archean crustal foundations, established around 2.5 Ga, were profoundly reconfigured during the Barramundi Orogeny, producing a craton that is broadly homogeneous but internally segmented by concealed sutures. These tectonic inheritances provided the structural template upon which Proterozoic basins were established and reactivated, directly impacting metallogenic fertility.

Recent reviews of NAC basement terranes highlight that while isotopic compositions of ca. 1870–1840 Ma magmatic rocks appear homogeneous across much of the craton, notable differences in structural styles and localised geophysical anomalies reveal cryptic discontinuities that represent deep-seated crustal boundaries (Kumwenda et al., 2023). These boundaries, often masked by basin cover, were repeatedly reactivated during subsequent tectonic cycles and controlled the geometry of basin development, subsidence patterns, and accommodation space for sediments.

Integrating aeromagnetic, gravity and seismic datasets with isotopic mapping has been particularly effective in resolving these hidden fabrics (Kumwenda et al., 2024). Forward modelling of potential-field data in the Tennant Creek region, for example, shows that major basement faults extend to mid-crustal depths and exert only a partial influence on overlying basins. Such work underscores the importance of distinguishing between structures that are crustal-scale sutures versus those that are shallow, basin-bounding features. This recognition has direct implications for exploration, as crustal-scale discontinuities tend to focus long-lived deformation and fluid flow, enhancing mineral system fertility (Iaccheri, 2019).

The recognition of Archean protoliths stitched together with Paleoproterozoic juvenile additions further illustrates the composite nature of the NAC. Similar isotopic heterogeneity is observed along its southern margin, where zircon U–Pb–Hf and Nd isotopic studies confirm that Paleoproterozoic supracrustal rocks were accreted to older Neoarchean nuclei, producing cryptic suture zones that are not apparent in surface geology (Iaccheri, 2019). Such results highlight the critical role of inherited basement structure in guiding the long-term tectonic and metallogenic evolution of the craton.

From an exploration perspective, integrated isotopic–geophysical methods significantly enhance predictive capability in underexplored terrains. By identifying crustal provinces beneath thick sedimentary cover, they allow correlation of concealed domains with exposed mineral provinces, providing vectors toward concealed mineral systems. This has wider global significance: similar approaches are increasingly applied in cratonic regions in Africa, Canada and India where isotopic domains, when tied to geophysical fabrics, reveal first-order controls on crustal growth and resource distribution (Wellman, 1988; Pryer & Connors, 2015).

Ultimately, the NAC provides a natural laboratory for evaluating how Archean–Proterozoic inheritance governs subsequent tectonic behaviour. The combination of crustal-scale isotopic mapping, high-resolution geophysics, and basin analysis demonstrates that cryptic sutures not only record continental assembly but also continue to influence lithospheric architecture for billions of years. In northern Australia, these structures exerted direct control on the localisation of the McArthur, Isa, and Tanami basins and on the development of associated world-class mineral systems, reaffirming the significance of inherited basement architecture as a long-lived control on continental growth, basin evolution and metallogenic fertility.

6.2. Link between basement faults and sedimentary basins

Basement faults are fundamental controls on the architecture and evolution of sedimentary basins. In the NAC, cryptic faults within concealed basement terranes have long been suspected of guiding basin localisation, influencing both the structural compartmentalisation of basins and the pathways of mineralising fluids. However, their geometry and tectonic significance remain poorly constrained beneath the thick Proterozoic cover sequences that dominate much of northern Australia (Betts & Giles, 2006; Li et al., 2014). These uncertainties limit our ability to fully reconstruct Proterozoic tectonic events and to predict the distribution of basins and associated mineral systems.

The Tennant Creek Block provides a critical natural laboratory to address these challenges. It preserves a unique record of the Warramunga Formation, a turbiditic sequence intruded by ca. 1860–1850 Ma felsic rocks of the Tennant Creek Supersuite, together with younger rift-related successions. This geological diversity makes it one of the few regions in the NAC where relationships between basement architecture and basin development can be directly observed at surface. Importantly, it also lies at the intersection of major craton-wide lineaments, where crustal-scale discontinuities are inferred to project beneath cover and exert long-lived tectonic control.

By combining geophysical mapping, forward modelling of aeromagnetic and gravity data, and isotopic constraints, this study aims to refine the geometry, distribution, and tectonic role of basement faults in the Tennant Creek region (Figure 72). This integrated approach allows us to move beyond surface observations and probe the concealed basement framework at crustal scale. The results not only improve our understanding of the structural template that influenced basin formation and evolution but also provide a foundation for predictive models of mineral system fertility across the NAC.

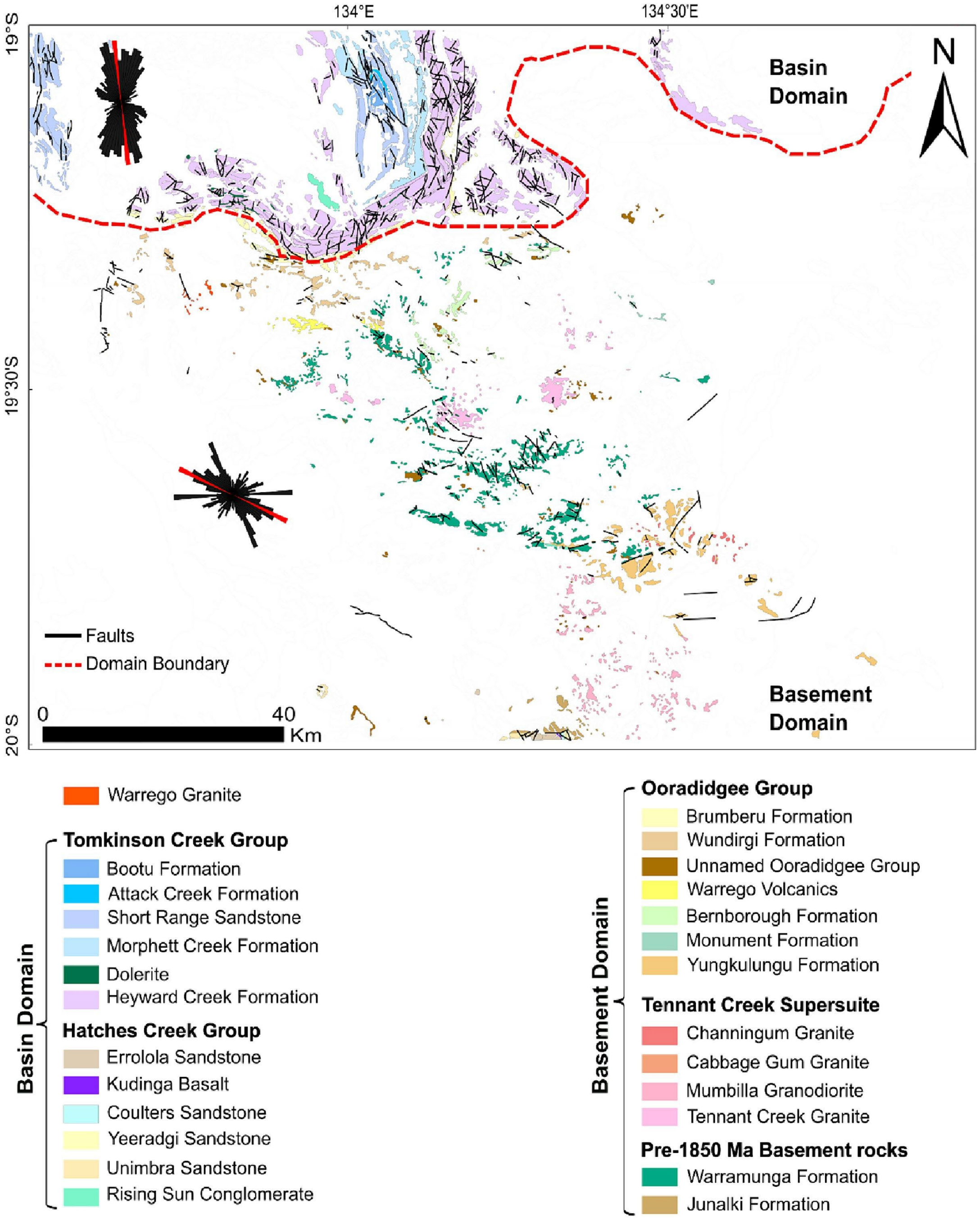

Figure 72. Simplified geology of the Tennant Creek Block showing basement lithologies and major faults.

6.2.1. Methodology

Aeromagnetic and gravity datasets were systematically analysed to characterise structural fabrics and fault domains across the Tennant Creek region (Figure 72). Data were processed using standard reduction-to-pole and tilt derivative filters, which enhance the continuity of linear anomalies and aid in identifying crustal structures beneath basin cover. Automated lineament extraction algorithms were applied to the processed aeromagnetic grids, highlighting a dominant WNW-trending fabric, together with subordinate N–S and NE-trending features. These extracted lineaments were subsequently cross-validated against mapped geology and known faults to reduce noise and minimise artefacts introduced during processing.

Forward modelling of potential-field data provided a three-dimensional perspective on crustal-scale architecture. Gravity anomalies were modelled using density contrasts derived from geological maps and constrained by available seismic reflection profiles (Figure 73). This approach allowed the imaging of deep-seated structures, such as crustal-scale shear zones and the geometry of sedimentary half-grabens, which are not readily resolved in surface mapping alone. Iterative refinement between gravity modelling and seismic interpretation improved confidence in the location and geometry of major fault systems, particularly those bounding the Tennant Creek inliers.

Isotopic datasets, including whole-rock Sm–Nd and zircon U–Pb ages, were integrated with the geophysical interpretations to discriminate between distinct basement domains (Figure 74). Negative εNd(t) values and older model ages (T_DM) were taken as indicators of reworked Archean crust, while more juvenile isotopic signatures marked Paleoproterozoic additions. These isotopic domains were then spatially correlated with the extracted lineaments, highlighting zones where isotopic boundaries coincide with geophysically mapped structures, consistent with the presence of long-lived sutures or reactivated crustal-scale faults.

Geological mapping from Pine Creek, Tanami and Halls Creek provided an independent validation framework for the integrated geophysical–isotopic model. By comparing surface geology with subsurface fabrics identified in potential-field models, it was possible to extrapolate tectonic domains beneath sedimentary cover, refining the structural and tectonic framework of the North Australian Craton.

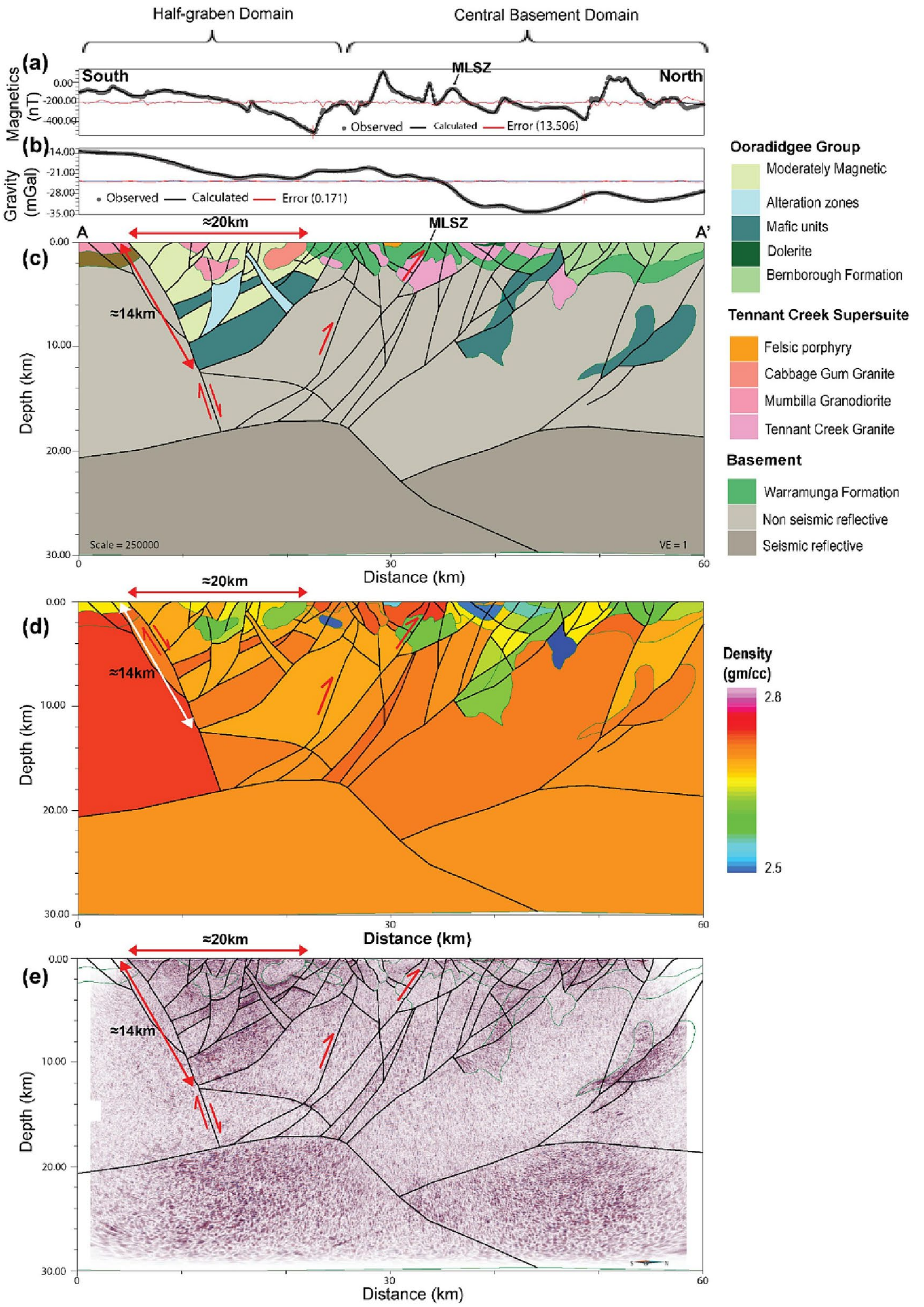

Figure 73. Forward modelled section (a) observed and calculated magnetic data, (b) observed and calculated gravity data, (c) modelled geological section, (d) density model, and (e) interpreted seismic section along (Line 101). MLSz along the profile stands for Mary Lane Shear zone.

6.2.2. Results and findings

The analysis reveals a strong spatial relationship between basement faults and basin architecture in the Tennant Creek Block. Three major basement domains (BD1–BD3) were identified on the basis of magnetic and gravity signatures (Figure 74). These domains are bounded by WNW-striking crustal faults that extend to depths of ~20 km, representing long-lived zones of weakness inherited from Paleoproterozoic orogenesis (Betts & Giles, 2006; Li et al., 2014). The integration of aeromagnetic and gravity data highlights that these crustal faults not only partition the basement into discrete domains but also coincide with changes in isotopic signatures, supporting their interpretation as terrane boundaries reactivated during later tectonic events (Kumwenda et al., 2023).

Forward modelling of potential-field data confirms the presence of a 20 km-wide, southward-deepening half-graben beneath the Ooradidgee Group (~1840 Ma), bounded by a northeast-dipping normal fault (Figure 74). The geometry of this half-graben indicates that early basin development was strongly controlled by basement anisotropies, with extensional reactivation of pre-existing Paleoproterozoic structures creating accommodation space (Rawlings, 1999; Betts et al., 2006). Seismic reflection profiles further support this interpretation, showing fault-bounded wedge geometries consistent with syn-sedimentary subsidence during Ooradidgee deposition (NTGS, 2019).

By contrast, younger basins such as the Tomkinson Creek Group (~1820–1740 Ma) exhibit a dominant north–south structural grain that is oblique to the older WNW-trending basement faults (Figure 74e). This shift in orientation reflects a change in regional stress regime during basin development, with limited reactivation of earlier faults. Instead, new fault sets nucleated under the prevailing N–S extension, giving rise to a structural fabric misaligned with the inherited basement domains (Jackson et al., 2000; Kumwenda et al., 2023). The histograms of fault trends (Figure 74e) illustrate this contrast clearly, with WNW-trending fabrics dominating the basement but N–S and NE-trending fabrics defining basin-scale architecture.

These results demonstrate that sedimentary basin development in the NAC is structurally controlled by inherited basement fault systems, but that the degree of reactivation varies with tectonic setting. Faults that played a dominant role in Warramunga and Ooradidgee basin formation were less influential in younger successions such as the Tomkinson Creek Group, reflecting evolving stress orientations and shifting tectonic drivers through time (Betts et al., 2006; Champion, 2013). This multi-phase tectonic inheritance highlights the composite nature of the Tennant Creek Block, where cryptic basement structures exerted a first-order influence on basin geometry but were variably expressed depending on the geodynamic regime.

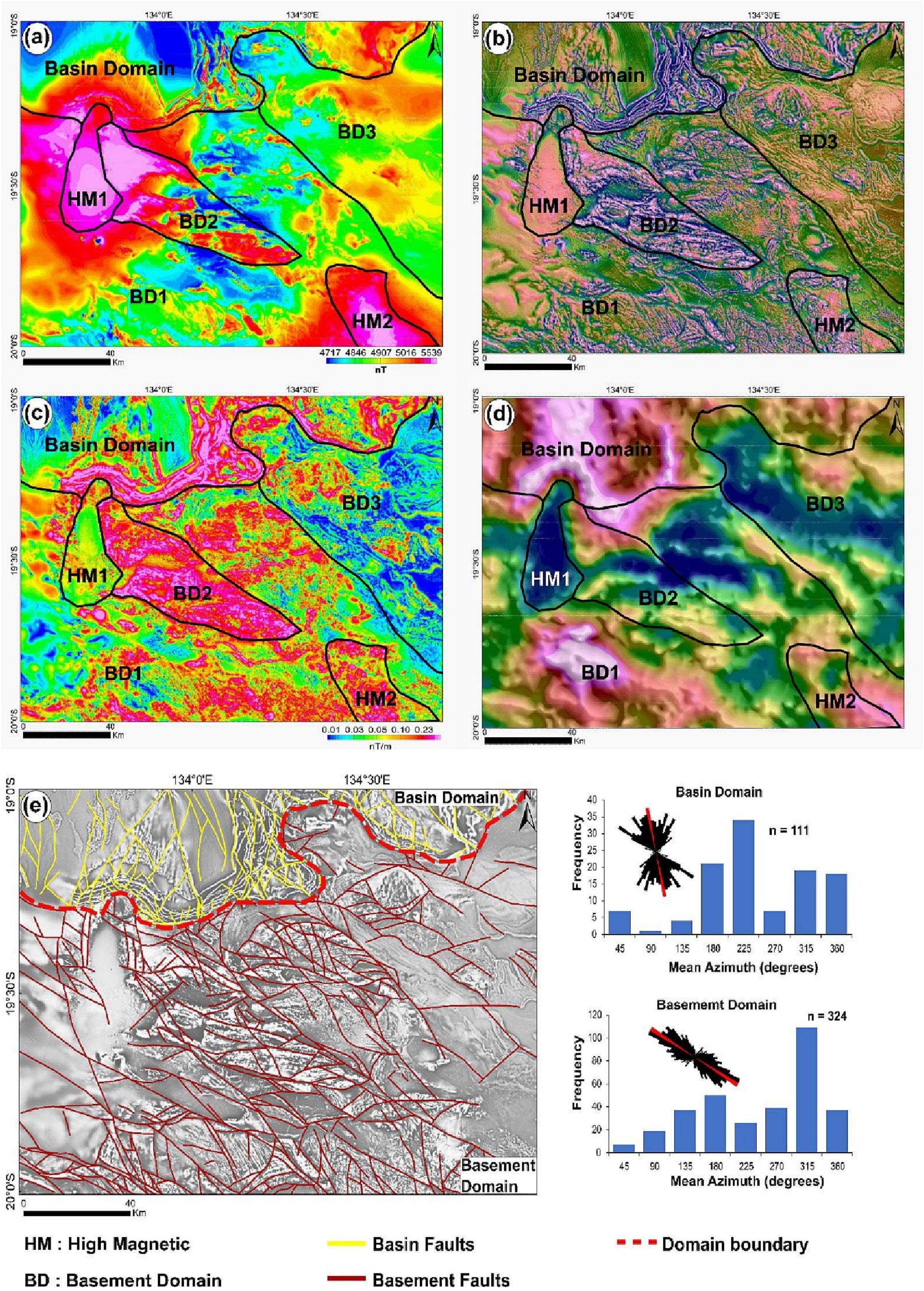

Figure 74. Geophysical domains of the Tennant Creek Block superimposed on (a) Reduced to Pole (RTP) magnetic map, (b) Tilt Derivative (TDR) of RTP grayscale (40% transparency draped on First Vertical Derivative (1VD) coloursheded map, (c) Analytical Signal (AS) of Total Magnetic Intensity (TMI) map, (d) TDR of upward continuation 500 m Bouguer grayscale draped on Bouguer coloursheded map and (e) Shows fault orientation between the basin and basement domain in the Tennant Creek Block. The histograms highlight the trend in the basin and the basement.

6.2.3. Discussion

The results from this study highlight the fundamental role of basement structures in shaping basin architecture and mineral system distribution in the Tennant Creek Block (Figure 67, Figure 72, Figure 74). The identification of WNW-striking basement faults as long-lived zones of weakness inherited from Paleoproterozoic orogenesis underscores their significance in guiding both basin formation and the localisation of metallogenic systems. These structures acted as primary templates during the development of early half-grabens, such as that beneath the Ooradidgee Group (~1840 Ma), where extensional reactivation of pre-existing fabrics created accommodation space. In contrast, the younger Tomkinson Creek Group (~1820–1740 Ma) exhibits a markedly different N–S structural grain, reflecting a shift in tectonic regime and a reduced influence of the inherited WNW-trending fabric. This transition demonstrates the dynamic interplay between inherited crustal anisotropies and changing regional stress fields through time, consistent with the multi-phase tectonic history of the NAC (Kumwenda et al., 2024; Clark et al., 2022).

A key implication of these findings is the recognition that inherited basement faults not only influenced basin subsidence patterns but also delineated isotopically distinct crustal domains. The coupling of geophysical interpretations with isotopic data (Nd and zircon U–Pb) reveals that structural boundaries often coincide with transitions between reworked Archean crust and juvenile Paleoproterozoic additions. Such crustal heterogeneities likely controlled the localisation of fluid pathways and mineralising systems, as observed in the Tennant Creek Au–Cu–Bi mineral field, where mineralisation is concentrated along reactivated basement faults (Johnstone, 2001; Betts et al., 2016). This reinforces the argument that geophysical–isotopic integration is an essential tool for exploration under cover, allowing concealed suture zones and fertile fault networks to be identified (Jiang et al., 2022).

At the craton scale, the findings contribute to a broader understanding of the NAC as a composite entity that, while isotopically homogeneous in bulk, is internally segmented by cryptic discontinuities (Kumwenda et al., 2023). These discontinuities, stitched during the Barramundi Orogeny (~1870–1850 Ma), continued to influence tectonic and basin evolution throughout the Proterozoic. Their reactivation under varying tectonic regimes highlights the longevity of inherited structures as first-order controls on basin distribution and mineral system fertility. Comparable patterns are documented in other Precambrian terranes globally, including the South Australian and Indian cratons, where basement faults beneath sedimentary cover act as enduring guides to tectonic and metallogenic development (Armit, 2016; Clark et al., 2022).

From a resource perspective, these insights are highly significant. The localisation of mineral systems in the Tennant Creek Block, particularly ironstone-hosted Au–Cu–Bi deposits, is intimately tied to the geometry and reactivation history of basement faults (Rattenbury, 1994; Large et al., 1988). Magnetotelluric studies further indicate that such faults acted as deep crustal to lithospheric-scale conduits, linking fertile mantle or lower-crustal reservoirs with depositional sites in the upper crust (Jiang et al., 2022). This supports a holistic mineral systems model in which inherited structural fabrics not only governed basin subsidence but also served as long-lived fluid pathways, enhancing the metallogenic fertility of the region.

Overall, the Tennant Creek Block exemplifies the importance of inherited basement architecture in Precambrian terranes. By combining aeromagnetic and gravity datasets with isotopic and geochronological constraints, this study refines our understanding of the NAC as a craton shaped by repeated cycles of reactivation, refertilisation, and overprinting. The approach demonstrates the predictive power of integrated isotopic–geophysical methods for mapping concealed crustal boundaries, with direct applications for exploration targeting in underexplored regions of northern Australia and beyond.

6.3. Lineament analysis and crustal architecture of the NAC

The NAC represents one of the largest preserved Precambrian provinces globally, yet much of its internal basement architecture is obscured beneath Paleoproterozoic to Phanerozoic basins (Figure 65). Although scattered inliers such as Pine Creek, Arnhem Land, Tennant Creek, Tanami, Halls Creek, and Mount Isa provide critical exposure, they offer only fragmented insights into the crustal mosaic of the proto-NAC. This poor exposure has long complicated efforts to identify terrane boundaries, delineate sutures, and reconstruct the tectonic evolution of the craton (Betts et al., 2016; Cawood & Korsch, 2008).

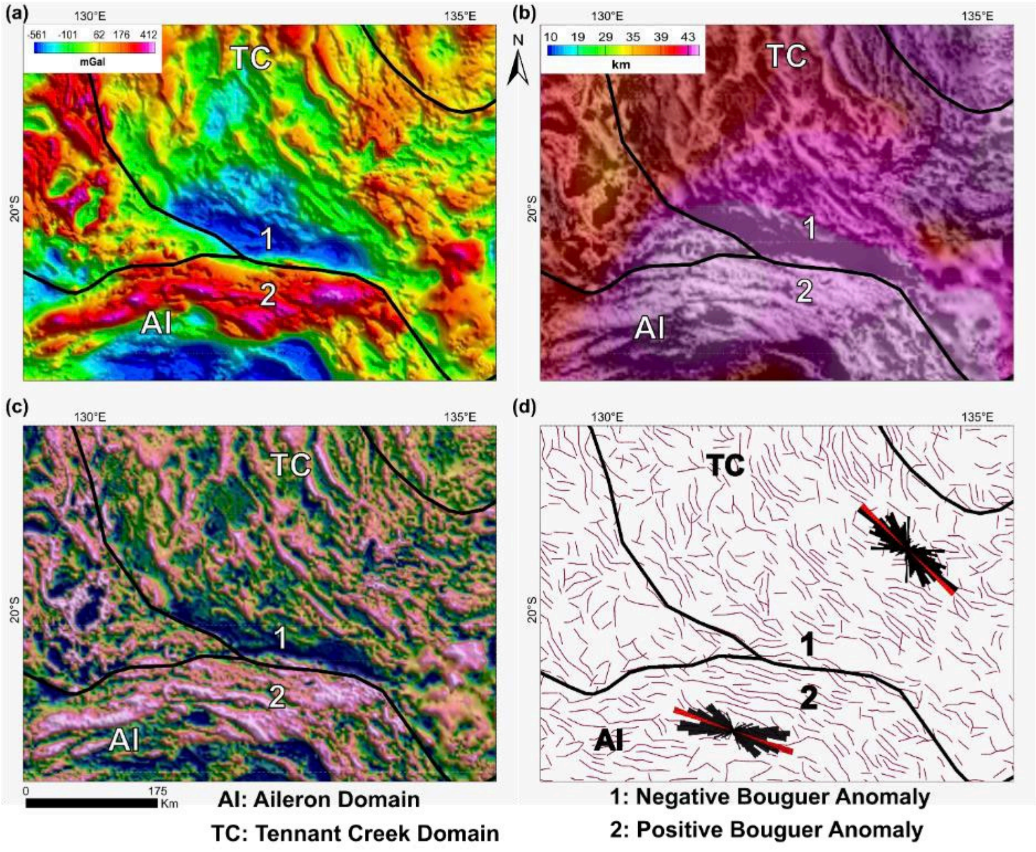

Figure 75. Mapping domain boundaries using lineaments, paired gravity anomalies and crustal thickness. Interpreted domain boundaries (black lines) superimposed on (a) Bouguer Gravity map, (b) 1VD Bouguer Gravity map (grayscale, 50% transparency) overlain on Moho map (colour), (c) TDR Bouguer Gravity map (grayscale, 50% transparency) overlain on 1VD Bouguer Gravity (colour), in order to highlight anomaly trend, and (d) Lineaments extracted from 1VD Upward Continuation (500 m) Bouguer Gravity map. The rose diagrams highlight the trend of lineaments within the domains.

In such covered terranes, geophysical datasets provide a powerful alternative. High-resolution gravity and aeromagnetic surveys reveal long-wavelength anomalies that can be transformed to highlight discontinuities associated with major lithospheric boundaries (Dentith & Mudge, 2014; Gunn et al., 1997). These linear features, or lineaments, reflect crustal faults, shear zones, and sutures that have acted as persistent zones of weakness, repeatedly reactivated through successive tectonic cycles (McDonald et al., 1997; Champion, 2013). Lineament analysis—using both manual interpretation of derivative grids and automated extraction algorithms—enables systematic mapping of such basement structures and the recognition of domain boundaries within the concealed NAC (Figure 75 and Figure 76).

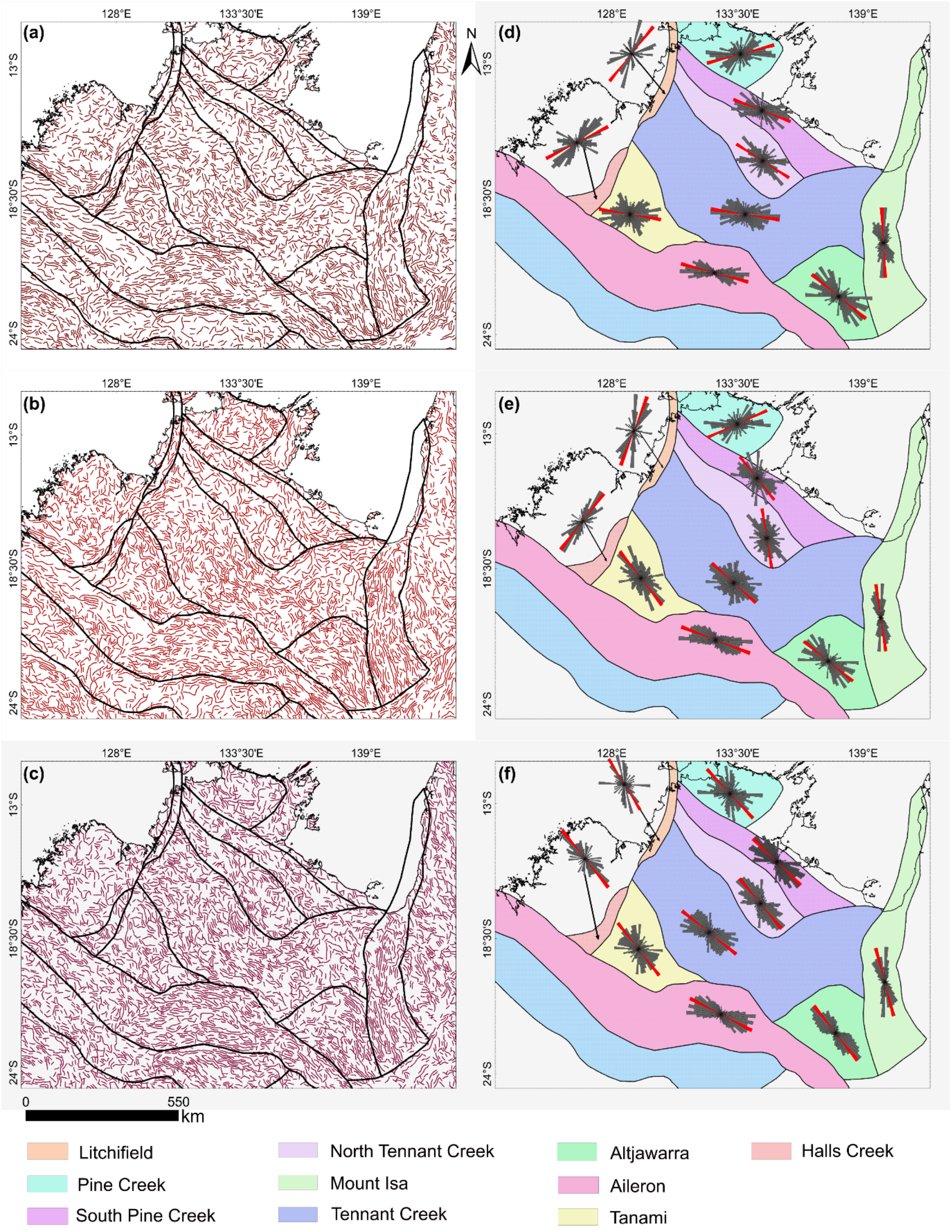

Figure 76. The geophysical domains of the North Australian Craton superimposed on (a) lineaments extracted from 1VD of upward continued (500 m) magnetic grid, (b) lineaments extracted from 1VD of upward continued (1500 m) magnetic grid, (c) lineaments extracted from 1VD of upward continued (500 m) Bouguer gravity grid rose diagrams representing the trend of lineaments extracted from 1VD upward continued (500 m) RTP magnetic grid superimposed on each domain. Adjacent maps show the trend of lineaments in each domain represented by rose

diagrams, (d) map representing the trend of lineaments for Figure (a), (e) map showing the trend of lineaments corresponding to Figure (b), (f) map showing the trend of lineaments for Figure (c).

Geophysical studies across Australia have demonstrated the value of integrating potential field lineament mapping with isotopic and geochronological datasets to resolve concealed crustal blocks (Betts et al., 2003; Crawford et al., 2010). Within the NAC, this approach has identified a series of WNW–NW trending basement fabrics (Figure 77; Figure 78) that correlate with crustal-scale sutures separating distinct domains such as Pine Creek, Arnhem, North Tennant, Tennant Creek, and Tanami–Altjawarra (Figure 79). Importantly, many of these features coincide with basin margins and metallogenic belts, highlighting the structural control that inherited crustal fabrics exert on both basin geometry and mineralisation (NTGS, 2019; Huston et al., 2020).

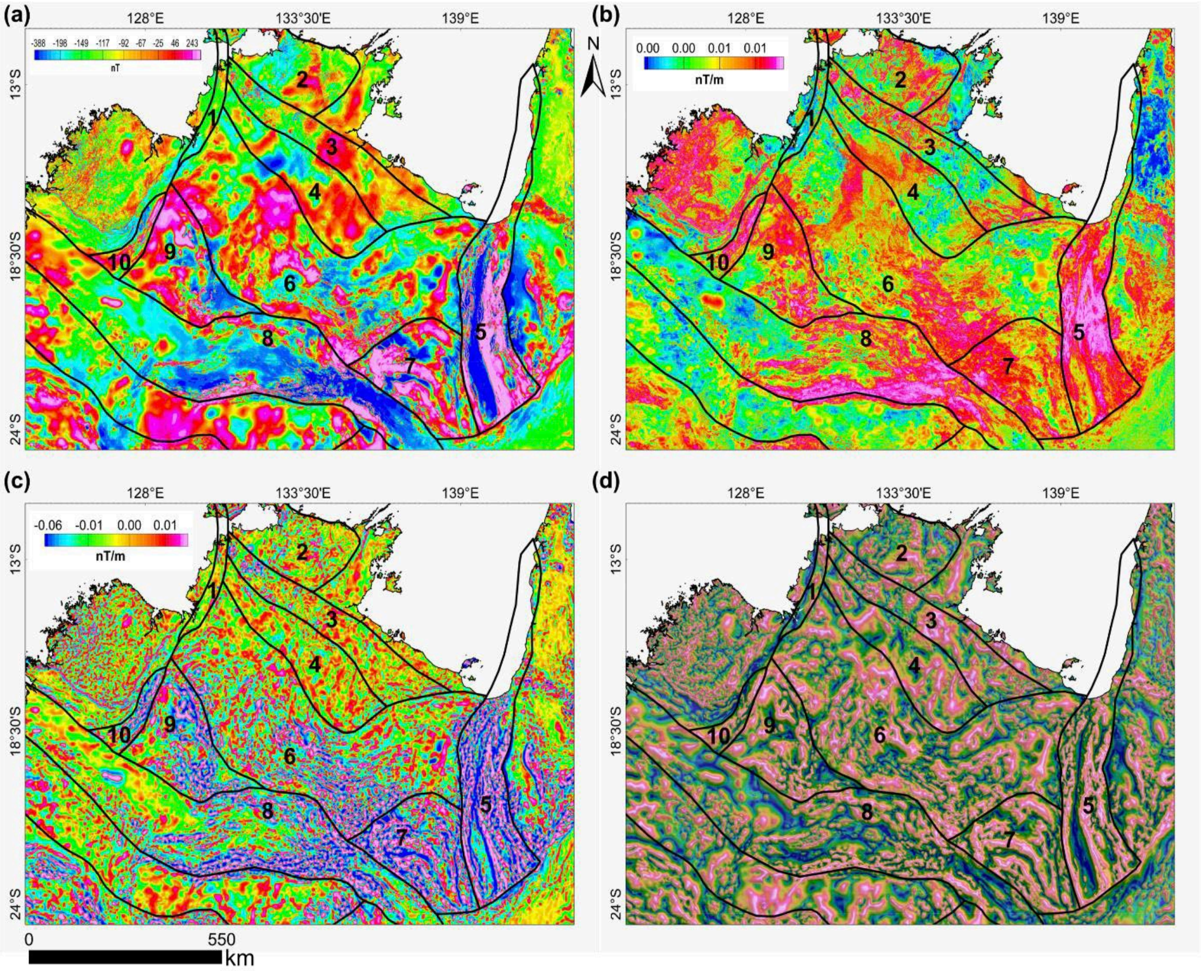

1. Litchfield
2. Pine Creek
3. South Pine Creek
4. North Tennant Creek
5. Mount Isa
6. Tennant Creek
7. Altjawarra
8. Aileron
9. Tanami
10. Halls Creek

Figure 77. Geophysical domains of the North Australian Craton superimposed on (a) coloured RTP magnetic map, (b) Analytic Signal of TMI magnetic map, (c) AGC of 1VD RTP magnetic map, (d) First vertical derivative (1VD) of upward continued (5 km) RTP magnetic map (grayscale 50% transparency) overlain on Tilt derivative (TDR) map of upward continued (5 km) (colour) magnetic map. The grids were upward continued to 5 km to enhance long wavelength features in the data.

In this section, we expand upon earlier syntheses by integrating geophysical lineament analysis, forward modelling of gravity and magnetic datasets, and isotopic correlations to refine the crustal architecture of the NAC. The results provide new constraints on the spatial distribution of crustal domains, the geometry of their boundaries, and the staged tectonic assembly of the proto-craton during the late Archean and Paleoproterozoic.

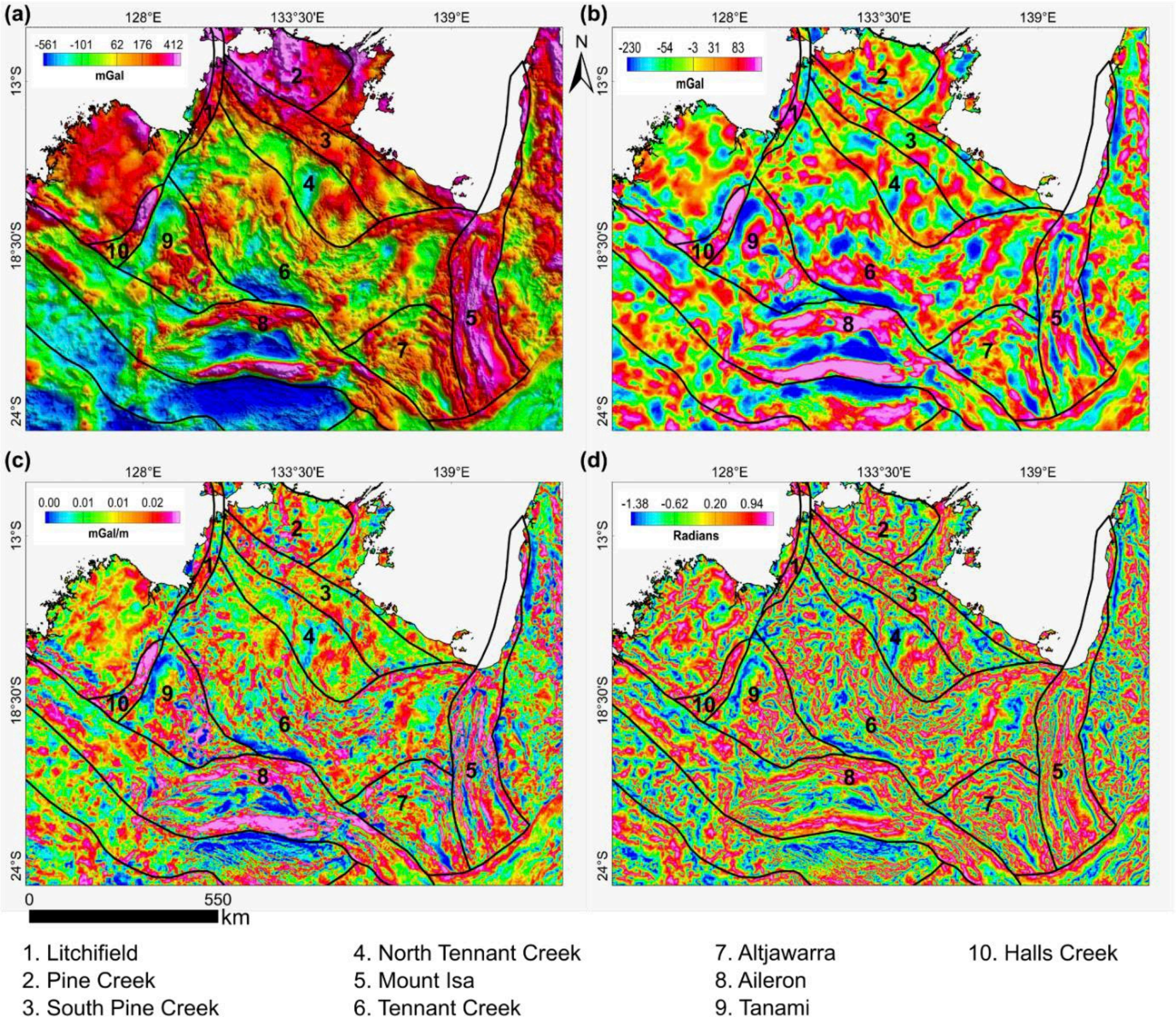

Figure 78. Geophysical domain of the North Australian Craton superimposed on gravity grids (a) coloured Bouguer gravity map, (b) Band pass (5-200 km wavelength) filtered Bouguer gravity map (pseudocolour), (c) First vertical derivative (1VD) of upward continuation (1000 m) pseudocolour gravity map, (d) Tilt derivative (TDR) of upward continuation (1000 m) gravity map.

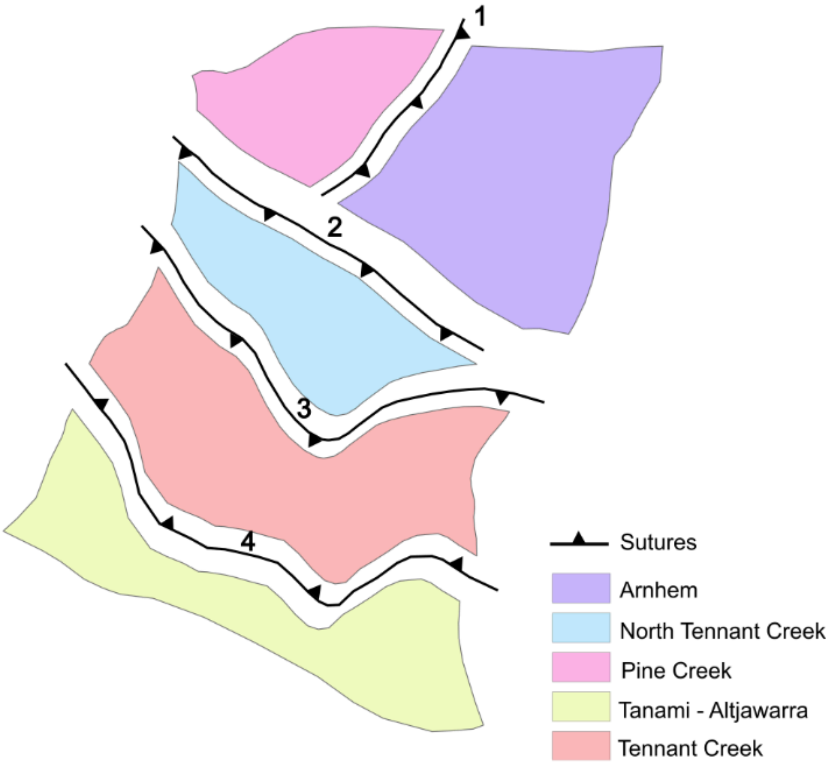

Figure 79. Proposed geophysical domains and location of sutures within the interior of North Australian Craton. Numbers 1-4 represent boundaries: (1) Pine Creek and Arnhem, (2) Pine Creek-Arnhem and North Tennant Creek, (3) North Tennant Creek and Tennant Creek, (4) Tennant Creek and Tanami-Altjawarra.

6.3.1. Methodology

The concealed basement architecture of the NAC was investigated using a combined geophysical and geological workflow. This approach integrated processing of regional-scale gravity and magnetic datasets, lineament analysis, forward modelling, and isotopic correlation to constrain crustal domains and their boundaries.

6.3.1.1. Geophysical data processing

High-resolution gravity and magnetic datasets were sourced from Geoscience Australia and the Northern Territory Geological Survey. To enhance structural trends, grids were processed using first vertical derivative (1VD), tilt derivative (TDR), analytic signal, and upward continuation filters. These transformations emphasise lateral variations in density and magnetisation, enabling subtle basement features to be detected against regional trends (Gunn et al., 1997; Dentith & Mudge, 2014).

6.3.1.2. Lineament extraction

Both manual and automated techniques were applied to identify basement structures. Manual interpretation was performed on derivative grids to delineate continuous linear anomalies consistent with faults and terrane boundaries (McDonald et al., 1997). Automated extraction, using directional filtering and edge-detection algorithms (Farahbakhsh et al., 2018; O'Leary et al., 1976), provided an unbiased dataset of lineaments that were then analysed for orientation and spatial density. Rose diagrams summarised dominant structural trends, allowing comparison across basement domains (Figure 78).

6.3.1.3. Forward modelling

Selected gravity and magnetic profiles were forward modelled to test the depth extent and geometry of major structures. Models constrained by seismic reflection data provided estimates of fault dip, crustal thickness, and density contrasts between basement blocks. This approach helped to resolve large-scale features such as half-graben geometries and steeply dipping terrane-bounding faults, which are not always evident in map-view datasets.

6.3.1.4. Integration with isotopic and geochronological datasets

Geophysical interpretations were cross-checked with U–Pb geochronology and Sm–Nd isotopic data from granitoid and sedimentary rocks. Correlation of geophysical sutures with isotopic breaks and distinct magmatic provinces provided independent confirmation of crustal domains (Champion, 2013; Betts et al., 2016). This integration reduced ambiguity inherent in potential field interpretation and anchored the geophysical architecture of the NAC within its tectonic evolution.

6.3.2. Results and findings

The geophysical analysis demonstrates that the crust of the North Australian Craton is dissected by an extensive array of linear features, dominated by WNW–NW-trending structures with subordinate NE-oriented fabrics. These lineaments are evident in both aeromagnetic and gravity datasets, where they appear as continuous high-gradient anomalies extending for tens to hundreds of kilometres (Figure 78). Depth-to-source estimates and forward modelling confirm that many of these features dip steeply and can be traced to depths of 15–25 km (Figure 73), consistent with crustal-scale fault zones rather than shallow discontinuities (Gunn et al., 1997; Dentith & Mudge, 2014).

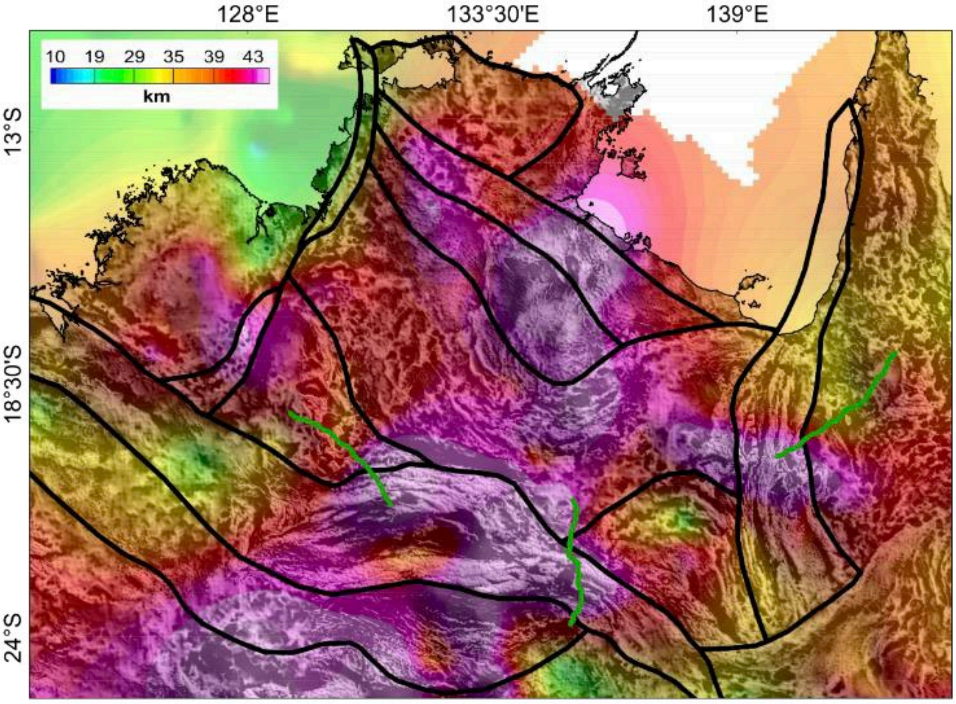

Figure 80. Interpreted geophysical domains of the interior of the North Australian Craton overlain on the first vertical derivative (1VD) Bouguer gravity map (grayscale 50% transparency) superimposed on the Moho map (Colour). The green lines cutting across the boundaries represent crustal scale seismic reflection lines.

By integrating lineament maps with potential field grids, five major crustal elements can be defined within the proto-NAC: Pine Creek, Arnhem, North Tennant, Tennant Creek, and Tanami–Altjawarra. The boundaries between these blocks are rarely exposed at the surface but are clearly resolvable geophysically. They are expressed as sharp magnetic and gravity gradients, in some cases paired positive–negative anomalies, interpreted as marking deep-seated crustal breaks (Figure 79 and Figure 80). For example, the boundary between the Pine Creek and Arnhem elements is marked by a prominent northeast-trending magnetic lineament, while the contact between North Tennant and Tennant Creek is associated with a composite gravity–magnetic anomaly that can be traced across several hundred kilometres. These findings highlight the ability of geophysical methods to resolve domain boundaries that remain cryptic in the field (Betts et al., 2003; Champion, 2013).

Gravity modelling provides additional constraints on the internal structure of these domains. Profiles across key boundaries show that crustal thickness varies substantially, with domains containing both relatively dense, reworked Archean basement and lower-density, juvenile Paleoproterozoic additions. Fault-controlled geometries are particularly clear in the Tennant Creek region, where modelling reveals sharp density contrasts across domain boundaries. Several of these fault zones spatially coincide with granitoid plutons and known mineralised belts, indicating that basement structures exerted a strong control on subsequent magmatism and metallogenesis (Huston et al., 2020).

A striking example of these relationships is provided by the Ooradidgee half-graben, imaged in the eastern Tennant Creek region. Forward modelling indicates that the graben is ~20 km wide and up to ~14 km deep, with its depocentre filled by Paleoproterozoic Ooradidgee Group sediments. The structure is bounded by a major northeast-dipping normal fault, which is also expressed as a pronounced magnetic and gravity gradient. The geometry of the Ooradidgee half-graben illustrates the close coupling between basement lineaments and basin development, demonstrating how fault-controlled accommodation space governed early Proterozoic sedimentation (Betts et al., 2004).

Taken together, these results show that the NAC basement comprises a heterogeneous mosaic of crustal blocks separated by steep, through-going fault systems. These structures are clearly expressed in geophysical datasets even where surface exposure is lacking, underscoring the value of potential field methods for reconstructing basement architecture beneath extensive sedimentary cover. The ability to resolve block geometries, fault dips, and crustal thickness variations directly from geophysical modelling provides a robust foundation for interpreting the assembly and subsequent evolution of the NAC, which is explored further in the discussion.

6.3.3. Discussion

The geophysical results presented above reveal a basement architecture for the NAC that is both highly structured and deeply inherited. The dominance of WNW–NW-trending faults, together with subsidiary NE-trending features, indicates that the crust was dissected early by steep, through-going structures extending to mid- and lower-crustal depths. These lineaments are interpreted as long-lived sutures and terrane boundaries, many of which originated during the assembly of the proto-NAC and were reactivated during subsequent tectonic events (McDonald et al., 1997; Champion, 2013). Their persistence across multiple orogenic cycles underscores the importance of inherited lithospheric fabrics in shaping cratonic architecture.

The definition of five major crustal elements—Pine Creek, Arnhem, North Tennant, Tennant Creek, and Tanami–Altjawarra—supports a model of polyphase assembly in which Archean crustal nuclei were sutured to juvenile Paleoproterozoic additions during the Barramundi Orogeny (1900–1800 Ma). This interpretation is consistent with isotopic studies that demonstrate marked Nd model age contrasts across these boundaries (Champion, 2013), as well as U–Pb geochronology that documents magmatic and metamorphic events contemporaneous with terrane amalgamation (Betts et al., 2016). The steeply dipping, crustal-scale faults imaged in this study represent the fossil sutures of these accretionary processes, and their continued expression in the geophysical data highlights their lithospheric significance.

The results also show that these inherited sutures exerted a first-order influence on the localisation of later basins and magmatism. The Ooradidgee half-graben provides a compelling example: its bounding fault coincides with a geophysically resolvable crustal boundary, suggesting that Paleoproterozoic extension exploited pre-existing zones of weakness. This relationship mirrors observations elsewhere in northern Australia, where Proterozoic basins frequently nucleated along inherited basement structures (Betts et al., 2004; NTGS, 2019). The waning influence of these fabrics on younger basins, such as the Tomkinson Creek Group, suggests a progressive shift in tectonic regime, from one dominated by reactivation of deep-seated sutures to one controlled more by intraplate stresses and lithospheric thinning.

Inherited basement architecture also had direct implications for mineral system development. Several major mineral provinces of the NAC—including Pine Creek, Tennant Creek, and Tanami—are spatially coincident with the crustal sutures and block boundaries defined in this study. This spatial correlation reinforces the concept that crustal-scale faults acted as pathways for hydrothermal fluids and loci for magmatic intrusions, thereby controlling the distribution of mineralisation (Huston et al., 2020). The strong structural control demonstrated here underscores the importance of integrating geophysical mapping of basement fabrics into metallogenic models for northern Australia.

More broadly, the NAC offers an instructive analogue for other covered cratonic regions. Similarities can be drawn with the Dharwar Craton in India and the Zimbabwe Craton in Africa, where potential field studies have likewise revealed cryptic sutures and basement fabrics that control both basin evolution and metallogenic fertility. The NAC case study demonstrates how inherited lithospheric structures, though concealed beneath thick cover, can be resolved using modern geophysical methods and shown to play a decisive role in shaping crustal evolution and mineral system potential.

In summary, the discussion highlights three key insights: (1) the NAC basement reflects a polyphase assembly of Archean and Paleoproterozoic domains along crustal-scale sutures; (2) these inherited fabrics strongly influenced subsequent basin development and mineralisation; and (3) the NAC provides a broader template for interpreting concealed cratonic terranes globally. These findings reinforce the value of integrated geophysical and isotopic approaches in reconstructing the architecture and evolution of covered cratons.

6.4. Discussion

The multi-disciplinary investigation of the NAC presented in this section highlights the complex, composite nature of one of Earth’s largest preserved Precambrian provinces. By integrating isotopic, geochronological, geological, and geophysical datasets, a clearer picture of the craton’s crustal architecture has emerged: one in which Archean foundations were repeatedly reworked, amalgamated with Paleoproterozoic juvenile additions, and segmented by cryptic but long-lived sutures that continue to shape its tectonic and metallogenic evolution.

The isotopic and geochronological record (Section 6.1) confirms that the NAC preserves a major phase of Archean crustal growth around 2.5 Ga, which subsequently acted as the protolith for large-scale reworking during the Barramundi Orogeny (~1870–1850 Ma). Nd isotopic values, zircon U–Pb ages, and inherited zircon populations demonstrate that Archean crust was stitched to younger juvenile additions, forming a composite lithosphere. The identification of isotopically distinct domains, such as Pine Creek, Tanami, and Halls Creek, highlights that the NAC is not a uniform block but a mosaic of terranes, separated by deep crustal boundaries that correlate with major geophysical features.

Geophysical and isotopic integration (Section 6.2) shows that these boundaries exerted a profound influence on basin development. In the Tennant Creek region, WNW-trending basement faults were repeatedly reactivated, creating accommodation space for Paleoproterozoic basins such as the Ooradidgee half-graben. Forward modelling demonstrates that these faults extend to mid-crustal depths and coincide with isotopic contrasts, confirming their interpretation as terrane-bounding sutures. Importantly, their influence on basin geometry diminished in younger successions such as the Tomkinson Creek Group, reflecting changes in the regional stress regime and a transition away from structural inheritance toward intraplate-controlled extension. This highlights the dynamic interplay between inherited lithospheric fabrics and evolving tectonic drivers across Proterozoic time.

The broader geophysical analysis of the NAC (Section 6.3) places these findings in a craton-wide context. Lineament extraction and potential-field modelling reveal a dense network of WNW–NW-trending structures, many of which dip steeply and extend to depths of 15–25 km. These features define at least five major crustal elements—Pine Creek, Arnhem, North Tennant, Tennant Creek, and Tanami–Altjawarra—separated by sutures resolvable only in geophysical datasets. The geometry and persistence of these fabrics show that the craton's present-day architecture is the cumulative product of Archean crustal growth, Paleoproterozoic accretion, and repeated reactivation of inherited structures.

Collectively, these results emphasise three key themes. First, the NAC's architecture reflects a polyphase assembly in which Archean nuclei were amalgamated with Paleoproterozoic juvenile terranes along crustal-scale sutures. Second, these inherited fabrics exerted long-lived controls on basin evolution, fluid pathways, and mineralisation, with structures such as the Ooradidgee half-graben providing clear examples of fault-controlled sedimentation. Third, the NAC serves as an analogue for other covered cratonic regions globally, such as India and Africa, where isotopic and geophysical datasets similarly reveal cryptic basement fabrics that govern tectonic and metallogenic processes.

From an applied perspective, the integration of isotopic and geophysical methods enhances predictive capability in mineral exploration. By correlating isotopic provinces with concealed geophysical domains, the study identifies fertile structures that not only influenced Proterozoic basin development but also controlled mineral system localisation. This holistic view demonstrates that basement inheritance is not simply a record of ancient tectonics but an active driver of metallogenic fertility across geological time.

The NAC can be understood as a structurally segmented, isotopically heterogeneous, and metallogenically fertile craton, whose present-day form reflects the interplay of Archean foundations, Paleoproterozoic accretion, and the long-lived influence of inherited basement fabrics. The combined insights from isotopic, geochronological, and geophysical approaches underscore the enduring value of multidisciplinary investigations for unravelling the evolution of concealed Precambrian terranes and for guiding resource exploration in covered cratonic provinces worldwide.

7. Conclusions

This study provides comprehensive and predictive assessment of the crustal architecture, basin evolution, and metallogenic framework of the NAC. By integrating isotopic, geochronological, geological, geophysical, analogue, and numerical modelling datasets, it demonstrates that the NAC is a polyphase, composite craton in which Archean foundations were repeatedly reworked and amalgamated with Paleoproterozoic juvenile terranes during major orogenic events such as the Barramundi Orogeny (~1870–1850 Ma, Champion, 2013; Betts et al., 2016). These amalgamation processes stitched together isotopically and structurally distinct blocks, producing cryptic sutures that are now resolvable through potential-field data, forward geophysical modelling, and Nd–Hf isotopic contrasts (Kumwenda et al., 2023; Iaccheri, 2019).

High-resolution gravity and magnetic datasets, jointly modelled with seismic constraints, resolve the three-dimensional architecture of the NAC at crustal and lithospheric scales. Forward models across the Tennant Creek Block show that WNW-trending basement faults dip steeply to depths of ~18–25 km, where they coincide with isotopic boundaries, confirming their interpretation as long-lived terrane sutures. These models capture density contrasts between Archean and Paleoproterozoic domains, quantifying the heterogeneous crustal makeup of the NAC. The Ooradidgee half-graben provides a striking example: potential-field forward models, locally constrained by seismic reflection profiles, reveal a 20 km-wide, southward-deepening basin bounded by a northeast-dipping normal fault that offsets basement by ~14 km and extends to mid-crustal depths. Within this wedge, seismic reflectivity and magnetic susceptibility variations map mafic packages and alteration zones, demonstrating how inherited basement anisotropies were reactivated to create accommodation space during Paleoproterozoic extension. The Warramunga Formation, modelled with densities of 2.61–2.74 g/cm^3 and magnetic susceptibilities up to 0.008 cgs, illustrates how forward modelling resolves both the depth and internal complexity of deformed crustal blocks. At the lithospheric scale, integration with seismic tomography and gravity inversions shows that the NAC is underlain by a cold, depleted mantle with low effective elastic thickness (<20 km), implying a decoupled crust–mantle system conducive to lower crustal flow. Taken together, these results demonstrate that geophysics is not merely descriptive but predictive: it bridges surface geology, isotopic mapping, and deep lithospheric structure, revealing how crustal inheritance and lithosphere-scale architecture govern basin nucleation, inversion, and mineral system fertility.

The NAC is exceptional in preserving five superimposed, unconformity-bound basins between ca. 1800–1300 Ma (the Redbank, Glyde, Favenc, and Wilton packages and their equivalents). Their architecture records repeated episodes of extension, uplift, and inversion (Allen & Allen, 2005). Analogue modelling validates that such geometries could evolve from oblique extension across inherited weaknesses, producing en-echelon and multi-directional faults comparable to those in the Isa Superbasin and Tennant Creek regions (Betts et al., 2004; Aitken & Betts, 2009). Importantly, these experiments demonstrate that the same inherited faults could accommodate both extension and later inversion, eliminating the need to invoke entirely new fault systems for successive tectonic phases.

Numerical simulations undertaken in this study further reveal that Proterozoic basins cannot be understood through the lens of modern analogues. Unlike younger Phanerozoic basins, they developed within a hotter, weaker lithosphere strongly influenced by Archean–Paleoproterozoic inheritance. The models show that oblique extension alone can generate complex, multi-directional fault networks that mimic the overprinting of multiple tectonic events. Inherited weaknesses were capable of accommodating both extension and subsequent inversion under shifting stress regimes, producing geometries that have long been misinterpreted as evidence for distinct orogenies. This finding compels a critical re-evaluation of Proterozoic basin histories and highlights the need for tectonic models that explicitly account for early Earth rheology, lithospheric inheritance, and oblique plate motions.

Magnetotelluric (MT) imaging adds a deep lithospheric dimension to the geophysical framework. Vertically integrated, low-resistivity conductors align with crustal-scale sutures and basin boundaries. These are interpreted as mantle-tapping corridors linking metasomatised lithosphere to the upper crust, explaining why world-class mineral systems such as Mount Isa Pb-Zn, Ernest Henry Cu, and Tennant Creek Au-Cu are spatially associated with basement discontinuities (Heinson et al., 2006; Huston et al., 2020; Betts et al., 2006). Together, forward geophysical modelling and MT imaging provide a coherent picture from crust to lithosphere, uniting isotopic, structural, and metallogenic observations into a single tectonic framework.

The integration of approaches in this study demonstrates the transformative potential of Predictive Integrated Data Exploration (pide). By synthesising isotopic, geophysical, analogue, and numerical datasets, pide not only resolves concealed crustal architecture but also quantifies tectonic inheritance and identifies fertile structures under cover. More than a descriptive tool, it provides a predictive framework for basin analysis and mineral exploration that is transferable to other covered cratonic provinces such as the Dharwar (India), Zimbabwe, and Superior (Canada).

The broader synthesis confirms that NAC basins were not isolated entities but part of an interconnected Proterozoic system extending into the Gawler Craton, Curnamona Province, and Aileron Province Figure 78; Li et al., 2014). Their evolution is best explained within a plate-tectonic framework involving north-dipping subduction, rollback, and back-arc extension rather than simple intraplate subsidence (Cawood & Korsch, 2008). Structural inheritance interacted with these far-field geodynamic drivers to shape basin geometries, stratigraphic segmentation, and metallogenic fertility.

Implications for the NAC

- Polyphase assembly and concealed sutures — The NAC formed through successive accretion of Archean and Paleoproterozoic terranes stitched along lithospheric-scale sutures. These boundaries remain cryptically preserved in isotopic and geophysical datasets (Champion, 2013; Betts et al., 2016) and continue to partition the crust into distinct structural and isotopic domains.
- Inherited control on basin evolution — Reactivated crustal-scale faults provided the structural framework for half-graben nucleation, basin inversion, and stratigraphic segmentation across key basins such as McArthur, Isa, and Tanami. Geophysical forward modelling constrains their geometry, while analogue and numerical models replicate their behaviour, demonstrating that oblique tectonics alone can generate fault patterns historically attributed to multiple tectonic events (Betts & Giles, 2006; Kumwenda et al., 2023).

- Metallogenic fertility from deep lithospheric structure — Magnetotelluric imaging shows that inherited sutures are vertically integrated into the lithosphere, functioning as long-lived conduits for magma and fluids. Their repeated reactivation directly correlates with the localisation of world-class mineral systems such as those at Tennant Creek, Isa, and Tanami (Huston et al., 2020; Jiang et al., 2022).

Broader implications for Proterozoic basins

- Craton growth through inheritance — Proterozoic basins worldwide reflect the same polyphase assembly and concealed sutures, showing that early cratons are mosaics of reworked Archean and juvenile Paleoproterozoic crust. This inheritance is fundamental to any tectonic model.
- Rethinking basin evolution — Numerical and analogue models confirm that oblique extension across inherited fabrics can mimic multi-event tectonic histories. This finding forces a re-evaluation of long-standing interpretations and demonstrates that Proterozoic basins cannot simply be read through modern analogues.
- Deep lithosphere–mineralisation link — The NAC shows that metasomatised, vertically integrated lithospheric corridors are critical for focusing fluids and enhancing mineral fertility. This provides a predictive framework for exploration in other covered cratonic provinces (e.g., Dharwar, Zimbabwe, Superior), where similar deep structures likely controlled basin evolution and mineral system localisation.

Ultimately, this study shows that Precambrian cratons are not static blocks but dynamic systems, where inherited lithospheric fabrics govern tectonics, basin evolution, and mineralisation over billions of years. By demonstrating that Proterozoic basins must be interpreted on their own terms, not through modern analogues, this work reshapes our understanding of early Earth tectonics and provides a powerful predictive foundation for mineral exploration in covered terrains worldwide.

8. Recommendations for Further Work

The findings of this study provide a robust foundation for understanding the crustal architecture, basin evolution, and metallogenic framework of the North Australian Craton (NAC). However, several important avenues remain for future research to refine these results, reduce uncertainty, and extend their application to other Precambrian provinces.

A priority area is the continued refinement of analogue modelling approaches. While the present study successfully reproduced key features of Proterozoic rifting and inversion, further progress requires systematic exploration of parameter space. Analogue materials should be more precisely calibrated to natural rheologies through targeted testing of density–viscosity–friction relationships. Future experiments could incorporate additional complexities such as multiphase deformation, variable sediment loading, or evolving thermal gradients. Importantly, analogue modelling should increasingly be embedded within coupled analogue–numerical workflows, where physical models provide geometries and scaling constraints that can be tested and extended through thermo-mechanical simulations.

Numerical modelling represents another critical frontier. The results of this project emphasise that Proterozoic basins cannot be interpreted solely through Phanerozoic analogues, owing to their development within a hotter, more ductile lithosphere. Future work should therefore move beyond two-dimensional representations toward fully three-dimensional thermo-mechanical simulations capable of resolving oblique extension, nappe collapse, and selective inversion in realistic geometries. Key targets include improved quantification of radiogenic heating, variable lithospheric thickness, and evolving strain rates. Comparative studies across other cratonic settings (e.g., Dharwar, Superior, and Zimbabwe cratons) will be essential to test whether the NAC reflects general Proterozoic behaviour or unique local conditions.

A further priority is the development of integrated predictive frameworks that combine experimental and numerical insights. The Predictive Integrated Data Exploration (PIDE) workflow presented here provides a foundation, but its capability could be enhanced through probabilistic inversions, multi-parameter data integration, and explicit uncertainty quantification. Such frameworks should remain computationally lightweight and open-access, enabling broad adoption across research groups. Iterative cross-comparison between PIDE outputs, analogue models, and numerical simulations will allow more rigorous testing of tectonic and basin evolution hypotheses.

Another key opportunity lies in better integration of fluid flow modelling with structural and rheological evolution. The movement, focusing, and trapping of mineralising fluids are closely linked to the spatial and temporal evolution of strain and permeability. Future studies should explicitly couple mechanical deformation models with fluid flow simulations to predict fluid pathways, pressure gradients, and potential zones of mineral precipitation. Experimental work could explore analogue fluids with density and viscosity contrasts to visualise flow focusing along fault zones, while numerical models could incorporate transient permeability fields and reactive transport processes. Integrating these approaches will provide a more direct bridge between tectonic processes and metallogenic outcomes, enhancing predictive capability for mineral systems within the NAC and comparable Precambrian terranes.

Finally, there is significant scope for methodological innovation. Analogue models could be adapted to incorporate time-dependent rheologies (e.g., visco-elasto-plastic behaviour), while numerical models could explore hybrid scaling schemes that integrate analogue-derived parameters. Incorporating synthetic geophysical observables—such as strain-derived magnetotelluric conductivity or seismic anisotropy—into both analogue and numerical outputs would also help bridge the gap between models and real-world datasets.

In summary, this study demonstrates the value of integrating geophysical, analogue, and numerical methods in unravelling Proterozoic tectonic evolution. The next steps lie in tighter coupling between modelling approaches, systematic parameter exploration, and integrated predictive frameworks that explicitly link deformation, fluid flow, and mineralisation. These are achievable goals for academic research groups, requiring creativity and collaboration rather than large-scale investment, and they promise to significantly advance our understanding of NAC evolution and Precambrian tectonics more broadly.

9. References

Ahmad, M., & Hollis, J. A. (2013). Geological framework of the Pine Creek Orogen. *Geoscience Australia Record*.

Ahmad, M., Hollis, J. A., Lally, J. H., & Carson, L. (2013a). Chapter 2: Pine Creek Orogen. In M. Ahmad & A. Hollis (Eds.), *Geology and mineral resources of the Northern Territory* (pp. 13–34). Northern Territory Geological Survey, Special Publication 5.

Ahmad, M., & Lally, J. H. (2003). *McArthur Basin, Northern Territory* (2nd ed.). Northern Territory Geological Survey, Digital Information Package 007.

Ahmad, M., Lally, J. H., & Hollis, J. A. (2013b). Chapter 3: McArthur Basin. In M. Ahmad & A. Hollis (Eds.), *Geology and mineral resources of the Northern Territory* (pp. 35–64). Northern Territory Geological Survey, Special Publication 5.

Ahmad, M., & McCready, A. J. (2001). Pine Creek Orogen. In D. A. Hutton, I. W. Withnall, & D. M. Bain (Eds.), *Geology of the Australian Proterozoic* (pp. 32–40). Geological Society of Australia, Special Publication 23.

Ahmad, M., & Scrimgeour, I. R. (2013). *Geology and mineral resources of the Northern Territory*. Northern Territory Geological Survey, Special Publication.

Ahmad, M., & Wygralak, A. S. (1989). Gold mineralisation in the Pine Creek Inlier, Northern Territory. Northern Territory Geological Survey, Report 5.

Aitken, A. R. A., Altinay, C., & Gross, L. (2015). Australia's lithospheric density field, and its isostatic equilibration. *Geophysical Journal International, 203*(3), 1961–1976. doi:10.1093/gji/ggv396

Aitken, A. R. A., Salmon, M. L., & Kennett, B. L. N. (2013). Australia's Moho: A test of the usefulness of gravity modelling for the determination of Moho depth. *Tectonophysics, 609*, 468–479. doi:10.1016/j.tecto.2012.06.049

Allemand, P., & Brun, J. P. (1991). Width of continental rifts and rheological layering of the lithosphere. *Tectonophysics, 188*(1–2), 63–69. doi:10.1016/0040-1951(91)90314-I

Allen, P. A., & Allen, J. R. (2005). *Basin analysis: Principles and applications* (2nd ed.). Malden, M. A.: Blackwell Publishing. https://doi.org/10.1002/9781444347166

Allen, C. M., Hand, M., & Barovich, K. M. (2015). Tectonic evolution and metallogenesis of Proterozoic Australia. In Z.-X. Li, D. A. D. Evans, & J. B. Murphy (Eds.), *Supercontinent cycles through Earth history* (pp. 191–226). Geological Society, London, Special Publications, 424. doi:10.1144/SP424.10

Allen, C. M., Murphy, D. T., & Nutman, A. P. (2015). Proterozoic tectonics of northern Australia: Insights from U–Pb zircon geochronology. *Precambrian Research, 271*, 176–196. doi:10.1016/j.precamres.2015.10.002

Autin, J., Bellahsen, N., Leroy, S., Husson, L., Beslier, M. O., & d'Acremont, E. (2010). Fault orientation and basin geometry in oblique rifting. *Geology, 38*(5), 403–406. doi:10.1130/G30695.1

Bagas, L., Bierlein, F. P., Nelson, D. R., & Maas, R. (2014). Paleoproterozoic crustal evolution of the Litchfield Province, Northern Territory, Australia: Constraints from SHRIMP U–Pb zircon geochronology and Sm–Nd isotopes. *Precambrian Research, 249*, 84–100. doi:10.1016/j.precamres.2014.05.007

Beaumont, C., Jamieson, R. A., Nguyen, M. H., & Lee, B. (2000). Orogeny and basin inversion in narrow rifts. *Tectonics, 19*(4), 693–718. doi:10.1029/1999TC001133

Betts, P. G., Ailleres, L., & Raimondo, T. (2016). Australian Proterozoic geodynamics and mineral systems: A review. *Ore Geology Reviews, 76*, 213–250. doi:10.1016/j.oregeorev.2015.06.013

Betts, P. G., Armit, R., Stewart, J., & Ailleres, L. (2008). Australia's Proterozoic "triple point": Implications for Rodinia reconstructions. *Precambrian Research, 166*, 358–373. doi:10.1016/j.precamres.2007.07.009

Betts, P. G., Armit, R. J., Stewart, J., Aitken, A. R. A., Ailleres, L., Donchak, P., Hutton, L., Withnall, I., & Giles, D. (2016). Australia and Nuna. In P. A. Cawood & C. J. Hawkesworth (Eds.), *Earth's Oldest Rocks* (Geological Society Special Publication 424, pp. 47–81). Geological Society of London. doi:10.1144/SP424.2

Betts, P. G., Giles, D., Lister, G. S., & Frick, L. R. (2006). Evolution of the Australian lithosphere. *Australian Journal of Earth Sciences, 53*(1), 151–176. doi:10.1080/08120090500499295

Betts, P. G., Giles, D., Lister, G. S., & Frick, L. R. (2006). Synthesis of the Proterozoic evolution of the Mt Isa Inlier. *Australian Journal of Earth Sciences, 53*(3), 285–301. doi:10.1080/08120090500499239

Betts, P. G., Valenta, R. K., & Finlay, J. (2003). Evolution of the Mount Woods Inlier, northern Gawler Craton, Southern Australia: An integrated structural and aeromagnetic analysis. *Tectonophysics, 366*(1–2), 83–111. doi:10.1016/S0040-1951(03)00062-3

Blaikie, T. N., Betts, P. G., Ailleres, L., & Armit, R. J. (2017). The role of inherited structures during orogenesis in the Palaeoproterozoic Mount Isa Inlier. *Precambrian Research, 292*, 75–93. doi:10.1016/j.precamres.2017.01.019

Blaikie, T. N., & Kunzmann, M. (2020). Basin architecture and tectonic evolution of the McArthur Basin. *Precambrian Research, 338*, 105588. doi:10.1016/j.precamres.2019.105588

Blake, D. H. (1987). *Geology of the Mount Isa Inlier and environs, Queensland and Northern Territory*. Bureau of Mineral Resources, Geology and Geophysics, Bulletin 225.

Blake, D. H., Stewart, A. J., Sweet, I. P., & Hone, I. G. (1979). *Geology of the Proterozoic terrains in the Mount Isa–McArthur River region, Northern Australia*. Bureau of Mineral Resources, Geology and Geophysics, Bulletin 197.

Bott, M. H. P. (1976). Formation of sedimentary basins of graben type by extension of the continental crust. In M. H. P. Bott (Ed.), *Developments in Geotectonics* (Vol. 12, pp. 77–86). Elsevier. doi:10.1016/B978-0-444-41549-3.50009-8

Bradshaw, B. E., Khider, K., MacFarlane, S., Carr, L., & Henson, P. (2021). Tectonostratigraphic evolution of the Centralian Superbasin (Australia) revealed through three-dimensional well correlations. *Geoscience Australia Record*. doi:10.11636/Record.2021.001

Brun, J. P. (1999). Narrow rifts versus wide rifts: Inferences for the mechanics of rifting from laboratory experiments. *Philosophical Transactions of the Royal Society of London A, 357*(1753), 695–712. doi:10.1098/rsta.1999.0349

Brun, J. P., & Nalpas, T. (1996). Graben inversion in nature and experiments. *Tectonics, 15*(3), 677–687. doi:10.1029/95TC03853

Buck, W. R. (1991). Modes of continental lithospheric extension. *Journal of Geophysical Research: Solid Earth, 96*(B12), 20161–20178. doi:10.1029/91JB01485

Buck, W. R., Lavier, L. L., & Poliakov, A. N. B. (1999). How to make a rift wide. *Philosophical Transactions of the Royal Society of London A, 357*(1753), 671–693. doi:10.1098/rsta.1999.0348

Buiter, S. J. H., et al. (2009). The numerical sandbox: Comparison of model results for a shortening and an extension experiment. *Geosphere, 5*(5), 1–31. doi:10.1130/GES00563.1

Cawood, P. A., & Korsch, R. J. (2008). Assembling Australia: Proterozoic building of a continent. *Precambrian Research, 166*(1–4), 1–35. doi:10.1016/j.precamres.2008.08.006

Champion, D. C. (2013). The crustal evolution of northern Australia. *Geoscience Australia Record*.

Champion, D. C. (2013). Neodymium depleted mantle model age map of Australia: Explanatory notes and user guide. *Geoscience Australia Record 2013/44*. doi:10.11636/Record.2013.044

Chen, Y., Saygin, E., Kennett, B., Qashqai, M. T., Hauser, J., Lumley, D., & Sandiford, M. (2023). Next-generation seismic model of the Australian crust from synchronous and asynchronous ambient noise imaging. *Nature Communications, 14*(1), 1192. doi:10.1038/s41467-023-36514-z

Chenin, P., et al. (2018). Lithospheric thinning and thermomechanical controls on rift evolution. *Tectonics, 37*(10), 4199–4229. doi:10.1029/2018TC005152

Claoué-Long, J. C., & Hoatson, D. M. (2009). Guide to using the map of Australian Proterozoic large igneous provinces. *Geoscience Australia Record*.

Codd, A. L., Gross, L., & Aitken, A. (2021). Fast multi-resolution 3D inversion of potential fields with application to high-resolution gravity and magnetic anomaly data from the Eastern Goldfields in Western Australia. *Computers & Geosciences, 157*, 104941. doi:10.1016/j.cageo.2021.104941

Corti, G. (2009). Continental rift evolution: From rift initiation to incipient break-up in the Main Ethiopian Rift, East Africa. *Earth-Science Reviews, 96*(1–2), 1–53. doi:10.1016/j.earscirev.2009.06.005

Crawford, B. L., Betts, P. G., & Aillères, L. (2010). An aeromagnetic approach to revealing buried basement structures and their role in the Proterozoic evolution of the Wernecke Inlier. *Precambrian Research, 177*(1–2), 81–92. doi:10.1016/j.precamres.2009.11.004

de Laat, J. I., Lebedev, S., Celli, N. L., Bonadio, R., Chagas de Melo, B., & Rawlinson, N. (2023). Structure and evolution of the Australian plate and underlying upper mantle from waveform tomography with massive data sets. *Geophysical Journal International, 234*(1), 153–189. doi:10.1093/gji/ggad062

Dentith, M., & Mudge, S. T. (2014). *Geophysics for the mineral exploration geoscientist*. Cambridge University Press. doi:10.1017/CBO9781139024358

Dunlap, W. J. (1992). The tectonic evolution of the Harts Range Metamorphic Complex, central Australia: Constraints from 40Ar/39Ar geochronology. *Tectonics, 11*(6), 1256–1274. doi:10.1029/92TC01003

Ebinger, C. J. (2005). Continental break-up: The East African perspective. *Astronomical and Geophysical Review, 43*, 379–410.

Eisenstadt, G., & Sims, D. (2005). Evaluating sand and clay models: Do rheological differences matter? *Journal of Structural Geology, 27*(9), 1399–1412. doi:10.1016/j.jsg.2005.04.010

Fishwick, S., & Rawlinson, N. (2012). 3-D structure of the Australian lithosphere from evolving seismic datasets. *Australian Journal of Earth Sciences, 59*(6), 809–826. doi:10.1080/08120099.2012.702319

Forman, D. J. (1971). *The geology of the Harts Range area, Northern Territory*. BMR Bulletin, 118.

Forsyth, D. W., & Uyeda, S. (1975). On the relative importance of the driving forces of plate motion. *Geophysical Journal International, 43*(1), 163–200. doi:10.1111/j.1365-246X.1975.tb00631.x

Fraser, G. L., Neumann, N. L., & Bodorkos, S. (2008). SHRIMP U–Pb zircon age constraints on Paleoproterozoic deformation in the Litchfield Province, Northern Territory. *Australian Journal of Earth Sciences, 55*(5), 663–677. doi:10.1080/08120090802120145

Geognostics. (2021). OZ SEEBASE® 2021 [Dataset]. Geognostics Australia Pty Ltd. doi:10.5281/zenodo.5632267

Glass, L. M., et al. (2010). Magmatism of the Kalkarindji Large Igneous Province: Petrogenesis of the oldest and most voluminous continental flood basalt province on Earth. *Lithos, 119*(3–4), 295–316. doi:10.1016/j.lithos.2010.07.014

Goleby, B. R., et al. (2009). Deep seismic reflection profiling in the Pine Creek Orogen: Implications for tectonic evolution and gold mineralisation. *Precambrian Research, 168*(3–4), 153–166. doi:10.1016/j.precamres.2008.09.002

Greene, D. (2010). Inversion tectonics of the Georgina Basin. *Australian Journal of Earth Sciences, 57*(4), 511–530. doi:10.1080/08120091003696788

Gross, L., Bourgouin, L., Hale, A. J., & Mühlhaus, H.-B. (2007). Interface modeling in incompressible media using level sets in Escript. *Physics of the Earth and Planetary Interiors, 163*(1–4), 23–34. doi:10.1016/j.pepi.2007.04.004

Gunn, P. J., Maidment, D., Milligan, P. R., & Morse, M. P. (1997). Interpreting aeromagnetic data in areas of limited outcrop. *AGSO Journal of Australian Geology & Geophysics, 17*(2), 175–185.

Haeger, C., Petrunin, A. G., & Kaban, M. K. (2022). Geothermal heat flow and thermal structure of the Antarctic lithosphere. *Geochemistry, Geophysics, Geosystems, 23*(10), e2022GC010501. doi:10.1029/2022GC010501

Hall, A. S., Holford, S., Schofield, N., Bunch, M., Collins, A. S., Blades, M. L., & Subarkah, D. (2024). The Derim Derim Dolerite, greater McArthur Basin, Australia: Using subsurface data to characterise a Mesoproterozoic magma plumbing system. *Marine and Petroleum Geology, 169*, 107072. doi:10.1016/j.marpetgeo.2024.107072

Hand, M., & Betts, P. G. (2006). The Proterozoic evolution of the North Australian Craton. *Australian Journal of Earth Sciences, 53*(1), 11–25. doi:10.1080/08120090500499295

Hansen, D. L., & Nielsen, S. B. (2003). Basin inversion and rheology. *Tectonophysics, 373*(1–4), 5–23. doi:10.1016/S0040-1951(03)00286-9

Hazzard, J. A. N., Richards, F. D., Goes, S. D. B., & Roberts, G. G. (2023). Probabilistic assessment of Antarctic thermomechanical structure: Impacts on ice sheet stability. *Journal of Geophysical Research: Solid Earth, 128*(5), e2023JB026653. doi:10.1029/2023JB026653

Hendrickx, M. A., et al. (2000). *Geology and tectonic evolution of the Tanami Region, Northern Territory*. Northern Territory Geological Survey, Report 11.

Hoggard, M. J., Czarnota, K., Richards, F. D., Huston, D. L., Jaques, A. L., & Ghelichkhan, S. (2020). Global distribution of sediment-hosted metals controlled by craton edge stability. *Nature Geoscience, 13*(7), 504–510. doi:10.1038/s41561-020-0593-2

Hoggard, M., Hazzard, J., Sudholz, Z., Richards, F., Duvernay, T., Austermann, J., Jaques, A. L., Yaxley, G., Czarnota, K., & Haynes, M. (2024). Thermomechanical models of the Australian plate. *Commonwealth of Australia (Geoscience Australia), Exploring for the Future: Extended Abstracts*. doi:10.26186/149411

Hollis, J. A., et al. (2009a). SHRIMP U–Pb geochronology of the eastern Pine Creek Orogen: Constraints on tectonic evolution. *Australian Journal of Earth Sciences, 56*(3), 341–357. doi:10.1080/08120090802673410

Hollis, J. A., et al. (2009b). Sedimentology and stratigraphy of the Pine Creek Orogen: Implications for basin development. *Precambrian Research, 168*(3–4), 168–189. doi:10.1016/j.precamres.2008.09.001

Hollis, J. A., et al. (2011). Geochronological constraints on Paleoproterozoic basin evolution in the Pine Creek Orogen. *Precambrian Research, 187*(1–2), 1–24. doi:10.1016/j.precamres.2011.02.005

Holzschuh, J., Gorbatov, A., Hejrani, B., Boehm, C., & Hassan, R. (2024). Tomographic model of the Australian region from seismic full waveform inversion. *Exploring for the Future: Extended Abstracts.*

Huismans, R. S., & Beaumont, C. (2011). Depth-dependent extension, two-stage breakup and cratonic underplating at rifted margins. *Nature, 473*(7345), 74–78. doi:10.1038/nature09988

Huston, D., Champion, D. C., Lyons, P., Lambeck, A., & Mernagh, T. (2020). Tectono-metallogenic framework of Australia: A review and synthesis. *Ore Geology Reviews, 127*, 103780. doi:10.1016/j.oregeorev.2020.103780

Iaccheri, L. M. (2017). *Isotopic and geochemical evolution of the Halls Creek Orogen* (Doctoral dissertation). University of Adelaide.

Iaccheri, L. M. (2019). Crustal growth and reworking in the Halls Creek Orogen: Constraints from zircon U–Pb–Hf and Sm–Nd isotopic data. *Precambrian Research, 324*, 1–21. doi:10.1016/j.precamres.2019.01.004

Ibrahim, Y., Rey, P. F., Whitney, D. L., Teyssier, C., Roger, F., & Bosse, V. (2023). From dome to duplex: Convergent gravitational collapse explains coeval intracratonic doming and nappe tectonics, central Australia. *Geology, 52*(3), 210–215. doi:10.1130/G51721.1

Jackson, M. J., Powell, T. G., & Summons, R. E. (2000). Stratigraphy and basin evolution of the Isa Superbasin. *Australian Journal of Earth Sciences, 47*(3), 403–420. doi:10.1046/j.1440-0952.2000.00789.x

Jackson, M. J., Scott, D. L., & Rawlings, D. J. (2000). Stratigraphic framework for the Leichhardt and Calvert Superbasins: Review and correlations of the pre-1700 Ma successions between Mt Isa and McArthur River. *Australian Journal of Earth Sciences, 47*(3), 381–403. doi:10.1046/j.1440-0952.2000.00789.x

Jiang, W., Korsch, R. J., Doublier, M. P., Duan, J., & Costelloe, R. (2019). Mapping deep electrical conductivity structure in the Mount Isa region, Northern Australia: Implications for mineral prospectivity. *Journal of Geophysical Research: Solid Earth, 124*(11), 10655–10671. doi:10.1029/2019JB017528

Joly, A., et al. (2010). Lithospheric architecture and gold metallogeny of the Tanami Region. *Precambrian Research, 183*(1), 1–24. doi:10.1016/j.precamres.2010.06.010

Kennett, B. L. N., Fichtner, A., Fishwick, S., & Yoshizawa, K. (2013). Australian Seismological Reference Model (AuSREM): Mantle component. *Geophysical Journal International, 192*(2), 871–887. doi:10.1093/gji/ggs065

Kennett, B. L. N., Gorbatov, A., Yuan, H., Agrawal, S., Murdie, R., Doublier, M. P., Eakin, C. M., Miller, M. S., Zhao, L., Czarnota, K., O'Donnell, J. P., Dentith, M., & Gessner, K. (2023). Refining the Moho across the Australian continent. *Geophysical Journal International, 233*(3), 1863–1877. doi:10.1093/gji/ggad035

Klöcking, M., Czarnota, K., Champion, D., Jaques, A., & Davies, D. R. (2020). Spatio-temporal evolution of Australian lithosphere–asthenosphere boundary from mafic volcanism. *Commonwealth of Australia (Geoscience Australia), Exploring for the Future: Extended Abstracts*. doi:10.11636/135075

Kohanpour, F., et al. (2018). Geochemical and isotopic signatures of Paleoproterozoic granitoids in the Tanami Region. *Precambrian Research, 309*, 235–250. doi:10.1016/j.precamres.2018.03.012

Kohanpour, F., et al. (2020). U–Pb zircon geochronology and Nd isotopic constraints on crustal evolution in the Tanami Region. *Precambrian Research, 340*, 105602. doi:10.1016/j.precamres.2019.105602

Korsch, R. J., et al. (2011). Geodynamic synthesis of the North Australian Craton. *Episodes, 34*(1), 19–31. doi:10.18814/epiiugs/2011/v34i1/004

Korsch, R. J., et al. (2012). Deep seismic reflection profiling in the NAC. *Tectonophysics, 572–573*, 76–99. doi:10.1016/j.tecto.2012.02.027

Kositcin, N., et al. (2018). Precambrian crustal evolution of northern Australia: SHRIMP and Nd isotope constraints. *Australian Journal of Earth Sciences, 65*(2), 221–241. doi:10.1080/08120099.2018.1424047

Kraus, S., et al. (2015). U–Pb geochronology of Paleoproterozoic events in the NAC. *Precambrian Research, 269*, 203–220. doi:10.1016/j.precamres.2015.07.010

Kruse, P. D., et al. (2010). *Stratigraphy and tectonics of the McArthur Basin*. Northern Territory Geological Survey, Report 20.

Kumwenda, J., Betts, P., & Armit, R. (2024). Geophysical insights into basement faults influencing basin evolution: Tennant Creek Block, NAC. *Precambrian Research, 406*, 107403. doi:10.1016/j.precamres.2023.107403

Kumwenda, H., Betts, P. G., Raimondo, T., Donnellan, N., & Lyons, P. (2023). Exposing basement terranes of the North Australian Craton using integrated geophysical and isotopic datasets. *Earth-Science Reviews, 237*, 104310. doi:10.1016/j.earscirev.2023.104310

Kumwenda, H., Betts, P. G., Raimondo, T., Donnellan, N., & Lyons, P. (2024). Mapping crustal provinces beneath cover: Integrated isotopic–geophysical approaches in the North Australian Craton. *Tectonics, 43*(5), e2024TC007567. doi:10.1029/2024TC007567

Lally, J. H. (2002). *Geology and mineral resources of the Katherine region*. Northern Territory Geological Survey, Report 17.

Large, R. R., Bull, S. W., McGoldrick, P. J., & Walters, S. (2005). Stratiform and strata-bound Zn-Pb-Ag deposits in Proterozoic sedimentary basins, northern Australia. *Economic Geology, 100th Anniversary Volume*, 931–963. doi:10.5382/AV100.30

Li, L., Aitken, A. R. A., Gross, L., & Codd, A. (2025). Resolving mantle composition suggests a warmer East Antarctic mantle. *Journal of Geophysical Research: Solid Earth, 130*(3), e2024JB029677. doi:10.1029/2024JB029677

Li, Z. X., Bagas, L., Bodorkos, S., Maidment, D., Wingate, M. T. D., & Johnson, S. P. (2014). Tectonothermal evolution of the Palaeoproterozoic Litchfield Province: Implications for Nuna amalgamation. *Precambrian Research, 249*, 190–211. doi:10.1016/j.precamres.2014.05.016

Li, Z. X., et al. (2014). Tectonic models for Paleoproterozoic assembly of Australia. *Precambrian Research, 243*, 1–24. doi:10.1016/j.precamres.2013.12.012

Lindsey, M., et al. (2016). Isotopic evidence for multiple Paleoproterozoic magmatic events in northern Australia. *Precambrian Research, 282*, 123–139. doi:10.1016/j.precamres.2016.07.009

Lösing, M., Moorkamp, M., & Ebbing, J. (2023). Joint inversion based on variation of information—A crustal model of Wilkes Land, East Antarctica. *Geophysical Journal International, 232*(1), 162–175. doi:10.1093/gji/ggac334

MacFerrin, M., Amante, C., Carignan, K., Love, M., & Lim, E. (2025). The Earth Topography 2022 (ETOPO 2022) global DEM dataset. *Earth System Science Data, 17*(5), 1835–1849. doi:10.5194/essd-17-1835-2025

Magrini, F., Kästle, E., Pilia, S., Rawlinson, N., & De Siena, L. (2023). A new shear-velocity model of continental Australia based on multi-scale surface-wave tomography. *Journal of Geophysical Research: Solid Earth, 128*(7), e2023JB026688. doi:10.1029/2023JB026688

Maidment, D. C., et al. (2013). Tectonic evolution of the Pine Creek Orogen and links to Nuna assembly. *Geoscience Australia Record* 2013/25.

Maidment, D. C., et al. (2020). Paleoproterozoic orogenesis in northern Australia: New SHRIMP zircon ages. *Precambrian Research, 343*, 105713. doi:10.1016/j.precamres.2020.105713

Maidment, D. W., Shaw, R. D., & Hand, M. (2013). Crustal architecture of the Arunta Inlier and implications for Proterozoic tectonics. *Gondwana Research, 23*(1), 114–132. doi:10.1016/j.gr.2012.02.012

Maidment, D. W., Williams, H., & Hand, M. (2013). Tectonic evolution of the Arunta Inlier: Implications for Proterozoic Australia. *Precambrian Research, 230*, 1–20. doi:10.1016/j.precamres.2013.01.014

Maidment, D. W., et al. (2013). The tectonic framework of the Arunta Region, central Australia: Implications for mineral exploration. *Precambrian Research, 246*, 1–19. doi:10.1016/j.precamres.2013.07.004

McDonald, B., Goleby, B. R., Swager, C. P., Etheridge, M. A., & Wellman, P. (1997). Crustal architecture of the Yilgarn Craton, Western Australia. *AGSO Journal of Australian Geology & Geophysics, 17*, 79–91.

McDonald, B., et al. (1997). Basement terranes of northern Australia. *AGSO Journal of Australian Geology & Geophysics, 17*(2), 63–76.

Mencos, J., Muñoz, J. A., Carrera, N., Beamud, E., & Brown, D. (2015). Influence of rift basin geometry on the subsequent orogenic evolution: The case of the Basque–Cantabrian Basin (Pyrenees–Cantabrian Mountains). *Geological Society, London, Special Publications, 413*(1), 187–208. doi:10.1144/SP413.6

Molnar, J., Cruden, A. R., & Betts, P. G. (2017). Interplay of rheology and strain rate in lithospheric-scale analogue experiments. *Tectonophysics, 694*, 272–284. doi:10.1016/j.tecto.2016.11.033

Molnar, J., et al. (2017). Crustal inheritance and reactivation of basement faults. *Journal of Structural Geology, 94*, 1–15. doi:10.1016/j.jsg.2016.11.005

Moorkamp, M., Heincke, B., Jegen, M., Roberts, A. W., & Hobbs, R. W. (2011). A framework for 3-D joint inversion of MT, gravity and seismic refraction data. *Geophysical Journal International, 184*(1), 477–493. doi:10.1111/j.1365-246X.2010.04856.x

Morgan, P., & Ramberg, H. (1987). Physical models of basement control of sedimentary basin evolution. *Tectonophysics, 132*(1–3), 31–45. doi:10.1016/0040-1951(87)90315-6

Moro, P. S., Aitken, A. R. A., Kohanpour, F., & Jessell, M. W. (2024). Anomalously fertile subcontinental lithospheric mantle beneath the intracontinental Canning Basin, Western Australia. *Geophysical Journal International, 239*(2), 769–797. doi:10.1093/gji/ggae258

Myers, J. S., Shaw, R. D., & Tyler, I. M. (1996). Precambrian geology of the Northern Territory. *AGSO Journal of Australian Geology and Geophysics, 16*(3), 1–21.

Needham, R. S., Stuart-Smith, P. G., & Page, R. W. (1988). Tectonic evolution of the Pine Creek Inlier, Northern Territory. *BMR Bulletin, 229*.

Neumann, N., & Fraser, G. (2007). Proterozoic basin evolution, central NAC. *Australian Journal of Earth Sciences, 54*(5), 691–711. doi:10.1080/08120090701305277

Nimis, P., & Taylor, W. R. (2000). Single clinopyroxene thermobarometry for garnet peridotites. Part I. Calibration and testing of a Cr-in-Cpx barometer and an enstatite-in-Cpx thermometer. *Contributions to Mineralogy and Petrology, 139*(5), 541–554. doi:10.1007/s004100000156

Nixon, A. L., Glorie, S., Collins, A. S., Blades, M. L., Simpson, A., & Whelan, J. A. (2022). Inter-cratonic geochronological and geochemical correlations of the Derim Derim–Galiwinku/Yanliao reconstructed Large Igneous Province across the North Australian and North China cratons. *Gondwana Research, 103*, 473–486. doi:10.1016/j.gr.2021.10.027

Northern Territory Geological Survey (NTGS). (2019). *Solid geology of the North Australian Craton*. Digital GIS dataset. Darwin: NTGS.

Offler, R., & Ferguson, J. (1976). Progressive low-grade metamorphism in the Proterozoic McArthur Basin, Northern Territory. *Journal of the Geological Society of Australia, 23*(4), 377–392. doi:10.1080/00167617608728973

O'Neill, C., Lenardic, A., & Moresi, L. (2007). Dynamics of cratons in an evolving mantle. *Lithos, 102*(1–2), 12–24. doi:10.1016/j.lithos.2007.05.010

Pang, K., et al. (2022). Integrated magnetotelluric imaging of Proterozoic basins in northern Australia. *Earth and Planetary Science Letters, 593*, 117707. doi:10.1016/j.epsl.2022.117707

Pesonen, L. J., Elming, S. Å., Mertanen, S., Pisarevsky, S. A., D'Agrella-Filho, M. S., Meert, J. G., … & Smethurst, M. A. (2003). Paleomagnetic constraints on the Proterozoic supercontinent Nuna. *Gondwana Research, 6*(1), 67–85. doi:10.1016/S1342-937X(05)70965-9

Pether, J., et al. (2016). Proterozoic basin inversion and mineralisation in northern Australia. *Ore Geology Reviews, 76*, 251–268. doi:10.1016/j.oregeorev.2015.11.003

Poudjom Djomani, Y. H., O'Reilly, S. Y., Griffin, W. L., & Morgan, P. (2001). The density structure of subcontinental lithosphere through time. *Earth and Planetary Science Letters, 184*(3–4), 605–621. doi:10.1016/S0012-821X(00)00362-9

Pryer, L. L., & Connors, K. A. (2015). The influence of crustal architecture on mineral systems in northern Australia. *Ore Geology Reviews, 71*, 575–592. doi:10.1016/j.oregeorev.2015.02.009

Rawlings, D. J., et al. (2008). Stratigraphic evolution of the McArthur Basin. *Australian Journal of Earth Sciences, 55*(1), 3–31. doi:10.1080/08120090701689359

Rawlinson, N., Kennett, B. L. N., Vanacore, E., Glen, R. A., & Fishwick, S. (2014). Rapid multi-scale inversion of seismic data to map lithospheric structure beneath eastern Australia. *Journal of Geophysical Research: Solid Earth, 119*(8), 6688–6711. doi:10.1002/2014JB011163

Rawlinson, N., Pilia, S., Young, M., Salmon, M., & Kennett, B. L. N. (2016). Seismic tomography beneath Australia: Recent advances and future prospects. *Journal of Asian Earth Sciences, 111*, 56–70. doi:10.1016/j.jseaes.2015.06.013

Reeve, J. S., et al. (1990). Geology of the Mount Isa Inlier. *BMR Bulletin, 235*.

Rey, P. F., Teyssier, C., Whitney, D. L., & Roger, F. (2010). The role of lithospheric inheritance in the evolution of orogenic systems. *Tectonophysics, 480*(1–4), 33–47. doi:10.1016/j.tecto.2009.09.027

Ritzmann, O., Faleide, J. I., Bungum, H., Mooney, W. D., & Detweiler, S. (2007). Crustal structure of the Barents Sea: New constraints from gravity and seismic data. *Geophysical Journal International, 171*(2), 901–916. doi:10.1111/j.1365-246X.2007.03554.x

Roche, V., et al. (2018). Oblique extension and basin segmentation in analogue experiments. *Tectonophysics, 746*, 682–698. doi:10.1016/j.tecto.2018.02.021

Rosenbaum, G., & Allen, C. M. (2017). Proterozoic tectonic evolution of Australia: A review. *Earth-Science Reviews, 173*, 1–27. doi:10.1016/j.earscirev.2017.07.004

Rosenbaum, G., Giles, D., Saxon, M., Betts, P. G., Weinberg, R. F., & Duboz, C. (2005). Subduction rollback and the tectonic evolution of the Lachlan Orogen. *Tectonics, 24*(1), TC1009. doi:10.1029/2004TC001679

Rudge, J. F., McKenzie, D., & Haynes, C. (2008). A theoretical model for U–Pb isotopic evolution of zircon. *Earth and Planetary Science Letters, 273*(1–2), 138–149. doi:10.1016/j.epsl.2008.06.015

Sandiford, M., Hand, M., & McLaren, S. (1998). Tectonic feedback, intraplate orogeny and crustal force balance. *Earth-Science Reviews, 44*(3–4), 91–134. doi:10.1016/S0012-8252(98)00020-1

Scott, D. L., et al. (2000). Tectonic framework and basin evolution of the North Australian Craton. *Geoscience Australia Record*.

Shaw, R. D., Etheridge, M. A., & Lambeck, K. (1991). Development of the Australian lithosphere. *Geological Society of Australia Special Publication, 17*, 1–16.

Shuster, D. L., & Farley, K. A. (2005). Diffusion kinetics of proton-induced ^{4}He production in apatite, zircon, and titanite: Implications for (U–Th)/He thermochronometry. *Geochimica et Cosmochimica Acta, 69*(9), 2349–2359. doi:10.1016/j.gca.2004.11.002

Silver, P. G., & Behn, M. D. (2008). Intermittent plate tectonics? *Science, 319*(5859), 85–88. doi:10.1126/science.1148399

Simpson, C., & Schmid, S. M. (1983). An evaluation of criteria to deduce the sense of movement in sheared rocks. *Geological Society of America Bulletin, 94*(11), 1281–1288. doi:10.1130/0016-7606(1983)94<1281:AEOCTD>2.0.CO;2

Spaggiari, C. V., Kirkland, C. L., Smithies, R. H., Occhipinti, S. A., Wingate, M. T. D., & Belousova, E. (2015). Tectonostratigraphic evolution of the Albany-Fraser Orogen. *Precambrian Research, 266*, 440–463. doi:10.1016/j.precamres.2014.11.001

Stern, R. J. (2005). Evidence from ophiolites, blueschists, and ultrahigh-pressure metamorphic terranes that the modern episode of subduction tectonics began in Neoproterozoic time. *Geology, 33*(7), 557–560. doi:10.1130/G21365.1

Stewart, J., Betts, P. G., & Hall, M. (2001). Mesoproterozoic tectonic framework and basin evolution of northern Australia. *Australian Journal of Earth Sciences, 48*(6), 987–1001. doi:10.1046/j.1440-0952.2001.00905.x

Sun, S. S., & McDonough, W. F. (1989). Chemical and isotopic systematics of oceanic basalts: Implications for mantle composition and processes. In A. D. Saunders & M. J. Norry (Eds.), Magmatism in the Ocean Basins (Vol. 42, pp. 313–345). *Geological Society, London, Special Publications*. doi:10.1144/GSL.SP.1989.042.01.19

Sweet, I. P., Brakel, A. T., & Rawlings, D. J. (1999). Mount Isa Basin stratigraphy. *Australian Journal of Earth Sciences, 46*(3), 337–354. doi:10.1046/j.1440-0952.1999.00707.x

Tappert, R., Stachel, T., Harris, J. W., Muehlenbachs, K., Ludwig, T., & Brey, G. P. (2005). Subducting oceanic crust: The source of deep diamonds. *Geology, 33*(7), 565–568. doi:10.1130/G21270.1

Torsvik, T. H., Van der Voo, R., Preeden, U., Mac Niocaill, C., Steinberger, B., Doubrovine, P. V., … & Cocks, L. R. M. (2012). Phanerozoic polar wander, palaeogeography and dynamics. *Earth-Science Reviews, 114*(3–4), 325–368. doi:10.1016/j.earscirev.2012.06.007

Veevers, J. J. (2000). *Billion-year Earth history of Australia and neighbours in Gondwanaland*. GEMOC Press, Sydney.

Veevers, J. J., & Powell, C. M. (1984). Relative motions of Australia and Antarctica since the Early Cretaceous. *Bureau of Mineral Resources, Geology and Geophysics Bulletin 187*.

Wellman, P. (1988). Mapping of geophysical domains in the Australian continental crust. *Australian Journal of Earth Sciences, 35*(3), 263–279. doi:10.1080/08120098808729440

Whitmeyer, S. J., & Karlstrom, K. E. (2007). Tectonic model for the Proterozoic growth of North America. *Geosphere, 3*(4), 220–259. doi:10.1130/GES00055.1

Williams, H., Betts, P. G., & Ailleres, L. (2009). Evolution of Proterozoic Australia: Implications from 4D geodynamic modelling. *Precambrian Research, 168*(3–4), 250–259. doi:10.1016/j.precamres.2008.09.004

Wyborn, L. A. I., Henson, P. A., & Heinrich, C. A. (1998). Australian Proterozoic mineral systems: Essential ingredients and mappable criteria. *Australian Journal of Earth Sciences, 45*(6), 977–1008. doi:10.1080/08120099808728414

Yakymchuk, C., & Brown, M. (2019). Extrusion and exhumation of partially molten crust during orogenesis. *Tectonophysics, 789*, 228549. doi:10.1016/j.tecto.2019.228549

Zhao, J., McCulloch, M. T., & Bennett, V. C. (2002). Nd and Sr isotopic constraints on the age and origin of crustal components of the northern Australian lithosphere. *Precambrian Research, 113*(1–2), 1–22. doi:10.1016/S0301-9268(01)00214-7

Zhao, J.-X., McCulloch, M. T., & Korsch, R. J. (1994). Sm–Nd isotopic study of Proterozoic basement rocks in northern Australia: Implications for crustal evolution. *Precambrian Research, 67*(1–2), 1–35. doi:10.1016/0301-9268(94)90057-4